UNIVERSITÀ DEGLI STUDI DI MILANO

FACOLTÀ DI SCIENZE E TECNOLOGIE

Ph.D. School in Physics, Astrophysics and Applied Physics

Cycle XXXVI

Observational constraints of the interaction between planets and protoplanetary disks

Supervisor:
Prof. Leonardo Testi

Co-Supervisors:
Prof. Marco Lombardi
Dr. Francesco Borsa

Director of the Ph.D. School:
Prof. Roberta Vecchi

Ph.D. Candidate:
Pietro Curone

Academic Year 2022 - 2023

Commission of the final examination:

External Referees:
Prof. Cornelis P. Dullemond
Prof. Laura M. Pérez

External Members:
Prof. Cornelis P. Dullemond
Dr. François Ménard

Internal Member:
Prof. Giuseppe Lodato

Final examination:

Date 5th of February 2024

Università degli Studi di Milano, Dipartimento di Fisica, Milano, Italy

Cover illustration:

Gallery of observations and simulations of the protoplanetary disks studied in this Thesis. Top left panels: ALMA observations and numerical simulations of CIDA 1. Top right panels: ALMA and VLA observations of CX Tau. Bottom panels: ALMA observations of the exoALMA disks.

MIUR subjects:

FIS/05

PACS:

97.82.Jw, 97.10.Gz

Contents

CHAPTER 1

From exoplanet search to protoplanetary disks

The International Astronomical Union (IAU) defines a planet[1] as an object orbiting a star, massive enough to overcome rigid body forces, resulting in a (nearly) round shape, and capable of clearing its orbit from other objects. While historical knowledge was limited to the planets within the Solar System, our current understanding has broadened to include the existence of thousands of planets orbiting stars other than our Sun, called *exoplanets*. The very first detection of an exoplanet was announced by Wolszczan & Frail (1992), who discovered a planetary system around the millisecond pulsar PSR1257 + 12. The first planet found orbiting a main sequence star was reported by Mayor & Queloz (1995), with the discovery of 51 Pegasi b, a gas giant planet around a star similar to the Sun. This finding inaugurated a new research field: the investigation of exoplanets. Immediately, it posed a challenge to contemporary theories of planet formation, as the newfound planet differed significantly from those in our the Solar System. Termed a "hot Jupiter", this planet orbits its host star at 0.05 au, in contrast to the gas giant planets in the Solar System located at 5 au and beyond.

Over nearly three decades, the exoplanet research has witnessed a huge progress, marked by the development of diverse detection techniques. The pivotal discovery of 51 Peg b was achieved through the *radial velocity* method. This approach involves measuring shifts in a stellar velocity toward us, induced by the gravitational pull of an orbiting planet, and measured through Doppler effect-induced changes in the star's spectral lines. The *direct imaging* method captures the light emitted by the planet itself, providing a direct visual observation separate from the host star as depicted in Fig. 1.1. The most prolific approach for exoplanet discovery became the *transit* method, consisting in the observation of the slight dimming of a star's light as a planet passes in front of it. The Kepler spacecraft, launched by NASA in 2009 and operative until 2018, played a crucial role in exoplanet search using the transit method.

These methods have led to the discovery of more than 5500 exoplanets[2], enabling to build a statistical view of their properties. Figure 1.2 illustrates the relation between the planetary mass and the orbital semi-major axis for confirmed exoplanets and planets within the Solar System. The main insight from this plot is the distinct position of all the planets in the Solar System, with the exception of Jupiter, which appear as outliers in

[1] https://www.iau.org/public/themes/pluto/
[2] As of November 2023 from https://exoplanet.eu/home/

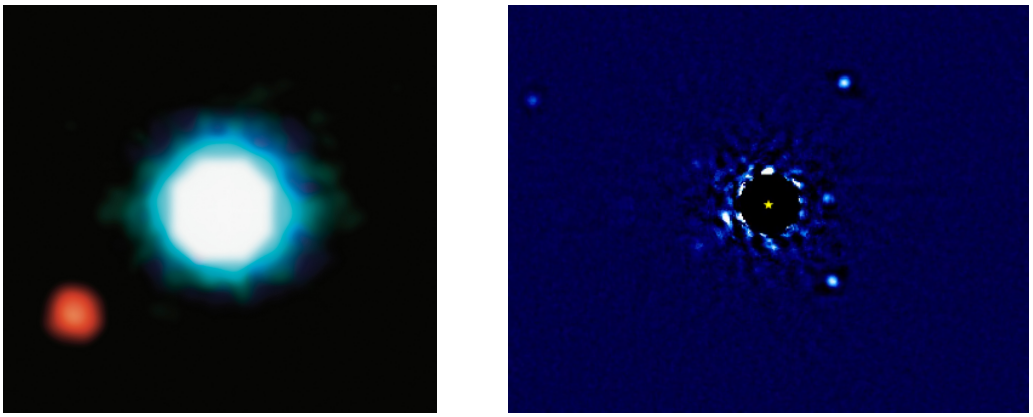

Figure 1.1: Notable examples of directly imaged exoplanets. *Left panel*: The first image of an exoplanet, orbiting around the brown dwarf 2M120 and observed with VLT/NACO (Chauvin et al. 2004). *Right panel*: The planetary system consisting of four gas giants around HR 8799 imaged by the W. M. Keck Observatory (Wolszczan & Frail 1992).

the broader population. The plot delineates three denser regions, corresponding to the three most prevalent types of exoplanets. These include Super-Earths, characterized by masses greater than Earth but less than Neptune; Hot Jupiters, planets akin to Jupiter in size and mass but with much closer orbits to their host stars; and cold gas giants resembling Jupiter. It is noteworthy that the Solar System lacks Super-Earths or Hot Jupiters, and, interestingly, we have not yet discovered exoplanets resembling the planets in the Solar System, except for Jupiter, even though observational biases must be taken into account. To comprehend the reasons behind the differences between our Solar System and the observed exoplanetary systems, it is imperative to delve into the process of planet formation.

The star and planet formation process happens in *Giant Molecular Clouds* (GMC), structures composed of gas (mostly molecular hydrogen) and dust, with a dust-to-gas mass ratio of the order of 1:100. GMCs are dominated by turbulence (Larson 1981) and present over-dense regions called *molecular cloud cores*. Star formation starts from the collapse of these cores, caused by gravitational instability. Observations of star forming regions showed that molecular cloud cores are characterized by rotation (Goodman et al. 1993). As a consequence, the conservation of angular momentum plays a key role in the collapse of cloud cores, increasing the angular velocity of the contracting core. This generates a strong centrifugal force, that prevents a radial collapse in favor of the formation of a disk, called *protostellar/protoplanetary disk*. Planets eventually emerge from the material within this disk.

A system transitioning from a collapsing molecular cloud to a stable main sequence star is referred to as *Young Stellar Objects* (YSOs). YSOs are characterized by three main components:

- *Pre-main-sequence star*. It is still in a contraction phase and emits radiation both by nuclear fusion and releasing gravitational energy during the collapse.

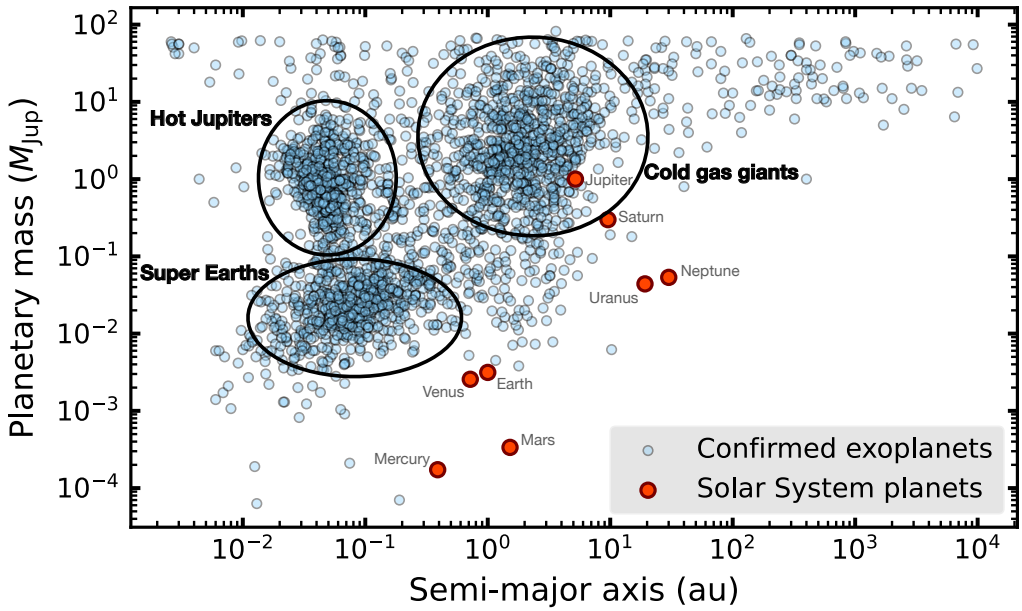

Figure 1.2: Planetary mass as a function of orbital semi-major axis for all the confirmed exoplanets and the Solar System planets. Data are from https://exoplanet.eu/home/.

- *Disk*. Its luminosity arises from a combination of accretion, where gravitational energy is transformed into radiation, and the presence of stellar light either scattered by the disk surface or absorbed and subsequently re-emitted at infrared or sub-μm wavelengths.
- *Spherical envelope*. This external cold envelope surrounds the other components and absorbs and re-emits at lower wavelengths their radiative emissions.

YSOs are classified by their *Spectral Energy Distribution* (SED) in the infrared part of the spectrum (Lada & Wilking 1984). Defining F_λ the flux per unit wavelength and F_ν the flux per unit frequency, we have $\lambda F_\lambda = \nu F_\nu$. SEDs are described by their *spectral index*

$$s \equiv \frac{\mathrm{d}\log(\lambda F_\lambda)}{\mathrm{d}\log\lambda} = -\frac{\mathrm{d}\log(\nu F_\nu)}{\mathrm{d}\log\nu}, \tag{1.1}$$

typically measured in the range of wavelengths from $\sim 2\,\mu\mathrm{m}$ to $\sim 50 - 100\,\mu\mathrm{m}$. As illustrated in Figure 1.3, YSOs are divided in four different classes (Andre et al. 2000):

- Class 0, where s is undefined, because there is no emission in near-IR, but only in the far-IR and longer wavelengths. These objects are supposed to be protostars obscured by the surrounding envelope.
- Class I, for $s > 0$. The emission peaks at $\sim 100\,\mu\mathrm{m}$ and is characterized by a strong *infrared excess* emission caused by the reprocessing of star radiation by the circumstellar material.

- Class II, for $-4/3 < s < 0$. This emission peaks at $\sim 1\,\mu\mathrm{m}$ and is interpreted as due to the black body spectrum of the central star with an infrared excess coming from the surrounding dusty disk.
- Class III, for $s < -4/3$, generally $s \approx -3$. This is essentially a black body spectrum with a small infrared excess, coming from the disk that has not been fully dissipated yet.

Along with this IR classification of YSOs, there is also an optical classification. Stars are divided in spectral types by absorption lines in their visible spectra. There are seven types of star, in order of decreasing temperature indicated by the letters: O, B, A, F, G, K, M. O-type stars are the least common, emit most of their light in the ultraviolet and are extremely hot, with surface temperatures over $30\,000\,\mathrm{K}$. M-type stars are by far the most numerous, their emission peaks in the red and are the coldest, with surface temperatures around $3500\,\mathrm{K}$. The Sun is a G-type star, with a surface temperature $T_\odot \approx 5800\,\mathrm{K}$ and a mass $M_\odot \approx 2 \times 10^{33}\,\mathrm{g}$. Based on these spectral types, YSOs can be classified as:

- *T Tauri* stars. Their spectral types are from F to M and their masses are below $2\,M_\odot$. They are characterized by variability, nebulosity and emission lines, in particular the Hα, often associated with accretion processes. In case of a strong Hα emission, they are called *Classical T Tauri Stars* (CTTS), usually related to Class II YSOs, while if Hα emission is weak, they are called *Weak-line T Tauri Stars* (WTTS), usually associated with Class III.
- *Herbig* stars. Stars with masses $2\,M_\odot \lesssim M_\star \lesssim 8\,M_\odot$ and spectral types A or B, they also present nebulosity and emission lines. They are also called HAeBe, where "A" and "B" stand for the spectral types and "e" indicates the presence of line emissions.

There are no YSOs with masses $M_\star \gtrsim 8\,M_\odot$, because such massive stars enter main sequence before the disk has formed, so the strong stellar winds, produced by the ignition of hydrogen nuclear fusion, dissipate the surrounding material. On the other hand, protoplanetary disks do form around low-mass objects, where two types of astronomical sources are defined:

- *Very low-mass stars* (VLMS). They posses masses that are found to be within the range $0.08\,M_\odot \lesssim M_\star \lesssim 0.3\,M_\odot$, where the lower extreme is the minimum mass that a star can have, from which hydrogen burning is possible.
- *Brown dwarfs* (BDs). These are substellar objects which are not massive enough to sustain nuclear fusion of hydrogen, but burn deuterium instead. BDs have masses ranging from ~ 0.01 to $0.08\,M_\odot$ (so from ~ 13 to $80\,M_{\mathrm{Jup}}$).

The first direct evidences of protoplanetary disks were obtained by the Hubble Space Telescope, launched in the 1990. As depicted in Fig. 1.4, these observations reveal the presence of disks surrounding young stars. These disks are detected in visible light and manifest as absorption silhouettes against the luminous background of the Orion Nebula. The advent of radio interferometers and enhanced observational techniques significantly increased disk detections in subsequent years, fostering substantial growth in this

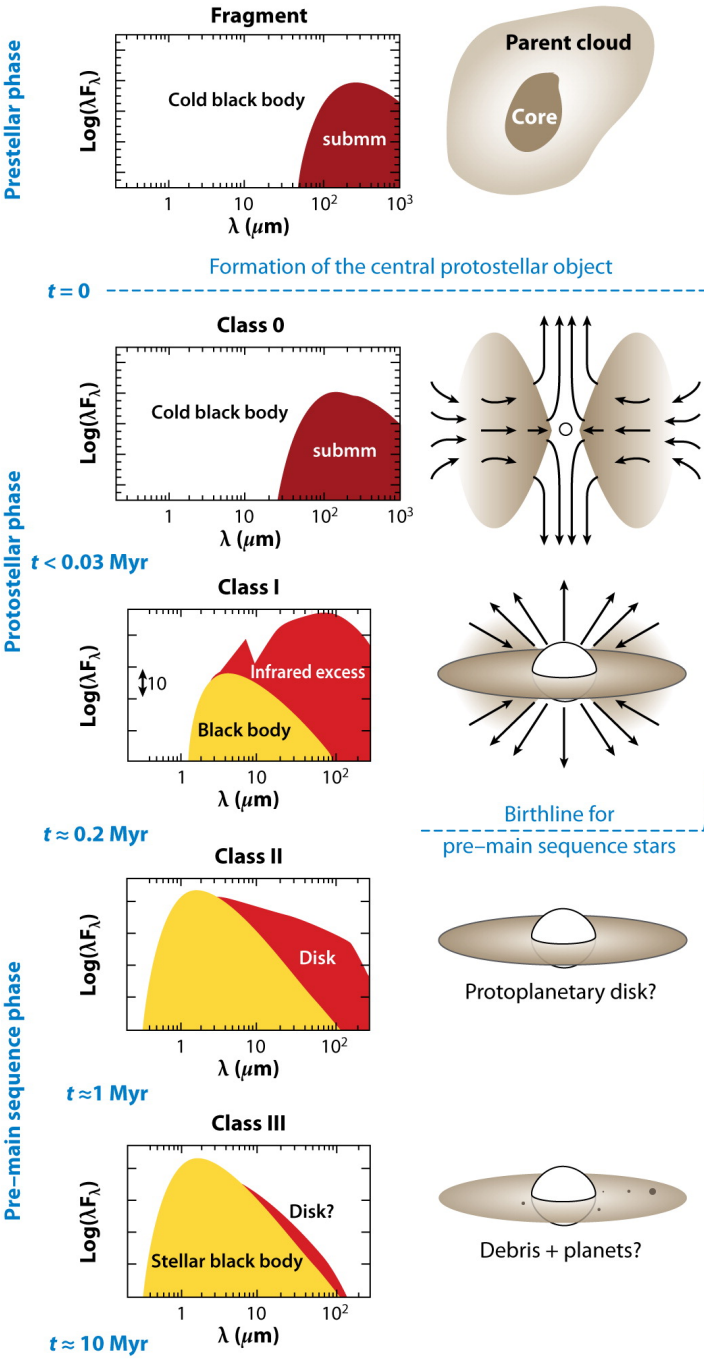

Figure 1.3: YSOs classification based on their SEDs. Image from André (2002).

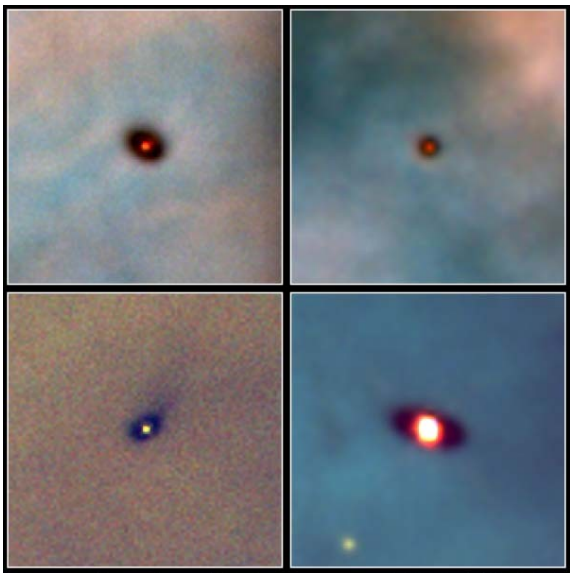

Figure 1.4: Sample of protoplanetary disks in the Orion Nebula observed by the Hubble Space Telescope. Image adapted from McCaughrean & O'dell (1996).

research field. Particularly, several surveys in (sub-)millimeter wavelengths (e.g., Andrews & Williams 2005, 2007b,a) were focus on detecting the emission from a large sample of protoplanetary disks, inferring disk properties in various star-forming regions.

This research field experienced a revolution with the advent of high-resolution observations, largely credited to The Atacama Large Millimeter/submillimeter Array (ALMA). It is an observatory located in the Atacama Desert in Chile, on a plateau at an elevation of $5000\,\mathrm{m}$ above sea level, which stands as one of the premier locations on Earth for astronomical observations. Its high altitude and dry air minimize atmospheric effects, particularly radiation absorption by water vapor. Inaugurated in 2013, the construction and operations of ALMA are led by the European Southern Observatory (ESO), the National Radio Astronomy Observatory (NRAO) of the United States, and the National Astronomical Observatory of Japan (NAOJ). Comprising fifty four 12-m antennas and twelve 7-m antennas, ALMA can be setup in various configuration, ranging from its most compact (with a maximum distance between antennas of $\sim 150\,\mathrm{m}$) to its most extended configuration (with a maximum distance between antennas of $\sim 16\,\mathrm{km}$), enabling an unprecedented angular resolution of $0.01''$. Considering the most extensively studied nearby star forming regions, this results in an angular resolution of $1.4\,\mathrm{au}$ for Taurus, ρ-Ophiuchi, and Upper Scorpius at an average distance of approximately $140\,\mathrm{pc}$, $1.6\,\mathrm{au}$ for Lupus and Corona Australis at $160\,\mathrm{pc}$, $2.0\,\mathrm{au}$ for Chameleon at $200\,\mathrm{pc}$, and $4.0\,\mathrm{au}$ for Orion at $400\,\mathrm{pc}$ (distances from Gaia Collaboration et al. 2021).

ALMA is capable of observing in nine different wavelength bands, spanning from $8.5\,\mathrm{mm}$ to $0.3\,\mathrm{mm}$. This spectral range is particularly well-suited for observing protoplanetary disks, where the emission is primarily from the thermal radiation of cold dust with a typical temperature of $\sim 20 - 30\,\mathrm{K}$. While dust thermal radiation dominates disk

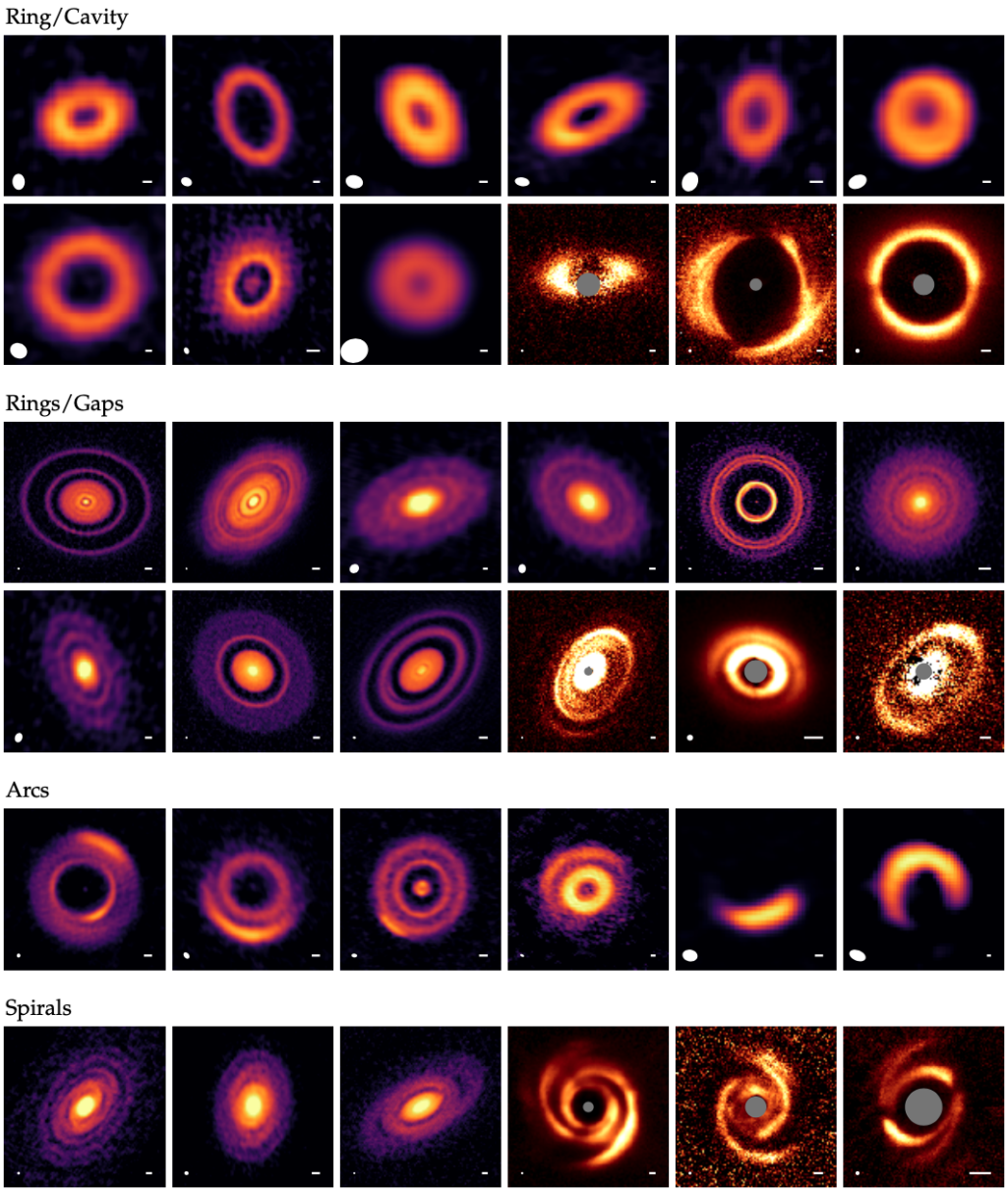

Figure 1.5: Gallery of substructures in protoplanetary disks observed in millimeter continuum or near-infrared scattered light. Image from the review of Andrews (2020).

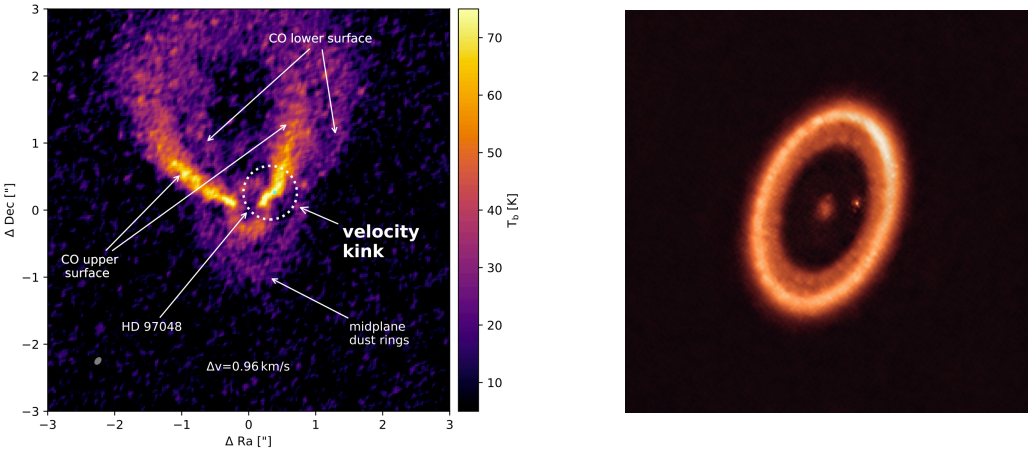

Figure 1.6: Direct evidences of planets embedded in protoplanetary disks. *Left panel*: Planet-induced perturbation in the CO emission of the disk HD 97048, coincident with a gap in the dust emission (Pinte et al. 2019a). *Right panel*: First evidence of a circumplanetary disk detected in dust emission around the planet PDS 70c (Benisty et al. 2021).

emission, ALMA allows for the study of gas as well. Molecular hydrogen (H_2), the most abundant gas component, is challenging to observe due to its null electric dipole moment and weak emission. Therefore, other tracers, such as the rotational line emission of carbon monoxide (^{12}CO and its isotopologues), are commonly used. This line emission enables the study of disk dynamics, as the Doppler effect causes material in rotation coming towards us to be blueshifted, while receding material is redshifted. Tracing both dust and gas in protoplanetary disks is of great relevance, since, as will be shown in Sections 2.1 and 2.2, they exhibit different behaviors.

In addition to ALMA, another instrument that has facilitated the detection of disk substructures is SPHERE (Spectro-Polarimetric High-contrast Exoplanet REsearch). It is installed on Unit Telescope 3 of the Very Large Telescope (VLT), situated at an altitude of $2635\,\mathrm{m}$ in the Atacama Desert in Chile. Operational since 2014, SPHERE operates in the visible and near-infrared wavelengths, allowing to observe stellar light scattered by μm dust grains in protoplanetary disk reaching a resolution of $\sim 0.02''$. This corresponds to an angular resolution of 2.8 au for Taurus, ρ-Ophiuchi, and Upper Scorpius, 3.2 au for Lupus and Corona Australis, 4.0 au for Chameleon, and 8.0 au for Orion. SPHERE employs coronagraphs and adaptive optics. Coronagraphy is a technique that enables the blocking of most radiation from the central star, which would otherwise dominate at these wavelengths. Adaptive optics is a technology that deforms mirrors to correct for distortion caused by atmospheric turbulence.

Figure 1.5 shows a gallery from the review of Andrews (2020) summarizing all the various disk substructures morphologies resolved at mm and near-infrared wavelengths in the last decade. Different physical mechanisms can explain the diverse substructures, with the interaction with one or more planets emerging as a relevant possibility. Evidence of the planet-disk interaction came from the observations of localized perturba-

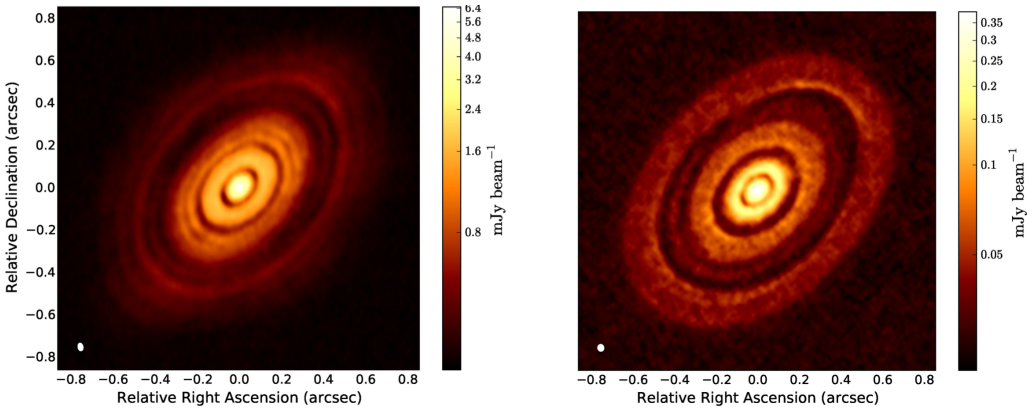

Figure 1.7: Comparison between the observed dust emission of HL Tau (*left panel*) and the simulation performed by Dipierro et al. (2015a) (*right panel*).

tions of the gas line emission (see review by Pinte et al. 2023). These perturbations can be attributed to the presence of a massive planet directly affecting the gas kinematics. While the direct detection of a protoplanet within a disk remains uncommon, it has been accomplished in two specific cases: PDS70 (Keppler et al. 2018; Benisty et al. 2021) and HD169142 (Hammond et al. 2023). In these instances, detection was achieved either by observing the direct emission from the planet or by detecting the emission from material accreting onto the planet, leading to the formation of a circumplanetary disk.

Advancements in observations have been accompanied by significant progress in theoretical and numerical techniques, essential for understanding the origins of observed disk substructures. Hydrodynamical codes, such as PHANTOM (Price et al. 2018b) and FARGO (Benítez-Llambay & Masset 2016), were developed to accurately model the behavior of gas and dust in protoplanetary disks. It's crucial to highlight the synergy between these hydrodynamical codes, simulating material distribution in the disk, and radiative transfer codes, which calculate how such material emits radiation. Radiative transport codes like MCFOST (Pinte et al. 2006, 2009), RADMC-3D (Dullemond et al. 2012), and POLARIS (Reissl et al. 2016) play a pivotal role in generating synthetic observations directly comparable to ALMA data. The power of these numerical techniques is exemplified in Fig.1.7, where a comparison is made between the dust emission of HL Tau observed by ALMA and the results of hydrodynamical and radiative transfer simulations by Dipierro et al. (2015a). They successfully replicated the observed gaps by introducing three embedded planets.

The work presented in this Thesis contributes to multiple research directions. It involves the use of hydrodynamical and radiative transfer simulations, high-resolution millimeter observations, and a multiwavelength approach spanning from centimeter to submillimeter wavelengths. The Thesis focuses on examining both large protoplanetary disks with evident dust substructures and a compact disk appearing structureless.

1.1 Thesis outline

This Thesis is structured as follows:

- **Part I** provides a theoretical and observational background. In **Chapter 2**, the focus is on the theoretical aspects of gas and dust dynamics, including gas viscous evolution and dust-gas interactions. **Chapter 3** offers a brief overview of core accretion and gravitational instability theories related to planet formation. It then delves into the detailed examination of planet-disk interaction, encompassing mechanisms such as gap opening and planet migration. **Chapter 4** is dedicated to the observation of disks at millimeter wavelengths using aperture synthesis interferometry, the technique employed for all datasets presented in this Thesis.

- **Part II** explores the impact of massive outer planets (beyond $\gtrsim 5\,\mathrm{au}$) on extended disks, leading to the creation of visible substructures in the dust emission. **Chapter 5** is focused on numerical simulations and presents the modeling effort on the protoplanetary disk around the very low-mass star CIDA 1, demonstrating that it might host a giant embedded planet, challenging current planet formation theories. **Chapter 6** is purely observational, concentrating on high sensitivity and high resolution observations from ALMA. The chapter presents the dust continuum emission from the ALMA Large Program exoALMA, highlighting 15 bright and extended protoplanetary disks that exhibit a variety of dust substructures.

- **Part III** focuses on compact protoplanetary disks and the indirect constraints regarding the presence of inner planets (within $\sim 5\,\mathrm{au}$). In **Chapter 7**, the focus is on compact disks, emphasizing their prevalence in the disk population and the necessity of unresolved substructures for their persistence over a few million years of evolution. The current limitations of observatories prevent direct exploration of the innermost regions of protoplanetary disks, making it challenging to provide direct evidence of embedded inner planets. However, the mere observation of these compact disks can serve as indirect evidence of such planets. **Chapter 8** introduces a multiwavelength analysis, spanning from submillimeter to centimeter wavelengths, of the compact disk CX Tau. Initially intended to derive indirect constraints on dust mass and, consequently, the ability to form planets, the study unexpectedly uncovers an unusual aspect of non-dust emission, suggesting an exceptionally high free-free variability or the presence of the elusive anomalous microwave emission.

Part I

Protoplanetary disk physics and observations

CHAPTER 2

Gas and dust dynamics in protoplanetary disks

As already introduced in Chap. 1, a protoplanetary disk emerges from the conservation of angular momentum during the gravitational collapse of a molecular cloud core. Figure 2.1 provides a schematic description of the process, where we have a central protostar, surrounded by collapsing material of the cloud core. Here, we consider a fluid element of the collapsing core, with mass m, rotating with an angular velocity Ω and a tangential velocity v_{rot} at a distance R from the protostar of mass $M_\star$. Neglecting the self-gravity of the core material, two forces are acting on the fluid element, the gravitational force and the centrifugal force:

$$F_{\rm g} = G\frac{M_\star m}{R^2} \qquad F_{\rm c} = m\frac{v_{\rm rot}^2}{R}. \tag{2.1}$$

Knowing that the specific angular momentum (angular momentum per unit mass) of the fluid element is $l = v_{\rm rot}R$ we can rewrite the centrifugal force as

$$F_{\rm c} = m\frac{l^2}{R^3}. \tag{2.2}$$

Comparing $F_{\rm g}$ and $F_{\rm c}$, we see that the gravitational force dominates at large scales, where we have a spherical collapse, while for smaller scales the contribute of the centrifugal force becomes predominant, leading to the formation of the disk. The scale separating these two phenomena can be found equating the two forces and obtaining the *circularization radius*

$$R_{\rm circ} = \frac{l^2}{GM_\star}. \tag{2.3}$$

Usually $R_{\rm circ} \sim 100\,$au, which is an estimate of the disk size, while the typical star radius is much smaller, around $0.005\,$au. This results in a problem, meaning that the initial rotation of the cloud core forces the material to orbit in a disk around the central protostar, without directly accreting onto it. However, protoplanetary disks are also called *accretion disks*, since observations show that the material in these disks do fall on the central protostar. Therefore, a mechanism must be found for allowing the mass accretion onto the central star. We will see in Section 2.1.4 that crucial roles in this context are played by conservation of angular momentum and disk viscosity.

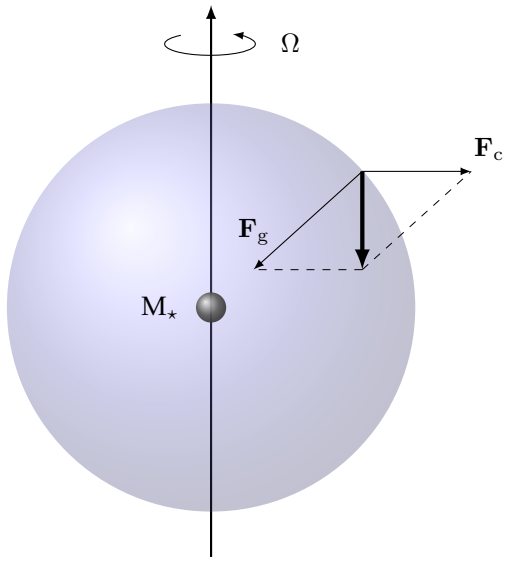

Figure 2.1: Schematic view of the molecular cloud core collapse at small scales, where gravitational and centrifugal forces are comparable, resulting in a vertical force toward the midplane leading to the formation of a protoplanetary disk.

2.1 Gas dynamics

Protoplanetary disks maintain the same dust-to-gas mass ratio of approximately 1:100 found in the interstellar medium and in the Giant Molecular Clouds, as recently proven by Veronesi et al. (2021) and Lodato et al. (2023). For this reason, the gas dictates the total disk dynamics. We focus now on the study of the gas dynamics, first described in the papers of Lynden-Bell & Pringle (1974) and Pringle (1981) and more recently reviewed by Lodato (2008). Our analysis relies on four assumptions:

1. The disk is thin, that is, the disk scale height H is much smaller than its radius R ($H/R \ll 1$).

2. The disk is axisymmetric and so it is useful to use cylindrical polar coordinates (R, z, φ), where all the quantities are independent on the azimuthal coordinate φ.

3. The radial component of velocity v_R is much smaller than the azimuthal component v_φ (i.e. $v_R \ll v_\varphi$).

4. The disk is non-self-gravitating and is influenced only by the gravitational force toward the central host star.

We introduce now some useful quantities, starting from the angular velocity, tangential velocity and specific angular momentum that characterize a Keplerian orbital motion:

$$\Omega_{\rm K} = \sqrt{\frac{GM_\star}{R^3}} \qquad v_{\rm K} = \sqrt{\frac{GM_\star}{R}} \qquad l_{\rm K} = \sqrt{GM_\star R}. \tag{2.4}$$

Since the disk is thin, it is convenient to define a surface density Σ, instead of the volume density ρ, eliminating the dependence from the coordinate z

$$\Sigma(R,t) = \int_{-\infty}^{+\infty} \rho(R,z,t)\mathrm{d}z. \tag{2.5}$$

Considering the disk material as a viscous fluid, we write now the basic equations of fluid dynamics. We start from the continuity equation

$$\frac{\partial \rho}{\partial t} + \nabla \cdot (\rho \mathbf{v}) = 0, \tag{2.6}$$

that using the formula for divergence in cylindrical coordinates and integrating over the z direction becomes

$$\frac{\partial \Sigma}{\partial t} + \frac{1}{R}\frac{\partial}{\partial R}(R\Sigma v_R) = 0. \tag{2.7}$$

The second equation that we need to describe a viscous fluid is the Navier-Stokes equation

$$\frac{\partial \mathbf{v}}{\partial t} + (\mathbf{v}\cdot\nabla)\mathbf{v} = -\frac{\nabla P}{\rho} - \nabla\Phi + \frac{1}{\rho}\nabla\cdot\boldsymbol{\sigma}, \tag{2.8}$$

where P is the pressure, Φ the gravitational potential and $\boldsymbol{\sigma}$ the viscous stress tensor

$$\sigma_{ij} = \eta\left(\frac{\partial v_i}{\partial x_j} + \frac{\partial v_j}{\partial x_i} - \frac{2}{3}(\nabla\cdot\mathbf{v})\delta_{ij}\right) + \zeta\left(\nabla\cdot\mathbf{v}\right)\delta_{ij} \tag{2.9}$$

with η shear viscosity coefficient and ζ bulk viscosity coefficient. Assuming as a first approximation that the disk rotation is Keplerian, this means that the disk rotates with a differential velocity, faster at shorter radii and slower further out. This difference in velocity between adjacent annuli creates a velocity gradient in the disk, and so a viscosity. The only non-zero component of the viscous stress tensor in a circular axisymmetric shear flow results in

$$\sigma_{R\varphi} = \sigma_{\varphi R} = \eta R\frac{\mathrm{d}\Omega}{\mathrm{d}R}. \tag{2.10}$$

Kinematic viscosity is defined as

$$\nu = \frac{\eta}{\rho}, \tag{2.11}$$

but we now introduce the vertically averaged kinematic viscosity

$$\langle\nu\rangle = \frac{\int_{-\infty}^{+\infty}\eta\mathrm{d}z}{\Sigma} = \frac{\int_{-\infty}^{+\infty}\rho\nu\mathrm{d}z}{\int_{-\infty}^{+\infty}\rho\mathrm{d}z} \tag{2.12}$$

and whenever we use the notation ν, it denotes $\langle\nu\rangle$.

Finally, we define a barotropic fluid as a fluid that is function of the density only $\big($i.e. $P = P(\rho)\big)$ and for a barotropic fluid the sound speed c_s is expressed by

$$c_\mathrm{s}^2 = \frac{\mathrm{d}P}{\mathrm{d}\rho}. \tag{2.13}$$

From the ideal gas law

$$PV = Nk_\mathrm{B}T, \tag{2.14}$$

where V is the volume, N the number of particles, k_B the Boltzmann constant and T the temperature, we obtain

$$P = \frac{N}{V} k_\mathrm{B} T = n k_\mathrm{B} T = \frac{\rho}{\mu m_\mathrm{p}} k_\mathrm{B} T, \tag{2.15}$$

with n the number density, μ the mean molecular weight and m_p the mass of a proton. If the fluid is isothermal we have

$$P = \rho \left(\frac{k_\mathrm{B} T}{\mu m_\mathrm{p}} \right) = \rho c_\mathrm{s}^2 \tag{2.16}$$

and then the sound speed is

$$c_\mathrm{s}^2 = \frac{P}{\rho} = \frac{k_\mathrm{B} T}{\mu m_\mathrm{p}}. \tag{2.17}$$

2.1.1 Vertical hydrostatic equilibrium

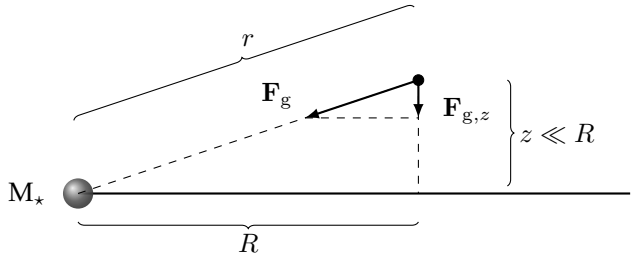

Figure 2.2: Geometrical scheme of the disk section used to calculate the disk vertical structure.

In order to study the disk vertical structure, we consider a thin isothermal disk and a fluid element at height z from the midplane and distance r from the central star of mass $M_\star$. The situation is represented in Figure 2.2. Since we are studying an equilibrium configuration, the left-hand side of the Navier-Stokes equation (2.8) is null and also the stress tensor along the z direction is zero. Under these conditions, the hydrostatic equilibrium equation between the pressure and gravitational forces is

$$\frac{1}{\rho} \frac{\mathrm{d}P}{\mathrm{d}z} = -\frac{\mathrm{d}\Phi}{\mathrm{d}z}, \tag{2.18}$$

and using the isothermal condition (2.17), we get

$$\frac{c_\mathrm{s}^2}{\rho} \frac{\mathrm{d}\rho}{\mathrm{d}z} = -\frac{\mathrm{d}\Phi}{\mathrm{d}z}. \tag{2.19}$$

Thanks to the thin disk approximation, the gravitational potential gradient can be written

$$\frac{\mathrm{d}\Phi}{\mathrm{d}z} = \frac{\mathrm{d}}{\mathrm{d}z}\left(-\frac{GM}{r} \right) = \frac{GM}{r^2} \frac{\mathrm{d}r}{\mathrm{d}z} = \frac{GM}{r^3} z \simeq \frac{GM}{R^3} z = \Omega_\mathrm{K}^2 z. \tag{2.20}$$

Thus, the differential equation to solve is

$$\frac{c_\mathrm{s}^2}{\rho}\frac{\mathrm{d}\rho}{\mathrm{d}z} = -\Omega_\mathrm{K}^2 z. \tag{2.21}$$

Defining the scale height

$$H \equiv \frac{c_\mathrm{s}}{\Omega_\mathrm{K}}, \tag{2.22}$$

the solution is a Gaussian curve

$$\rho = \rho_0 \exp\left(-\frac{z^2}{2H^2}\right). \tag{2.23}$$

The thin disk condition allows to write

$$H \ll R \quad \Longrightarrow \quad c_\mathrm{s} \ll \Omega_\mathrm{K} R = v_\mathrm{K}, \tag{2.24}$$

so, knowing that $v_\mathrm{K} \simeq v_\varphi$ (as we will show in the next Section), the rotation velocity in a disk is highly supersonic. Moreover, from (2.22), we see that the thermal pressure tends to increase the thickness of a disk against gravity.

2.1.2 Centrifugal balance

We analyze now the Navier-Stokes equation along the radial direction, where the viscous term vanishes. Calculating the $\big((\mathbf{v}\cdot\nabla)\mathbf{v}\big)_R$ operator in cylindrical coordinates and assuming $v_R \ll v_\varphi$, the centrifugal balance is given by

$$\frac{v_\varphi^2}{R} = \frac{1}{\rho}\frac{\mathrm{d}P}{\mathrm{d}R} + \frac{\mathrm{d}\Phi}{\mathrm{d}R}. \tag{2.25}$$

The gravitational potential radial gradient can be written

$$\frac{\mathrm{d}\Phi}{\mathrm{d}R} = \frac{\mathrm{d}}{\mathrm{d}R}\left(-\frac{GM}{R}\right) = \frac{GM}{R^2} = \frac{v_\mathrm{K}^2}{R} \tag{2.26}$$

and using the assumption of barotropic fluid we obtain

$$\frac{v_\varphi^2}{R} = \frac{c_\mathrm{s}^2}{\rho}\frac{\mathrm{d}\rho}{\mathrm{d}R} + \frac{v_\mathrm{K}^2}{R}. \tag{2.27}$$

The azimuthal component of the velocity is then

$$v_\varphi = v_\mathrm{K}\sqrt{1 + \left(\frac{c_\mathrm{s}}{v_\mathrm{K}}\right)^2 \frac{\mathrm{d}\ln\rho}{\mathrm{d}\ln R}}. \tag{2.28}$$

Since

$$\frac{c_\mathrm{s}}{v_\mathrm{K}} = \frac{H}{R} \tag{2.29}$$

and usually in a disk we have

$$\frac{\mathrm{d}\ln\rho}{\mathrm{d}\ln R} < 0, \tag{2.30}$$

the tangential velocity v_φ is slightly sub-Keplerian, with corrections of the order H/R, negligible in the case of a thin disk.

2.1.3 Angular momentum conservation

Finally, we study the Navier-Stokes equation along the azimuthal direction, where the pressure and gravitational potential gradients vanish, due to the assumption of axisymmetric disk. Integrating (2.8) along the z direction and considering the azimuthal component, we obtain

$$\Sigma\left[\frac{\partial \mathbf{v}}{\partial t}+(\mathbf{v}\cdot\nabla)\mathbf{v}\right]_{\varphi}=(\nabla\cdot\mathbf{T})_{\varphi}\qquad\text{with}\qquad\mathbf{T}=\int_{-\infty}^{\infty}\boldsymbol{\sigma}\mathrm{d}z. \tag{2.31}$$

Using the continuity equation (2.7) and calculating the operators $\big((\mathbf{v}\cdot\nabla)\mathbf{v}\big)_{\varphi}$ and $(\nabla\cdot\mathbf{T})_{\varphi}$, the equation of the conservation of angular momentum for a viscous fluid is then

$$\frac{\partial}{\partial t}(\Sigma R v_{\varphi})+\frac{1}{R}\frac{\partial}{\partial R}(R v_R \Sigma R v_{\varphi})=\frac{1}{R}\frac{\partial}{\partial R}\left(\nu\Sigma R^3\frac{\partial\Omega}{\partial R}\right). \tag{2.32}$$

The left-hand side has the form of a continuity equation for the quantity $\Sigma R v_{\varphi}$, which is the angular momentum surface density in the z direction, while on the right-hand side there is a term proportional to the torque

$$\mathcal{G}(R)=2\pi\nu\Sigma R^3\Omega', \tag{2.33}$$

that is due to the presence of viscosity and causes the specific angular momentum variations. We can also notice that the term on the right-hand side is a divergence and, thanks to the divergence theorem, it can be transformed into a flux, a transport term. Therefore, viscosity does not dissipate angular momentum, but instead causes its transport.

2.1.4 Disk evolution

From the continuity equation (2.7) and the angular momentum conservation equation (2.32), we can compute the radial velocity

$$v_R=\frac{1}{R\Sigma(R^2\Omega)'}\frac{\partial}{\partial R}\big(\nu\Sigma R^3\Omega'\big), \tag{2.34}$$

that in the Keplerian case $\Omega=\Omega_{\mathrm{K}}$ becomes

$$v_R=-\frac{3}{\Sigma R^{1/2}}\frac{\partial}{\partial R}\big(\nu\Sigma R^{1/2}\big). \tag{2.35}$$

Substituting the radial velocity (2.34) in the continuity equation (2.7), we obtain the evolution equation for the surface density

$$\frac{\partial\Sigma}{\partial t}=-\frac{1}{R}\frac{\partial}{\partial R}\left[\frac{1}{(R^2\Omega)'}\frac{\partial}{\partial R}\big(\nu\Sigma R^3\Omega'\big)\right], \tag{2.36}$$

that, in the case of Keplerian motion, can be written as

$$\frac{\partial\Sigma}{\partial t}=\frac{3}{R}\frac{\partial}{\partial R}\left[R^{1/2}\frac{\partial}{\partial R}\big(\nu\Sigma R^{1/2}\big)\right]. \tag{2.37}$$

It should be noted that the surface density evolves because of the viscosity and if $\nu = 0$ there is no evolution ($\partial\Sigma/\partial t = 0$). Performing a dimensional analysis on (2.37), we can estimate a viscous timescale for the disk evolution

$$t_\nu \sim \frac{R^2}{\nu}, \tag{2.38}$$

while from Eq. (2.34) we observe that the radial velocity scales as

$$v_R \sim \frac{\nu}{R} = \frac{R}{t_\nu}. \tag{2.39}$$

Since we initially assumed $v_R \ll v_\varphi \simeq v_\mathrm{K} = \Omega_\mathrm{K} R$, we can now write

$$\frac{R}{t_\nu} \ll \Omega_\mathrm{K} R \qquad \Longrightarrow \qquad t_\nu \gg \frac{1}{\Omega_\mathrm{K}} \equiv t_\mathrm{dyn}, \tag{2.40}$$

where we define another important timescale, the dynamical timescale t_dyn. This relation implies that the time requested for a fluid element to migrate to an inner orbit is much longer than the time to complete an orbit. In other words, the accretion process is much slower compared to the orbital motion.

It can be shown that the evolution equation (2.37) is a diffusion equation for the surface density, which means that disk material at a certain radius migrates both toward inner and outer radii. We want to focus now on the accretion problem, already mentioned at the beginning of this Chapter. Remembering that the Keplerian specific angular momentum is an increasing function of the radius

$$l_\mathrm{K} = \sqrt{G M_\star R} \propto R^{1/2}, \tag{2.41}$$

we observe that in order to move to inner regions, the disk material should lose its angular momentum. We consider now two annuli, with masses M_1 and M_2, radii R_1 and $R_2 > R_1$. They exchange angular momentum

$$\Delta J = \Delta M_1 \sqrt{G M_\star R_1} = \Delta M_2 \sqrt{G M_\star R_2} \tag{2.42}$$

and we obtain

$$\frac{\Delta M_1}{\Delta M_2} = \sqrt{\frac{R_2}{R_1}} > 0, \tag{2.43}$$

which means that the inner annulus gains mass and then there is actually accretion. Considering $R_2 \gg R_1$, we get $\Delta M_1 \gg \Delta M_2$, so it is sufficient that a little portion of disk mass migrates to large radii to have most of the disk material accreted onto the central star.

Time-dependent solutions

The problem in solving the evolution equation for the surface density (2.37) derives from the viscosity term ν, which can have complex dependencies with other fluid quantities. In this case, the equation must be solved numerically. However, analytical solutions can

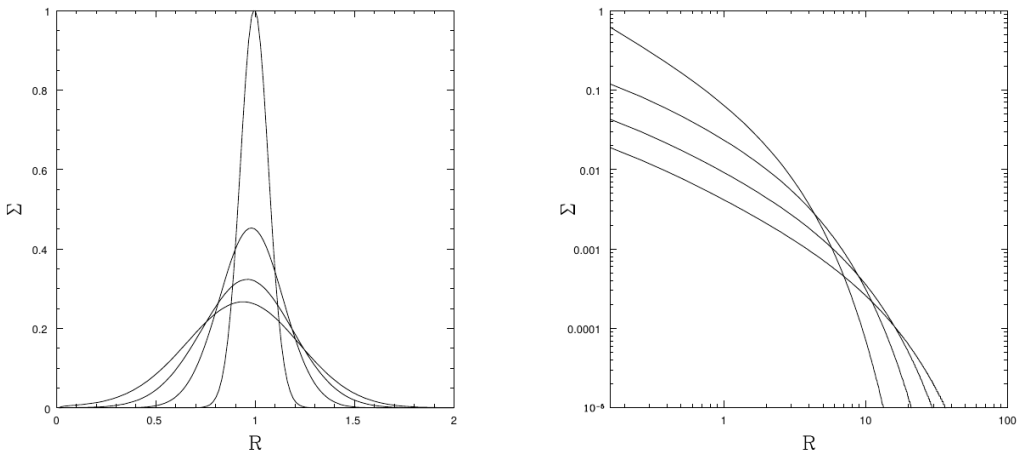

Figure 2.3: Spreading ring solution according to Eq. (2.47) (on the left) and self-similar solutions according to Eq. (2.50)(on the right) for different values of the τ parameter. Image from Lodato (2008).

be found by assuming that viscosity is only a simple function of radius (Lynden-Bell & Pringle 1974)

$$\nu \propto R^b. \tag{2.44}$$

We start from the simplest case

$$b = 0 \quad \Longrightarrow \quad \nu = \text{const.} \tag{2.45}$$

The solution is found through the method of Green's function, with initial condition

$$\Sigma(R, t = 0) = \frac{m}{2\pi R_0}\delta(R - R_0), \tag{2.46}$$

which means that, at the beginning, all the disk material is confined in an infinitesimal ring located at radius R_0. Defining a dimensionless radius $x = R/R_0$ and time $\tau = t/t_\nu$, where $t_\nu = R_0^2/12\nu$ is the viscous timescale, we obtain the surface density evolution

$$\Sigma(x, \tau) = \frac{m}{\pi R_0^2}\frac{x^{-1/4}}{\tau}\exp\left[-\frac{1+x^2}{\tau}\right] I_{1/4}\left(\frac{2x}{\tau}\right) \tag{2.47}$$

with $I_{1/4}$ modified Bessel function of order $1/4$. The time evolution of the surface density described by this equation is plotted in the left panel of Figure 2.3. Since its diffusive behavior, this solution is called *spreading ring* and it can be clearly noted that, due to viscosity, the initial ring spreads both inwards and outwards, as expected by the conservation of angular momentum. The transition between a net inward and outward motion occurs at a radius of $R_{\rm tr} \sim R_0(t/t_\nu)$. Thus, the portion of disk accreted increases with time and for $t \to \infty$ all the disk mass is accreted, with only a negligible amount of mass transporting angular momentum to infinitely large radii.

Another analytical solution of the surface density evolution equation can be found for the case

$$b = 1 \quad \Longrightarrow \quad \nu \propto R \tag{2.48}$$

with the initial condition

$$\Sigma(R, t = 0) = \frac{C}{3\pi\nu(R)} \exp\left(-\frac{R}{R_1}\right). \tag{2.49}$$

with C a normalization constant. The time-dependent solution is

$$\Sigma(R, t) = \frac{CT^{-3/2}}{3\pi\nu(R)} \exp\left(-\frac{R}{R_1 T}\right) \tag{2.50}$$

where $T = 1 + t/t_\nu$ and $t_\nu = R_1^2/3\nu(R_1)$ is the viscous timescale. Equation (2.50) is a power law with an exponential truncation at R_1, scale radius of the disk, that defines also a typical time-scale t_ν. This solution is called *self-similar* and it can be noted that, as represented in the right panel of Figure 2.3, over time the parameter T increases and the normalization decreases, while the exponential truncation shifts at larger radii. So, as for the spreading ring case, in the self-similar solutions the disk spreads both inwards and outwards. The transition between inwards and outwards moving portion of the disk occurs at a radius $R_{\rm tr} \sim R_1 T/2$, which increases with time.

Steady-state solutions

We describe now the steady-state solutions of the disk equations. Neglecting the time-dependent term, the continuity equation (2.7) becomes

$$\frac{1}{R}\frac{\partial}{\partial R}(R\Sigma v_R) = 0 \tag{2.51}$$

from which we deduce

$$R\Sigma v_R = \text{const} \tag{2.52}$$

that, multiplied by -2π, represents the accretion rate for a steady disk

$$\dot{M} = -2\pi R\Sigma v_R = \text{const}. \tag{2.53}$$

If $v_R < 0$ (i.e. directed inwards), $\dot{M} > 0$ and the mass flux across an annulus of the disk is constant at every radius.

Considering the conservation of angular momentum equation (2.32) in steady state, we can write

$$\frac{1}{R}\frac{\partial}{\partial R}(\Sigma R^2 \Omega R v_R) = \frac{1}{R}\frac{\partial}{\partial R}(\nu\Sigma R^3\Omega'), \tag{2.54}$$

then

$$\Sigma R^2 \Omega R v_R - \nu\Sigma R^3\Omega' = \text{const} \equiv -\frac{\dot{J}}{2\pi}, \tag{2.55}$$

and, by recalling torque (2.33) and accretion rate (2.53), we obtain

$$\dot{J} = \text{const} = -2\pi\Sigma R^2\Omega R v_R + 2\pi\nu\Sigma R^3\Omega' = \dot{M}\Omega R^2 + \mathcal{G}(R). \tag{2.56}$$

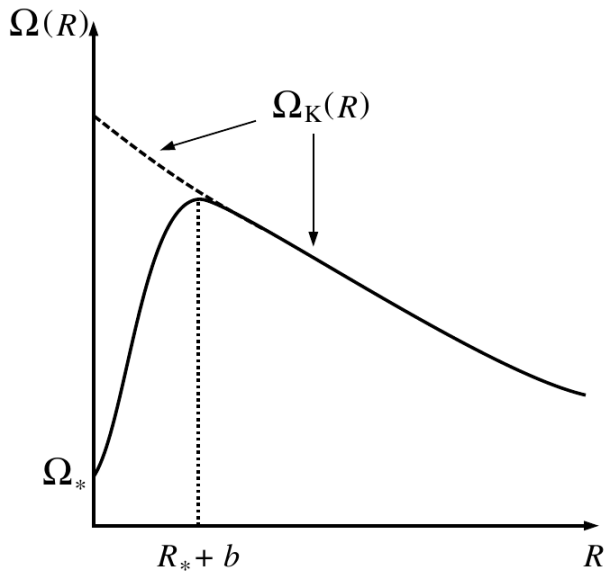

Figure 2.4: Illustration of the angular momentum profile, showing the connection between the disk Keplerian motion and the star rotation across the boundary layer. Image taken from Frank et al. (2002).

The quantity $\dot{J}$ is the constant net flux of angular momentum and is determined by two contributions: the first term indicates the angular momentum advected with the inward flow and the second term represents the viscous torque.

In a Keplerian disk we have

$$\dot{J} = \dot{M}\Omega R^2 - 3\pi\nu\Sigma\Omega R^2 \tag{2.57}$$

and to estimate the constant $\dot{J}$ we use the so-called *no torque* condition. We know that the material in a protoplanetary disk moves with an approximately Keplerian angular velocity $\Omega_{\rm K}(R)$, while the central star rotates with its angular velocity $\Omega_\star$ and we must have $\Omega_\star < \Omega_{\rm K}(R_\star)$, otherwise the star would break apart due to centrifugal force. To avoid a discontinuity, we assume the existence of a boundary layer, from $R_\star$ to $R_\star + b$ with $b \ll R_\star$, that connects the disk angular velocity with $\Omega_\star$, as depicted in Figure 2.4. This implies that at $R_\star + b$ the disk angular velocity profile flattens, i.e $\Omega'(R_\star + b) = 0$. Thus, from Eq. (2.33), $\mathcal{G}(R_\star + b) = 0$ and this is the reason why it is called "no torque" condition. Evaluating Eq. (2.56) at $R_\star + b$, we get

$$\dot{J} = \dot{M}\Omega R^2\Big|_{R_\star+b} \simeq \dot{M}\Omega R^2\Big|_{R_\star} = \dot{M}\sqrt{GMR_\star}. \tag{2.58}$$

and, inserting this in Eq. (2.57), we obtain

$$3\pi\nu\Sigma = \dot{M}\left(1 - \sqrt{\frac{R_\star}{R}}\right), \tag{2.59}$$

so, at large radii $R \gg R_\star$, the surface density profile becomes

$$\Sigma(R) = \frac{\dot{M}}{3\pi\nu(R)}. \tag{2.60}$$

2.1.5 Viscosity

We already mentioned in Section 2.1.3 the key role of viscosity for the angular momentum transport in a protoplanetary disk. Moreover, as stated in Section 2.1.4, the main problem in solving the surface density evolution equation (2.37) is the viscosity term ν and our lack of a precise description for it. We give now a brief introduction on the physical mechanisms that can explain the origin of viscosity in disks.

A first hypothesis is to consider ν as a standard collisional viscosity, resulting from collisions between gas molecules. Since ν has the dimensions of length times velocity, we can express the collisional viscosity as the product between the mean free path of molecules and their mean thermal velocity, i.e. the sound speed

$$\nu \sim \lambda_{\rm mfp} c_{\rm s}. \tag{2.61}$$

We can write the mean free path as

$$\lambda_{\rm mfp} = \frac{1}{n\sigma_{\rm coll}} = \frac{\mu m_{\rm p}}{\rho\sigma_{\rm coll}} \tag{2.62}$$

where n is the gas numerical density, $\sigma_{\rm coll}$ the collisional cross section, μ the mean molecular weight, $m_{\rm p}$ the proton mass and ρ the gas volume density. In the thin disk approximation $\rho \sim \Sigma/H$ and, knowing that $c_{\rm s} = H\Omega_{\rm K}$ from (2.22), the collisional viscosity becomes

$$\nu = \frac{\mu m_{\rm p}}{\Sigma\sigma_{\rm coll}} c_{\rm s} H = \frac{\mu m_{\rm p}}{\Sigma\sigma_{\rm coll}} H^2 \Omega_{\rm K}. \tag{2.63}$$

Recalling now the viscous timescale (2.38) and the dynamical timescale (2.40), we obtain

$$t_\nu \sim \frac{R^2}{\nu} \sim \left(\frac{\Sigma\sigma_{\rm coll}}{\mu m_{\rm p}}\right)\left(\frac{H}{R}\right)^{-2} t_{\rm dyn}. \tag{2.64}$$

For typical orders of magnitude $\Sigma \sim 10\,{\rm g/cm^2}$, $\sigma_{\rm coll} \sim 10^{-16}\,{\rm cm^2}$, $\mu \sim 1$, $m_{\rm p} \sim 10^{-24}\,{\rm g}$, $H/R \sim 10^{-1}$, $t_{\rm dyn} \sim 10^2\,{\rm yr}$, we find $t_\nu \sim 10^{13}\,{\rm yr}$, which means that the accretion in a protoplanetary disk would occur in a time longer than the age of the universe. Then, clearly, the hypothesis of a collisional viscosity regulating the exchange of angular momentum in disks has to be rejected.

The candidate able to explain the physical origin of viscosity in disks is turbulence. In fact, we can notice that

$$\frac{t_\nu}{t_{\rm dyn}} \sim \frac{R^2\Omega_{\rm K}}{\nu} = Re, \tag{2.65}$$

where Re is the *Reynolds number*, a coefficient that, if greater than $10^3 - 10^4$, indicates the fluid propensity for turbulence. Using the previously stated orders of magnitude,

we estimate $Re \sim 10^{11}$, suggesting that accretion disks are extremely prone to generate turbulence. Shakura & Sunyaev (1973) introduced the α-*prescription* to describe the kinematic viscosity:

$$\nu = \alpha c_{\rm s} H, \tag{2.66}$$

where all the uncertainties about the viscous mechanism are enclosed in the α unknown dimensionless parameter. We can constrain α by considering viscosity as the multiplication between the typical turbulent scales for velocity and length

$$\nu = v_{\rm t} l_{\rm t}. \tag{2.67}$$

We observe that the turbulent velocity must be subsonic, otherwise the turbulence would be dissipated by shocks, and that the length scale is limited by H, assuming an isotropic turbulence. Then we obtain

$$\nu < c_{\rm s} H \qquad \Longrightarrow \qquad \alpha < 1. \tag{2.68}$$

Observational measurements (Hartmann et al. 1998a; Andrews et al. 2009) constrained α typically in the range $[10^{-3}, 10^{-2}]$, though there are still uncertainties based on observational limitations.

2.2 Dust dynamics in protoplanetary disks

Dust grains in protoplanetary disks are a mixture of silicates, carbonaceous compounds and ice. They derive from the interstellar medium, with a size distribution ranging from nm to μm, while in disks they can grow up to cm and even to km-sized planetesimals. Even though dust is a minor component in disks, where the dust-to-gas mass ratio is of the order of 1:100, it is the primary building material for planets, according to the *core accretion model* we will present in Section 3.1. Moreover, dust determines the disk temperature structure and dominates the disk radiative emission. The interaction between the dust and gas components was first examined in the work of Weidenschilling (1977).

2.2.1 Dust-gas aerodynamical coupling

Given the low dust-to-gas ratio in disks, we can consider a single dust grain surrounded by a gas fluid. The drag force felt by the grain depends on its size and two regimes are defined:

$$\text{Epstein} \qquad a < \frac{9}{4}\lambda$$

$$\text{Stokes} \qquad a > \frac{9}{4}\lambda,$$

where a indicates the grain size and λ is the mean free path that we can estimate for a typical value of the gas volume density $\rho_{\rm g}$

$$\lambda = \frac{\mu m_{\rm p}}{\rho_{\rm g} \sigma_{\rm coll}} \sim 1\,{\rm cm} \left(\frac{\rho_{\rm g}}{10^{-9}\,{\rm g/cm^{-3}}} \right)^{-1}. \tag{2.69}$$

Thus, in the Epstein regime the small grains interact with single gas molecules, while in the Stokes regime the bigger grains feel a collective interaction with the gas fluid. The drag force in the Epstein regime is

$$\mathbf{F}_{\mathrm{drag,E}} = -\frac{4\pi}{3}\rho_{\mathrm{g}} a^2 v_{\mathrm{th}} \mathbf{v}_{\mathrm{rel}} \tag{2.70}$$

where $\mathbf{v}_{\mathrm{rel}}$ is the relative velocity between gas and dust

$$\mathbf{v}_{\mathrm{rel}} = \mathbf{v}_{\mathrm{d}} - \mathbf{v}_{\mathrm{g}} \tag{2.71}$$

and v_{th} is the thermal velocity of gas molecules

$$v_{\mathrm{th}} = \sqrt{\frac{8 k_{\mathrm{B}} T}{\pi \mu m_{\mathrm{p}}}} = \sqrt{\frac{8}{\pi\gamma}} c_{\mathrm{s}}. \tag{2.72}$$

with T the gas temperature and γ the adiabatic index. Since $\sqrt{8/\pi\gamma} \simeq 1$, we have $v_{\mathrm{th}} \simeq c_{\mathrm{s}}$. The drag force in the Stokes regime is

$$\mathbf{F}_{\mathrm{drag,S}} = -\frac{C_{\mathrm{D}}}{2}\pi\rho_{\mathrm{g}} a^2 |\mathbf{v}_{\mathrm{rel}}| \mathbf{v}_{\mathrm{rel}} \tag{2.73}$$

with

$$C_{\mathrm{D}} = \begin{cases} 24\, Re^{-1} & \text{for} \quad Re < 1 \\ 24\, Re^{-0.2} & \text{for} \quad 1 < Re < 800 \\ 0.44 & \text{for} \quad Re > 800 \end{cases} \tag{2.74}$$

where Re is the Reynolds number calculated not with the collective viscosity described by Shakura & Sunyaev (1973), but with the microscopical viscosity ν_{m}

$$Re = \frac{2a\, v_{\mathrm{rel}}}{\nu_m}. \tag{2.75}$$

Since the Stokes regime interests grains bigger than a cm, while our analysis will deal with grains approximately from sub-μm to mm, from now on we will consider only the Epstein regime. We introduce the *stopping time* t_{s}, which describes the typical timescale for drag to significantly modify the relative velocity between the dust grain and the gas

$$\mathbf{F}_{\mathrm{drag,E}} = -m_0 \frac{\mathbf{v}_{\mathrm{rel}}}{t_{\mathrm{s}}} \qquad \text{with} \qquad m_0 = \frac{4}{3}\pi a^3 \rho_0, \tag{2.76}$$

where m_0 is the mass of the single dust grain and ρ_0 its intrinsic density, usually around $3\,\mathrm{g/cm^3}$ (Armitage 2020). From Eq. (2.70) and (2.76) we find

$$t_{\mathrm{s}} = \frac{\rho_0 a}{\rho_{\mathrm{g}} v_{\mathrm{th}}} = \sqrt{\frac{\pi\gamma}{8}} \frac{\rho_0 a}{\rho_{\mathrm{g}} c_{\mathrm{s}}}. \tag{2.77}$$

We note that the stopping time increases with the gran size a (the same is true for Stokes regime, even though with different dependencies). In order to have an absolute estimate

of the dust-gas coupling, we compare the stopping time with the dynamic timescale, defining the *Stokes number*

$$\mathrm{St} \equiv \frac{t_\mathrm{s}}{t_\mathrm{dyn}} = \Omega_\mathrm{K} t_\mathrm{s}. \tag{2.78}$$

If $\mathrm{St} \ll 1$ dust is strongly coupled to the gas, while if $\mathrm{St} \gg 1$ dust is completely decoupled. In the Epstein regime, its value is

$$\mathrm{St} = \sqrt{\frac{\pi\gamma}{8}} \frac{\rho_0 a}{\rho_\mathrm{g} H_\mathrm{g}}, \tag{2.79}$$

where $H_\mathrm{g} = c_\mathrm{s}/\Omega_\mathrm{K}$ is the disk gas thickness. Recalling the density vertical profile (2.23), we can properly re-write it as

$$\rho_\mathrm{g} = \frac{\Sigma(R)}{\sqrt{2\pi} H_\mathrm{g}} \exp\left(-\frac{z^2}{2H_\mathrm{g}}\right) \tag{2.80}$$

and we can substitute it into the (2.79) obtaining

$$\mathrm{St}(R,z) = \gamma^{1/2} \frac{\pi}{2} \frac{\rho_0 a}{\Sigma(R)} \exp\left(\frac{z^2}{2H_\mathrm{g}}\right) \equiv \mathrm{St}_0(R) \exp\left(\frac{z^2}{2H_\mathrm{g}}\right). \tag{2.81}$$

From this expression, we observe that the Stokes number increases with the grain size, with the height from the midplane and with the distance from the center, since Σ generally decreases with R. We can also calculate the grain size at which $\mathrm{St} \sim 1$ finding

$$a \propto \Sigma(R) \exp\left(-\frac{z^2}{2H_\mathrm{g}}\right), \tag{2.82}$$

then grains that begin to decouple from the gas are usually bigger in the midplane and close to the central star, while they are smaller further out, both radially and vertically. For a quick estimate, we can derive

$$\mathrm{St}_0 \simeq 0.6 \left(\frac{\rho_0}{3\,\mathrm{g/cm^3}}\right) \left(\frac{a}{1\,\mathrm{mm}}\right) \left(\frac{\Sigma}{1\,\mathrm{g/cm^2}}\right)^{-1}, \tag{2.83}$$

which means that $1\,\mathrm{mm}$ dust grains are marginally coupled to the gas in the midplane of a disk with a typical mean surface density of $1\,\mathrm{g/cm^2}$.

2.2.2 Vertical settling

We analyze now the vertical motion of dust grains and its settling on the midplane. The equation of motion in the vertical direction of a single dust grain at a fixed radial distance from the central star is

$$\frac{\mathrm{d}^2 z}{\mathrm{d}t^2} = -\Omega_\mathrm{K}^2 z - \frac{1}{t_\mathrm{s}} \frac{\mathrm{d}z}{\mathrm{d}t}, \tag{2.84}$$

which is also the equation of a damped harmonic oscillator. On the right-hand side, the first term represents the gravitational acceleration projected on the z direction, while the second term is the acceleration due to drag force. Defining a dimensionless time

$$\tau \equiv \Omega_\mathrm{K} t \tag{2.85}$$

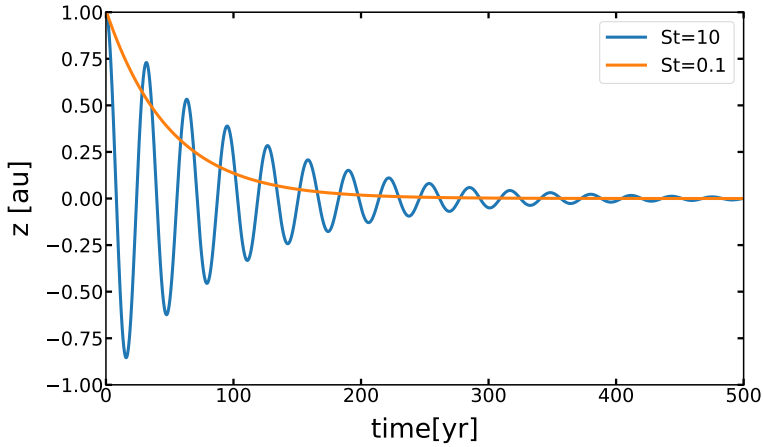

Figure 2.5: Dust vertical settling solutions for a particle starting at $z(0) = 1\,\mathrm{au}$ and at a radial distance of $10\,\mathrm{au}$ from a central star with mass $1\,M_\odot$, in the underdumped case (St = 10) and in the overdumped case (St = 0.1).

and using (2.78), we obtain

$$\frac{\mathrm{d}^2 z}{\mathrm{d}\tau^2} + \frac{1}{\mathrm{St}}\frac{\mathrm{d}z}{\mathrm{d}\tau} + z = 0, \tag{2.86}$$

where we consider the Stokes number a constant, neglecting its dependence from z. Then, this argument is valid only for dust grains with $z \ll H_\mathrm{g}$. Eq. (2.86) is a homogeneous second order differential equation and the solutions of its characteristic polynomial are

$$\lambda_{1,2} = -\frac{1}{2\mathrm{St}}\left[1 \mp \sqrt{1-(2\,\mathrm{St})^2}\right]. \tag{2.87}$$

The $\mathrm{St} > 1/2$ case is the *underdumped* solution, characterized by a sine curve with an exponential decay

$$z(\tau) = z(0)\sin(\omega\tau)\exp\left(-\frac{\tau}{2\,\mathrm{St}}\right). \tag{2.88}$$

So the weakly coupled dust grains oscillates across the midplane with decreasing amplitude, until they eventually settle on the midplane. The settling timescale is expressed by

$$t_\mathrm{settle} = \frac{2\,\mathrm{St}}{\Omega_\mathrm{K}} > \frac{1}{\Omega_\mathrm{K}} = t_\mathrm{dyn}, \tag{2.89}$$

from which we see that a dust grain completes several orbits before settling on the midplane.

The $\mathrm{St} < 1/2$ case represents the *overdumped* solution and, in the specific case of $\mathrm{St} \ll 1/2$, its form is

$$z(\tau) = z(0)\exp(-\mathrm{St}\,\tau), \tag{2.90}$$

with settling timescale

$$t_\mathrm{settle} = \frac{1}{\mathrm{St}\,\Omega_\mathrm{K}} \gg \frac{1}{\Omega_\mathrm{K}} = t_\mathrm{dyn}. \tag{2.91}$$

Therefore, dust grains coupled to the gas do not oscillate across the midplane and settle on it after many orbits. The underdumped and overdumped solution are plotted in Figure 2.5.

Vertical settling in presence of turbulence

So far, we have considered the motion of a single dust grain affected by drag resistance due to the presence of gas. However, we have neglected any collective gas motion, in particular its turbulence. Therefore, we now treat the case of a dust fluid with volume density ρ_d, interacting with a turbulent gas with density ρ_g. This situation is described by the advection-diffusion equation

$$\frac{\partial \rho_\mathrm{d}}{\partial t} = \frac{\partial}{\partial z}\left[D\rho_\mathrm{g}\frac{\partial}{\partial z}\left(\frac{\rho_\mathrm{d}}{\rho_\mathrm{g}}\right)\right] + \frac{\partial}{\partial z}(\Omega_\mathrm{K}\mathrm{St}\rho_\mathrm{d} z). \tag{2.92}$$

On the right-hand side, the first term represents diffusion, with D the diffusion coefficient, while the second is an advection term, where $v_\mathrm{settle} = \Omega_\mathrm{K}\mathrm{St}z$ is the settling velocity. Searching for stationary solutions, we find

$$D\rho_\mathrm{g}\frac{\partial}{\partial z}\left(\frac{\rho_\mathrm{d}}{\rho_\mathrm{g}}\right) + \Omega_\mathrm{K}\mathrm{St}\rho_\mathrm{d} z = \mathrm{const} = 0, \tag{2.93}$$

where the last equality is valid because at $z = 0$ the second term is null and the same is true for the first term, because of symmetry. In fact , the dust-to-gas ratio $\epsilon \equiv \rho_\mathrm{d}/\rho_\mathrm{g}$ varies in the same way going to the positive or negative direction of the z axis, so its derivative is null at $z = 0$. Recalling the expression for the Stokes number (2.81), we can write

$$\frac{1}{\epsilon}\frac{\mathrm{d}\epsilon}{\mathrm{d}z} = -\frac{\Omega_\mathrm{K}\mathrm{St}_0}{D} z \exp\left(\frac{z^2}{2H_\mathrm{g}^2}\right). \tag{2.94}$$

It can be shown that $D \sim \nu$, so using the α-prescription (2.66) and defining

$$x \equiv \frac{z^2}{2H_\mathrm{g}^2}, \tag{2.95}$$

we obtain

$$\frac{\mathrm{d}\epsilon}{\epsilon} = -\frac{\mathrm{St}_0}{\alpha} e^x \mathrm{d}x. \tag{2.96}$$

Assuming $x \ll 1$, the solution is

$$\epsilon(z) = \epsilon_0 \exp\left(-\frac{\mathrm{St}_0}{\alpha}\frac{z^2}{2H_\mathrm{g}}\right). \tag{2.97}$$

We re-write it in terms of the dust density, substituting ρ_g with (2.23), and get

$$\rho_\mathrm{d} = \rho_{\mathrm{d},0} \exp\left[-\frac{z^2}{2H_\mathrm{g}^2}\left(1 + \frac{\mathrm{St}_0}{\alpha}\right)\right] = \rho_{\mathrm{d},0} \exp\left(-\frac{z^2}{2H_\mathrm{d}^2}\right), \tag{2.98}$$

where we defined

$$\frac{1}{H_\mathrm{d}^2} \equiv \frac{1}{H_\mathrm{d}^2}\left(1 + \frac{\mathrm{St}_0}{\alpha}\right) \quad \Longrightarrow \quad H_\mathrm{d}^2 = H_\mathrm{g}^2\sqrt{\frac{\alpha}{\alpha + \mathrm{St}_0}} < H_\mathrm{g}. \tag{2.99}$$

As for the gas density, we obtain that the vertical structure of dust density in presence of turbulence is described by a Gaussian profile, with H_d the dust thickness. We note that if $\mathrm{St}_0 \to 0$, dust is strongly coupled to the gas and $H_\mathrm{d} \simeq H_\mathrm{g}$. On the other hand, if $\mathrm{St}_0 \gg \alpha$ we have

$$H_\mathrm{d} \simeq H_\mathrm{g}\sqrt{\frac{\alpha}{\mathrm{St}}}, \tag{2.100}$$

which means that the bigger the grain size, the thinner the dust disk will be, since $\mathrm{St}_0 \propto a$.

2.2.3 Radial drift

After evaluating the dust motion in the vertical direction, now we aim to describe its radial behavior, finding the combined solution of both the radial and azimuthal equations of motion for the dust component in protoplanetary disks. We consider dust as a pressureless fluid, so its azimuthal motion is approximately Keplerian, since there is no pressure that can support a sub-Keplerian motion as for the gas. Recalling (2.28), the difference between dust azimuthal velocity $v_{\mathrm{d},\varphi} \simeq v_\mathrm{K}$ and gas azimuthal velocity $v_{\mathrm{g},\varphi}$ is

$$\Delta v = v_{\mathrm{d},\varphi} - v_{\mathrm{g},\varphi} \simeq v_\mathrm{K} - v_\mathrm{K}\left[1 - \frac{1}{2}\left(\frac{c_\mathrm{s}}{v_\mathrm{K}}\right)^2 \frac{\mathrm{d}\ln\rho_\mathrm{g}}{\mathrm{d}\ln R}\right] \sim \frac{c_\mathrm{s}^2}{v_\mathrm{K}} = \left(\frac{H}{R}\right)^2 v_\mathrm{K}, \tag{2.101}$$

where we used $\mathrm{d}\ln\rho_\mathrm{g}/\mathrm{d}\ln R \sim 1$ and the expansion to first order of $v_{\mathrm{g},\varphi}$, since $c_\mathrm{s} \ll v_\mathrm{K}$. The equation of motion in the radial direction for dust is

$$\frac{\mathrm{d}v_{\mathrm{d},R}}{\mathrm{d}t} = \frac{v_{\mathrm{d},\varphi}^2}{R} - \frac{v_\mathrm{K}^2}{R} - \frac{v_{\mathrm{d},R} - v_{\mathrm{g},R}}{t_\mathrm{s}}, \tag{2.102}$$

where, on the right-hand side, the first term is the centrifugal acceleration, the second term is the gravitational acceleration caused by the central star and the third term is the acceleration due to the viscous force, depending on the difference between the dust and gas radial velocity and acting on a timescale of the stopping time. It is useful to describe the azimuthal motion through the angular momentum theorem per unit mass

$$\frac{\mathrm{d}}{\mathrm{d}t}\left(Rv_{\mathrm{d},\varphi}\right) = -R\frac{v_{\mathrm{d},\varphi} - v_{\mathrm{g},\varphi}}{t_\mathrm{s}}, \tag{2.103}$$

where the torque per unit mass is the multiplication between radius and viscous acceleration along the azimuthal direction. We can safely assume that $v_{\mathrm{d},R} \ll v_\mathrm{K}$, meaning that the removal of angular momentum occurs in a series of circular orbits. For this reason Eq. (2.103) becomes

$$-R\frac{v_{\mathrm{d},\varphi} - v_{\mathrm{g},\varphi}}{t_\mathrm{s}} = \frac{\mathrm{d}}{\mathrm{d}t}\left(Rv_{\mathrm{d},\varphi}\right) \simeq v_{\mathrm{d},R}\frac{\mathrm{d}}{\mathrm{d}R}\left(Rv_{\mathrm{d},\varphi}\right) \simeq \frac{1}{2}v_{\mathrm{d},R}v_\mathrm{K}, \tag{2.104}$$

so the difference in azimuthal velocity is

$$v_{\mathrm{d},\varphi} - v_{\mathrm{g},\varphi} \simeq -\frac{\mathrm{St}\, v_{\mathrm{d},R}}{2}. \tag{2.105}$$

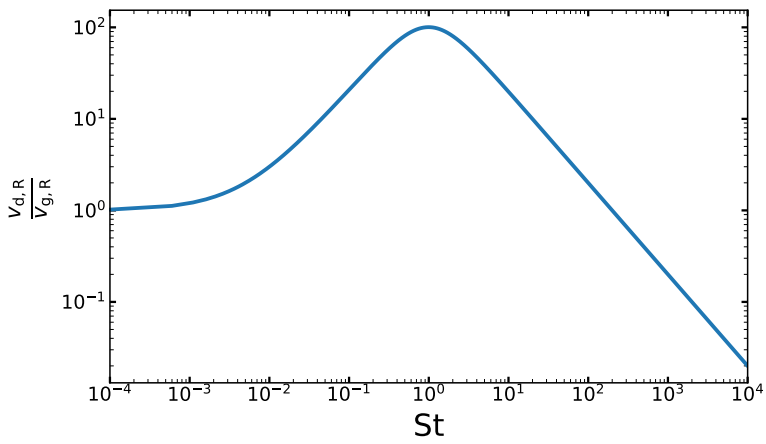

Figure 2.6: Profile of the dust radial velocity in units of gas radial velocity as a function of the Stokes number, according to Eq. (2.108) and assuming typical values $v_{g,R} = 10^2\,\mathrm{cm/s}$ and $\Delta v = 10^4\,\mathrm{cm/s}$.

We want to find the terminal velocity in (2.102), at which all the accelerations compensate, so setting to zero the left-hand side term we can write

$$0 = \frac{v_{d,\varphi}^2 - v_K^2}{R} - \frac{v_{d,R} - v_{g,R}}{t_s} \simeq \frac{2v_K\left(v_{d,\varphi} - v_K\right)}{R} - \frac{v_{d,R} - v_{g,R}}{t_s}. \tag{2.106}$$

Summing and subtracting the term $2v_{g,\varphi}v_K/R$ and substituting (2.105),we finally obtain

$$-\mathrm{St}\, v_{d,R} - 2\Delta v - \frac{v_{d,R}}{\mathrm{St}} + \frac{v_{g,R}}{\mathrm{St}} = 0, \tag{2.107}$$

from which we can extract the expression for the dust radial velocity

$$v_{d,R} = \frac{v_{g,R}}{1 + \mathrm{St}^2} - \frac{2\Delta v}{\mathrm{St} + \mathrm{St}^{-1}}. \tag{2.108}$$

The first term is called *viscous drag* and represents the effects of the gas radial motion that pulls dust with itself, while the second term is the called *radial drift* and it is caused by the friction felt by dust grains moving azimuthally among slower gas particles. It should be noted that always $v_{d,R} < 0$, meaning that dust moves inwards toward the central star, since $v_{g,R} < 0$ and $\Delta v > 0$. In the case of dust perfectly coupled to the gas (i.e. $\mathrm{St} \to 0$), the radial drift term goes to zero and we obtain $v_{d,R} \simeq v_{g,R}$, that is dust follows gas motion. If $\mathrm{St} \to \infty$ there is no interaction between dust and gas, therefore both terms in Eq. (2.108) become negligible and the dust grains do not migrate radially but simply remain in their Keplerian orbits. These behaviors are illustrated in Figure 2.6, where is plotted the ratio between dust and gas radial velocities as function of St. Here we observe that the maximum of the curve is reached at $\mathrm{St} \approx 1$. We can compare Δv and $v_{g,R}$, recalling (2.101), (2.39) and the α-prescription (2.66), finding that

$$\frac{|v_{g,R}|}{\Delta v} \sim \alpha \ll 1. \tag{2.109}$$

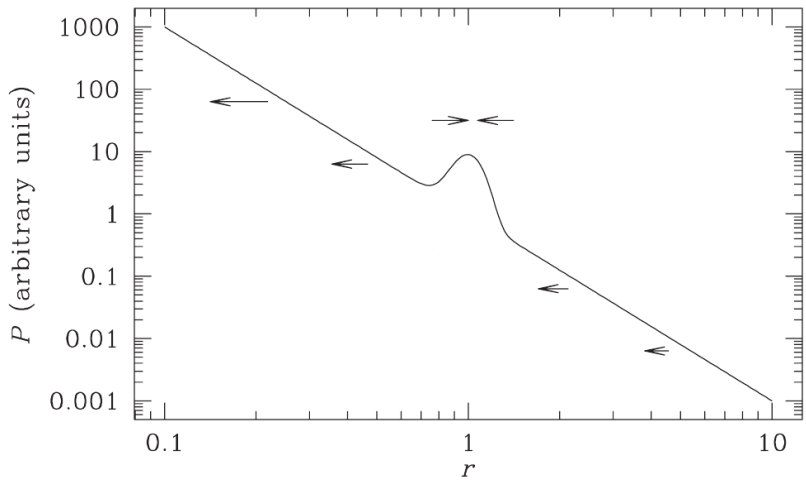

Figure 2.7: Illustration of the dust trap mechanism, where a local overpressure can stop the dust radial drift toward the central star. Image adapted from Armitage (2010).

Then, at $\mathrm{St} \approx 1$ the denominator in (2.108) are comparable and the radial drift dominates on the viscous drag. In this case, we can estimate the radial drift timescale:

$$t_{\mathrm{drift}} = \frac{R}{v_{\mathrm{d},R}} \simeq \frac{R}{\Delta v} \sim \left(\frac{H}{R}\right)^{-2} \frac{R}{v_{\mathrm{K}}} \sim 10^3\,\mathrm{yr}, \tag{2.110}$$

assuming $H/R = 0.05$, $R = 10\,\mathrm{au}$ and $M_\star = 1\,M_\odot$. This timescale is extremely short if compared to some Myr, the typical lifetime of a protoplanetary disk (e.g., Fedele et al. 2010). Moreover, ALMA observations of protoplanetary disks in the continuum detect the thermal radiation emitted from dust mostly with grain size $\sim 1\,\mathrm{mm}$, that usually correspond to $\mathrm{St} \sim 1$. These observations show that dust can be found even at $\sim 100\,\mathrm{au}$ from the central star in disks with an age of some Myr, while mm dust should have rapidly drifted inwards. Thus, there must be a way to slow down or stop the fast dust radial drift.

A candidate able to do so is a *dust trap*, that is a zone with a local maximum of gas pressure and, consequently, gas density. Dust tends to move toward areas of high pressure, both vertically, settling on the midplane, and radially, drifting toward the central star. Therefore, a ring of local higher pressure at a certain radius can attract the surrounding dust and block the radial drift of dust coming from outer regions. This scenario is illustrated in Figure 2.7. To understand this mechanism we should look at the dust radial drift equation (2.108) and focus on the sign of the term Δv, that dominates at $\mathrm{St} \sim 1$. Usually $v_{\mathrm{d},R} < 0$ because $\Delta v > 0$, since gas has an azimuthal sub-Keplerian motion. Recalling Eq. (2.28), this is due to

$$\frac{\mathrm{d}\ln\rho}{\mathrm{d}\ln R} = \frac{\mathrm{d}\ln P}{\mathrm{d}\ln R} < 0. \tag{2.111}$$

However, in case of an overpressure, the pressure gradient is positive for radii slightly

shorter than the radius corresponding to the pressure local maximum. Here gas is super-Keplerian and $\Delta v < 0$, leading to $v_{\mathrm{d},R} > 0$. Then, dust grains around a higher pressure ring migrate toward it, stopping their radial drift.

We now estimate the timescale for dust concentration in pressure bumps. If pressure is a simple power law, we have

$$\frac{\mathrm{d}\ln P}{\mathrm{d}\ln R} = \frac{\mathrm{d}P}{\mathrm{d}R}\frac{R}{P} \sim 1, \tag{2.112}$$

but, assuming a local pressure maximum with a width of ΔR, we find

$$\frac{\mathrm{d}\ln P}{\mathrm{d}\ln R} \simeq \frac{\Delta P}{\Delta R}\frac{R}{P} \sim \frac{R}{\Delta R}, \tag{2.113}$$

so $v_{\mathrm{d},R} \simeq \Delta v$ is increased by a factor $R/\Delta R$. In addition, dust grains have to move only a distance of order ΔR to reach the pressure local maximum and for the dust trapping timescale we obtain

$$t_{\mathrm{trap}} \simeq \frac{\Delta R}{\Delta v} \simeq \left(\frac{\Delta R}{H}\right)^2 \frac{R}{v_{\mathrm{K}}} \sim \left(\frac{\Delta R}{R}\right)^2 t_{\mathrm{drift}} < t_{\mathrm{drift}}. \tag{2.114}$$

So the dust trap process is able to effectively stop the dust radial drift.

CHAPTER 3

Planet formation and interaction with the disk

Following the exploration of the gas and dust dynamics in protoplanetary disks, in this Chapter, I introduce the presence of planets. I briefly outline the theories of core accretion and gravitational instability for planet formation and then discuss how a planet interacts with the disk.

3.1 Core accretion

The classical theory of planet formation is the core accretion theory (Safronov 1969; Goldreich & Ward 1973), which is based on the role of dust in protoplanetary disks and its evolution from sub-μm dust grains from the interstellar medium to km-sized planetesimals. Overall, this mechanism is slow and predicts that planet formation should take several Myr. Four stages can be identified by the size of the grains and their Stokes number:

1. **Dust growth** This first phase is characterized by dust evolution from sub-μm grains to m-sized objects. This growth occurs due to adhesive van der Waals forces between dust grains that come into contact. At the beginning of this passage, $\mathrm{St} \ll 1$ and, consequently, the dust-gas interaction is crucial. However, as explained in Section 2.2.1, approaching to mm-sized grains the Stokes number comes close to 1 and the fast dust radial drift becomes a problem. Indeed, $\mathrm{St} \approx 1$ dust grains would rapidly drift toward the central star, preventing further growth of grains into planetesimals. As described in Section 2.2.3, a mechanism that can stop this radial drift is a dust trap, a local pressure maximum where dust accumulates and can grow in size. On the other hand, it is still uncertain how dust traps can originate. One typical way to form a dust trap involves the interaction between the disk and a planet. Yet, it is required to arrest radial drift in order to form planets, presenting a kind of "chicken and egg" dilemma.

2. **Planetesimal formation** In this phase, dust aggregates grow from m-sized bodies to planetesimals, which are about 10 km wide, the same typical size of asteroids in our Solar System. Planetesimal formation is thought to be related to dust traps, but it is still overall unexplained. From ALMA observations of young disks (~ 1 Myr old), we already observe rings and cavities, usually associated with the presence

of planets. This means that planet formation must be rapid and, as a consequence, planetesimal formation must be even faster.

3. **Collisional growth** Once planetesimals are formed, they can increase in size thanks to collisions between them and generate bodies with masses of $1 - 10\ M_\oplus$ (where $M_\oplus \approx 6 \times 10^{27}\,\mathrm{g}$ indicates Earth masses). Such massive objects have $\mathrm{St} \gg 1$, so they are completely decoupled from the gas and they only feel the gravitational interactions between each other and the central star. These interactions lead to an *oligarchic growth* of planetesimals, meaning that the few planetesimals that form with slightly more mass than the others will end up accreting most of the available mass. If growth stops at this stage, the formed bodies are terrestrial planets, while, if growth continues, they constitute the cores for giant planet formation, that we will present in the next phase.

4. **Core accretion** If the planetary cores, generated by collisional growth from planetesimals, overcome a critical mass, they will be able to accrete gas from the disk and become gas giant planets with masses $\sim 1\ M_{\mathrm{Jup}}$ (where $M_{\mathrm{Jup}} \approx 318\ M_\oplus$). It can be shown that to form a giant planet within 1 Myr, the initial planetary core must have a mass larger than $\sim 20\ M_\oplus$ (Armitage 2020).

The core accretion model is able to explain the formation of both terrestrial and giant planets and predicts that every gas giant must have a central rocky core. However, this theory still present problems, as it does not provide for a mechanism to stop the dust radial drift or to rapidly form planetesimals and, in addition, it does not explain ALMA observations which show that planets can originate also at high distances ($\sim 100\,\mathrm{au}$) from the central star, where the material available is less and the accretion rate is slower.

3.2 Gravitational instability

In the 1990s, the discovery of the first extrasolar giant planet by Mayor & Queloz (1995) posed a significant challenge to existing theoretical models, particularly the core accretion model, due to the apparent inconsistency with the required timescales. Boss (1997) introduced gravitational instability as an alternative paradigm for the formation of giant planets, suggesting that gas fragmentation in the marginally gravitationally unstable outer part of the disk could rapidly give rise to planets. However, the initial mass of the fragment formed through this mechanism is approximately $10\,M_{\mathrm{Jup}}$, and subsequent accretion from the dense disk material leads to the formation of a stellar companion rather than a planet. While this resolves the timescale issue, the standard gravitational instability scenario faces challenges in explaining planet formation without invoking additional mechanisms. Ongoing research explores the potential of this mechanism in explaining giant planet formation in early disks like AB Aur (Cadman et al. 2021). Longarini et al. (2023b,a) performed an analytical and numerical analysis of gravitationally unstable disks that can explain the formation of protoplanets in the early stages of disk evolution. Gas spiral arms efficiently accumulate dust within their structures (Dipierro et al. 2014; Paneque-Carreño et al. 2021), possibly reaching concentrations at which the

influence of dust self-gravity becomes pronounced. In the early stages, protoplanetary disks are likely to be both self-gravitating and supportive of grain growth to sizes where particles are marginally coupled with the gas. Simultaneously, gas spiral arms possess the ability to stimulate solid particles, resulting in a "kicking" effect during each interaction. The potential for dust to undergo gravitational collapse within these spiral arms, potentially leading to the formation of planetary cores, depend on the interplay between these two effects. Longarini et al. (2023a) observe dust collapse in their simulations, resulting in clumps with masses ranging from 1 to 10 $M_\oplus$. Their findings suggest that if planet formation follows this mechanism, the most favorable conditions arise near the conclusion of the disk self-gravitating phase. Should these planetary cores endure in such environments, they have the potential to evolve into giant planets in the outer disk, acting as embryonic forms of class II protoplanets.

3.3 Planet-disk interaction

Planet-disk interactions have been studied since the works of Lin & Papaloizou (1979) and Goldreich & Tremaine (1980). The presence of a planet in a disk modifies the gravitational potential, so that this is not only provided by the central star, but also by the planet-induced perturbation. These perturbations can generate density waves able to add or subtract angular momentum to the planet and make it migrate. Density waves are generated in specific locations of the disk, where resonances arise. There are two types of resonances (see Figure 3.1):

Corotation resonance This resonance occurs where gas angular velocity Ω_g and planet angular velocity Ω_P are equal

$$\Omega_\mathrm{g}(R) = \Omega_\mathrm{P}. \tag{3.1}$$

The location of the corotation resonance R_CR is then the semi-major axis of the planet orbit a

$$R_\mathrm{CR} = a. \tag{3.2}$$

Lindblad resonance This resonance is generated where the difference between the gas and planet angular velocities is a submultiple of the epicyclic frequency κ

$$m\big[\Omega_\mathrm{g}(R) - \Omega_\mathrm{P}\big] = \pm\kappa, \tag{3.3}$$

where m is an integer and κ is a natural frequency of an orbiting body and is defined by

$$\kappa^2 = 4\Omega^2\left(1 + \frac{1}{2}\frac{\mathrm{d}\ln\Omega}{\mathrm{d}\ln R}\right). \tag{3.4}$$

For a Keplerian disk $\kappa = \Omega_\mathrm{K}$ and the resonance location is

$$R_\mathrm{LR} = a\left(1 \pm \frac{1}{m}\right)^{2/3}, \tag{3.5}$$

with a the semi-major axis of the planet orbit. A bigger m corresponds to a resonance closer to the planet and we can distinguish in outer Lindblad resonances (with the "+" sign in (3.5)) and inner Lindblad resonances (with the "−" sign).

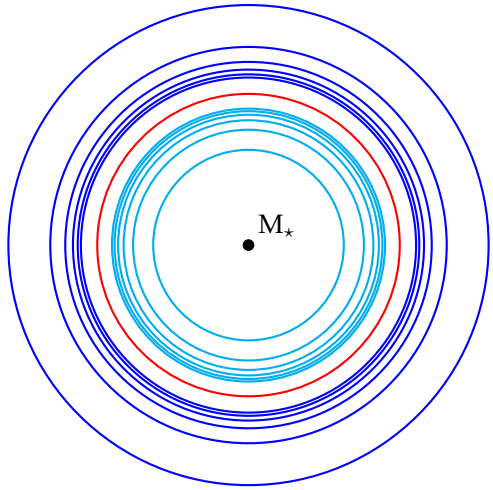

Figure 3.1: Illustration of resonance positions: in red is the corotation resonance, in blue the outer Lindblad resonances (for $m = 1 \dots 7$) and in cyan the inner Lindblad resonances (for $m = 2 \dots 8$).

3.3.1 Impulse approximation

In a rigorous treatment of the angular momentum exchange between planet and density waves we should calculate and sum all the torques exerted at every resonant location. However, we follow a simpler approach that will provide us with the same result, except for slightly different numerical coefficients. This approach is called *impulse approximation* and consists on a restricted three-body problem, where we consider a gas element and a planet orbiting a much more massive central star. The approximation relies on these assumptions:

1. Both the gas element and the planet follow a circular Keplerian orbit around the central star.

2. The interaction between gas element and planet is impulsive, meaning that it occurs only when these bodies are very close to each other.

3. This interaction is weak and causes only a small deflection of the gas element orbit.

4. After the interaction with the planet, the gas element continues to move on a circular orbit.

We consider a planet with mass $M_{\rm P}$ orbiting with velocity $v_{\rm P}$ and distance a around a star with mass $M_\star$. The planet interacts with a gas element orbiting the central star with velocity $v_{\rm g}$ and distance R and causes the deflection of gas element trajectory by an angle δ. We define the impact parameter b of the interaction

$$b \equiv |R - a|, \tag{3.6}$$

with $b \ll a$. The situation is depicted in Figure 3.2. The gas element velocity relative to

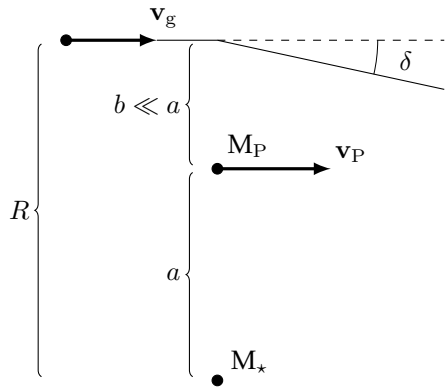

Figure 3.2: Schematic view of the context considered in the impulse approximation.

the planet is

$$v = v_\mathrm{g} - v_\mathrm{P} \qquad \text{with} \qquad \mathrm{sgn}(v) = \mathrm{sgn}(a - R), \tag{3.7}$$

because gas element and planet both follow a Keplerian orbit and $v_\mathrm{K} \propto r^{-1/2}$. The interaction here is a Rutherford scattering and this is true even though the system is not inertial, but it is orbiting around the star. Strictly speaking, in a rotating system there is not conservation of energy, but what is conserved is the Jacobi's integral

$$\epsilon_\mathrm{J} = E - \Omega_\mathrm{K} J, \tag{3.8}$$

where E is the energy of the system, Ω_K the Keplerian angular velocity, and J the angular momentum. It can be shown that

$$|E| \gg |\Omega_\mathrm{K} J| \qquad \Longrightarrow \qquad \epsilon_\mathrm{J} \simeq E, \tag{3.9}$$

so we can safely assume energy conservation.

In a Rutherford scattering, the deflection angle is

$$\cot\left(\frac{\delta}{2}\right) = \frac{bv^2}{GM_\mathrm{P}} \tag{3.10}$$

and considering small deflections we can write

$$\cos\delta - 1 \simeq -2\tan^2\left(\frac{\delta}{2}\right). \tag{3.11}$$

After the interaction, the azimuthal velocity of the gas element relative to the planet becomes $v_\varphi \simeq v\cos\delta$. Assuming $b \ll a$ and then $R \simeq a$, the variation of gas element angular momentum per unit mass caused by the interaction is

$$\Delta j_\mathrm{g} = a v_\varphi - a v \simeq a v(\cos\delta - 1) \simeq -2av\frac{1}{\cot^2\left(\frac{\delta}{2}\right)} = -\frac{2a(GM_\mathrm{P})^2}{b^2 v^3}. \tag{3.12}$$

There are two cases:

$$\begin{aligned} &\text{if} \quad R > a \quad \Longrightarrow \quad v < 0 \quad \Longrightarrow \quad \Delta j_{\rm g} > 0, \\ &\text{if} \quad R < a \quad \Longrightarrow \quad v > 0 \quad \Longrightarrow \quad \Delta j_{\rm g} < 0. \end{aligned} \tag{3.13}$$

Therefore, a gas element in an outer orbit respect to the planet gains angular momentum and migrates outward, while an inner gas element loses angular momentum and drifts inward. The net effect is that a planet pushes gas away from its orbit.

In order to calculate the torque exerted by the planet on the gas element, we need to know the typical timescale between two consecutive interactions. Assuming that the gas element continues to move on a circular orbit, we find

$$\Delta t = \frac{2\pi}{|\Omega_{\rm g} - \Omega_{\rm P}|} = \frac{2\pi a}{|v|}{\rm sgn}(v). \tag{3.14}$$

We can approximate the gas element velocity relative to the planet as

$$v = (a+b)\,\Omega_{\rm K}(a+b) - a\,\Omega_{\rm K}(a) \simeq -\frac{1}{2}\Omega_{\rm K}(a)b. \tag{3.15}$$

We can now calculate the torque per unit mass exerted by the planet on gas element

$$\Lambda_{\rm t} = \frac{\Delta j_{\rm g}}{\Delta t} = -\frac{{\rm sgn}(v)}{\pi}\frac{G^2 M_{\rm P}^2}{b^2 v^2} \simeq -\frac{4{\rm sgn}(a-R)}{\pi}\frac{G^2 M_{\rm P}^2}{G M_\star}\frac{a^3}{b^4}. \tag{3.16}$$

Calling f the initial numerical coefficients, defining $q \equiv M_{\rm P}/M_\star$ and rearranging the terms we finally obtain

$$\Lambda_{\rm t} = -f{\rm sgn}(a-R)q^2\Omega_{\rm K}^2 a^2\left(\frac{a}{R-a}\right)^4. \tag{3.17}$$

We note that $\Lambda_{\rm t}$ diverges if $R \to a$, but this cannot occur since we impose a condition on the minimum value of impact parameter

$$b \equiv |R-a| \geq \max[R_{\rm H}, H]. \tag{3.18}$$

$R_{\rm H}$ is the Hill radius

$$R_{\rm H} = \left(\frac{q}{3}\right)^{1/3} a \tag{3.19}$$

and defines a region of space where matter is gravitationally bound to the planet, then $b \geq R_{\rm H}$, otherwise the gas element would orbit around the planet and not the central star. The second condition requires $b \geq H$, because gas pressure modifies resonance locations , which cannot be closer to the planet orbit than the disk thickness, because a gap width smaller than this value would not be stable.

The specific torque in Eq. (3.17), modifies the evolution equation for gas surface density (2.37) with an additional term

$$\frac{\partial \Sigma}{\partial t} = \frac{3}{R}\frac{\partial}{\partial R}\left[R^{1/2}\frac{\partial}{\partial R}\left(\nu\Sigma R^{1/2}\right)\right] - \frac{2}{R}\frac{\partial}{\partial R}\left[\frac{\Lambda_{\rm t}\Sigma}{\Omega_{\rm K}}\right]. \tag{3.20}$$

The second term represents the tidal effect due to the presence of a planet, which pushes gas away from its orbit, while the first term describes the usual viscous evolution, that tends to fill the gap.

3.4 Gap opening

We now focus on the conditions for a planet to open a gap in the gas component of a protoplanetary disk. We assume to already have a gap of width Δ, which respects the condition $\Delta \geq \max[R_{\rm H}, H]$. We want to compare the viscous and tidal torques per unit mass, with the first trying to close the gap and the second to open it. Recalling (2.33), the viscous torque for a Keplerian disk is

$$\mathcal{G}_\nu = \left(2\pi\nu\Sigma R^3\Omega'\right)\big|_{R=a} = \left(-3\pi\nu\Sigma R^2\Omega_{\rm K}\right)\big|_{R=a} = -3\pi\nu\Sigma a^2\Omega_{\rm P}. \tag{3.21}$$

In order to obtain the viscous torque per unit mass, we divide the viscous torque by the mass of an annulus of width Δ

$$\Lambda_\nu = \frac{|\mathcal{G}_\nu|}{\Sigma 2\pi a\Delta} = \frac{3}{2}\nu\Omega_{\rm P}\left(\frac{a}{\Delta}\right) \tag{3.22}$$

From Eq. (3.17), the tidal torque per unit mass at the border of the gap is

$$\Lambda_{\rm t} = fq^2\Omega_{\rm P}^2 a^2\left(\frac{a}{\Delta}\right)^4. \tag{3.23}$$

To let the gap open the two specific torques must balance out, then imposing $\Lambda_\nu = \Lambda_{\rm t}$ we find

$$\left(\frac{\Delta}{a}\right)^3 = \frac{2}{3}fq^2\frac{\Omega_{\rm P}a^2}{\nu} = \frac{2}{3}fq^2 Re. \tag{3.24}$$

We note that for a massive planet (large q) or for a disk with low viscosity (large Re), the gap carved by the planet is wider. Using the α-prescription (2.66), the scale height relation $H = c_{\rm s}/\Omega_{\rm K}$ and neglecting the numerical coefficients, Eq. (3.24) can be re-written

$$q^2 \simeq \alpha\left(\frac{H}{R}\right)^2_{R=a}\left(\frac{\Delta}{a}\right)^3. \tag{3.25}$$

We now focus on the condition $\Delta \geq \max[R_{\rm H}, H]$. First, we want to estimate when $R_{\rm H} > H$ and, recalling the Hill radius definition (3.19), this is true for

$$q > 3\left(\frac{H}{R}\right)^3_{R=a}. \tag{3.26}$$

If $H/R \sim 0.05$ and $M_\star \sim 1\,M_\odot$, then $M_{\rm P} \gtrsim 0.4\,M_{\rm Jup}$. In case of $R_{\rm H} > H$, gap width has to satisfy the condition $\Delta > R_{\rm H}$ and this brings to

$$q > \frac{\alpha}{3}\left(\frac{H}{R}\right)^2_{R=a}. \tag{3.27}$$

On the other hand, if $H > R_{\rm H}$, we have to consider $\Delta > H$ and we obtain

$$q > \sqrt{\alpha}\left(\frac{H}{R}\right)^{5/2}_{R=a}. \tag{3.28}$$

With a numerical interpolation, Crida et al. (2006) provided a unified criterion for gap opening:

$$\frac{3}{4}\frac{H}{R_{\rm H}}+\frac{50}{q\,Re}\lesssim 1. \tag{3.29}$$

This criterion dictates the condition the parameters have to follow so that the planet carves a gap in the gas where density is 10 % of its unperturbed value.

3.5 Planet migration

So far, we focused on the effects that a planet causes on surrounding gas. However, thanks to Newton's third law of motion, the interaction between gas and planet induces also a change in planet angular momentum, leading to its migration. The equation describing this variation is

$$\frac{\mathrm{d}}{\mathrm{d}t}\left(M_{\rm P}\Omega_{\rm P}a^2\right)=-\int_{R_{\rm in}}^{R_{\rm out}}\Lambda_{\rm t}2\pi R\Sigma\mathrm{d}R. \tag{3.30}$$

Planetary migration can be divided in two types:

- Type I, which occurs when the planet is not massive enough to carve a gap, so the planet is completely embedded in the gaseous disk.
- Type II, which occurs when the planet is massive enough to open a gap in the disk.

Type I migration proceeds at a much faster rate compared to Type II. This is attributed to the absence of a gap, resulting in the planet being directly influenced by the nearby gas with the strongest Lindblad resonances. As shown by Tanaka et al. (2002), the torque on the planet is given by

$$\frac{\mathrm{d}J}{\mathrm{d}t}=-(1.36+0.54\xi)q^2\left(\frac{H}{R}\right)^{-2}\Sigma a^4\Omega_{\rm K}\,. \tag{3.31}$$

We focus on Type II migration in the next Section.

3.5.1 Type II migration

We consider the presence of a gap carved by a planet, locked at the center of the gap and exerting a torque on the disk that bridges the two sides of the gap. We also assume that the gap width is very small, so that gas-planet interaction is concentrated close to the planet orbit and we can study the angular momentum balance for $R=a$. Here we have the viscous torque of the gas $\mathcal{G}_\nu$ from Eq. (3.21) and the tidal torque $\mathcal{G}_{\rm t}$ exerted by the planet on the gas

$$\mathcal{G}_{\rm t}=-\frac{\mathrm{d}}{\mathrm{d}t}\left(M_{\rm P}\Omega_{\rm P}a^2\right)=-\frac{1}{2}M_{\rm P}\Omega_{\rm P}a\dot{a}. \tag{3.32}$$

The sum of these torques gives the gas angular momentum variation in time

$$\mathcal{G}_\nu+\mathcal{G}_{\rm t}=2\pi R v_R\Sigma\Omega R^2\big|_{R=a}. \tag{3.33}$$

Since the planet remains at the center of the gap, they migrate together and $v_R = \dot{a}$, so we can write

$$-3\pi\nu\Sigma a^2\Omega_{\rm P} - \frac{1}{2}M_{\rm P}\Omega_{\rm P}a\dot{a} = 2\pi\Sigma\Omega_{\rm P}a^3\dot{a}, \tag{3.34}$$

from which we find

$$\dot{a}\left(1 + \frac{M_{\rm P}}{4\pi a^2\Sigma}\right) = -\frac{3}{2}\frac{\nu}{a}. \tag{3.35}$$

The term on the right-hand side is the gas radial velocity toward the central star in absence ot the planet (see Eq. (2.35)). We define the ratio between the disk mass inside the planet orbit and the planet mass as

$$B \equiv \frac{4\pi a^2\Sigma}{M_{\rm P}} \tag{3.36}$$

and, from Eq. (3.35), we finally obtain

$$\dot{a} = -\frac{3}{2}\frac{\nu}{a}\frac{B}{1+B}. \tag{3.37}$$

We can identify now two cases:

- $B \gg 1$, called *disk dominated* regime. If planet mass is small compared to disk mass (but still high enough to carve a gap), we derive

  $$\dot{a} \simeq -\frac{3}{2}\frac{\nu}{a}. \tag{3.38}$$

  Therefore, the planet behaves like gas and transports angular momentum with tidal torque in exactly the same way gas would do through viscous torque.

- $B \ll 1$, called *planet dominated* regime. If the planet is much more massive than the disk, its migration velocity is decreased by a factor B

  $$\dot{a} \simeq -\frac{3}{2}\frac{\nu}{a}B. \tag{3.39}$$

  This means that the planet stabilizes its orbit and prevents material from outside to cross the gap. Then, this outer material accumulates outside the gap, while material inside planet orbit continues to accrete onto the central, without being refilled from the outside. The initial gap becomes a cavity in the region of the disk inside planet orbit, generating a transition disk.

CHAPTER 4

Interferometric observations of protoplanetary disks

In the last decade, the revolution in the study of protoplanetary disks has been lead by the spectacular images collected by the (sub-)millimeter interferometer ALMA, showing substructures in the emission of protoplanetary disks with an unprecedented detail (see Fig. 1.5). This has been made possible by the exquisite high resolution of ALMA.

It is common knowledge that the resolution of an optical system, as defined by Lord Rayleigh, relies on its capacity to distinguish between two separate point sources based on the overlap of their Airy discs created through diffraction. In the absence of atmospheric disturbances, the angular resolution of an ideal optical system is given by $\theta \sim 1.22\lambda/D$ where λ represents the wavelength, and D is the diameter of the optical system. In the field of astronomy, it becomes imperative to consider atmospheric disturbances that can distort the images of stars when observed through a telescope. Nevertheless, disregarding these atmospheric effects, a telescope's angular resolution is solely dictated by its diffraction limit. To achieve higher resolutions, one must either reduce the observing wavelength or increase the telescope's diameter.

4.1 The wavelength choice

The choice of the wavelength in an astronomical observation is clearly dictated by the specific phenomena being studied. As discussed in Chap. 1, the emission of a protoplanetary disk can be characterized by its SED. The shape of the SED can be explained with the multicolor blackbody emission model. As depicted in Fig. 4.1, in this model every disc annulus emits as a black body with temperature depending on the radius

$$T(R) = T_{\rm in}\left(\frac{R}{R_{\rm in}}\right)^{-q}, \tag{4.1}$$

where q is a coefficient and $T_{\rm in}$ is the temperature at the disc inner radius $R_{\rm in}$. In the same way, we call $T_{\rm out}$ the temperature at the disc outer radius $R_{\rm out}$. Typically, closer to the star a protoplanetary disc can reach a temperature of several hundred K, while at larger distances ($\sim 100\,{\rm au}$) the temperature is around $20\,{\rm K}$. The total flux for an observer at distance D, whose line of sight makes an angle i to the normal of the disc plane (where $i = 0$ represents the face-on case) is expressed by

$$\nu F_\nu = \frac{2\pi\cos i}{D^2}\int_{R_{\rm in}}^{R_{\rm out}} \nu B_\nu(T(R)) R {\rm d}R, \tag{4.2}$$

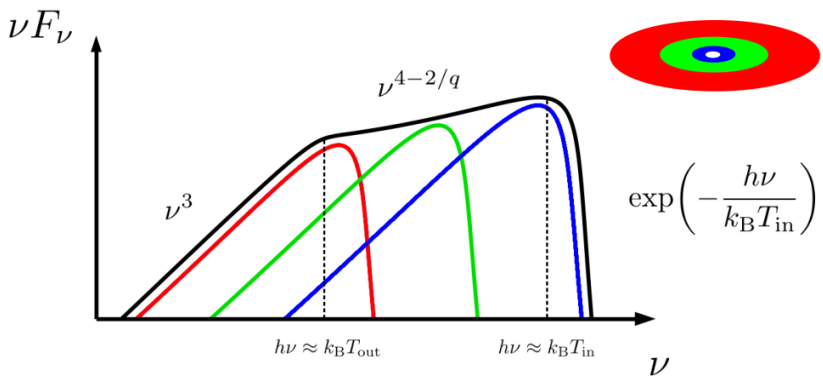

Figure 4.1: Multicolor black body model for SED, in bi-logarithmic scale. Adapted from Dipierro (2016).

where B_ν is the Planck function for the black body emission

$$B_\nu(T) = \frac{2\pi\nu^3}{c^2}\frac{1}{e^{h\nu/k_B T} - 1}. \tag{4.3}$$

In the Rayleigh-Jeans regime, so at low frequencies for $h\nu \ll k_B T_{out}$, we find

$$\nu F_\nu \propto \nu^3, \tag{4.4}$$

while in the Wien approximation, so at high frequencies for $h\nu \gg k_B T_{in}$, the exponential cutoff dominates

$$\nu F_\nu \propto \exp\left(-\frac{h\nu}{k_B T_{in}}\right). \tag{4.5}$$

For the intermediate regime $k_B T_{out} \ll h\nu \ll k_B T_{in}$, we first define

$$x \equiv \frac{h\nu}{k_B T(R)} = \frac{h\nu}{k_B T_{in}}\left(\frac{R}{R_{in}}\right)^q \tag{4.6}$$

and from this we derive

$$\frac{dx}{x} = q\frac{dR}{R} \qquad \text{and} \qquad R \propto \left(\frac{x}{\nu}\right)^{1/q}. \tag{4.7}$$

Substituting in Eq. (4.2) we find

$$\nu F_\nu \propto \int_{x_{in}}^{x_{out}} \left(\frac{x}{\nu}\right)^{2/q} \frac{\nu^4}{e^x - 1}\frac{dx}{x} = \nu^{4-2/q}\int_{x_{in}}^{x_{out}} \frac{x^{2/q-1}}{e^x - 1}dx, \tag{4.8}$$

with

$$x_{in} = \frac{h\nu}{k_B T_{in}} \ll 1 \qquad x_{out} = \frac{h\nu}{k_B T_{out}} \gg 1. \tag{4.9}$$

Thanks to these last conditions, we can safely change the integration extremes with 0 and ∞. In this way, the integral in Eq. (4.8) is simply a number and we finally obtain

$$\nu F_\nu \propto \nu^{4-2/q}. \tag{4.10}$$

The multicolor blackbody model can then explain the shape of a disk SED and is essential for understanding why the sub-millimeter wavelength range is optimal for observing the midplane region of a disk. Investigating the midplane of the disk is pivotal in comprehending the planet formation process, as it represents the region where the majority of the disk's mass is concentrated and where planets are expected to form. It is established that millimeter-sized dust particles with a Stokes number ($\mathrm{St} \sim 1$) in the disk undergo significant vertical settling and have a temperature of approximately $20\,\mathrm{K}$. According to Wien's displacement law, the thermal emission from this dust peaks in the range of $0.1 - 1, \mathrm{mm}\,(1000 - 300\,\mathrm{GHz})$. Furthermore, the multicolor blackbody model indicates that at these wavelengths, observations will predominantly capture the contribution of the cold dust in the outer disk, with negligible influence from the hotter material near the star or the star itself, as their thermal emissions substantially decrease in this wavelength range. While our focus has been on the thermal emissions from the star and dust, it's important to note that other emission mechanisms within a protoplanetary disk emit radiation detectable between the sub-millimeter and centimeter wavelength range, which will be discussed in Chapter 8.

4.2 The need for interferometry

Established that the optimal observing wavelength for capturing dust emission from the midplane is in the millimeter range, the sole alternative for enhancing angular resolution is to increase the diameter of the telescope. However, achieving a resolution of $10\,\mathrm{au}$ in a nearby star-forming region, situated at a distance of $150, \mathrm{pc}$ (such as Taurus or Lupus), demands an angular resolution of $0.07''$. To attain this resolution at a wavelength of $1\,\mathrm{mm}$, a telescope with a diameter of $3.8\,\mathrm{km}$ would be necessary. The biggest existing telescope ever built is the Five-hundred-meter Aperture Spherical radio Telescope (FAST) in southwest China. Building a single monolithic antenna with a diameter of several kilometres would become exceedingly expensive and operationally challenging.

Alternatively, astronomical interferometry offers a viable solution for achieving high-resolution observations using a cost-effective cluster of relatively small telescopes. In an interferometer, the angular resolution scales as $\theta \sim \lambda/b$, where b represents the baseline, i.e., the maximum distance between antennas. Consequently, an array of antennas with a maximum distance spanning several kilometers can achieve remarkable resolution. ALMA has a maximum baseline of $16\,\mathrm{km}$, corresponding to $0.013''$ ($2\,\mathrm{au}$ at $150, \mathrm{pc}$) at an observing wavelength of $1\,\mathrm{mm}$. However, breaking down a single antenna into multiple components in an interferometer incurs a trade-off, resulting in the loss of information corresponding to the absent portions of the hypothetical kilometer-sized antenna dish that the interferometer is effectively replacing. Consequently, this necessitates the application of image reconstruction techniques on the acquired data to "fill in" the missing details.

4.3 Basics of interferometry

In this Section, I present the fundamental concepts of astronomical interferometry. For more in-depth explanations of this technique and its various applications, refer to the books Wilson et al. (2012) and Burke et al. (2019). Additional valuable teaching resources can be accessed through the slides and video lectures available in the NRAO Imaging Synthesis Workshop[1].

4.3.1 Antenna beam pattern

From far-infrared to radio astronomy, telescopes transition to antennas because traditional lenses and mirrors are less effective due to the longer wavelengths involved. Antennas, particularly parabolic dishes, are better suited to capture and focus these longer wavelengths, making them more practical for observing in this wavelength range. The response of an antenna to electromagnetic radiation is characterized by its beam pattern, a mathematical function or graphical representation of the antenna capacity to receive or radiate[2] energy as a function of space coordinates, as depicted in Fig. 4.2. Lobes within the radiation pattern are categorized as major (or main) and minor lobes. The major lobe, also known as the main beam, encompasses the direction of maximum radiation. Conversely, minor lobes include all lobes aside from the major lobe, representing radiation in less desirable directions, such as towards the ground or the telescope itself. Radiation picked up in the antenna's minor lobes, termed spillover radiation, should be minimized to enhance antenna directivity.

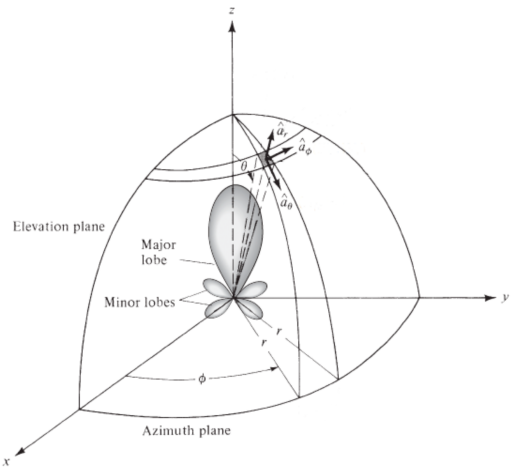

Figure 4.2: Beam pattern for a single antenna. Adapted from Balanis, (2008).

[1] https://science.nrao.edu/science/meetings/2014/14th-synthesis-imaging-workshop/lectures

[2] An essential characteristic of antennas is that the receiving pattern of an antenna, when used for receiving, is identical to the far-field radiation pattern of the same antenna when employed for transmitting. This symmetry is a direct outcome of the reciprocity theorem in electromagnetism. Consequently, an antenna can be regarded interchangeably as either a transmitter or a receiver.

Accompanying the antenna pattern is a parameter known as beamwidth. The beamwidth of a radiation pattern is the angular separation between two identical points on opposite sides of the pattern maximum. This parameter is also employed to describe the antenna's resolution capabilities in distinguishing between two adjacent radiating sources. The prevalent resolution criterion states that the antenna's resolution capability is equivalent to the Full Width Half Maximum (FWHM), defined by the angle between the two directions where the radiation intensity is half of the maximum pattern value.

4.3.2 Two element interferometer

We consider an interferometer consisting of two antennas. Figure 4.2 illustrates the geometry of this system collecting radiation from a small element of an extended celestial source. It can be demonstrated that the fundamental observable in interferometry is the visibility V, which is the Fourier transform of the sky brightness B:

$$V(u,v) = Ae^{i\phi} = \int \hat{A}(x,y)\, B(x,y)\, e^{-i2\pi(ux+vy)}\, \mathrm{d}x\mathrm{d}y\,. \tag{4.11}$$

Here, (u,v) are the coordinates of the baseline in units of wavelength λ, and (x,y) are the coordinates in the sky, measuring the relative distance to the reference point $(x = 0, y = 0)$ known as *phase center*. The (u,v) coordinates are also called *spatial frequencies*. $\hat{A}$ is a correction factor for the primary beam. The visibility V is a complex number having amplitude A, containing information on the intensity contribution of the different spatial scales, and phase ϕ, indicating where these spatial scales are contributing. The geometrical relation between the sky plane (x,y) and the baseline plane $(u,v$ is depicted in the right panel of Fig. 4.3. These two planes, namely the interferometer response and the source image in the sky, are connected by the Fourier transform in Eq. 4.11. This relationship is determined by the van Cittert-Zernike theorem, upon which aperture synthesis interferometry is built.

Our final goal is to reconstruct the radiation from the astronomical source, that is the sky brightness. Calling $B'(x,y) = \hat{A}B(x,y)$ the sky brightness corrected for the primary beam, we can reconstruct it from an inverse Fourier transform:

$$B'(x,y) = \int V(u,v)\, e^{i2\pi(ux+vy)}\, \mathrm{d}u\mathrm{d}v\,. \tag{4.12}$$

The observation made with a two-element interferometer provides us with a single component (u,v) of the Fourier transform. It is intuitive that to create a true "image" of the source, that is, to reconstruct $B(x,y)$, it is necessary to have multiple antennas available to correlate the signal received over a large number of baselines. This is the aperture synthesis interferometry.

4.3.3 Aperture synthesis

Combining signals from numerous antennas within a single interferometer improves the sampling of the uv-space, although complete and continuous coverage is unattainable. Equation 4.12 necessitates full and continuous uv-space coverage for the correct

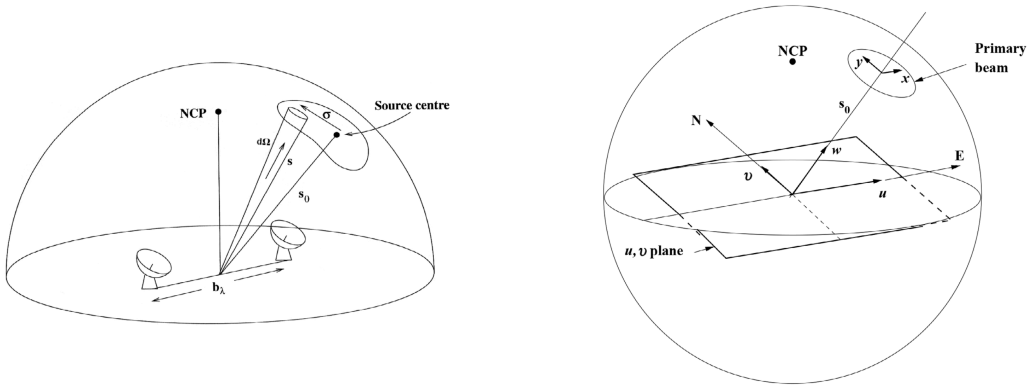

Figure 4.3: *Left panel*: The geometry of the radiation captured from a small segment of the extended source, encompassing a solid angle $\mathrm{d}\Omega$ in the direction of s, with s_0 denoting the reference phase position. *Right panel*: The geometrical relation among an interferometer, a celestial source, and the u, v plane, considered in relation to the celestial sphere. NCP indicates the North Celestial Pole. Images from Burke et al. (2019).

computation of the integral. However, the measured visibilities represent discrete samples corresponding to the response of antenna pairs, depending on the physical antenna locations, rather than forming a continuous function across the entire uv-plane. To optimize sampling in the uv-space, several strategies can be employed. Firstly, increasing the number of antennas enhances baseline coverage, following the formula $N(N-1)/2$, where N is the number of antennas (e.g., the ALMA 12-m array have 50 antennas). Secondly, antenna configurations can be changed, relocating antennas to different physical pads, and this allows for uv-plane sampling across multiple scales. Thirdly, Earth rotation is utilized to sample different baselines, capitalizing on the changing relative inclination between the astronomical source and the interferometer during rotation, thereby increasing baseline sampling. However, inherent limitations persist. Angular resolution is determined by the longest baselines, restricting information beyond this maximum baseline and limiting details at smaller scales. While short baselines offer insights into large spatial scales, the non-null minimum baseline, dictated by the physical extent of antenna dishes, leads to the unavoidable absence of information on very large scales, a phenomenon known as *spatial filtering*. Additionally, information gaps in various regions of the uv-plane contribute to the formation of side lobes.

The sensitivity of an interferometer is expressed by the equation

$$\sigma_{\mathrm{rms}} = \frac{1}{\eta_{\mathrm{s}}} \frac{S_{\mathrm{EFD}}}{\sqrt{N(N-1)\Delta\nu\tau}} \,. \tag{4.13}$$

Here, σ_{rms} represents the rms noise level of the flux density, η_{s} accounts for system efficiency, considering losses in electronics and digitalization, S_{EFD} is the system equivalent flux density, encompassing instrumental (antenna + receiver) and atmospheric noise, $\Delta\nu$ is the bandwidth, and τ is the observing time (integration time). This relationship reveals that, to enhance sensitivity and reduce noise levels, keeping fixed instrumental charac-

teristics and atmospheric noise dictated by the observatory location, an observer can increase either the bandwidth or the integration time.

Imaging

As we mentioned, with a limited number of antennas, the uv-plane is sampled in a discrete number of points. The *sampling function* $S(u, v)$ is the distribution of baselines in the uv-plane. Having M baselines in the points (u_k, v_k), it is defined by

$$S(u, v) = \sum_{k=1}^{M} \delta(u_k, v_k)\,. \tag{4.14}$$

The Fourier transform of the sampling function is referred to as *dirty beam*. The measured brightness distribution is called *dirty image* (indicated with $B_{\rm mis}(x, y)$) and is the Fourier transform of the product between the visibility function $V(u, v)$ and the sampling function. Using the properties of the Fourier transform (indicated with $\mathcal{F}$) and convolution, we can write:

$$B_{\rm mis}(x, y) = \mathcal{F}(V(u, v)S(u, v)) = \mathcal{F}(V(u, v)) * \mathcal{F}(S(u, v)), \tag{4.15}$$

where $\mathcal{F}(V(u, v))$ is the "true" image and $\mathcal{F}(S(u, v))$ is the dirty beam. Thus, the observed dirty image is a convolution of the true image with the dirty beam. These relations are illustrated in Fig. 4.4. To obtain the true image, it is necessary to deconvolve the dirty beam from the dirty image.

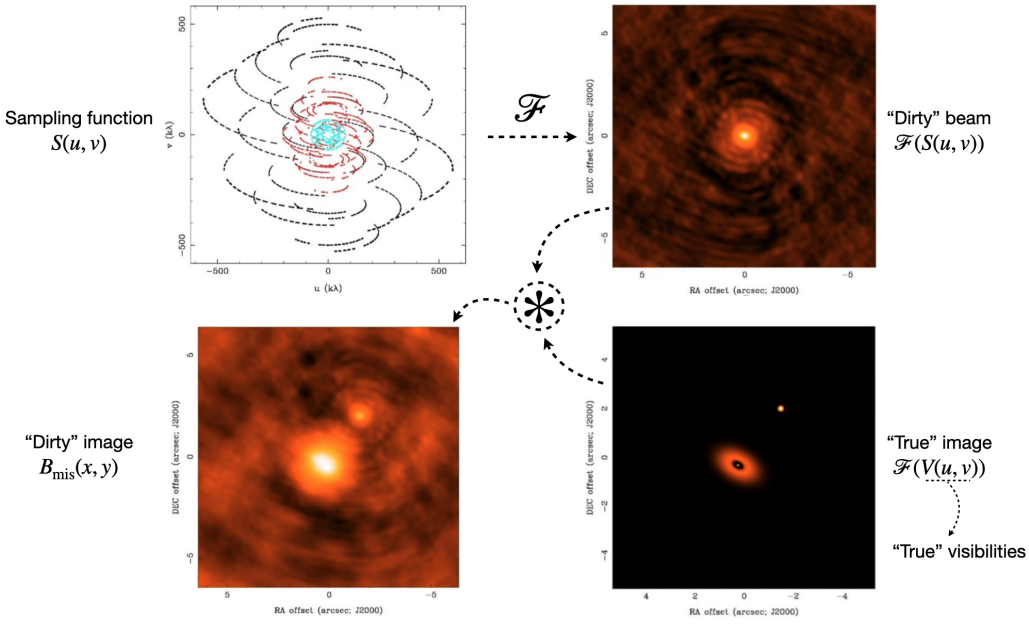

Figure 4.4: Graphical illustration of the relation between the concepts of sampling function, "dirty" map, "true" image and "dirty" map.

Before devonvolving the dirty image, it has to be computed from the observed visibilities. To do so, a Fast Fourier Transform is applied. This algorithm requires a regular grid, but measured visibilities are obtained on an irregular grid. Therefore, they are first mapped onto a regular grid, where the grid cells lacking uv-data are set to 0. Visibilities can be weighted and different weighting schemes W are possible when calculating the dirty beam (Briggs 1995)

$$B_{\rm mis}(x,y) = \frac{\sum_{k=1}^{M} \mathcal{F}[W_k(u,v)V(u,v)S(u,v)]}{\sum_{k=1}^{M} W_k(u,v)} \,. \tag{4.16}$$

Defining σ_k^2 as the noise variance for the visibility $V(u_k, v_k)$, *natural* weighting is represented by

$$W_k = \frac{1}{\sigma_k^2} \,. \tag{4.17}$$

It maximizes point source sensitivity while increasing the side-lobes. *Uniform* weighting is defined as

$$W_k = \frac{1}{\sigma_k^2 \, \rho(u_k, v_k)} \tag{4.18}$$

with $\rho(u_k, v_k)$ being the density of measured uv-point in a uv-cell. This scheme gives the finest angular resolution, while lowering the point source sensitivity. Then, *robust* weighting gives an intermediate choice between natural and uniform

$$W_k = \frac{1+s}{\sigma_k^2 \, [1 + s\rho(u_k, v_k)/\sigma_k^2]} \tag{4.19}$$

with s ranging from -2 to 2.

The most common algorithm for deconvolution is CLEAN (Högbom 1974). In its most basic version, it assumes that the sky is a linear combination of point sources. CLEAN is an iterative process, with the following steps:

1. The Fast Fourier Transform is employed to compute the dirty beam and dirty image.
2. Intensity peaks are identified.
3. A delta function is assigned to the position of the peak, with the measured amplitude assigned to a sky model.
4. A fraction of the model is subtracted from the residual map using a parameter gain.
5. The process returns to step 2 and continues iteratively until a predefined threshold for the maximum residual is reached.
6. The sky model is convolved with a Gaussian fit of the primary beam, and the residual map is added to obtain the final image.

The entire process is illustrated in Fig. 4.5. Fig. 4.6 shows the effect of uv coverage and weighting scheme on the protoplanetary disk RU Lup observed within the ALMA Large Program DSHARP (Andrews et al. 2018a).

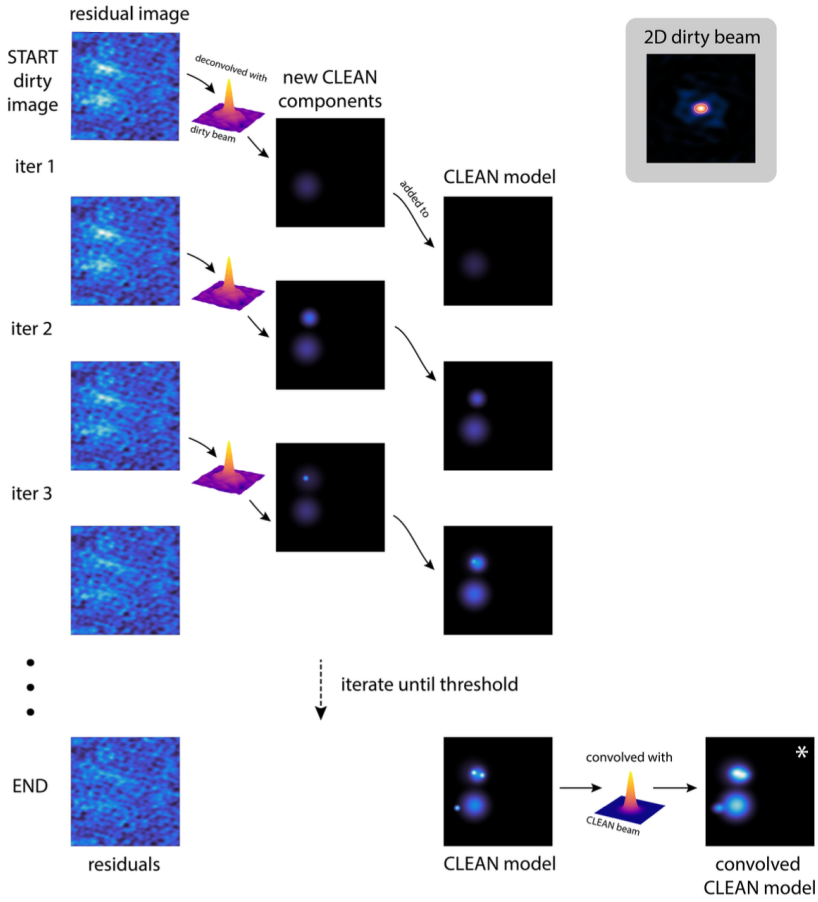

Figure 4.5: Schematization of the CLEAN-ing process by Czekala et al. (2021).

In addition to the original CLEAN algorithm, various procedures for image reconstruction have been developed. One notable modification is found in the Multi-Scale CLEAN (Cornwell 2008) where the sky model is composed by a linear combination of Gaussians with different FWHM values. Another variant is the Multi-Scale Multi-Frequency CLEAN (Rau & Cornwell 2011), adding the modeling of the wide-band sky brightness distribution by utilizing a multi-term Taylor polynomial. Alternative methods for image synthesis include Regularized Maximum Likelihood (RML) algorithms. These algorithms employ a non-parametric forward model with the objective of maximizing the likelihood of observed visibility data. They also integrate regularizers to enhance accuracy. Noteworthy codes applied to interferometric observations of protoplanetary disks include UVMEM (Casassus et al. 2006; Cárcamo et al. 2018) and MPOL (Czekala et al. 2023; Zawadzki et al. 2023).

A different approach to imaging disk visibilities is direct fitting. The primary advantages of this approach lie in better treatment of the uncertainties, avoiding convoluted error propagation in image reconstruction, and the potential to achieve sub-beam res-

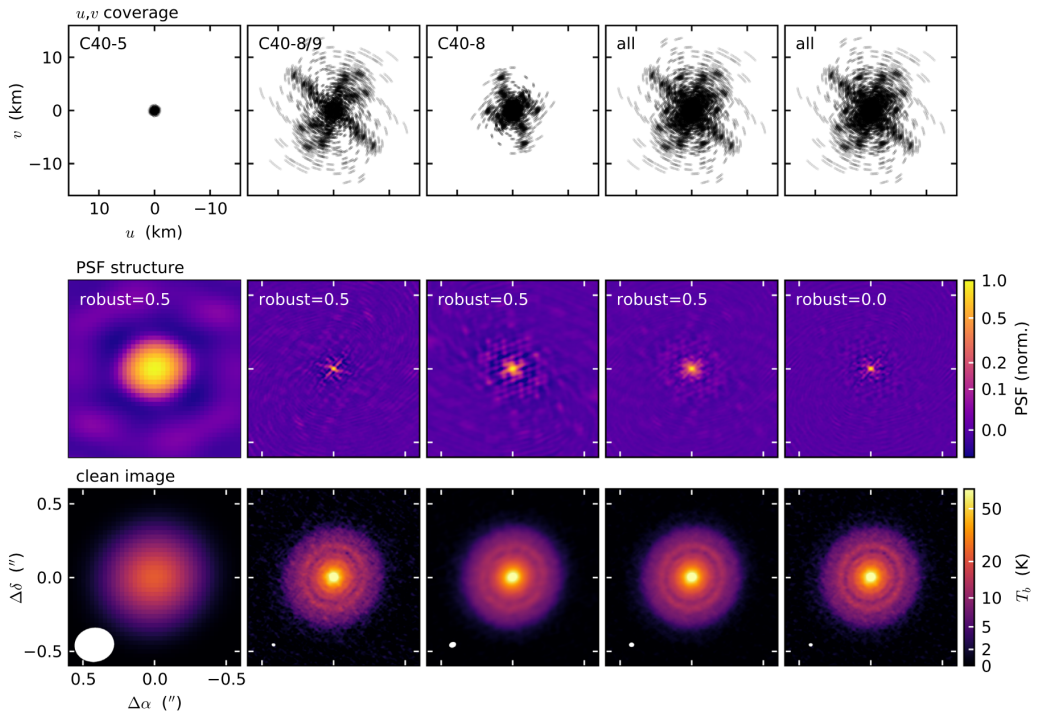

Figure 4.6: Illustration of the impact of spatial frequency coverage and visibility weighting on the Point Spread Function (PSF) structure and image morphology for the RU Lup disk from the DSHARP ALMA Large Program (Andrews et al. 2018a). The top panels exhibit the observed uv coverage, the middle panels depict the corresponding PSF structures labeled with the robust weighting parameter, and the bottom panels showcase resultant images on the same brightness temperature scale. FWHM beam dimensions are indicated in the lower left corners of each image.

olution. Codes such as `galario` (Tazzari et al. 2018) and `frank` (Jennings et al. 2020) adopt this approach, and their descriptions will be provided in Sect. 6.2.1 and 6.2.2.

Data calibration

Data collected by an interferometer need to be calibrated in order to obtain the "true" visibilities. This is the fundamental equation of calibration:

$$V_{ij}(t) = g_i(t)\, g_j^*(t)\, V^{\rm true}(t) + \epsilon_{ij}(t), \tag{4.20}$$

where t is time, V_{ij} is the visibility measured between antennas i and j, g_i is complex gains of antenna i, $V^{\rm true}$ is the true visibility and ϵ_{ij} is the noise (from the instrument and the atmosphere). In an interferometer composed of N antennas, calibration involves determining 2N parameters: N amplitudes and N phases for each complex gain. Calibration is feasible because each measurement yields N(N-1)/2 visibilities, rendering the system overdetermined.

Calibration is required to correct for the atmospheric effect of the troposphere and ionosphere on the wave front, and to correct for the variations of electronics instruments

over time. The optimal approach for solving the calibration equation involves using well-characterized and stable calibrators, particularly point sources that are bright in the millimeter-centimeter wavelength range. Assuming these sources are point-like, their phase is considered zero (if the phase center of the observations corresponds to the calibrator's location). Gain functions are then computed on these calibrators and applied to scientific observations. This process is known as *cross-calibration*. Each observation requires three fundamental calibrations: flux calibration, passband calibration (to correct for the spectral dependence), and phase calibration. If the astrophysical source is particularly bright, it becomes possible to solve the calibration equation using the source itself after applying cross-calibration. This practice is called *self-calibration* and offers advantages such as more frequent computation of gain functions (both phase and amplitude) and computation at the same location as the source, eliminating pointing changes that are required when observing other sources as calibrators. The main software used for the treatment of interferometric data from ALMA and VLA, encompassing tasks ranging from visibility manipulation to self-calibration and imaging , is the Common Astronomy Software Applications (CASA) CASA Team et al. (2022).

Part II

The role of outer planets in the formation of dust substructures

CHAPTER 5

Modeling planet-disk interactions in the disk around the very low-mass star CIDA 1

This chapter is based on the paper "A giant planet shaping the disk around the very low-mass star CIDA 1" by ***Pietro Curone****, Andrés F. Izquierdo, Leonardo Testi, Giuseppe Lodato, Stefano Facchini, Antonella Natta, Paola Pinilla, Nicolas T. Kurtovic, Claudia Toci, Myriam Benisty, Marco Tazzari, Francesco Borsa, Marco Lombardi, Carlo F. Manara, Enrique Sanchis, and Luca Ricci, published on Astronomy and Astrophysics in September 2022, 665, A25.*

Planets have been detected around very low-mass (VLM) stars, defined as stars with masses $\lesssim 0.3\,\mathrm{M}_\odot$ but still above the hydrogen-burning limit of $\sim 0.08\,\mathrm{M}_\odot$, below which the brown dwarf regime begins (Liebert & Probst 1987). Particularly fascinating are the cases of TRAPPIST-1, a $\sim 0.085\,\mathrm{M}_\odot$ star in the solar neighborhood with a system of seven rocky planets (Gillon et al. 2017), and Proxima Centauri, the closest star to the Sun, which has a mass of $\sim 0.12\,\mathrm{M}_\odot$ and hosts a terrestrial planet, a super-Earth candidate, and a newly discovered sub-Earth candidate (Anglada-Escudé et al. 2016; Damasso et al. 2020, Faria et al. 2022). In general, data from the Kepler spacecraft show that the occurrence rate of small planets (with radii of $1.0-2.8\,\mathrm{R}_\oplus$) is 3.5 times higher for M dwarfs than FGK stars (Mulders et al. 2015). Even more intriguingly, giant planets have been confirmed orbiting around VLM stars and brown dwarfs. Chauvin et al. (2005) directly imaged a $\sim 5\,\mathrm{M}_\mathrm{Jup}$ planet around a $\sim 25\,\mathrm{M}_\mathrm{Jup}$ young brown dwarf, and Morales et al. (2019) discovered a planet with a minimum mass of $0.46\,\mathrm{M}_\mathrm{Jup}$ orbiting a $\sim 0.12\,\mathrm{M}_\odot$ star. However, giant planet formation in this low-stellar-mass regime remains a conundrum.

Planets originate in protoplanetary disks and, generally, the most supported theory to explain their formation is the core accretion model (Pollack et al. 1996). Assuming this scenario, the main problems for planet formation around VLM stars are the fast dust radial drift (Pinilla et al. 2013) and the apparent lack of material necessary for disks in the low-stellar-mass regime to generate planets (Testi et al. 2016; Sanchis et al. 2020). Several theoretical studies (Payne & Lodato 2007; Liu et al. 2020; Miguel et al. 2020) performed numerical simulations to assess planet formation around VLM stars and brown dwarfs in a core accretion scenario. They have shown that rocky planet formation in this condition is possible, but the emergence of gas giants is always excluded. A viable explanation

for the formation of giant planets around VLM stars seems to be the fragmentation of a disk in its early stages due to gravitational instability (Mercer & Stamatellos 2020).

Observational evidence of protoplanetary disks around VLM stars and brown dwarfs has been collected for decades via multiple observatories (e.g., Comeron et al. 1998; Natta & Testi 2001; Natta et al. 2002; Mohanty et al. 2005). Nowadays, high-resolution and high-sensitivity observations from the Atacama Large Millimeter/submillimeter Array (ALMA) can provide essential information to shed light on planet formation in this low-stellar-mass regime (Ricci et al. 2014; Testi et al. 2016). Nonetheless, only a minimal sample of protoplanetary disks in the low-mass regime has been resolved at high resolution. The reason lies in their smaller size and fainter emission compared to disks around more massive stars (Hendler et al. 2017; Rilinger et al. 2019; Sanchis et al. 2020). Hence, they require more demanding observations.

Recently, Kurtovic et al. (2021) presented the first small survey of disks around VLM stars at high resolution observed by ALMA ($\sim 0.1''$ at $0.87\,\mathrm{mm}$, Band 7). The authors selected a sample of six low-mass disks located in the Taurus star-forming region, focusing on the brightest objects to maximize the likelihood of observing substructures. Three sources showed structures in their dust emission, which could be explained by the interaction with massive planets. Among these disks is CIDA 1 (2MASS J04141760+2806096), the subject of our work.

This source was first observed by Briceno et al. (1993), and the circumstellar disk was detected by Schaefer et al. (2009) in millimeter wavelengths. Then, with observations from ALMA Cycle 0 at an angular resolution of about $0.4''$ (corresponding to $\sim 55\,\mathrm{au}$ at $137.5\,\mathrm{pc}$, the estimated distance to CIDA 1[1]), Ricci et al. (2014) showed a dust disk and detected the CO ($J = 3{-}2$) line emission.

An inner cavity with a radius of $\sim$ 20 au in the dust emission was first detected by Pinilla et al. (2018), using observations in Band 7 from ALMA Cycle 3 with a resolution of $0.21'' \times 0.12''$ ($\sim 29 \times 17\,\mathrm{au}$). To explain such structure, the authors exploited the Crida et al. (2006) criterion for gap opening in the gas, assuming a Shakura & Sunyaev (1973) viscosity value of 10^{-4} and a stellar mass $M_\star = 0.1\,\mathrm{M}_\odot$. They found that a planet with a minimum mass of $\sim 0.3\,\mathrm{M}_\mathrm{Jup}$ orbiting at a distance of $15\,\mathrm{au}$ from the central star could carve the observed cavity.

The most recent high-resolution observation of CIDA 1 was presented by Pinilla et al. (2021). They showed ALMA Cycle 6 observations (ALMA project 2018.1.00536.S, PI: A. Natta) for dust continuum in Band 7 (0.9 mm) and Band 4 (2.1 mm) at a resolution of $\sim 0.050'' \times 0.034''$ ($\sim 7 \times 5\,\mathrm{au}$). These images clearly reveal a dust ring, whose emission peaks at $\sim$ 20 au from the star, surrounding a gap with an unresolved inner disk (see Fig. 5.1). Furthermore, these observations also detected the gas line emission from ^{12}CO ($J = 3{-}2$) and ^{13}CO ($J = 3{-}2$). The authors used 1D dust evolution simulations and excluded that a planet more massive than $M_\star = 0.5\,\mathrm{M}_\mathrm{Jup}$ could create the dust gap.

[1]Throughout the work, we assume this value as the distance to CIDA 1 for consistency with Pinilla et al. (2021). Recently, Bailer-Jones et al. (2021) used Gaia EDR3 (Gaia Collaboration et al. 2021) and derived a distance of $133.4^{+0.7}_{-0.9}\,\mathrm{pc}$. Such a distance differs by $\approx 3\%$ from the value in Pinilla et al. (2021), implying a systematic difference of the same order in the spatial scales derived from our models and a discrepancy of $\sim 6\%$ in the estimated value of the disk mass.

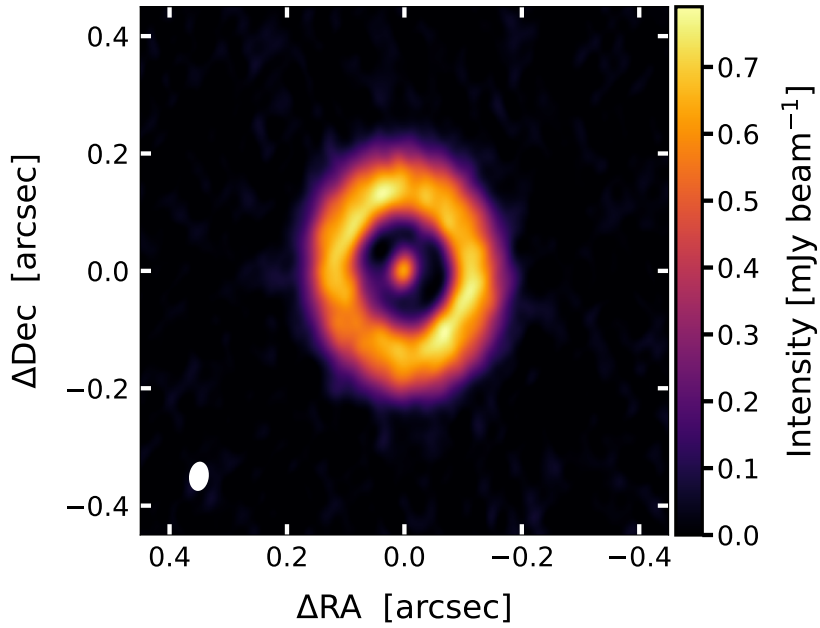

Figure 5.1: ALMA observation in Band 7 (0.9 mm) of the system CIDA 1 (Pinilla et al. 2021), with a full width at half maximum (FWHM) beam size of $0.050'' \times 0.034''$, indicated by the white ellipse in the bottom-left corner.

In this work we aim to reproduce the observed dust and gas emission of the disk to evaluate whether the presence of the observed substructures can be explained by the interactions of the disk with an embedded planet. While Pinilla et al. (2021) assumed an analytical gap shape, we obtain it from hydrodynamical simulations. We employed full 3D modeling to take the dynamical and radiative aspects of the disk into account, along with the effects introduced by interferometric observations with ALMA. Furthermore, in our work we compared the results of our models not only with observed dust emission but also gas emission. We used 3D hydrodynamical simulations to study how planets with different masses influence the dynamics of gas and dust in a disk around a VLM star. After that, we used 3D Monte Carlo radiative transfer simulations to compute the dust continuum emission and the gas line emission. Finally, we treated the output results as real interferometric observations and compared our models to the collected data. The key parameters that we derive are the mass and position of the supposed planet around CIDA 1. The presence of a gas giant planet around a young VLM star would call into question our current theory of planet formation.

This work is organized as follows: In Sect. 5.1 we describe the numerical simulations and procedures used to obtain the final synthetic observations. In Sect. 5.2 we present the results on the modeling of the dust and gas emission, comparing them with the ALMA observations of CIDA 1. Section 5.3 is devoted to the discussion of our findings: we analyze the simulated spectral index and optical depth, evaluate whether planet-induced perturbations could be detected in the gas line emission, and constrain the minimum

and maximum mass of the putative planet. We also compare our modeling with previous mass estimates of the planet and investigate its possible origin. Finally, in Sect. 5.4 we summarize our results.

5.1 Methods

5.1.1 Gas and dust hydrodynamical simulation

We performed a set of five hydrodynamical simulations with the smoothed particle hydrodynamics (SPH) code PHANTOM (Price et al. 2018b, see more details in Appendix B). This code has been extensively used for the modeling of protoplanetary disks, with the intent of reproducing the observed structures in both the dust and gas emission (e.g., Dipierro et al. 2015b, Ragusa et al. 2017, Pinte et al. 2018, Price et al. 2018a, Cuello et al. 2019, Ubeira Gabellini et al. 2019, Toci et al. 2020a, Veronesi et al. 2020, Toci et al. 2020b). SPH formulation, and the PHANTOM implementation in particular, includes exact conservation of mass, momentum, and angular momentum, along with a self-consistent computation of the stellar and planet accretion rates and migrations (Price et al. 2018b). We used the one-fluid (Laibe & Price 2014; Ballabio et al. 2018) multigrain (Hutchison et al. 2018) algorithm, which discretizes the disk with a single set of SPH particles, each containing information of gas and dust with different grain sizes. This method is suitable for treating dust grains not fully decoupled from the gas. Such a condition is fulfilled if the midplane Stokes number $\mathrm{St} \propto \rho_0 a_\mathrm{d}/\Sigma_\mathrm{g} < 1$, where ρ_0 is the dust grain intrinsic density, a_d the grain size, and Σ_g the gas surface density.

Disk model

We selected the initial parameters for our simulations, listed in Table 5.1, based on the observations and estimates of Pinilla et al. (2018, 2021). The system consists of a central star surrounded by a disk composed of gas and dust, sampled by $N_\mathrm{SPH} = 10^6$ SPH particles. The disk has a gas mass of $M_\mathrm{gas} = 1.5 \times 10^{-3}\,\mathrm{M}_\odot$ and initially extends from $R_\mathrm{in} = 1$ au to $R_\mathrm{out} = 100$ au. Following a common practice (e.g., Toci et al. 2020a), we assumed a power law with an inner and an outer taper for the initial gas surface density profile,

$$\Sigma_\mathrm{g}(R) = \Sigma_\mathrm{c} \left(\frac{R}{R_\mathrm{in}}\right)^{-p} \exp\left[-\left(\frac{R}{R_\mathrm{c}}\right)^{2-p}\right] \left(1 - \sqrt{\frac{R_\mathrm{in}}{R}}\right), \tag{5.1}$$

where Σ_c is a normalization constant depending on the total disk mass, $R_\mathrm{c} = 80$ au is the characteristic radius of the outer exponential taper, and we set $p = 1.5$ (as assumed in Pinilla et al. 2018). Our model adopts a locally isothermal equation of state $P = \rho_\mathrm{g} c_\mathrm{s}^2$, with the following sound speed radial profile:

$$c_\mathrm{s}(R) = c_\mathrm{s,in} \left(\frac{R}{R_\mathrm{in}}\right)^{-q}, \tag{5.2}$$

where ρ_g is the gas volume density, $c_\mathrm{s,in}$ is the sound speed at the inner disk radius and $q = 0.3$ (derived from the spectral energy distribution; see Appendix 5.1.1). The gas in

Table 5.1: Initial parameters used for the simulations with PHANTOM.

Parameters	Value
$N_{\rm SPH}$	10^6
$M_\star [\mathrm{M}_\odot]$	0.2
$R_{\star\,\rm acc}$ [au]	1
$R_{\rm in}$ [au]	1
$R_{\rm out}$ [au]	100
$R_{\rm c}$ [au]	80
p	1.5
q	0.3
$H(R_{\rm in})/R_{\rm in}$	0.08
$\alpha_{\rm SS}$	5×10^{-3}
$\alpha_{\rm AV}$	0.36
$\langle h \rangle / H$	0.14
$M_{\rm gas}$ [$\mathrm{M}_\odot$]	1.5×10^{-3}
$M_{\rm dust}/M_{\rm gas}$	10^{-2}
$a_{\rm d}$ [cm]	$[a_{\rm min} = 1.6 \times 10^{-5}, a_{\rm max} = 0.1, N = 11]$
ξ	3.5
ρ_0 [g cm^{-3}]	2
$R_{\rm P\,acc}$ [au]	1/4 of Hill radius
$d_{\rm P,0}$ [au]	10.0
$M_{\rm P,0}$ [$\mathrm{M}_{\rm Jup}$]	$0.1, 0.5, 1.0, 1.5, 2.0$

Notes. Each entry is commented on in the main text.

the disk is in vertical hydrostatic equilibrium, which leads to the following aspect ratio:

$$\frac{H(R)}{R} = \frac{c_{\rm s}(R)}{v_{\rm K}(R)} = \frac{H(R_{\rm in})}{R_{\rm in}} \left(\frac{R}{R_{\rm in}}\right)^{1/2-q}, \tag{5.3}$$

where $v_{\rm K}$ is the Keplerian velocity and the aspect ratio at the inner radius is $H(R_{\rm in})/R_{\rm in} = 0.08$. With this choice of parameters, the mean value of the ratio between the azimuthally averaged SPH smoothing length $\langle h \rangle$ and the scale height H is $\langle h \rangle / H \approx 0.14$, implying that the disk is vertically resolved. We modeled the disk viscosity, which regulates the angular momentum transport, using the SPH artificial viscosity $\alpha_{\rm AV}$ introduced by Lodato & Price (2010). We set the Shakura & Sunyaev (1973) viscosity $\alpha_{\rm SS} = 5 \times 10^{-3}$, corresponding to $\alpha_{\rm AV} = 0.36$. This value directly affects the timescale regulating the disk viscous evolution (higher viscosity generally leading to faster evolution) and on the interaction between the disk and a planet, especially regarding the gas gap carved by a planet (see Sect. 5.3.5).

The dust component is initially distributed as the gas, following the same surface density profile (Eq. 5.1). The initial dust-to-gas mass ratio in the disk is 10^{-2} (the stan-

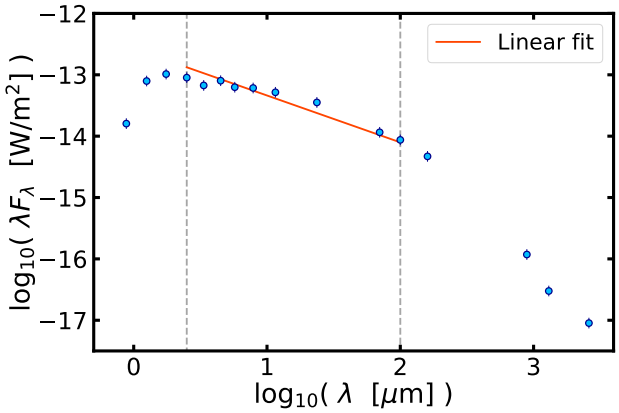

Figure 5.2: SED of CIDA 1. Data are from Hendler et al. (2017), and a typical uncertainty of 20% is assumed for each flux measurement. The orange line represents the linear fit performed on the data in the wavelength range $2.5-100\,\mu\mathrm{m}$, between the two vertical dashed gray lines.

dard value assumed for the interstellar medium, Bohlin et al. 1978), and it is constant throughout the disk. We simulated 11 different grain sizes, logarithmically spaced between $0.16\,\mu\mathrm{m}$ and $1\,\mathrm{mm}$. The grain size distribution follows the power law relation $\mathrm{d}N(a_\mathrm{d})/\mathrm{d}a_\mathrm{d} \propto a_\mathrm{d}^{-\xi}$, truncated at the minimum and maximum grain size, where a_d indicates the grain size and $N(a_\mathrm{d})$ is the number of dust grains per grain size. In our simulation, we assumed the typical value $\xi = 3.5$ for the distribution power law (Mathis et al. 1977). Simulating various grain sizes allows different levels of coupling between dust and gas to be tested. The intrinsic density of dust grains is $\rho_0 = 2\,\mathrm{g\,cm^{-3}}$.

Sound speed power law exponent from the SED

The profile of the sound speed in the SPH simulations follows a power law (Eq. 5.2). It is possible to derive the value of its exponent from the disk spectral energy distribution (SED), assuming that the disk emits as a multicolor blackbody (Beckwith et al. 1990). In the frequency range $k_\mathrm{B}T_\mathrm{out} \ll h\nu \ll k_\mathrm{B}T_\mathrm{in}$ (where k_B is the Boltzmann constant, T_in and T_out are the disk temperatures at the inner and outer radii of the disk, respectively), usually corresponding to a wavelength range roughly between $2\,\mu\mathrm{m}$ and $100\,\mu\mathrm{m}$, the slope of the SED is connected to the exponent q of the disk sound speed profile by this relation:

$$\frac{\mathrm{d}\log_{10}(\lambda F_\lambda)}{\mathrm{d}\log_{10}(\lambda)} = -4 + \frac{1}{q}. \tag{5.4}$$

The measured SED of CIDA 1 is reported in Hendler et al. (2017). We performed a linear fit of the value of $\log_{10}(\lambda F_\lambda)$ with respect to $\log_{10}(\lambda)$ in the wavelength range $2.5-100\,\mu\mathrm{m}$ (Fig. 5.2), obtaining a slope of ≈ -0.62. Using the (5.4), we derive that $q \approx 0.3$.

Properties of the central star and the embedded planet

The central star and the planet are modeled as sink particles, which are free to migrate and accrete gas and dust. The stellar mass of CIDA 1 is known to be in the range $\sim 0.1 - 0.2\,\mathrm{M}_\odot$ (Pinilla et al. 2021). Kurtovic et al. (2021) estimate a mass of $\sim 0.19\,\mathrm{M}_\odot$ using the Pascucci et al. (2016) method with the distance of $137.5\,\mathrm{pc}$ (Pinilla et al. 2021). In our simulations, we adopted a stellar mass $M_\star = 0.2\,\mathrm{M}_\odot$. The star accretion radius is $R_{\star\,\mathrm{acc}} = 1\,\mathrm{au}$ and defines a region where incoming SPH particles are considered accreted onto the star. The planet accretion radius is chosen to be $R_{\mathrm{P\,acc}} = 1/4\,R_\mathrm{H}$, where R_H is the planet Hill radius, defined as

$$R_\mathrm{H} = \left(\frac{1}{3}\frac{M_\mathrm{P}}{M_\star}\right)^{1/3} d_\mathrm{P}\,, \tag{5.5}$$

where d_P is the distance of the planet from the central star.

We performed a set of SPH simulations, each with an embedded planet starting at a distance $d_{\mathrm{P},0} = 10.0\,\mathrm{au}$ from the star. We varied the initial planet mass $M_{\mathrm{P},0}$: the chosen values are 0.1, 0.5, 1.0, 1.5, and $2.0\,\mathrm{M}_\mathrm{Jup}$. We let the simulations evolve until they reach a stable configuration. We analyzed the simulation results at $4 \times 10^4\,\mathrm{yrs}$, corresponding to about 560 planet orbits. To check that no major transients are neglected with this choice, we also computed the dust emission synthetic observations for a longer evolution time of $8 \times 10^4\,\mathrm{yrs}$, equivalent to about 1120 planet orbits.

For illustrative purposes, we show in Fig. 5.3 the face-on surface densities of the gas and the 11 dust populations from the simulation with initial planet mass $M_{\mathrm{P},0} = 1.5\,\mathrm{M}_\mathrm{Jup}$, evaluated after $4 \times 10^4\,\mathrm{yrs}$. Here, the dust radial drift and the dust trap induced by the planet (Pinilla et al. 2012b) can be appreciated. This is because the massive planet creates a pressure bump in the gas outside of its orbit, which attracts nearby dust and intercepts dust migrating from the outer regions toward the central star. The faster motion of larger grains (from ~ 0.1 to $1\,\mathrm{mm}$) results in ring-shaped dust distributions, whereas smaller grains present wider radial profiles of their density, because they have a slower radial drift being more coupled to the gas.

After this first suite of simulations, we aim at better constraining the minimum and maximum planet mass able to reproduce the observed dust emission by running additional simulations. In these cases, the embedded planet is placed at different initial radial distances from the star to find the best match with the peak intensity of the observed ring. The minimum mass of the planet is discussed in Sect. 5.3.5, where we present the results of two simulations: the first with $M_{\mathrm{P},0} = 0.5\,\mathrm{M}_\mathrm{Jup}$ and $d_{\mathrm{P},0} = 12.0\,\mathrm{au}$, the second with $M_{\mathrm{P},0} = 1.0\,\mathrm{M}_\mathrm{Jup}$ and $d_{\mathrm{P},0} = 11.0\,\mathrm{au}$. The maximum mass of the planet is assessed in Sect. 5.3.6, considering a simulation with $M_{\mathrm{P},0} = 4.0\,\mathrm{M}_\mathrm{Jup}$ and $d_{\mathrm{P},0} = 9.0\,\mathrm{au}$.

Limitations of the modeling

High-resolution ALMA images of the dust continuum emission from CIDA 1 (Fig. 5.1) show a dust ring peaking at $\sim 20\,\mathrm{au}$ from the star, a large gap, and an unresolved inner disk at the center, indicating the presence of dust within a few astronomical units of the

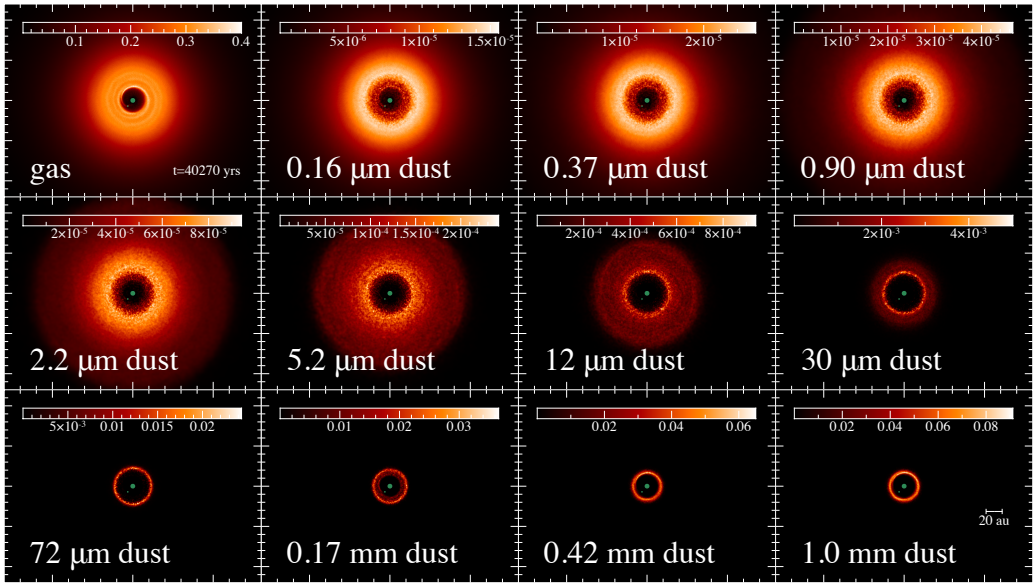

Figure 5.3: Face-on gas and dust surface density, in units of $\mathrm{g\,cm^{-2}}$, from the PHANTOM simulation with an initial planet mass of $1.5\,\mathrm{M_{Jup}}$ and a final planet mass of $2.0\,\mathrm{M_{Jup}}$ after $\approx 4 \times 10^4$ yrs ($\approx$560 planet orbits). Gas density is displayed in the top-left corner, and the remaining panels present the surface density for the 11 simulated dust grain sizes. The bigger central green dot represents the star, and the smaller green dot indicates the planet position. Images were produced using the tool SPLASH (Price 2007).

star. We focus on modeling the external dust ring, whereas reproducing the inner disk is beyond the aim of this work, given the setup we use for the SPH simulations.

In our models, we adopted $R_{\star\,\mathrm{acc}} = 1\,\mathrm{au}$; that is, we are not simulating the dynamics of the material within a radius of $1\,\mathrm{au}$ from the central star. Adopting a smaller R_{acc} rapidly causes a substantial increase in computational time due to a higher dynamic range. SPH particles closer to the central star move faster, so smaller time steps and a greater computational cost are needed to simulate their motion.

Furthermore, an intrinsic consequence of the artificial viscosity implementation in PHANTOM is that $\alpha_{\mathrm{SS}} \propto \langle h \rangle \propto \rho^{-1/3}$ (in 3D), meaning that the disk viscosity increases wherever the density decreases (Lodato & Price 2010). A local increase in viscosity leads to a shorter viscous timescale and, therefore, a faster transport of angular momentum in the disk. This description applies to our simulations: if the embedded planet is massive enough to carve a gap in the disk, in that region, the viscosity rises, and this eventually brings to a faster depletion of the inner material accreting onto the central star.

However, these numerical limitations only apply to the inner area, within the first few astronomical units. They do not affect the simulation in outer regions, where the observed dust ring is located and most of the dust flux and mass lie.

5.1.2 Radiative transfer

Linking PHANTOM to POLARIS

For the radiative transfer simulations, we employ the 3D Monte Carlo code POLARIS (Reissl et al. 2016), coupled for the first time with PHANTOM SPH simulations using the SF3DMODELS code as interface (Izquierdo et al. 2018). POLARIS is a flexible code that can handle multiple dust compositions, each of them defined by dust material, intrinsic grain density, and grain size distribution between a minimum and maximum grain size. Each dust population is associated with a spatial density distribution. From each SPH simulation, we acquired density distributions for 11 grain sizes, logarithmically spaced between $0.16\,\mu\mathrm{m}$ and $1\,\mathrm{mm}$. To have a more precise model, we obtained more dust density distributions from this initial data. Considering a single SPH particle, at first, we extrapolated densities for smaller grains. Under the assumption that small dust grains well-coupled to the gas maintain their initial size distribution (i.e., $\mathrm{d}N(a_\mathrm{d})/\mathrm{d}a_\mathrm{d} \propto a_\mathrm{d}^{-3.5}$, which can be rearranged as $\rho_\mathrm{d} \propto a_\mathrm{d}^{0.5}$, with ρ_d indicating the dust mass density), we fitted the values of $\log_{10}\rho_\mathrm{d}$ associated with the two smallest simulated grain sizes ($0.16\,\mu\mathrm{m}$ and $0.37\,\mu\mathrm{m}$) using a straight line with slope $\sim$0.5. With this relation, we sampled 10 density values logarithmically spaced between $5\,\mathrm{nm}$ and $0.37\,\mu\mathrm{m}$. For larger dust grains, we performed a cubic spline interpolation for $\log_{10}\rho_\mathrm{d}$ values related to the remaining simulated grain sizes. Thanks to this interpolation, we sampled 50 density values, logarithmically spaced between $0.37\,\mu\mathrm{m}$ and $1\,\mathrm{mm}$. This procedure is illustrated in Fig. 5.4. We repeated this operation for every SPH particle and obtained in total 60 dust density spatial distributions, 10 for grain sizes between $5\,\mathrm{nm}$ and $0.37\,\mu\mathrm{m}$ and 50 related to grain sizes between $0.37\,\mu\mathrm{m}$ and $1\,\mathrm{mm}$.

While in SPH the information is contained in point particles, POLARIS needs data to be sampled on a 3D grid for the radiative transfer simulations. To maintain the spatial distribution of physical properties as close as possible to the simulation output we used a Voronoi grid. Given a distribution of N points, a Voronoi grid is a partition of space into N convex polygonal cells, each containing exactly one generating point such that any portion of space inside a specific cell is closer to its generating point than to any other (Okabe et al. 2000). To avoid numerical artifacts where fewer SPH particles are present, as in the case of gaps and cavities in disks, we introduced a set of "dummy" grid points (as in Izquierdo et al. 2021a), which are artificially added particles to which we assigned a negligible density value ($10^{-42}\,\mathrm{g\,cm^{-3}}$). We randomly distributed $1/5\,N_\mathrm{SPH}$ dummy points; then, we accepted only those located in low-density areas, less sampled by SPH particles. After that, we used the SPH particles and the accepted dummy points as generating points for the Voronoi grid.

POLARIS simulations

With the 60 dust distributions sampled on a Voronoi grid obtained from the initial SPH models, we then performed the radiative transfer simulations with POLARIS. We considered the same dust composition adopted in Ricci et al. (2010). Here, dust grains are spheres composed of astronomical silicates (10% in volume, optical properties from

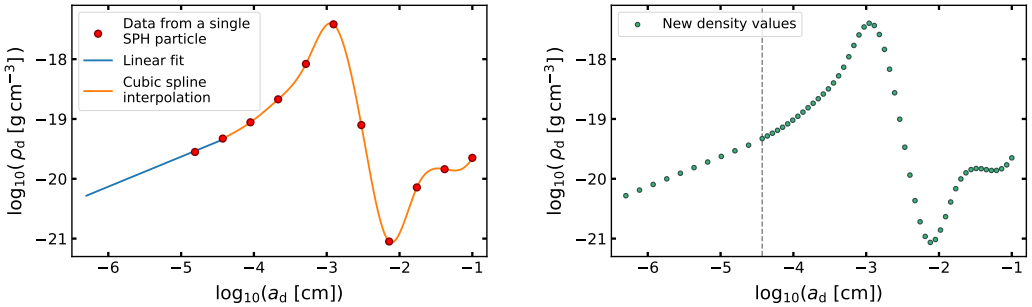

Figure 5.4: Refinement of the hydrodynamical model for the radiative transfer simulation via the extrapolation and interpolation of the dust densities for a single SPH particle. In the *left panel*, starting from dust density values obtained with SPH simulations (red dots), we perform a linear fit for $\log \rho_\mathrm{d}$ values associated with the two smallest simulated grain sizes to obtain densities for grains down to $5\,\mathrm{nm}$ (blue line). Then, we use a cubic spline interpolation on the remaining $\log \rho_\mathrm{d}$ values (orange line). In the *right panel*, with the linear fit, we obtain ten dust densities related to grain sizes between $5\,\mathrm{nm}$ and $0.37\,\mu\mathrm{m}$ (to the left of the vertical dashed gray line), while with the cubic spline interpolation we obtain 50 densities for grain sizes between $0.37\,\mu\mathrm{m}$ and $1\,\mathrm{mm}$ (to the right of the vertical dashed gray line).

Draine 2003), carbonaceous materials (20%, Zubko et al. 1996), water ice (30%, Warren & Brandt 2008), and a porosity of 40%.

First, with POLARIS, we computed the dust temperature using a Monte Carlo approach. From the estimates of Pinilla et al. (2021), CIDA 1 has a luminosity $L_\star = 0.15 \pm 0.03\,\mathrm{L}_\odot$. In our simulations, we modeled the radiation as 10^8 photon packages emitted by the central star, which is assumed as a black body with a surface temperature $T_\mathrm{eff} = 3050\,\mathrm{K}$ and a radius $R_\star = 1.3\,\mathrm{R}_\odot$, whose total luminosity equals the observed value. Second, the dust continuum emission and the gas line emission are computed via ray-tracing. We fixed the distance of CIDA 1 at $137.5\,\mathrm{pc}$. From the analysis of Pinilla et al. (2021), we used an inclination angle $i = 37.5°$ and a position angle $\mathrm{PA} = 11°$ for the disk.

The synthetic images are computed at the same wavelengths observed by ALMA. We simulated the dust continuum emission in Band 7 ($0.9\,\mathrm{mm}$) and Band 4 ($2.1\,\mathrm{mm}$). The gas line emission is calculated for ^{12}CO and ^{13}CO in the $J = 3{-}2$ transition. For the radiative transfer simulation of the gas emission, we assumed that the system is in local thermodynamic equilibrium and that the gas temperature is the same as that of the dust. Works by Bruderer et al. (2012), Bruderer (2013), and Facchini et al. (2018) show that gas and dust in protoplanetary disks in certain conditions may not be fully thermally coupled. However, given the uncertainty in this context, mainly due to a strong dependence on disk turbulence and dust grain size distribution, we made the assumption that gas and dust temperature are coupled and do not introduce further parameters in our simulations. The systemic velocity in our models is fixed at $6.25\,\mathrm{km\,s^{-1}}$, because this value led to the best match with the spatial distribution of the observed channel maps. We adopted a gas turbulent velocity of $100\,\mathrm{m\,s^{-1}}$. We included freeze-out and photo-dissociation for CO following the parameterizations in Williams & Best (2014).

The condition $T_{gas} < 20\,K$ defines the freeze-out region (Bergin et al. 2007). CO is assumed photo-dissociated by UV radiation from the central star and the interstellar radiation field where the gas column density (calculated in the vertical direction) is lower than a critical value $N_{dissoc} = 1.3 \times 10^{21}\,cm^{-2}$ (Visser et al. 2009). Therefore, in the warm molecular layer between the frozen-out midplane and the photo-dissociated regions at higher altitudes, we set the ^{12}CO abundance relative to H_2 $[^{12}CO/H_2] = 5 \times 10^{-5}$, and the isotopologue abundance ratio $[^{12}CO/^{13}CO] = 70$ (Wilson & Rood 1994); elsewhere, the CO abundance is zero.

To match the velocity resolution of the observed gas channel maps, namely $0.5\,km\,s^{-1}$ for ^{12}CO and $1.0\,km\,s^{-1}$ for ^{13}CO, we first computed the simulated channel maps at a higher velocity resolution of $0.045\,km\,s^{-1}$. Then, to obtain the final spectrally convoluted synthetic channels, we averaged 11 contiguous simulated ^{12}CO channels, centered at the same velocities of the observed channels. We repeated the same procedure for the computed ^{13}CO channels, averaging 22 channels to match the velocity resolution of the observations.

5.1.3 Synthetic observations

To obtain the final beam-convoluted synthetic images from our simulations, we treated the full-resolution dust continuum images and gas channel maps computed by POLARIS as the actual ALMA observations. Initially, we employed the task `sampleImage` from the package GALARIO (Tazzari et al. 2018) to compute the synthetic visibilities of the dust continuum images from our models at the same (u, v) points of the ALMA observations, in Band 7 and Band 4, respectively. After that, we calculated the residuals between the observations and the simulations. Finally, we performed the imaging and acquired the synthetic observations using the `tclean` algorithm from the software CASA, version 5.7 (McMullin et al. 2007). We applied the same parameters used to obtain the dust continuum Band 7 and Band 4 images in Pinilla et al. (2021): the Briggs weighting scheme and a robust parameter of 0.5. We performed the same method to obtain the ^{12}CO and ^{13}CO synthetic channel maps, working channel by channel. In the cleaning process, we used a Briggs robust parameter of 1 and applied a uv-tapering with a Gaussian of $0.035''$ to recover the same beam size of the observations.

We consider the total dust mass of our models as a free parameter that can be rescaled by a constant factor in the radiative transfer simulations to match the flux emitted in Band 7 ($0.9\,mm$) from the observed external dust ring. In our simulations, the dust-to-gas mass ratio always remains $\ll 1$. This condition allows this method to be applied without altering the disk dynamics since the dust back-reaction onto the gas remains insignificant. As explained in Sect. 5.1.1, in our modeling, we focus on reproducing the observed external dust ring. For this reason, we take as reference flux the one emitted only by the external ring in the ALMA Band 7 observation. In particular, we consider the area contained in the two green dashed ellipses depicted in the top panel of Fig. 5.5. The outer ellipse is positioned in the image center, has a semimajor axis of $0.27''$, a semiminor axis of $0.22''$, and an inclination of $11°$; for the inner ellipse, we only change the semiaxis length to $0.13''$ and $0.10''$. The flux contained in this elliptical annulus is $29.0\,mJy$. In

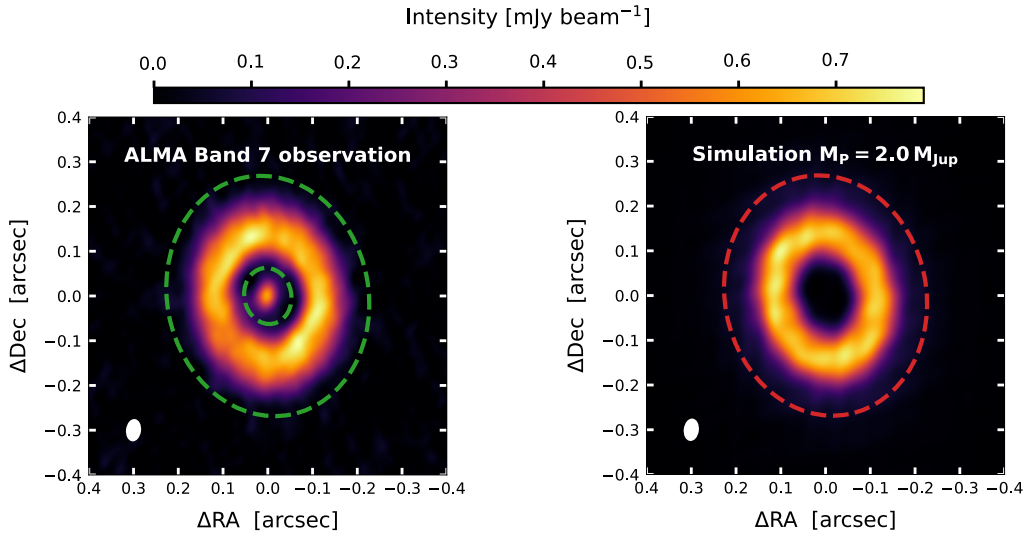

Figure 5.5: Visual representation of the areas considered for the flux calculation to rescale the total dust masses in our simulations. We take as a reference the flux from the ALMA observation in Band 7, which is contained in the region between the two dashed green ellipses in the *left panel*. Then, we rescale the total dust mass in our simulations so that, from the synthetic images in Band 7, the flux within the dashed red ellipse shown in the *right panel* matches the reference flux from the observation. In the *right panel*, we display, as an example, the image obtained from the simulation where the planet reaches a mass of $2.0\,\mathrm{M_{Jup}}$ after 4×10^4 yrs.

our synthetic images, without an inner disk, we consider the flux contained within the red dashed ellipse in the bottom panel of Fig. 5.5, which has the same parameters as the outer ellipse used for the observation image. We accept the total dust masses that lead to fluxes from our synthetic images from 28.5 to $29.5\,\mathrm{mJy}$.

5.2 Results

The resulting parameters of our models are listed in Table 5.2, for each simulation with different initial planet mass and for the two considered times $t_{\mathrm{Sim}} = 4 \times 10^4\,\mathrm{yrs}$ and $t_{\mathrm{Sim}} = 8 \times 10^4\,\mathrm{yrs}$. We note little difference in planet mass (M_{P}) and distance from the central star (d_{P}) in each simulation at the two times, meaning that $4 \times 10^4\,\mathrm{yrs}$ are sufficient for the planet to reach a slowly evolving configuration. In SPH simulations with PHANTOM, the planet accretion of gas and dust contained in the disk is self-consistently computed, and the planet migration is directly calculated from the disk gravitational torque, without the need for any prescriptions (Price et al. 2018b). In Fig. 5.6, we report how planet-star distance and planet mass change with time, in the case of the simulation with an initial planet mass of $1.5\,\mathrm{M_{Jup}}$. In both plots, a fast transient is evident in the first $10^4\,\mathrm{yrs}$, corresponding to the phase of gap opening. After that, the planet stabilizes in a slow type II migration with a smaller increase in mass. If the planet is massive enough, such a situation corresponds to the case in which the planet has already carved

Table 5.2: Resulting parameters for our simulations with different initial planet masses.

$M_{\mathrm{P},0}$ ($\mathrm{M_{Jup}}$)	t_{Sim} (yrs)	M_{P} ($\mathrm{M_{Jup}}$)	d_{P} (au)	M_{dust} ($\mathrm{M_\odot}$)	$M_{\mathrm{dust}}/M_{\mathrm{gas}}$
0.1	4×10^4	0.2	9.4	6.0×10^{-6}	6.3×10^{-3}
	8×10^4	0.2	9.2	4.3×10^{-6}	5.6×10^{-3}
0.5	4×10^4	0.9	9.3	4.8×10^{-6}	5.8×10^{-3}
	8×10^4	0.9	9.4	3.3×10^{-6}	5.1×10^{-3}
1.0	4×10^4	1.4	9.4	7.0×10^{-6}	8.7×10^{-3}
	8×10^4	1.5	9.4	4.0×10^{-6}	6.4×10^{-3}
1.5	4×10^4	2.0	9.4	7.0×10^{-6}	8.9×10^{-3}
	8×10^4	2.0	9.5	5.4×10^{-6}	8.8×10^{-3}
2.0	4×10^4	2.5	9.4	7.3×10^{-6}	9.4×10^{-3}
	8×10^4	2.6	9.6	6.4×10^{-6}	1.1×10^{-2}

Notes. Planet masses are evaluated at two different times during the simulation (t_{Sim}), namely 4×10^4 yrs and 8×10^4 yrs, corresponding to about 560 and 1120 orbits of the embedded planet. $M_{\mathrm{P},0}$ indicates the initial planet mass, while M_{P} and d_{P} are the planet mass and distance from the central star at the considered t_{Sim}. All planets started at $d_{\mathrm{P},0} = 10.0$ au.

an internal cavity both in the gas and in the dust, as in the case illustrated in Fig. 5.3. We can notice that at 4×10^4 yrs, the evolution time at which most of our analyses are performed, the simulation has overcome the initial transient and is in a slowly evolving phase. From the upper plot in Fig. 5.6, a spread in the planet-star distance is visible, indicating an elliptical orbit of the planet in our simulation. Knowing the periastron r_{p} and apoastron r_{a}, we can calculate the planet orbital eccentricity:

$$e = \frac{r_{\mathrm{a}} - r_{\mathrm{p}}}{r_{\mathrm{a}} + r_{\mathrm{p}}}\,, \tag{5.6}$$

obtaining a value $e \approx 0.01$ after 8×10^4 yrs.

5.2.1 Dust continuum emission

The first aim of our work is reproducing the dust thermal emission of the dust ring in CIDA 1 observed by ALMA in Band 7 (0.9 mm) and Band 4 (2.1 mm), and reported in Pinilla et al. (2021). We present in Fig. 5.7 the comparison at both wavelengths between the dust continuum image from the ALMA observation and the synthetic image from our simulation with a final planet mass of 2.0 $\mathrm{M_{Jup}}$ after 4×10^4 yrs, together with their residuals. In the case of this particular simulation, we note that our model is able to generally reproduce the morphology and the intensity of the observed emission from the ring. As expected, our synthetic images do not present the inner disk, which persists in the residuals. Moreover, we note that the residuals in both bands show some areas,

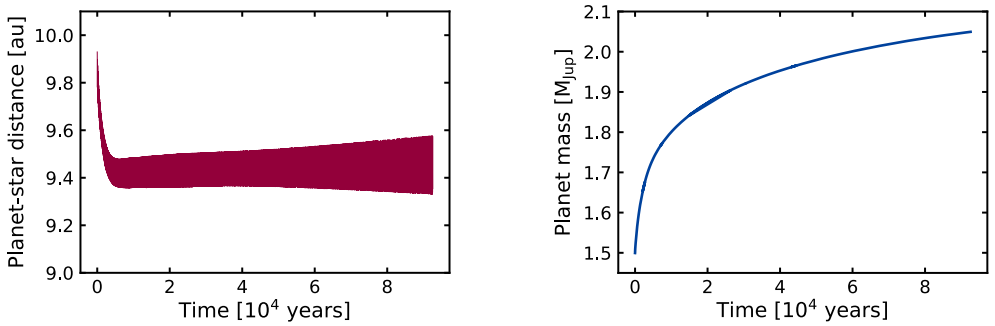

Figure 5.6: Time evolution of planet-star distance (*left panel*) and planet mass (*right panel*) from the simulation with an initial planet mass of $1.5\,\mathrm{M_{Jup}}$.

located in the region of the ring and the gap, above the 5σ value or below the -5σ value. Slight shifts in the simulated image centroids could not eliminate these differences. Such inequalities between our model and the observations might be caused by an imperfect estimate of the disk inclination and position angle that we assumed in the simulations or by some actual non-axisymmetric features in the observations.

A thorough comparison between the dust continuum emission from the observations and all our set of simulations after $4 \times 10^4\,\mathrm{yrs}$ is presented in Fig. 5.8. We show the azimuthally averaged radial profiles of the intensity in the two bands from the observations, all our simulations, and their residuals.

The smallest simulated planet, with a final mass of $0.2\,\mathrm{M_{Jup}}$, does not produce any major effect on the disk morphology. The $0.9\,\mathrm{M_{Jup}}$ planet is massive enough to carve a central cavity, but the intensity peak is significantly shifted inward compared to the peak in the observation profiles. The third model, with a planet mass of $1.4\,\mathrm{M_{Jup}}$, shows a good match with the observation, except for a slight offset in the location of the ring. The two remaining models, hosting the most massive planets with a mass of 2.0 and $2.5\,\mathrm{M_{Jup}}$, respectively, best reproduce the observed emission in both Band 7 and Band 4. Looking at Table 5.2 and considering the results after an evolution time of $4 \times 10^4\,\mathrm{yrs}$, we note that these last three cases also share consistent estimates of the total dust mass needed to match the observed flux, $\sim 7 \times 10^{-6}\,\mathrm{M_\odot}$, with a dust-to-gas mass ratio of $\sim 9 \times 10^{-3}$.

Results for the dust emission from the simulations after a longer evolution time of $8 \times 10^4\,\mathrm{yrs}$ are presented in Fig. 5.9. Compared to the results after $4 \times 10^4\,\mathrm{yrs}$ (Fig. 5.8), dust grains had more time to undergo radial drift and possibly accrete onto the star. We still note that a final planet mass of at least $2.0\,\mathrm{M_{Jup}}$ best reproduces the observations. The slight intensity excess just outside the dust ring has been removed by radial drift. The small mismatch in the peak flux for the simulation with $M_\mathrm{P} = 2.0\,\mathrm{M_{Jup}}$ and $M_\mathrm{P} = 2.6\,\mathrm{M_{Jup}}$ in Band 4 is due to the fact that, at this time, the bigger millimeter-sized grains with faster radial drift accreted more onto the central star, thus reducing the continuum emission at this longer wavelength. Nonetheless, the evident similarities between dust emission after 4×10^4 and $8 \times 10^4\,\mathrm{yrs}$ prove that, at these times, the disks in our simulations have already overcome the initial fast transient phase and are in a dynamically slowly evolving condition, in the absence of dust evolution.

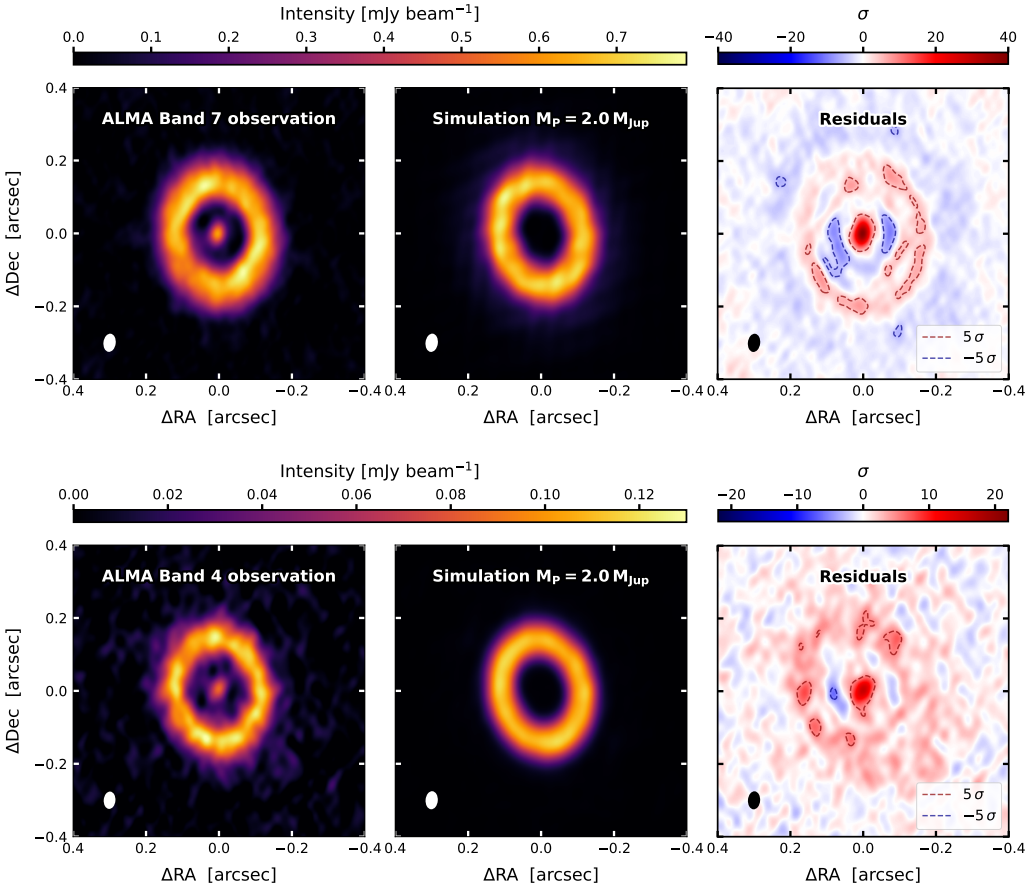

Figure 5.7: Band 7 ($0.9\,\mathrm{mm}$, *top panels*) and Band 4 ($2.1\,\mathrm{mm}$, *bottom panels*) comparison between dust continuum images from the ALMA observation and our synthetic observations obtained from the simulation with a final planet mass of $2.0\,\mathrm{M_{Jup}}$ after 4×10^4 yrs, along with their residuals. The synthesized beam ($0.050'' \times 0.034''$ for Band 7, $0.048'' \times 0.032''$ for Band 4, FWHMs) is shown in the bottom-left corner of each image. The contours in the residuals represent the 5σ and -5σ flux levels, respectively, for Band 7 and Band 4.

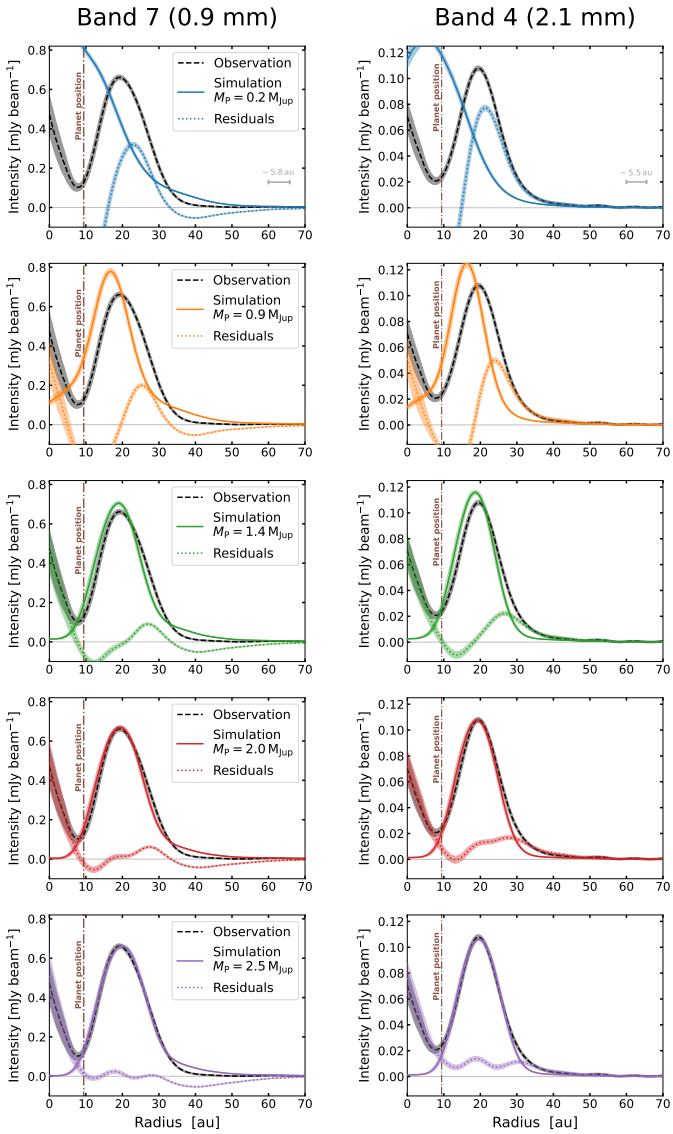

Figure 5.8: Comparison between radial profiles of azimuthally averaged intensities from the observations, simulations, and corresponding residuals, after the simulations have evolved for 4×10^4 yrs. *The left-hand panels* show results in Band 7, while the right-hand panels refer to Band 4. Each row contains the intensity profiles from the same simulation with a specific final planet mass, ranging from $0.2\,\mathrm{M_{Jup}}$ (*top row*) to $2.5\,\mathrm{M_{Jup}}$ (*bottom row*). The distance of the planet from the central star is indicated by the vertical dash-dotted brown line. The mean FWHMs of the synthesized beam in Band 7 and Band 4 are shown as horizontal bars in the *top row panels*. The radial intensity profiles are obtained by deprojecting the disk, using the disk inclination angle $i = 37.5°$, and dividing it into overlapping annuli, whose widths correspond to the averaged synthesized beam diameter. For each bin, uncertainties are calculated by taking the intensity standard deviation for each pixel in the annulus and dividing it by the square root of the number of synthesized beams contained in the area of the annulus.

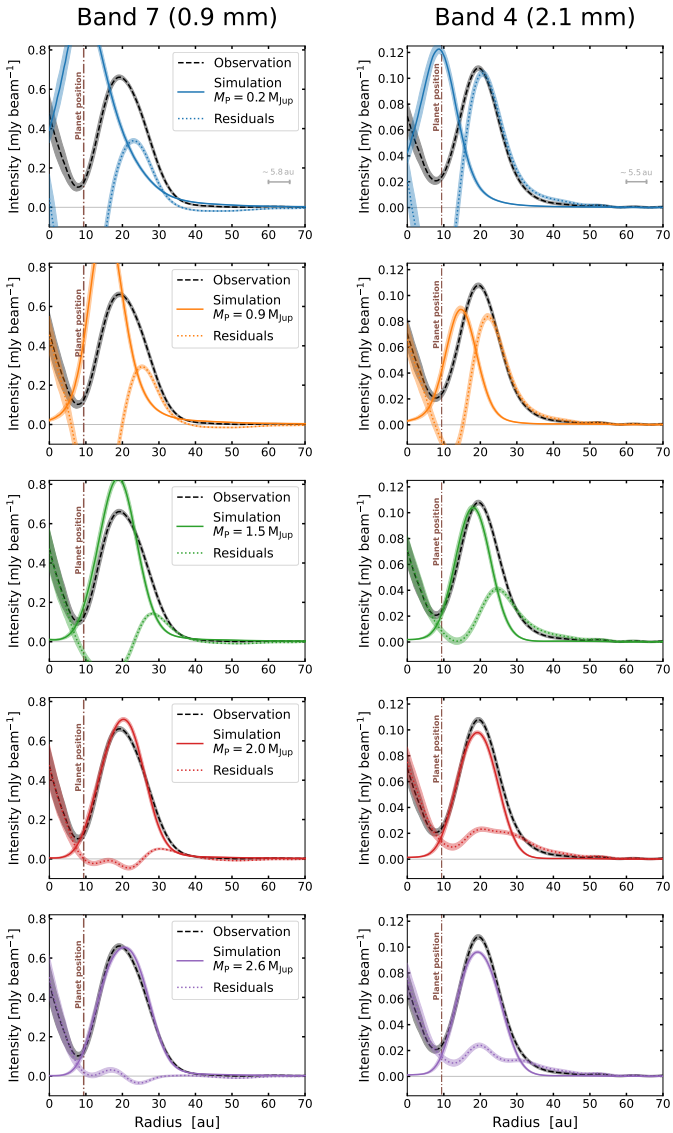

Figure 5.9: As in Fig. 5.8, but for the case of simulations evolved for 8×10^4 yrs.

5.2.2 Gas line emission

The dust continuum modeling shown in Fig. 5.8 proves that, while obtaining a good match in the case of a $1.4\,M_{Jup}$ planet, the minimum planet mass able to best replicate the observed dust emission is $2.0\,M_{Jup}$. Therefore, we decided to use the model with such a planet to compute the ^{12}CO ($J = 3{-}2$) and ^{13}CO ($J = 3{-}2$) channel maps.

In Fig. 5.10 we compare the ^{12}CO channel maps observed by ALMA to our synthetic gas emission images. In our model, we set a systemic velocity of $6.25\,km\,s^{-1}$. Strong cloud absorption is evident in the central channels of the observation, from $\sim$5.5 to $7.5\,km\,s^{-1}$. We analyze the cloud contamination effects in Sect. 5.3.3, using previous observations of the gas emission from the Taurus molecular cloud by Davis et al. (2010).

Our simulation reproduces appropriately the spatial extent of the channels centered at the velocities $v = 4.0,\ 4.5,\ 5.0,\ 8.0,\ 8.5,\ 9.0\,km\,s^{-1}$. This is more evident in Fig. 5.11, which shows for these channels the comparison between the observed and simulated ^{12}CO emission in terms of intensity contour levels at $5,\ 10,\ 15\,mJy\,beam^{-1}$ and intensity profiles along the PA $= 11°$. The channels $v = 4.5,\ 5.0,\ 8.0\,km\,s^{-1}$ are characterized by a significant difference in intensity values between the observation and the model. This effect can be explained by a still-present influence of the cloud on these channels, which are just outside the most absorbed velocities. Intensities are more similar in the channels $v = 4.0,\ 8.5,\ 9.0\,km\,s^{-1}$, where the cloud contamination in the observation is weaker, and the emission comes from regions of the disk well sampled by our simulation. The observed channel maps also show gas emission from the innermost regions, near the inner disk detected in the dust continuum. This material is also the cause of the central emission in high-velocity channels, such as those at $v = 3.5\,km\,s^{-1}$ and $v = 9.5{-}10.0\,km\,s^{-1}$. As explained in Sect. 5.1.1, our model does not aim at describing this inner region.

We follow the same procedure for the analysis of the ^{13}CO emission. Figure 5.12 presents the comparison between the ^{13}CO channel maps observed by ALMA and the synthetic ones computed from our simulation. Here, we have a lower velocity resolution of $1.0\,km\,s^{-1}$. In the observations, we note that the $6.5\,km\,s^{-1}$ channel is completely affected by cloud absorption, which also impacts the channel at $v = 5.5\,km\,s^{-1}$. In Fig. 5.13, we compare the contour levels at $3,\ 6,\ 9\,mJy\,beam^{-1}$ and the intensity profiles at PA $= 11°$ from the observed and simulated ^{13}CO emission. Even in this case, our models are able to reproduce the spatial distribution of the observed emission while presenting higher intensity values, except for the $8.5\,km\,s^{-1}$ channel. In particular, we note a strong cloud absorption for the observed intensity profile of the $5.5\,km\,s^{-1}$ channel, but the corresponding contour plot shows a good agreement in the extent of the emission between observation and simulation. As for the ^{12}CO, there is some observed inner emission for the high-velocity channels at 3.5 and $9.5\,km\,s^{-1}$, which cannot be reproduced by our model due to its empty inner cavity.

From all of these results, we realize that our single model with a final planet mass of $2.0\,M_{Jup}$ is able to globally reproduce both the dust and gas emission observed in CIDA 1. In particular, this case perfectly recovers the external dust ring as observed both in Band 7 and Band 4, along with replicating the spatial distribution of the gas emission as traced by ^{12}CO ($J = 3{-}2$) and ^{13}CO ($J = 3{-}2$).

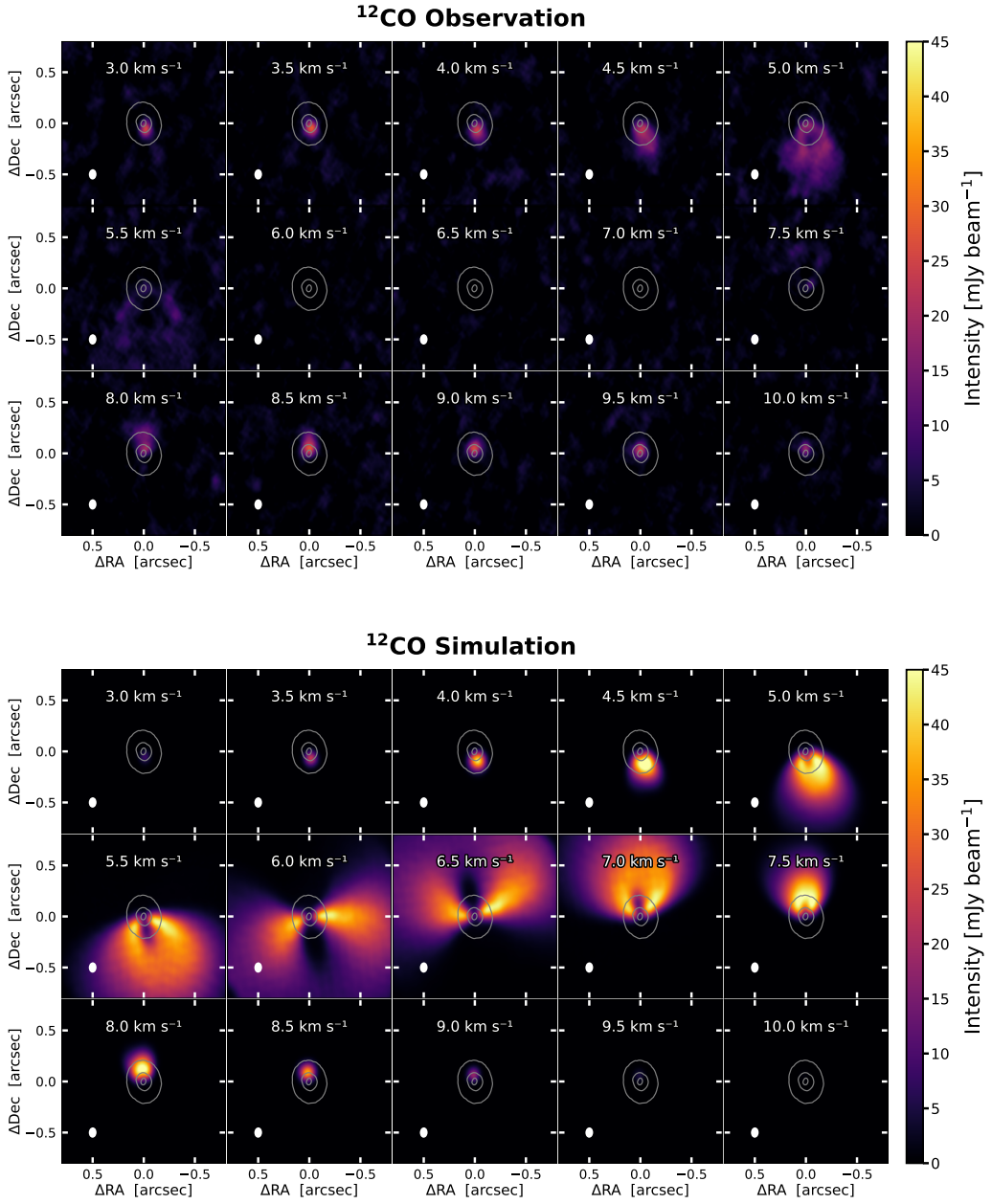

Figure 5.10: Comparison between the ALMA observation (*top panels*) and the synthetic images (*bottom panels*) of CIDA 1 ^{12}CO ($J = 3{-}2$) channel maps. Color scales are the same in the *top and bottom panels*. Synthetic images are obtained from the simulation with a final planet mass of $2.0\ \mathrm{M_{Jup}}$ after an evolution time of 4×10^4 yrs. We fixed the systemic velocity at $6.25\,\mathrm{km\,s^{-1}}$. The contour level traces the 15σ emission from the Band 7 continuum image. The velocity resolution is $0.5\,\mathrm{km\,s^{-1}}$, and the central velocities of each channel are indicated on the top of each panel. The synthesized beam ($0.101'' \times 0.075''$, FWHM) is shown in the lower-left corner of each panel.

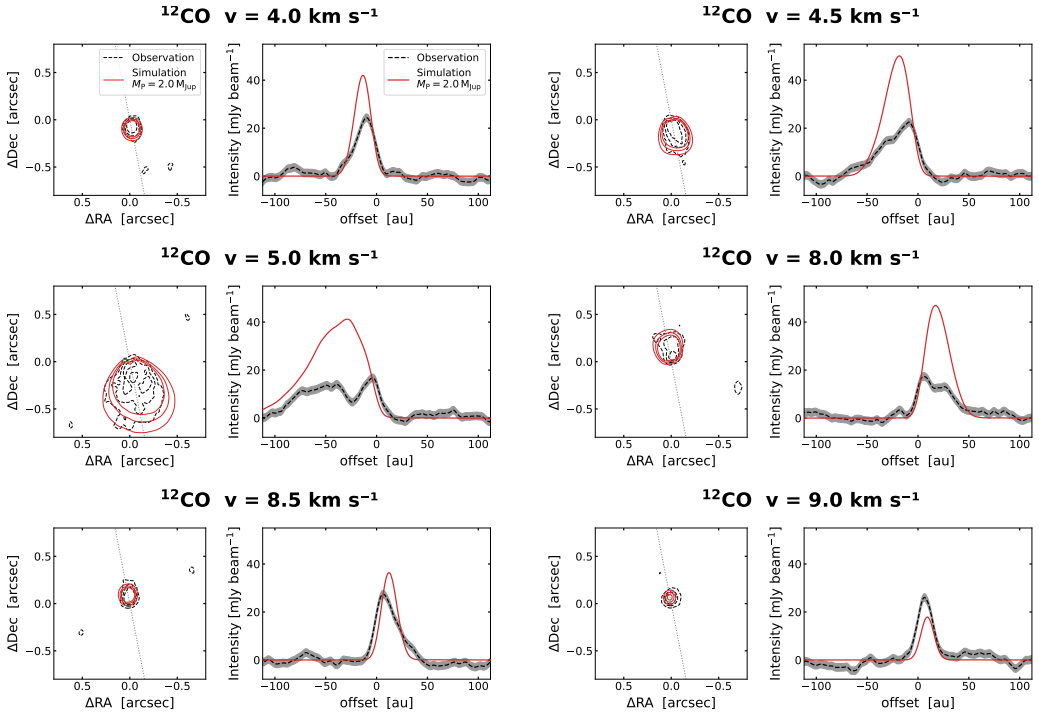

Figure 5.11: Contour levels (*left panel* in each subplot) at $5,\ 10,\ 15\,\mathrm{mJy\,beam^{-1}}$, and intensity profile comparisons (*right panel* in each subplot) between the ^{12}CO observation and simulation with a $2.0\ \mathrm{M_{Jup}}$ planet mass after 4×10^4 yrs, in the six channels not completely obscured by the cloud ($v = 4.0,\ 4.5,\ 5.0,\ 8.0,\ 8.5,\ 9.0\,\mathrm{km\,s^{-1}}$). Intensity profiles are taken along the $\mathrm{PA} = 11^\circ$ of the disk, and the direction is indicated by the dotted gray line in the contour levels plots. The uncertainty in the observation intensity profile is the 1σ noise level ($1.6\,\mathrm{mJy\,beam^{-1}}$).

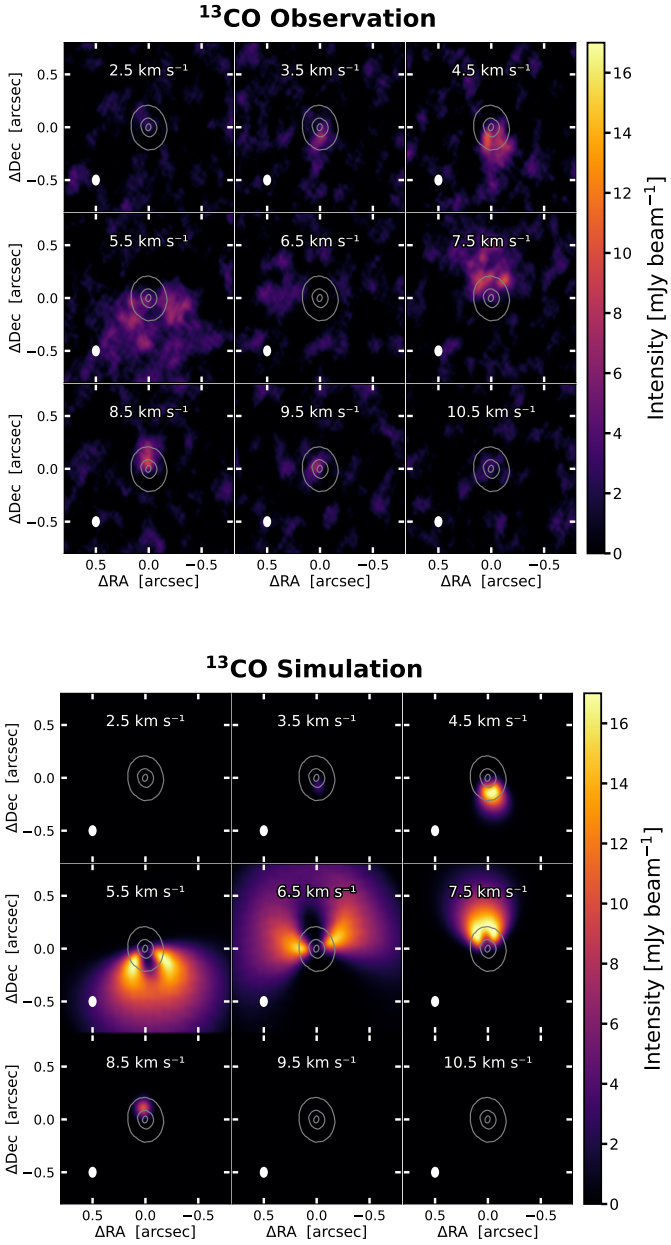

Figure 5.12: Comparison between the ALMA observation (*top panels*) and the synthetic images (*bottom panels*) of CIDA 1 ^{13}CO ($J = 3{-}2$) channel maps. Color scales are the same in the *top and bottom panels*. Synthetic images are obtained from the simulation with a final planet mass of 2.0 $M_{\rm Jup}$ after an evolution time of 4×10^4 yrs. We fixed the systemic velocity at $6.25\,{\rm km\,s^{-1}}$. The contour level traces the 15σ emission from the Band 7 continuum image. The velocity resolution is $1\,{\rm km\,s^{-1}}$, and the central velocities of each channel are indicated on the top of each panel. The synthesized beam ($0.104'' \times 0.076''$, FWHM) is shown in the lower-left corner of each panel.

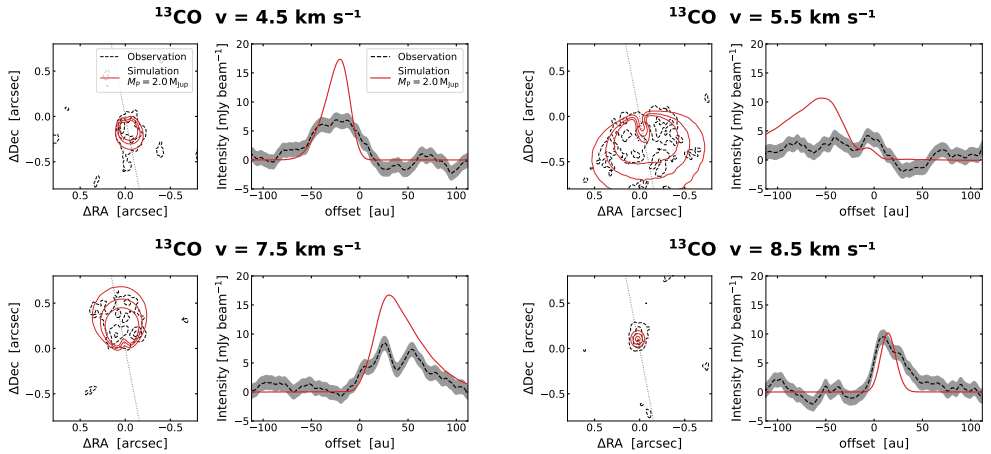

Figure 5.13: Contour levels (*left panel* in each subplot) at 3, 6, 9 mJy beam^{-1}, and intensity profile comparisons (*right panel* in each subplot) between the ^{13}CO observation and simulation with a 2.0 M_{Jup} planet mass after 4×10^4 yrs, in the four channels not completely obscured by the cloud ($v = 4.5, 5.5, 7.5, 8.5$ km s^{-1}). Intensity profiles are taken along the PA $= 11°$ of the disk, and the direction is indicated by the dotted gray line in the contour levels plots. The uncertainty in the observation intensity profile is the 1σ noise level (1.2 mJy beam^{-1}).

5.3 Discussion

5.3.1 Stellar mass and systemic velocity

Our models allow fundamental information regarding the CIDA 1 system to be recovered. In the observations, the ^{12}CO and ^{13}CO channel maps are strongly affected by cloud absorption in the channels near the systemic velocity (Sect. 5.2.2 and Sect. 5.3.3). Hence, we compare our synthetic images to the observations only in those channels probing higher velocities in the disk (Fig. 5.11 and 5.13). Models are consistent with observations, being able to reproduce the spatial distribution of the emission. The stellar mass $M_\star = 0.2\,M_\odot$ and systemic velocity $v_{sys} = 6.25$ km s^{-1} assumed in our simulations are therefore reasonable estimates of these properties in CIDA 1. This stellar mass is compatible with the known range $\sim 0.1 - 0.2\,M_\odot$ (Pinilla et al. 2021) and is in very good agreement with the estimate of $0.19\,M_\odot$ by Kurtovic et al. (2021). We also simulated the case with $M_\star = 0.1\,M_\odot$, but the morphology of the resulting gas channel maps differed significantly from the observed ones; therefore, we decided not to include these models in the simulation sample.

5.3.2 Spectral index and optical depth

Having dust emission data at two different wavelengths allows us to compare the observed and simulated spectral index. Given the fluxes and frequencies corresponding to Band 7 and Band 4, respectively F_{B7}, ν_{B7}, and F_{B4}, ν_{B4}, the spectral index $\alpha_{B7,\,B4}$ is

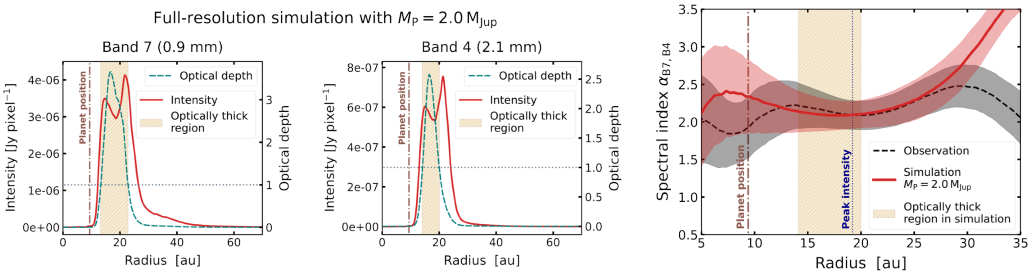

Figure 5.14: Optical depth in our models and comparison between observed and simulated spectral indices. *Left and central panels*: Azimuthally averaged radial profiles of the optical depth along the line of sight and the intensities from the full-resolution dust emission image of the simulation (i.e., not convoluted with the synthesized beam) with a final planet mass of 2.0 M_{Jup} after 4×10^4 yrs, in Band 7 and Band 4. The vertical dash-dotted brown line indicates the location of the planet, and the horizontal dotted gray line marks the optical depth $\tau = 1$ level. The region where the emission is optically thick (optical depth $\tau \geq 1$) is shown in beige. *Right panel*: Azimuthally averaged radial profiles of the spectral index from the ALMA observation and our simulation with a final planet mass of 2.0 M_{Jup} after 4×10^4 yrs. Values are obtained using Eq. 5.7 and the synthetic image intensity profiles in Fig. 5.8. Uncertainties include the original error in the intensity profiles and a 10% flux error due to calibration. As a reference, the distance of the planet from the central star is indicated by the vertical dash-dotted brown line, and the position of the peak intensity is displayed by the vertical dotted blue line. The beige-shaded area marks the radii where the full-resolution simulated emission is optically thick ($\tau \geq 1$) in both Band 7 and Band 4.

Table 5.3: Fluxes in Band 7 and Band 4 and the resulting spatially integrated spectral index for the ALMA observation (accounting only for flux from the external dust ring) and our model from the simulation with a final planet mass of 2.0 M_{Jup} after 4×10^4 yrs.

	Observation (external ring)	Simulation $M_P = 2.0\,M_{Jup}$
F_{B7} [mJy]	29.0 ± 2.9	28.6 ± 2.9
F_{B4} [mJy]	4.7 ± 0.5	4.0 ± 0.4
Spectral index $\alpha_{B7,\,B4}$	2.08 ± 0.16	2.26 ± 0.16

Notes. The areas considered when calculating the spectral index are the same used for the dust mass rescaling process (Sect. 5.1.3). The uncertainties for the observations are obtained as the root sum square of the observed noise (σ) and a 10% flux error due to calibration. The uncertainties for our simulation only include the 10% flux error.

calculated as

$$\alpha_{\mathrm{B7,\,B4}} = \frac{\log_{10}\left[F_{\mathrm{B7}}/F_{\mathrm{B4}}\right]}{\log_{10}\left[\nu_{\mathrm{B7}}/\nu_{\mathrm{B4}}\right]}\,. \tag{5.7}$$

Assuming that opacity follows a power-law $\kappa_\nu \propto \nu^\beta$, the emission is optically thin and within the Rayleigh-Jeans regime, then the spectral index can be approximated as $\alpha_{\mathrm{B7,\,B4}} \approx 2 + \beta$ (Testi et al. 2014). The value of β depends on the maximum dust grain size, while not being influenced by the minimum grain size. A low β (i.e., $\beta < 1$, meaning that $\alpha_{\mathrm{B7,\,B4}} < 3$) could be indicative of the presence of grains with size $\gtrsim 0.1\,\mathrm{mm}$, suggesting that grain growth in the disk may have occurred (Draine 2006). Protoplanetary disks around VLM stars or brown dwarfs with low spectral indices have been observed (e.g., Ricci et al. 2014; Pinilla et al. 2017).

The left and central panels of Fig. 5.14 present the azimuthally averaged radial profiles of the intensity from our simulations with final planet mass of $2.0\ \mathrm{M_{Jup}}$ in Band 7 and Band 4, along with the corresponding profiles of the optical depth along the line of sight. All profiles were produced directly from the full-resolution images computed by POLARIS, without any convolution with a synthesized beam. Here, we note that the emission at both wavelengths is partially optically thick, that is, the optical depth τ is above 1. We calculate that $\approx$51% of the emission in Band 7 is optically thick, whereas this fraction decreases to $\approx$38% in Band 4. These results are consistent with the findings in Tazzari et al. (2021), showing similar optically thick fractions in a sample of disks located in the Lupus star-forming region. Such a mixture of optically thin and thick emission in our model leads us to interpret with caution the spectral index in CIDA 1. Moreover, the dust temperature predicted in our simulation ($\sim$20 K in the disk midplane, where most of the settled dust is located) lies at the limit of the Rayleigh-Jeans domain. In this spectral region, and for a temperature of 20 K, dropping the Rayleigh-Jeans approximation but retaining the optically thin one, we calculate that the spectral index is $\alpha_{\mathrm{B7,\,B4}} \approx 1.7 + \beta$.

Pinilla et al. (2021) find that the spatially integrated spectral index of CIDA 1 is 2.0 ± 0.2 (the uncertainty includes the observed root mean square of the noise and a 10% flux error from calibration). Table 5.3 compares the flux in Band 7, Band 4, and the spatially integrated spectral index between the observation (considering only flux coming from the external dust ring) and our simulation with a final planet mass of $2.0\,\mathrm{M_{Jup}}$ after 4×10^4 yrs. We note that the spatially integrated spectral index of our model is consistent with the observed value within the uncertainties.

A more detailed comparison is presented in the right panel of Fig. 5.14, which shows the azimuthally averaged radial profiles of the spectral index from the observation and, again, from the simulation with a final planet mass of $2.0\,\mathrm{M_{Jup}}$ after 4×10^4 yrs. Our model best reproduces the observed spectral index profile between $\sim$10 au and $\sim$30 au, where the dust ring is detected. Since we focus on reproducing the external dust ring, we do not display the spectral index profiles within a distance of 5 au from the central star. Then, we note that the spectral indices start diverging beyond $\sim$30 au. This effect is due to a slight intensity excess in the model in Band 7 that does not perfectly match the observed Band 7 profile at these radii (see Fig. 5.8). Between $\sim$14 au and $\sim$20 au the dust emission is optically thick in both Band 7 and Band 4, meaning that the low

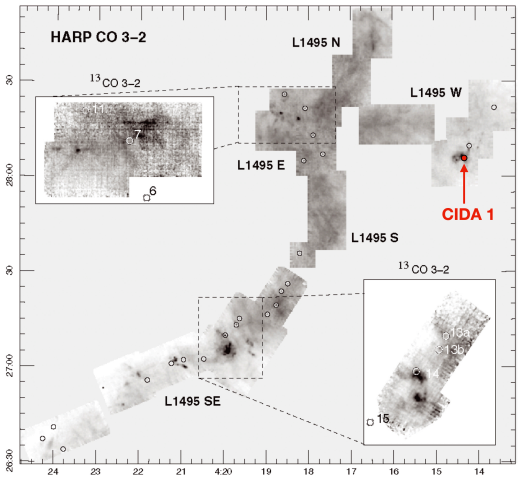

Figure 5.15: Map of the Taurus molecular cloud obtained by the James Clerk Maxwell Telescope using the ^{12}CO ($J = 3{-}2$) emission (integrated between 2.0 and $11.0\,\mathrm{km\,s^{-1}}$). Areas also mapped with ^{13}CO ($J = 3{-}2$) emission (integrated between 4.9 and $9.1\,\mathrm{km\,s^{-1}}$) are indicated by rectangular boxes. We calculated the optical depth property in the subregion L1495 E, whereas CIDA 1 is located in the region L1495 W. The image is adapted from right-hand panel of Fig. 1 in Davis et al. (2010).

spectral index in this region cannot be linked to the presence of millimeter-sized grains. However, this is not the case for the region between $\sim$20 au and $\sim$30 au, still showing a spectral index around $\sim 2{-}2.5$ associated with optically thin emission. Such behavior is expected in our simulation, where we know that millimeter-sized grains are present at the dust ring location, but this strong match between our model and the observation can indicate that grain growth and migration have occurred in CIDA 1.

5.3.3 Cloud absorption

We aim here to qualitatively estimate the cloud absorption affecting the observed gas channel maps. Davis et al. (2010) mapped the ^{12}CO emission at the transition $J = 3{-}2$ in the region of the Taurus molecular cloud, using the Heterodyne Array Receiver Programme (HARP) on the James Clerk Maxwell Telescope. Figure 5.15 shows the ^{12}CO map of Taurus that they obtained. The authors divided the region into five different subregions, and in a couple of them, namely L1595 E and L1495 SE, they also collected the ^{13}CO $J = 3{-}2$ emission. CIDA 1 is located in the subregion L1495 W. Since in this area the ^{13}CO data are missing, we consider the nearby subregion L1595 E for our estimates.

Figure 5.16 reports the ^{12}CO and ^{13}CO spectra of the antenna temperature (T_A^*). As stated in Davis et al. (2010), assuming the abundance ratio $[^{12}\mathrm{CO}/^{13}\mathrm{CO}] = 70$, the ^{12}CO optical depth τ_{12} can be calculated as:

$$\frac{\int T_\mathrm{A}^*(^{12}\mathrm{CO})\,\mathrm{d}v}{\int T_\mathrm{A}^*(^{13}\mathrm{CO})\,\mathrm{d}v} = \frac{1-\mathrm{e}^{-\tau_{12}}}{1-\mathrm{e}^{-\tau_{13}}}\,, \tag{5.8}$$

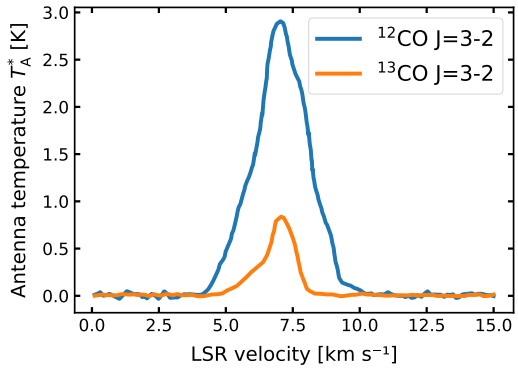

Figure 5.16: ^{12}CO ($J = 3{-}2$) and ^{13}CO ($J = 3{-}2$) spectra with respect to the local standard of rest (LSR) in the Taurus subregion L1495 E. The spectra are averaged over the entire extent of the subregion. Data are from Davis et al. (2010).

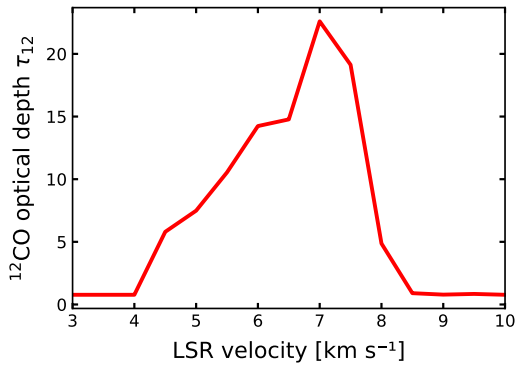

Figure 5.17: ^{12}CO ($J = 3{-}2$) optical depth in the Taurus subregion L1495 E, calculated from the spectra in Fig 5.16 using Eq. 5.8. We focus only on the velocity interval where line emission is detected. Bins replicate the central velocity and resolution of the observed ^{12}CO channel maps.

where $\tau_{13} = \tau_{12}/70$ is the ^{13}CO optical depth. We integrate the antenna temperatures along velocity intervals with the same centers and width of the observed ^{12}CO channel maps (top panels in Fig. 5.10). The resulting ^{12}CO optical depth is presented in Fig. 5.17. The morphology of the optical depth spectrum follows approximately the cloud absorption behavior on the ^{12}CO observation, being strongest at $\sim 6.0{-}7.0\,\mathrm{km\,s^{-1}}$ while fading at $\sim 4.0\,\mathrm{km\,s^{-1}}$ and $\sim 8.5\,\mathrm{km\,s^{-1}}$, where there is a better match between the intensity profiles from our model and the ones from the observation (Fig. 5.11). Nonetheless, it must be stressed that our estimates on the ^{12}CO spectrum are based on data from a region nearby the one hosting CIDA 1 and, furthermore, these data refer to the total emission of the cloud along the line of sight, while the position of CIDA 1 in this direction, and so the gas column density between us and the source, is unknown.

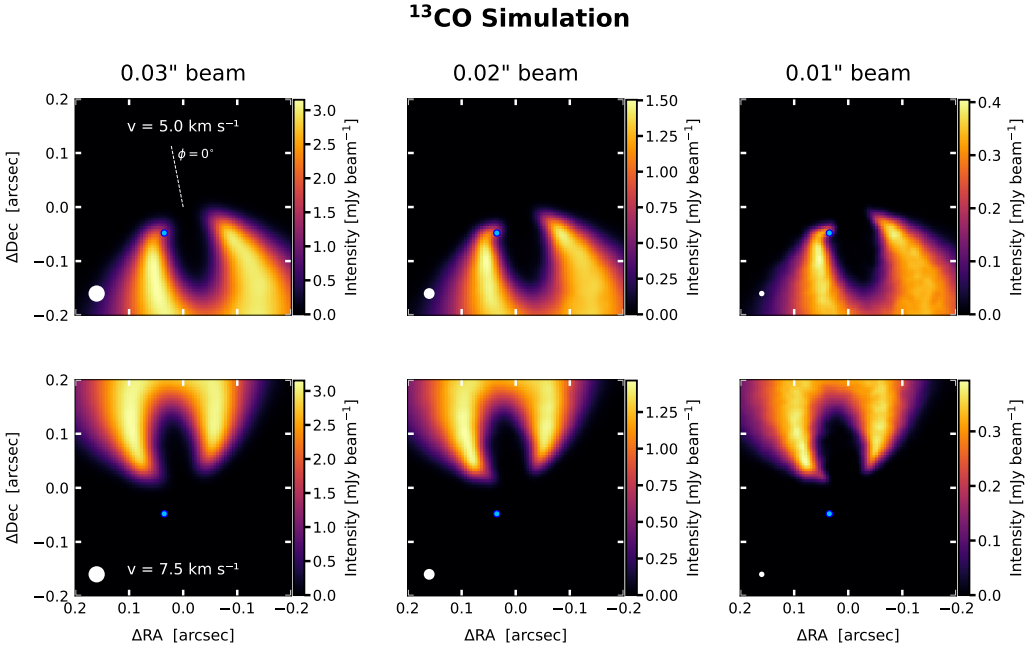

Figure 5.18: Synthetic images of the ^{13}CO ($J = 3{-}2$) emission from our simulation with $M_{\rm P} = 2.0\,{\rm M_{Jup}}$ after an evolution time of 4×10^4 yrs. We compute the images at two different channels: $v = 5.0\,{\rm km\,s^{-1}}$ (*top panels*) and $v = 7.5\,{\rm km\,s^{-1}}$ (*bottom panels*), with a velocity resolution of $0.5\,{\rm km\,s^{-1}}$. We use three different circular beam sizes: $0.03''$, $0.02''$, and $0.01''$ (FWHMs, *from left to right*), indicated by the white circles in the lower-left corner of each plot. The blue dot represents the planet position at the azimuthal angle $\phi = 145°$ (relative to the angle $\phi = 0°$, which is located at the disk major axis indicated by the dashed white line in the *top-left panel*).

5.3.4 Planet-induced perturbations in synthetic gas channel maps

The presence of substructures, such as rings, gaps, and cavities, in the dust continuum images of protoplanetary disks can be interpreted as the result of tidal interactions between the disk and a planet. A more direct way to reveal the effects of planet-disk interactions is to look for localized velocity perturbations in the gas channel maps, namely "kinks" (Pinte et al. 2018, 2019b, 2020; Izquierdo et al. 2021b; Bollati et al. 2021).

In the channel maps of CIDA 1 observed by ALMA in ^{12}CO ($J = 3{-}2$) and ^{13}CO ($J = 3{-}2$) (top panels in Fig. 5.11 and Fig. 5.13, respectively), there is no clear sign of a deviation from the Keplerian rotation. Here, we investigate whether, with sufficient sensitivity and both spectral and spatial resolution, a perturbation could be detected in one of the channels that are not affected by cloud absorption.

We consider our simulation with a final planet mass of $2.0\,{\rm M_{Jup}}$ after $4 \times 10^4\,{\rm yrs}$. We explore different velocity resolutions and beam sizes. The synthetic observations are computed by convolving the full-resolution images obtained from the radiative transfer simulations with a circular Gaussian beam. In the ^{12}CO emission, there is no evidence of kinks in any channels. On the other hand, a local perturbation nearby the planet

is visible in the ^{13}CO emission. Figure 5.18 compares the simulated ^{13}CO emission at three different angular resolutions: $0.03''$, $0.02''$, and $0.01''$. We show the channels at $v = 5.0\,\mathrm{km\,s^{-1}}$ and $v = 7.5\,\mathrm{km\,s^{-1}}$. These velocities, equidistant from the systemic velocity, are just outside the window where the cloud totally absorbs ^{13}CO emission. We only show the results with a channel width of $0.5\,\mathrm{km\,s^{-1}}$ since a higher velocity resolution does not lead to any major change. The planet is located at the azimuthal angle $\phi = 145°$ with respect to the disk major axis (see Fig. 5.18). We note that a velocity perturbation near the planet is visible at a resolution of $0.02''$ in the $5.0\,\mathrm{km\,s^{-1}}$ channel, becoming more evident at $0.01''$. Instead, no kink is detected in the $7.5\,\mathrm{km\,s^{-1}}$ channel. Therefore, this analysis proves that a planet-induced kink would be visible only in ^{13}CO emission and at a very high resolution of at least $0.02''$, assuming that the planet is located in a favorable position that allows the perturbation to be detected in a channel not obscured by the cloud. The sensitivity needed to clearly detect ^{13}CO emission at such a high angular resolution leads to an inaccessible observing time (about several tens of days) with current ALMA capabilities.

We identify two main reasons why the planet-induced perturbation is only detected in ^{13}CO and not in ^{12}CO in our simulations. First, the emission of ^{12}CO comes from regions at high altitudes, whose dynamics could be less affected by the planet orbiting on the midplane (Rabago & Zhu 2021), whereas ^{13}CO is emitted closer to the midplane. Second, the spatial resolution of our models naturally becomes coarser at higher altitudes, where ^{12}CO is emitted, thus making it more challenging to detect localized perturbations induced by a planet. So far, published detections of planet-induced kinematical kinks in real ALMA observations of disks have involved only ^{12}CO (Pinte et al. 2018, 2019b, 2020). The explanation is that ^{12}CO has a bright line emission, allowing for very high signal-to-noise ratios even at high spectral and spatial resolution. Kinks in ^{13}CO have a larger kinematical signal, but are more difficult to detect because of its fainter line brightness.

5.3.5 Minimum planet mass

The comparison in Fig. 5.8 shows that final planet masses of $0.9\ \mathrm{M_{Jup}}$ and $1.4\ \mathrm{M_{Jup}}$ are able to open a gap in the dust, though producing a ring that is shifted with respect to the observed one. While all planets considered in Fig. 5.8 have an equal initial distance $d_{\mathrm{P},0}$ from the central star of $10.0\,\mathrm{au}$, now, we aim to better constrain the minimum planet mass able to explain the observed dust ring by modifying the parameter $d_{\mathrm{P},0}$. Using the same initial planet masses that eventually resulted in $0.9\ \mathrm{M_{Jup}}$ and $1.4\ \mathrm{M_{Jup}}$, that is, $M_{\mathrm{P},0} = 0.5$ and $1.0\ \mathrm{M_{Jup}}$, respectively, we explore different values of $d_{\mathrm{P},0}$. The best cases are presented in Fig. 5.19, after an evolution time of 4×10^4 yrs.

The planet with $M_{\mathrm{P}} = 0.9\,\mathrm{M_{Jup}}$ and $d_{\mathrm{P}} = 11.0\,\mathrm{au}$ is not able to reproduce the observed profiles. As explained in Sect. 5.1.1, our numerical resolution prevents us from trusting the dust morphology inside the first few astronomical units of the disk. In this case, therefore, we do not deem the apparent presence of an inner ring within 4 au significant (which might be reminiscent of the observed inner disk in CIDA 1), but we clearly see an excess emission between $\sim$4 and $\sim$10 au (a region properly mapped by

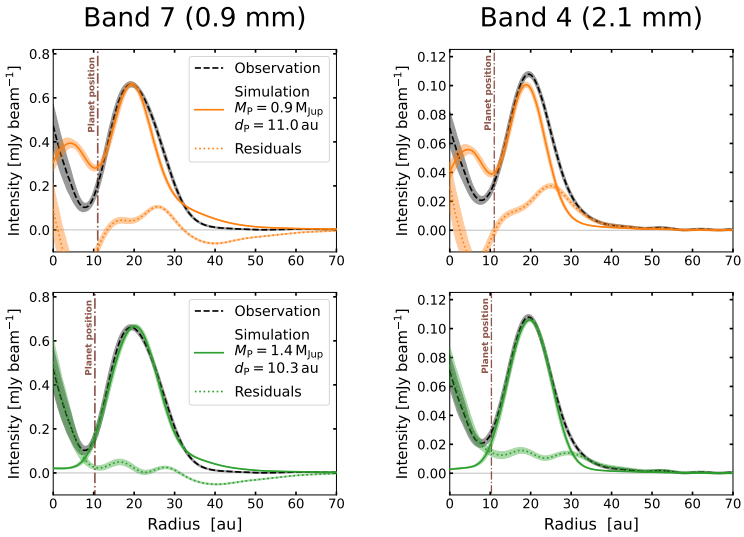

Figure 5.19: As in Fig. 5.8, but for the cases of simulations with final planet masses 0.9 and $1.4\,\mathrm{M_{Jup}}$ with different initial distances from the star. For the simulation in the *first row*, $M_{\mathrm{P},0} = 0.5\,\mathrm{M_{Jup}}$ and $d_{\mathrm{P},0} = 12.0\,\mathrm{au}$, and, after an evolution time of 4×10^4 yrs, $M_{\mathrm{P}} = 0.9\,\mathrm{M_{Jup}}$ and $d_{\mathrm{P}} = 11.0\,\mathrm{au}$. *Second row*: $M_{\mathrm{P},0} = 1.0\,\mathrm{M_{Jup}}$ and $d_{\mathrm{P},0} = 11.0\,\mathrm{au}$, and, after the same evolution time, $M_{\mathrm{P}} = 1.4\,\mathrm{M_{Jup}}$ and $d_{\mathrm{P}} = 10.3\,\mathrm{au}$.

SPH particles in our simulation), which is significantly higher than what is observed. In addition, the morphology of the external dust ring is slightly different, particularly in Band 4. Conversely, we note an excellent match between the observed dust ring and the one obtained from a planet with $M_{\mathrm{P}} = 1.4\,\mathrm{M_{Jup}}$ and $d_{\mathrm{P}} = 10.3\,\mathrm{au}$ in both Band 7 and Band 4. Therefore, we conclude that a minimum mass of $\sim 1.4\,\mathrm{M_{Jup}}$ can explain the observed dust ring.

Such constraints on the planet mass have been obtained by varying the initial planet mass and location but always fixing the initial value of the disk viscosity at $\alpha_{\mathrm{SS}} = 5 \times 10^{-3}$. Through a set of hydrodynamical simulations of disks with a planet, Facchini et al. (2018) prove that the dust gap width (which they define as the distance between the peak of the dust ring and the center of the gas gap) remains substantially unchanged when varying the disk viscosity by an order of magnitude (from $\alpha_{\mathrm{SS}} = 10^{-3}$ to 10^{-4}), thus showing its effective independence from viscosity (see Fig. 11 in their paper). On the contrary, the CO gap width appears to be dependent on viscosity (Fig. 13 in Facchini et al. 2018).

Beyond viscosity, in our simulations we maintained the same initial values of all the other parameters characterizing the disk (see Table 5.1) and the same dust composition. Given the computational cost of each simulation, a full exploration of all these parameters is out of the scope of this work.

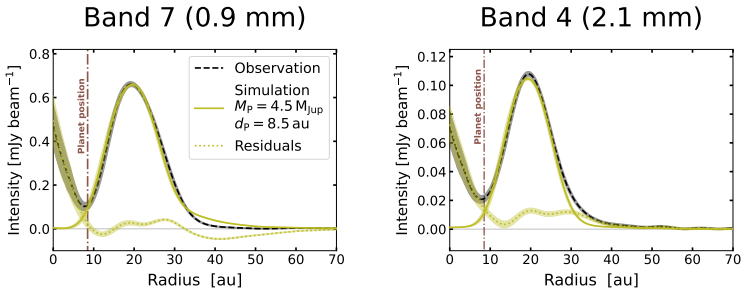

Figure 5.20: As in Fig. 5.8, but for the case of a simulation with higher planet mass. The planet started with $M_{\rm P,0} = 4.0\,{\rm M_{Jup}}$ and $d_{\rm P,0} = 9.0\,{\rm au}$, and, after an evolution time of 4×10^4 yrs, it reached $M_{\rm P} = 4.5\,{\rm M_{Jup}}$ and $d_{\rm P} = 8.5\,{\rm au}$.

5.3.6 Maximum planet mass

The simulations reported in Fig. 5.8 do not allow an estimation of the maximum planet mass able to recover the dust ring in the observations. The cases with the highest final planet masses, 2.0 and $2.5\,{\rm M_{Jup}}$, starting at a distance of $10.0\,{\rm au}$ from the central star, both produce an accurate match with the observed dust emission morphology. We try to constrain the maximum planet mass by simulating a new case with a higher initial planet mass of $M_{\rm P,0} = 4.0\,{\rm M_{Jup}}$. Choosing an initial location $d_{\rm P,0} = 9.0\,{\rm au}$, after 4×10^4 yrs the planet reached $d_{\rm P} = 8.5\,{\rm au}$ with $M_{\rm P} = 4.5\,{\rm M_{Jup}}$, and also this model reproduces the observed dust ring in both Band 7 and Band 4 (see Fig. 5.20).

Thus, we followed another approach to give an estimate of the possible maximum planet mass. Lodato et al. (2019) report an empirical relation according to which the width of an observed dust gap scales with the planet Hill radius (see Eq. 5.5) in case of low disk viscosity ($\alpha_{\rm SS} \lesssim 0.01$; Dodson-Robinson & Salyk 2011; Pinilla et al. 2012a; Rosotti et al. 2016; Fung & Chiang 2016; Facchini et al. 2018). Averaging results from hydrodynamical simulations (Clarke et al. 2018; Liu et al. 2019), they derive

$$\Delta = 5.5 R_{\rm H}\,, \tag{5.9}$$

where Δ is defined as the distance between the minimum intensity in the gap and the peak intensity in the ring. Hence, we take the value of 2Δ as the total dust gap width. This relation assumes that the planet position coincides with the location of the dust gap, and that the gap is opened by a single planet. With such an analytical approach, we do not suffer from the numerical limitations of the hydrodynamical simulations (see Sect. 5.1.1). Instead, we can place an upper limit to the planet mass by requiring the dust gap that it produces not to be so wide as to prevent the formation of the observed inner disk (which we did not reproduce in the hydrodynamical simulations).

From the intensity radial profile of CIDA 1 observed in both Band 7 and Band 4 (see Fig. 5.8), the total dust gap width is $19.2\,{\rm au}$. We measured this distance from the peak of the inner disk emission (i.e., the center of the disk) to the peak of the dust ring. We assumed that the observed inner disk is not a fast transient feature, but a long-lived structure. We fixed the star mass at $0.2\,{\rm M_\odot}$ and adopted a planet location between $9.5\,{\rm au}$,

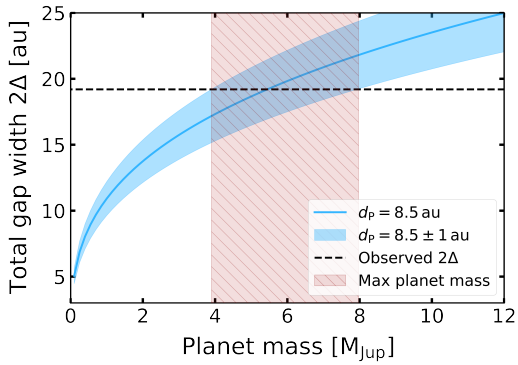

Figure 5.21: Total gap width in the dust as a function of the planet mass, derived from Eq. (5.9). The red-shaded area indicates the maximum planet mass that could fit the observed total gap width, assuming that the planet is located between 7.5 and $9.5\,\mathrm{au}$ from the star..

consistent with the values in Table 5.2, and $7.5\,\mathrm{au}$, assuming that a higher-mass planet needs a shorter distance from the star to correctly reproduce the observed dust ring, as occurred with the case of the $4.5\,\mathrm{M_{Jup}}$ planet (Fig. 5.20). Employing Eq. 5.9 with these values, we obtained the total dust gap width 2Δ versus the planet mass, as depicted in Fig. 5.21. Comparing the computed gap widths with the observed one, we find that the maximum planet mass able to create the CIDA 1 gap should be $\sim 4-8\,\mathrm{M_{Jup}}$. A more massive planet would carve a wider gap, either generating the dust ring at a greater distance from the star or depleting the inner disk.

5.3.7 Comparison with previous estimates of the planet mass

Assuming a stellar mass of $0.1\,\mathrm{M_\odot}$, a disk viscosity $\alpha_{\mathrm{SS}} = 10^{-3}$, and that the gap is carved by a single planet located at the minimum of the gap ($\sim 8\,\mathrm{au}$), Pinilla et al. (2021) employed the Crida et al. (2006) criterion and estimated that the minimum planet mass to open a gap in the gas is $\sim 0.4\,\mathrm{M_{Jup}}$. However, such a planet would generate a pressure maximum at $\sim 13\,\mathrm{au}$. So, either a more massive planet or a higher distance from the star is needed to retrieve the observed dust ring at $\sim 20\,\mathrm{au}$. Following this argument, the authors computed dust evolution simulations considering two cases: a $2.4\,\mathrm{M_{Jup}}$ planet located at $8\,\mathrm{au}$ and a $0.5\,\mathrm{M_{Jup}}$ planet at $12\,\mathrm{au}$, assuming a gap shape obtained analytically. Their 1D models evolved for $10^6\,\mathrm{yrs}$, starting from micron-sized dust particles and then considering dust growth, fragmentation and erosion. Both planets were able to form a dust ring at the observed location. The $2.4\,\mathrm{M_{Jup}}$ planet case was excluded: the formed gap was too deep to allow replenishment of dust from the outer region to an inner disk, resulting in an empty internal cavity. The $0.5\,\mathrm{M_{Jup}}$ planet case, instead, was able to reproduce the contrast between the inner disk and the ring after $10^5\,\mathrm{yrs}$ of evolution. At longer times, however, the inner disk became fainter.

The models presented in this work differ significantly from those in Pinilla et al. (2021). Our hydrodynamical simulations take into account all the complex dynamical interactions between the disk gas and dust components and the planet in 3D. The com-

putational effort needed inevitably leads to evolution times shorter than 10^6 yrs. We did not include the effects of dust evolution such as grain growth or fragmentation, but we assumed that dust growth has already occurred, simulating the dynamical behavior of different dust populations with fixed grain sizes, ranging from submicron to millimeter scales. In our models, most of the dust mass is contained in the bigger grain sizes, allowing us to reproduce the observed low value of the spectral index. On the other hand, the simulations of Pinilla et al. (2021) struggled to produce large dust grains, leading to higher values of the spatially-integrated spectral index ($\sim$2.6). The numerical limitations described in Sect. 5.1.1 prevent us from reproducing the inner disk, but the final synthetic images in our models allow, nonetheless, a careful match with the observed dust ring and the gas emission morphology. Moreover, thanks to the comparison between the simulated and observed gas channel maps, we find that a better estimate of the stellar mass is $0.2\,M_\odot$, whereas Pinilla et al. (2021) assumed a $0.1\,M_\odot$ central star. This difference in the stellar mass, along with a disk viscosity $\alpha_{SS} = 10^{-3}$, lower than the initial value of 5×10^{-3} adopted in our simulations, might explain why Pinilla et al. (2021) predict a planet mass of $\sim 0.5\,M_{Jup}$ while our models require a minimum planet mass of $\sim 1.4\,M_{Jup}$ to reproduce the observed dust ring.

The two modeling approaches are different, and neither is fully complete. Future studies need to take into account the phenomena of dust growth and fragmentation within comprehensive hydrodynamical and radiative transfer simulations. Including all of these effects, each with its typical timescale, may end up reducing the uncertainty on the mass of the planet that can generate the observed substructures in CIDA 1. Moreover, it is important to note that our work and the one by Pinilla et al. (2021) aim at reproducing the observed disk morphology with a single planet. It remains to be explored whether a multi-planet system could reproduce the disk emission, and future simulations including more than one embedded planet are needed to test such a scenario.

5.3.8 Implications for planet formation around VLM stars

Our analysis of the CIDA 1 system is consistent with the presence of a planet more massive than Jupiter around a $0.2\,M_\odot$ star. Even considering that CIDA 1 may be an outlier in terms of the initial disk mass or its properties, it can still provide relevant constraints on planet formation theories. It is thus important to compare what we find in this system with the prediction of the leading theories.

Core accretion model (Pollack et al. 1996) is based on the dynamics of dust in disks and how it evolves from submicron dust grains in the interstellar medium to kilometer-sized planetesimals through collisions. During this process, when dust grains reach millimeter size, they should rapidly drift toward the central star, preventing grains from growing into planetesimals and planetary cores (Weidenschilling 1977). This barrier for planet formation is even harder to overcome for disks around VLM stars since dust radial drift is more efficient in these environments (Pinilla et al. 2013; Zhu et al. 2018). Furthermore, the disk mass content is crucial to determine whether planet formation may occur. Disk population studies in nearby star-forming regions (e.g., Barenfeld et al. 2016; Ansdell et al. 2016; Testi et al. 2016; Pascucci et al. 2016; Cieza et al. 2019a; Williams et al.

2019; Sanchis et al. 2020; Villenave et al. 2021) prove that the scaling relation between disk mass and stellar mass is steeper than linear. Therefore, it appears that disks in the low-stellar-mass regime do not possess enough material to form the known planetary systems (Manara et al. 2018), unless the planet-formation efficiency is 100% (Mulders et al. 2021). However, these studies consider disks with a mean age $> 10^6$ yrs, whereas planet formation via gravitational instabilities should occur at earlier times (Kratter & Lodato 2016). The properties of disks in the early Class 0/I protostars is an active area of research and the properties of such disks are highly uncertain and debated at the moment, both on observational and modeling grounds (Maury et al. 2019; Tychoniec et al. 2020; Lebreuilly et al. 2021). Nevertheless, it seems likely that at least some young disks will be prone to undergo gravitational instabilities and possibly form massive planets early on through this path.

Various theoretical studies employing numerical simulations have been performed to investigate planet formation through core accretion or gravitational instability in the low-stellar-mass regime. Payne & Lodato (2007) assessed planet formation around brown dwarfs adapting models for higher stellar masses based on core accretion. Through Monte Carlo simulations, they found that Earth-like planets can form in this condition and the planet mass depends strongly on the disk mass. However, none of their simulations showed a planetary rocky core accreting a gaseous envelope to form a giant planet. A way to overcome the radial drift barrier is a rapid rocky core growth. Pebble accretion is a mechanism able to speed up significantly the giant planet formation process (i.e., Lambrechts & Johansen 2012; Bitsch et al. 2015). Liu et al. (2020) carried out a theoretical study on planet formation driven by pebble accretion in the (sub)stellar mass range between 0.01 and $0.1\,\mathrm{M}_\odot$. First, they calculated the initial masses of protoplanets by extrapolating previous numerical simulations conducted in previous literature. Next, they performed a population synthesis study to track the growth and migration of a large sample of protoplanets under the influence of pebble accretion. Their results show that, around a $0.01\,\mathrm{M}_\odot$ brown dwarf, planets can grow up to $0.1{-}0.2\,\mathrm{M}_\oplus$, while, around $0.1\,\mathrm{M}_\odot$ stars, planets can reach a maximum mass of $2{-}3\,\mathrm{M}_\oplus$. Findings from this study show that even pebble accretion does not seem to be sufficient to form gas giants around VLM stars and brown dwarfs. Miguel et al. (2020) used a population synthesis approach based on planetesimal accretion to explore planet formation in the stellar mass range between 0.05 and $0.25\,\mathrm{M}_\odot$. They let the synthetic population of planetary systems evolve for 10^8 yrs. The authors find that to form planets with masses higher than $0.1\,\mathrm{M}_\oplus$ they need stars of at least $0.07\,\mathrm{M}_\odot$, implying that planet formation around brown dwarf may not be a usual outcome. Then, stars with masses higher than $0.15\,\mathrm{M}_\odot$ are necessary to form planets more massive than the Earth. Therefore, from all of these studies, we conclude that core accretion model currently cannot explain the presence of gas giants around VLM stars or brown dwarfs. Either the core accretion theory is incomplete, or another mechanism for planet formation is needed. This is confirmed by Lodato et al. (2005), who discussed the origin of the $5\,\mathrm{M}_\mathrm{Jup}$ planet detected around the $25\,\mathrm{M}_\mathrm{Jup}$ brown dwarf 2MASSW J1207334-393254 (Chauvin et al. 2005). They found that the core accretion mechanism is far too slow to generate such a planet in less than 10^7 yrs, the estimated age of the system. Therefore, the authors proposed gravitational

instabilities arising during the early phases of the disk lifetime as a viable possibility for the formation of the planet.

Haworth et al. (2020) assessed the susceptibility for disk fragmentation due to self-gravity depending on the properties of the disk and the host star. They performed a set of SPH simulations and accounted for the stellar irradiation. Their results show that disks around VLM stars are less prone to fragment with respect to disks around more massive stars. Fragmentation can occur around VLM stars only if the disk is optically thick to stellar irradiation and there is a high disk-to-star mass ratio ($M_{\rm disk}/M_\star \gtrsim 0.3$). Mercer & Stamatellos (2020) focused on the role of disk instability for planet formation around low-mass stars. They conducted a set of SPH simulations to study the fragmentation conditions of initially gravitationally stable disks, whose mass was slowly but steadily incremented. They considered stars with masses between 0.2 and $0.4\,{\rm M}_\odot$. The authors find that, via gravitational instabilities, protoplanets form very fast, within a few thousand years, provided that the disk is massive enough ($M_{\rm disk}/M_\star \gtrsim 0.3$). The formed planets have masses between 2 and $6\,{\rm M}_{\rm Jup}$ and they are initially distant from the central star, between 15 and $105\,{\rm au}$, but may migrate afterward. Hence, a plausible origin of a giant planet around CIDA 1 might be the fast fragmentation of the disk due to gravitational instabilities, assuming the disk was massive enough in its early stages.

5.4 Conclusions

In this work we inspect the origin of the substructures observed by ALMA in the protoplanetary disk around CIDA 1, one of the very few young VLM stars with high-resolution data. Assuming the presence of an embedded planet, we self-consistently reproduced the observed continuum emission from the dust ring and the gas line emission morphology with a single model. We performed 3D hydrodynamical simulations of gas and multigrain dust, considering initial planet masses from 0.1 to $4.0\,{\rm M}_{\rm Jup}$ and starting at a radial distance of between 9 and $11\,{\rm au}$ from the central star. Then, we computed the dust and gas emission using radiative transfer modeling. Finally, we treated the obtained images as actual ALMA observations to acquire the final synthetic images. Here we summarize our main findings:

- We compared the observed and simulated dust emission profiles in Band 7 ($0.9\,{\rm mm}$) and Band 4 ($2.1\,{\rm mm}$). We find that the observed dust ring can be explained by the presence of a giant planet with a minimum mass of $\sim 1.4\,{\rm M}_{\rm Jup}$ located at a distance of $10.3\,{\rm au}$ from the central star. The formation of such a massive planet around a VLM star such as CIDA 1 challenges our current theoretical models based on core accretion theory. A valid explanation for its origin may involve gravitational instabilities in the early stages of disk evolution.

- Our numerical models cannot directly constrain the maximum planet mass consistent with observations. Thus, we used an empirical relation between the observed dust gap width and the Hill radius of the planet and estimate a maximum planet mass of $\sim 4-8\,{\rm M}_{\rm Jup}$.

- Assuming that dust is composed of porous grains with a mixture of astronomical silicates, carbonaceous materials, and water ice, we match the observed flux with a total dust mass in our models of $\sim 7 \times 10^{-6}\,\mathrm{M}_{\odot}$, corresponding to a dust-to-gas mass ratio of $\sim 10^{-2}$.

- The observed ^{12}CO and ^{13}CO channel maps are strongly affected by cloud absorption. Nonetheless, our model with a final planet mass of $2.0\,\mathrm{M}_{\mathrm{Jup}}$ can recreate the spatial extent of the gas emission in the channels where it was detected, except for the channels that probe the highest velocities in the innermost regions, which are not considered in our model. Our simulation include a dust-to-gas mass ratio of $\sim 10^{-2}$, a ^{12}CO abundance of $[^{12}\mathrm{CO}/\mathrm{H}_2] = 5 \times 10^{-5}$, and an isotopologue abundance ratio $[^{12}\mathrm{CO}/^{13}\mathrm{CO}] = 70$. Since we can recreate the spatial extent and rotation pattern of the disk, we conclude that the assumed stellar mass of $0.2\,\mathrm{M}_{\odot}$ and systemic velocity of $6.25\,\mathrm{km\,s^{-1}}$ are solid estimates for the actual properties of CIDA 1.

- In the case of our simulation with a final planet mass of $2.0\,\mathrm{M}_{\mathrm{Jup}}$, we are able to reproduce the low spectral index (~ 2) observed at the location of the dust ring ($10-30\,\mathrm{au}$). The simulated dust emission in both Band 7 and Band 4 is optically thick in the range $14-20\,\mathrm{au}$, with a total fraction of optically thick emission corresponding to $\sim 40-50\%$. However, the emission from our model is optically thin between 20 and $30\,\mathrm{au}$. The low spectral index in this region is expected in our simulations that contain millimeter-sized dust particles, but the match with the observation hints at the occurrence of grain growth and migration in CIDA 1.

- The $2.0\,\mathrm{M}_{\mathrm{Jup}}$ planet creates a velocity perturbation that is predicted to be extremely arduous to observe. It would require ^{13}CO channel maps at a very high angular resolution of at least $0.02''$, with a velocity resolution of $0.5\,\mathrm{km\,s^{-1}}$.

Our results suggest that the observed structures in CIDA 1 can indeed be explained by the presence of a massive embedded planet. It remains to be understood whether CIDA 1 constitutes a unique case or if other disks around VLM stars may also have undergone giant planet formation.

CHAPTER 6

Characterization of the dust continuum substructures in the exoALMA disks

*This chapter is based on the paper in preparation "Analysis of the continuum emission in the exoALMA sample" by **Pietro Curone**, Stefano Facchini, Leonardo Testi, and the exoALMA collaboration.*

6.1 exoALMA sample

The exoALMA Large Program (2021.1.01123.L) targeted 15 protoplanetary disks with deep observations at high angular and spectral resolution. The main objective is to study the physical and dynamical structure of the gas in these disks, revealing perturbations produced by embedded planets (exoALMA paper I, Teague et al. - including Curone, in prep.). Observations were carried out at a wavelength of $\sim$0.9 mm ($\sim$331 GHz, ALMA Band 7) combining the ALMA configurations C-6 and C-3 (and the ACA for the most extended sources), having one spectral window with a bandwidth of 1875 MHz dedicated to the continuum emission. This resulted in continuum images with an angular resolution of $\sim 0.09''$ of and an high sensitivity of $\sim 40\,\mu\mathrm{Jy\,beam^{-1}}$. The sample contains bright disks from different star-forming regions, the majority of which have already been observed in continuum by ALMA at high angular resolution, revealing a variety of dust substructures indicative of planet-disk interactions. The exoALMA observations provide the deepest data ever taken on such disks. The data calibration procedure will be described in the exoALMA paper II (Loomis et al. - including Curone, in prep.). We present a gallery of the continuum emission from the disks in the exoALMA sample in Figs. 6.1 and 6.2, while the properties of the observed continuum images for each target are reported in Table 6.1.

6.2 Methods for the continuum analysis

The first aim of our continuum data analysis is to perform a morphological characterization of the observed substructures in each disk. To do so, we relied on the tool

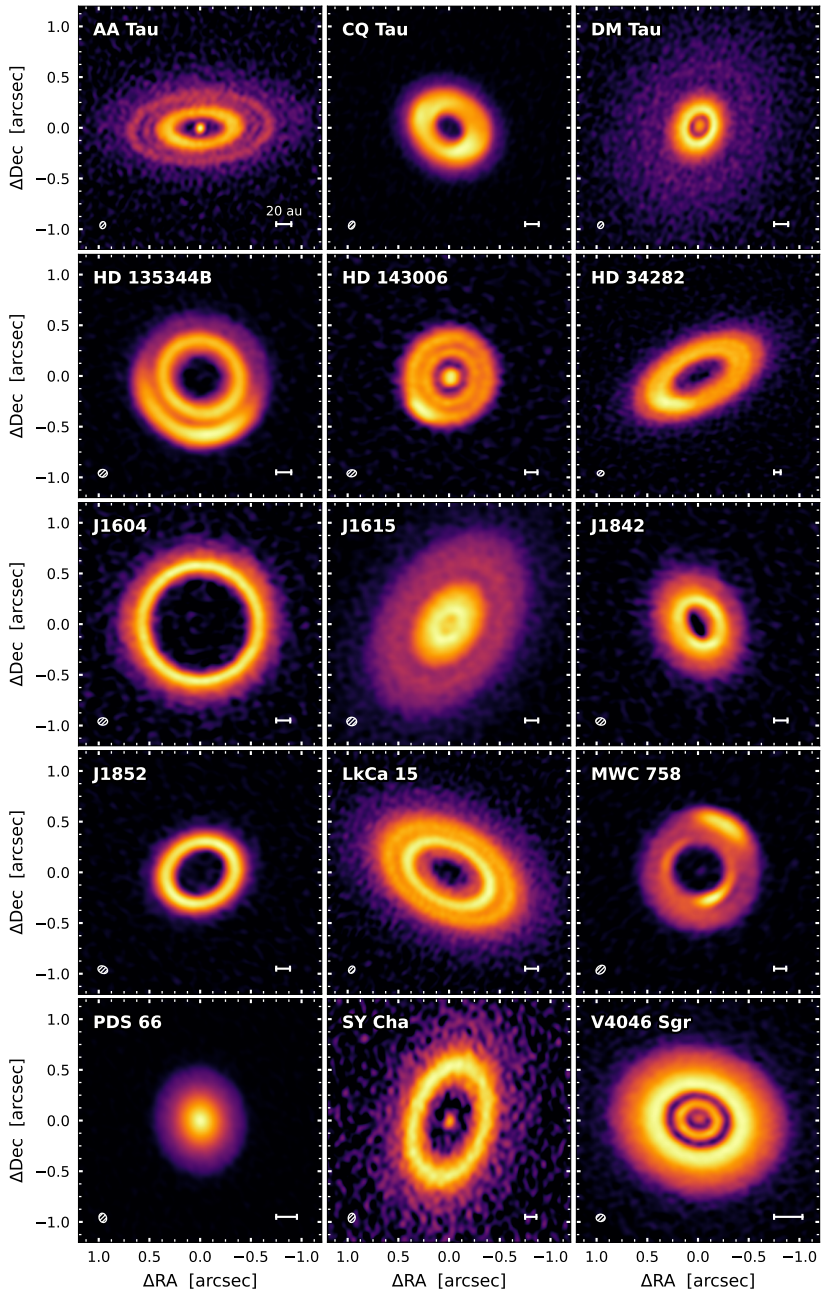

Figure 6.1: Gallery of continuum images at 0.9 mm (331 GHz) of the exoALMA sample, obtained with the CLEAN algorithm and robust of -0.5. The source order is alphabetical. Spatial scales in the sky (ΔRA and ΔDec extremes) are consistent across all images. The FWHM of the synthesized beams and the 20 au scalebars are indicated in the lower left and right corners of each plot, respectively. The color scale ranges from null to peak intensity for each disk. An asinh stretch is applied to the color scale to visually enhance the fainter emission. A linear stretch version is presented in Figure 6.2.

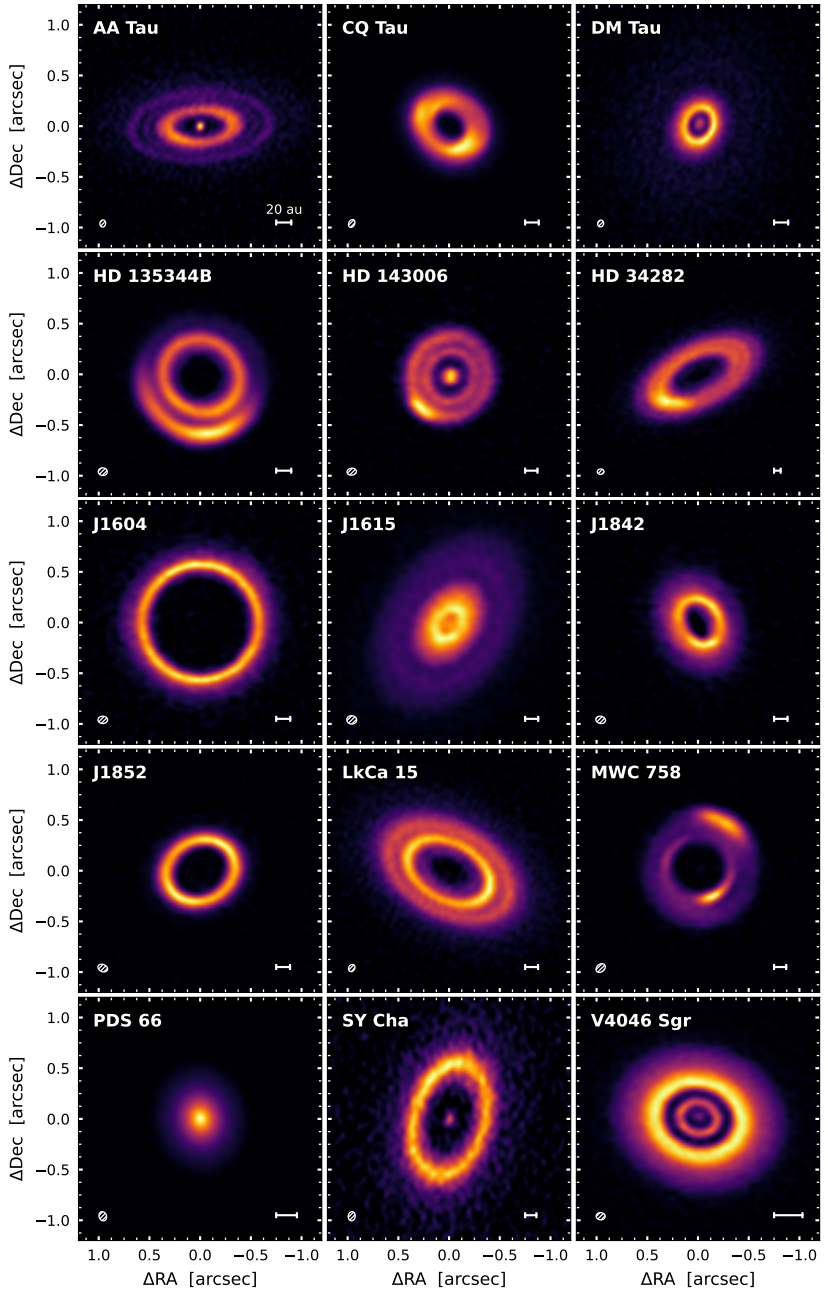

Figure 6.2: Same as in Fig. 6.1 but with a linear stretch in the color scale to highlight the changes in intensity within the brightest regions.

Table 6.1: Continuum image properties.

Source	$\theta_{\rm b}$ (mas, au)	PA$_{\rm b}$ (deg)	Rms noise (μJy beam^{-1}, K)	Peak I_ν, $T_{\rm b}$ (mJy beam^{-1}, K)	F_ν (mJy)	d (pc)	$M_{\rm d}$ ($M_\oplus$, $M_{\rm Jup}$)
(1)	(2)	(3)	(4)	(5)	(6)	(7)	(8)
AA Tau	70×57, 9×8	168	45, 3.3	2.76, 7.7	189	134.7	37, 0.12
CQ Tau	82×59, 12×9	153	40, 3.1	8.11, 18.6	434	149.4	104, 0.33
DM Tau	68×58, 10×8	162	40, 3.2	2.99, 8.3	233	144.0	52, 0.16
HD 135344B	90×76, 12×10	85	45, 3.0	6.44, 10.5	421	135.0	82, 0.26
HD 143006	94×68, 15×11	97	46, 3.0	3.45, 6.0	155	167.3	45, 0.14
HD 34282	67×54, 21×17	95	39, 3.3	3.79, 11.7	340	308.6	348, 1.09
J1604	95×73, 14×11	91	44, 2.9	2.70, 4.3	196	144.6	44, 0.14
J1615	97×83, 15×13	85	43, 2.8	5.82, 8.0	379	155.6	98, 0.31
J1842	97×72, 15×11	78	43, 2.9	3.59, 5.8	141	151.0	34, 0.11
J1852	99×71, 15×10	67	37, 2.8	4.50, 7.1	151	157.1	35, 0.11
LkCa 15	75×59, 12×9	150	35, 3.1	2.75, 6.9	401	157.2	106, 0.33
MWC 758	101×75, 17×13	130	56, 3.0	6.87, 10.0	212	155.9	64, 0.20
PDS 66	93×73, 9×7	19	47, 3.0	16.19, 26.4	336	97.9	34, 0.11
SY Cha	91×68, 16×12	171	57, 3.1	1.55, 2.8	155	180.7	54, 0.17
V4046 Sgr	89×72, 6×5	88	39, 2.9	5.17, 9.0	655	71.6	36, 0.11

Notes. All properties were obtained from CLEAN images with robust -0.5. The mean frequency is 331.6 GHz for each image. Column (1): target name. Column (2): synthesized beam FWHM major and minor axes. Column (3): synthesized beam position angle. Column (4): image rms noise, calculated in an annulus between $3''$ and $4''$ centered on the disk. Column (5): image peak intensity. Note that the noise and peak brightness temperature were computed using the full Planck law. Column(6): total flux density obtained from the value of the `frank` fit on the visibilities at null baseline. Column (7): distances from Bailer-Jones et al. (2021). Column (8): estimated dust mass, calculated employing the integrated flux density in column (6) and following the relation of Hildebrand (1983) $M_{\rm d} = F_\nu d^2/(B_\nu(T)k_\nu)$, where d is the distance, $B_\nu(T)$ is the blackbody surface brightness at a given temperature, and k_ν is the opacity. We assumed a temperature of 20 K (as in, e.g., Ansdell et al. 2016) and an opacity $k_\nu = 3.5\,{\rm cm}^2/{\rm g} \times 870\,\mu{\rm m}/\lambda$ (Beckwith et al. 1990).

`frankenstein` (Jennings et al. 2020, hereafter `frank`) which fits the visibilities non-parametrically (Sect. 6.2.2). However, `frank` requires as an input the values of the disk geometric properties, that is, inclination, position angle and the offsets in RA and Dec from the disk phase center. To obtain accurate estimates of these values we employed the code `galario` (Tazzari et al. 2018) and fit the visibilities, assuming an intensity parametric model and using a Markov chain Monte Carlo (MCMC) approach (Sect. 6.2.1).

We considered only the spectral window dedicated to the continuum because including the other three spectral windows dedicated to the lines (after proper flagging of the line emission) resulted in a higher noise in the visibilities at long baselines. The visibilities in the continuum spectral windows were spectrally averaged down to one channel for each execution block and averaged in time down to 30 second bins. We tested that this averaging did not introduce any alterations in the continuum analysis. All the manipulation of the visibilities was conducted with the software CASA, version 6.2 (CASA Team et al. 2022).

6.2.1 `galario` fit

`galario` assumes a 1D or 2D model representing the emission in the image plane and performs a Fourier transform to derive the synthetic visibilities at the same uv-points as the observation. The best-fit model is determined by minimizing the χ^2 through an MCMC approach, utilizing the `emcee` package for parameter sampling (Foreman-Mackey et al. 2013). In employing this methodology, our primary focus was not an exhaustive characterization of the substructures, a task reserved for the application of `frank`. Instead, our objective was to derive solid estimates of the geometrical parameters of each disk, specifically inclination, position angle and offsets in RA and Dec from the disk phase centre. This is reflected by our choices of the parametric models, selected so that they could globally represent the disk observed morphology. Among the 15 sources, 10 were characterized using 1D axisymmetric intensity profiles. Each profile includes one or more Gaussian rings $I(R) = f_0 \exp[-(R-R_0)^2/2\sigma^2]$, where R is the radial coordinate, f_0 is a normalization term, R_0 denotes the radial location of the Gaussian peak, and σ is the standard deviation. For sources displaying an inner emission, we added either a central Gaussian $I(R) = f_0 \exp[-R^2/2\sigma^2]$ or a central point source, in case of an unresolved emission $I(R) = f_0\,\delta(R)$, where $\delta(R)$ is the Dirac delta function. For the five disks showing strong non-axisymmetries (CQ Tau, HD 135344B, HD 143006, HD 34282, and MWC 758), we employed 2D models. These models combined axisymmetric rings with one or more arcs, defined as Gaussian rings with azimuthal tapering: $I(R,\phi) = f_0 \exp[-(R-R_0)^2/2\sigma^2] \exp[-\phi_0^2/2\sigma_\phi^2]$, where ϕ is the azimuthal coordinate, ϕ_0 is the azimuthal center of the arc, and σ_ϕ is its azimuthal extent. Uniform priors were applied, and the intensity normalization factor f_0 was logarithmically sampled. For each 1D run, we used $\sim$100 walkers that converged after $\sim 10^4$ steps, while the 2D runs required a higher number of steps to converge, between $\sim 3 \times 10^4$ and $\sim 10^5$. The chosen `galario` models and the resulting estimates of the geometrical parameters for each disk are reported in Table 6.2.

Table 6.2: Dust disk geometries.

Source	inc	PA	ΔRA	ΔDec	`galario` model	R_{68}	R_{90}	R_{95}
	(deg)	(deg)	(mas)	(mas)		(au, arcsec)	(au, arcsec)	(au, arcsec)
(1)	(2)	(3)	(4)	(5)	(6)	(7)	(8)	(9)
AA Tau	$58.54^{0.02}_{0.02}$	$93.77^{0.02}_{0.03}$	$-5.46^{0.11}_{0.11}$	$4.83^{0.07}_{0.08}$	Central point source + 4 rings	92.2, 0.68	139.4, 1.03	158.6, 1.18
CQ Tau	$35.24^{0.02}_{0.02}$	$53.87^{0.02}_{0.02}$	$-8.71^{0.05}_{0.05}$	$0.99^{0.04}_{0.04}$	2 rings + 2 arcs (2D)	55.8, 0.37	73.1, 0.49	85.4, 0.57
DM Tau	$35.97^{0.05}_{0.05}$	$155.60^{0.08}_{0.07}$	$-5.51^{0.07}_{0.07}$	$-6.59^{0.09}_{0.09}$	Central Gaussian + 3 rings	118.6, 0.82	201.9, 1.40	244.8, 1.70
HD 135344B	$20.73^{0.02}_{0.02}$	$28.92^{0.09}_{0.06}$	$0.80^{0.05}_{0.05}$	$-3.21^{0.05}_{0.05}$	1 ring + 1 arc (2D)	78.7, 0.58	90.2, 0.67	94.4, 0.70
HD 143006	$18.69^{0.09}_{0.09}$	$7.53^{0.35}_{0.32}$	$8.27^{0.14}_{0.13}$	$26.42^{0.16}_{0.16}$	2 rings + 1 arc (2D)	68.5, 0.41	78.8, 0.48	83.7, 0.51
HD 34282	$59.82^{0.01}_{0.01}$	$117.80^{0.01}_{0.01}$	$12.82^{0.06}_{0.06}$	$8.38^{0.04}_{0.04}$	3 rings + 1 arc (2D)	179.8, 0.58	239.4, 0.78	289.3, 0.94
J1604	$8.72^{0.09}_{0.07}$	$123.24^{0.07}_{0.15}$	$-74.82^{0.07}_{0.07}$	$-16.67^{0.06}_{0.06}$	2 rings	94.0, 0.65	112.4, 0.78	122.2, 0.84
J1615	$47.10^{0.01}_{0.01}$	$146.14^{0.02}_{0.02}$	$-44.32^{0.05}_{0.04}$	$-5.88^{0.04}_{0.05}$	Central Gaussian + 1 ring	116.1, 0.75	169.6, 1.09	204.2, 1.31
J1842	$39.22^{0.03}_{0.04}$	$26.35^{0.06}_{0.06}$	$-3.16^{0.07}_{0.07}$	$-30.69^{0.07}_{0.07}$	3 rings	62.7, 0.42	85.2, 0.56	100.8, 0.67
J1852	$32.50^{0.03}_{0.05}$	$117.61^{0.03}_{0.03}$	$-23.41^{0.04}_{0.04}$	$1.91^{0.04}_{0.04}$	3 rings	58.0, 0.39	69.9, 0.47	79.8, 0.54
LkCa 15	$50.59^{0.01}_{0.02}$	$61.57^{0.01}_{0.01}$	$-16.84^{0.05}_{0.05}$	$20.83^{0.05}_{0.05}$	4 rings	111.0, 0.71	156.3, 0.99	181.0, 1.15
MWC 758	$7.27^{0.23}_{0.17}$	$76.17^{0.13}_{0.10}$	$25.48^{0.13}_{0.13}$	$18.42^{0.12}_{0.12}$	2 rings + 2 arcs (2D)	85.4, 0.51	98.1, 0.59	103.3, 0.62
PDS 66	$32.02^{0.03}_{0.03}$	$8.91^{0.05}_{0.05}$	$-3.59^{0.02}_{0.02}$	$6.68^{0.03}_{0.03}$	2 rings	31.7, 0.32	46.9, 0.48	51.5, 0.53
SY Cha	$51.65^{0.03}_{0.02}$	$165.77^{0.04}_{0.04}$	$-12.66^{0.12}_{0.13}$	$28.16^{0.18}_{0.18}$	Central Gaussian + 2 rings	132.3, 0.73	197.7, 1.09	228.1, 1.26
V4046 Sgr	$33.36^{0.01}_{0.01}$	$76.02^{0.02}_{0.01}$	$-50.94^{0.03}_{0.02}$	$-45.18^{0.02}_{0.02}$	Central Gaussian + 3 rings	46.5, 0.65	60.9, 0.85	71.8, 1.00

Notes. Column (1): target name. Column (2): disk inclination. Column (3): disk position angle. Column (4): offset in Right Ascension from the disk phase center. Column (5): offset in Declination from the disk phase center. Column (6): `galario` parametric model of the intensity map employed to obtain the geometrical parameters in columns (2) - (5), where the associated statistical uncertainties represent the 16th and 18th percentiles of the MCMC marginalized distribution. The label "(2D)" indicates non-axisymmetric models, while all the others are axiysimmetric. Columns (7), (8), (9): radial extent of the continuum emission enclosing 68%, 90%, and 95% of the continuum intensity, respectively. Values were computed from `frank` model intensity profiles.

6.2.2 `frank` fit

For a thorough characterization of the intensity profiles as a function of disk radius we used the code `frank` (Jennings et al. 2020). It nonparametrically fits the real component of the deprojected and unbinned visibilities as a function of baseline with a Fourier-Bessel series. Then, the intensity profile is computed using a discrete Hankel transform. The fit is one-dimensional, assuming the axisimmetry of the source, and employs a Gaussian process for regularization. Moreover, the disk emission is assumed geometrically flat and optically thick. `frank` allows to solidly recover sub-beam resolution features that remain undetected in both the CLEAN image and its azimuthally averaged intensity profile, while maintaining high sensitivity (Jennings et al. 2022a; Andrews et al. 2021; Ilee et al. 2022).

We performed the `frank` fit in logarithmic intensity space, which enforces the intensity to be non-negative and prevented the high-frequency oscillations in the reconstructed intensity profile when compared to the fit in linear space. We verified that the choice of hyperparameters had minimal impact on the resulting fit, given the high sensitivity of our data. We selected, nonetheless, conservative values to minimize the chance of artifacts generated by fitting low signal-to-noise features and set $\alpha = 1.3$, and $w_{\rm smooth} = 0.01$. The hyperparameter $R_{\rm max}$, indicating the point beyond which `frank` assumes zero emission, was established at 1.5 times the radius of the outer extent of observed emission ($R_{\rm out}$), determined by the contour reaching twice the rms noise (see Table 6.1) in the synthesized image. The rms noise was measured in an annulus centered on the disk between $3''$ and $4''$. The N hyperparameter, determining the radial gridding, was set to 400, and p_0, acting in the regularization of the emission power spectrum, was fixed to 10^{-35}, the standard value for logarithmic intensity space fitting. A comparison of the observed visibility profiles as a function of deprojected baseline with the `galario` and `frank` fits is presented in Fig. 6.3.

As explained by Jennings et al. (2020, 2022a), obtaining a solid estimate of the uncertainty associated with the `frank` fit is not feasible. This limitation arises from the inherently ill-posed nature of reconstructing brightness from Fourier data. Specifically, there is no robust method to accurately extrapolate visibility amplitudes in a given dataset beyond the longest baseline fitted by `frank`. Therefore, we do not show a formal uncertainty of the intensity profile reconstructed by `frank` (see Fig. 6.4). For the same reason, in this work, we do not assign a formal uncertainty to the parameters retrieved from the `frank` profile. These parameters include the dust disk extent (columns (7), (8), and (9) in Table 6.2), the radial location and width of each axisymmetric substructure, and the gap depth (columns (3), (4), and (5) in Table 6.3).

6.3 Results

6.3.1 Axisymmetric substructures

We employed the intensity profile from the `frank` fit to define the annular axisymmetric features, that is, rings and gaps. Figure 6.4 presents the intensity profiles as a function of disk radius of the deprojected and azimuthally averaged observed data compared to

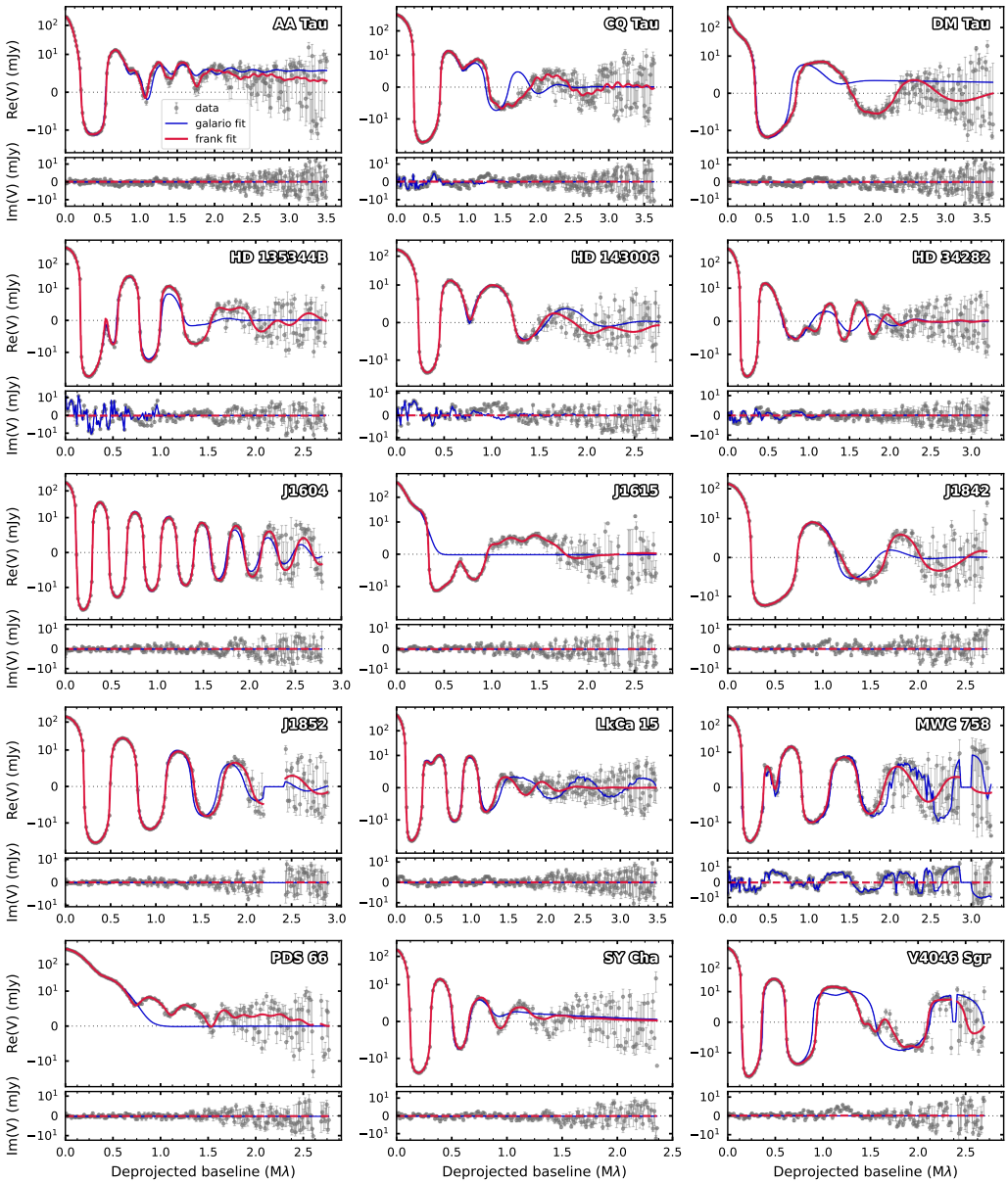

Figure 6.3: Real and imaginary part of the recentered and deprojected visibilities azimuthally averaged into 15 kλ wide bins on an asinh scale as a function of the deprojected baseline length for the data (gray points) and the best-fit models from `galario` (blue line) and `frank` (red line). Note that the imaginary part is fitted only when employing a 2D non-axisymmetric `galario` model (i.e., for CQ Tau, HD 135344B, HD 143006, HD 34282, and MWC 758), while the imaginary components of the `frank` and 1D `galario` axisymmetric models are null for all spatial frequency by definition.

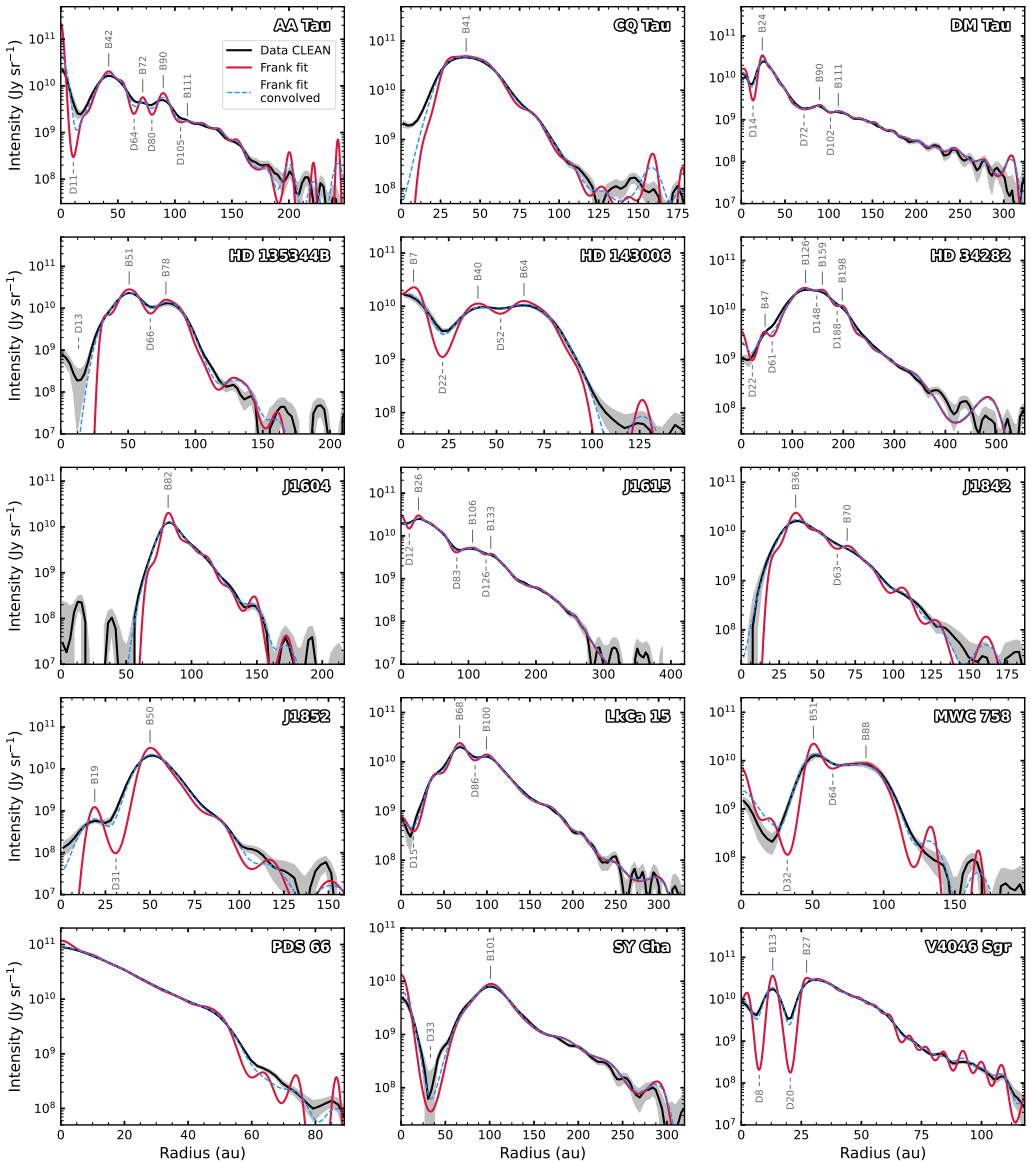

Figure 6.4: Gallery of radial intensity profiles on a logarithmic scale of the deprojected and azimuthally averaged data (black solid line), the `frank` model (solid red line), and the `frank` model convolved with the observed synthesized beam (dashed light blue line). The source order is alphabetical. The gray shade represents the data uncertainty, calculated as the 1σ scatter at each radial bin divided by square root of the number of beams contained in the associated radial annulus. The radial location of rings and gaps is marked. Each gap is indicated by a dashed segment and a label with the letter "D" (for *dark*) and the distance from the central star in au. Solid segments and labels with letter "B" (for *bright*) indicate the rings.

the `frank` model and the `frank` model convolved with the observed synthesized beam. The deprojection and azimuthal averaging of the observed image were performed with the package `GoFish` (Teague 2019). The uncertainty was determined by dividing the 1σ scatter at each intensity radial bin by the square root of the number of beams within the corresponding radial annulus. Remarkably, the convolved `frank` model consistently matches the observed profile. This correspondence highlights the ability of `frank` to trace substructures with sub-beam resolution.

Labelling the rings with the letter "B" (for *bright*) and the gaps with "D" (for *dark*), we applied four criteria to assess what can be robustly defined as a substructure and determine its radial location ($R_{\rm B}$ and $R_{\rm D}$, respectively). First, considering only the `frank` model intensity radial profile, rings and gaps must correspond to local maxima and minima, respectively. Additionally, their radial location should fall within the radius enclosing 90% of the source flux (R_{90}). Then, the peak intensity of each ring must be higher than the rms noise. Finally, a pair of gap-ring is accepted if this condition on the gap depth is met: $I_{\rm D}/I_{\rm B} \leq 0.97$, where $I_{\rm D}$ is the intensity of the gap minimum at $R_{\rm D}$ and $I_{\rm B}$ is the ring peak intensity at $R_{\rm B}$. The gap depth definition aligns with that in Huang et al. (2018). We also adopted their method for determining the substructure width. Briefly, it involves deriving the width based on the inner and outer edges of a substructure rather than employing a Gaussian fit, a more suitable method for structures deviating from a Gaussian shape. Applying these criteria to our `frank` model intensity profiles, for a gap-ring pair, the dividing point between the outer edge of the gap and the inner edge of the ring, denoted as $R_{\rm B,out}$, is defined as the radius at which the intensity equals $I_{\rm mean} = (I_{\rm D} + I_{\rm B})/2$. The radius of the gap inner edge $R_{\rm B,in}$ is the largest radius with $R < R_{\rm D}$ and $I(R) = I_{\rm mean}$. The radius of the ring outer edge is the smallest radius with $R > R_{\rm B}$ and $I(R) = I_{\rm mean}$. Consequently, the gap width is given by $R_{\rm D,out} - R_{\rm D,in}$ and the ring width is $R_{\rm B,out} - R_{\rm D,out}$. For more details on this procedure see Sect 3.2 and Appendix B of Huang et al. (2018).

All the substructure properties for each disk are presented in Table 6.3. PDS 66 is the only source were no annular substructures were detected.

Table 6.3: Properties of the continuum substructures.

Source	Feature	Radial location (au, arcsec)	Width (au, mas)	Depth	Non-axisymmetry factor
(1)	(2)	(3)	(4)	(5)	(6)
AA Tau	D11	11.0, 0.082	28.1, 209	0.01	1.73
	B42	42.0, 0.312	22.7, 168	...	
	D64	64.3, 0.478	8.1, 60	0.44	
	B72	71.8, 0.533	6.9, 51	...	
	D80	79.8, 0.593	11.1, 83	0.34	
	B90	89.8, 0.666	8.8, 66	...	
	D105	105.3, 0.782	4.9, 36	0.94	
	B111	110.9, 0.823	5.9, 44	...	
CQ Tau	B41	41.2, 0.276	33.4, 223	...	12.19
DM Tau	D14	13.5, 0.094	12.7, 88	0.08	1.25

Source	Feature	Radial location (au, arcsec)	Width (au, mas)	Depth	Non-axisymmetry factor
(1)	(2)	(3)	(4)	(5)	(6)
	B24	24.1, 0.167	10.7, 74	…	
	D72	71.8, 0.498	18,7, 130	0.78	
	B90	89.5, 0.622	10.6, 74	…	
	D102	102.5, 0.712	6.6, 46	0.92	
	B111	110.6, 0.768	9.4, 65	…	
HD 135344B	D13	13.2, 0.098	40.8, 302	0.00	25.55
	B51	50.8, 0.376	17.3, 128	…	
	D66	66.5, 0.493	11.4, 84	0.47	
	B78	78.1, 0.578	13.6, 101	…	
HD 143006	B7	6.7, 0.040	5.4, 33	…	9.06
	D22	21.8, 0.132	18.3, 111	0.10	
	B40	40.3, 0.244	12.6, 76	…	
	D52	52.2, 0.316	13.8, 84	0.58	
	B64	64.4, 0.390	12.9, 78	…	
HD 34282	D22	21.8, 0.071	28.4, 92	0.2	4.71
	B47	46.8, 0.152	16.7, 54	…	
	D61	60.6, 0.197	45.9, 149	0.1	
	B126	125.8, 0.408	44.4, 144	…	
	D148	148.0, 0.479	10.8, 35	0.96	
	B159	159.1, 0.515	9.0, 29	…	
	D188	188.2, 0.610	7.8, 25	0.96	
	B198	197.9, 0.641	7.6, 25	…	
J1604	B82	81.2, 0.568	9.5, 66	…	1.47
J1615	D12	12.3, 0.079	14.0, 90	0.49	1.35
	B26	25.9, 0.167	15.7, 101	…	
	D83	82.6, 0.531	14.0, 90	0.77	
	B106	105.6, 0.679	23.4, 150	…	
	D126	125.5, 0.807	6.3, 41	0.97	
	B133	132.9, 0.854	6.2, 40	…	
J1842	B36	35.8, 0.237	14.0, 92	…	2.74
	D63	63.2, 0.419	5.9, 39	0.87	
	B70	69.7, 0.461	5.9, 39	…	
J1852	B19	19.0, 0.129	7.2, 49	…	1.21
	D31	30.9, 0.210	22.3, 152	0.01	
	B50	50.0, 0.340	12.3, 84	…	
LkCa 15	D15	14.6, 0.093	51.4, 327	0.02	1.76
	B68	68.2, 0.434	22.9, 146	…	
	D86	86.3, 0.549	12.2, 78	0.76	
	B100	99.5, 0.633	12.7, 81	…	
MWC 758	D32	32.3, 0.193	41.3, 247	0.01	17.00
	B51	50.7, 0.303	11.2, 67	…	
	D64	64.3, 0.384	9.3, 55	0.77	
	B88	87.6, 0.523	22.6, 135	…	
PDS 66	…	…	…	…	0.97
SY Cha	D33	33.3, 0.184	73.9, 409	0.04	1.08

Source	Feature	Radial location (au, arcsec)	Width (au, mas)	Depth	Non-axisymmetry factor
(1)	(2)	(3)	(4)	(5)	(6)
	B101	101.2, 0.560	40.0, 221	...	
V4046 Sgr	D8	7.5, 0.105	7.6, 107	0.01	2.08
	B13	13.1, 0.184	3.4, 47	...	
	D20	20.4, 0.285	10.1, 141	0.01	
	B27	27.2, 0.380	15.4, 216	...	

Column (1): target name. Column (2): annular substructure label. "B" (for *bright*) indicates a ring, while "D" (for *dark*) indicates a gap. The number in the label is the feature distance from the central star measured in au. Column (3): substructure radial location, extracted as explained in Sect. 6.3.1. Column (4): annular substructure width. Column (5): gap depth. Substructure width and gap depth are derived following the criteria of Huang et al. (2018). Column (6): level of non-axisymmetry, measured in the residual image with robust -0.5. This factor is computed as the standard deviation of the residual SNR image within a mask defined by the radius enclosing 95% of the continuum flux density (R_{95}).

6.3.2 Non-axisymmetric substructures

We extracted the non-axisymmetric substructures by computing the residuals between the observed data and the axisymmetric `frank` fit. Initially, we sampled the `frank` model at the same uv-coordinates of the observed data, generating the synthetic visibilities for the fit. Then, we calculated the residual visibilities by subtracting these synthetic visibilities from the corresponding observed ones at each uv-location. We imaged the residual visibilities using the CASA `tclean` algorithm. We present in Figs. 6.5, 6.6, 6.7, 6.8, 6.9, 6.10, 6.11, 6.12 a gallery for each disk displaying the image of the observed data, the `frank` profile swept over 2π, the `frank` model imaged with CLEAN, the non-axisymmetric residuals, and the polar plots of the data and the non-axisymmetric residuals. The residuals are expressed in terms of the observed rms noise, indicating the non-axisymmetry signal-to-noise ratio (SNR). Both the data and the residuals are imaged with robust -0.5, which constituted the best compromise between angular resolution and SNR. The polar plots were computed by deprojecting and then mapping the intensity distribution onto a plot having the radial coordinate as a function of the azimuthal angle. For the azimuthal angle, we adopted the same convention presented in the Appendix A of Huang et al. (2018). Specifically, $\phi = 0°$ corresponds to the direction along the disk semi-minor axis east of north from the disk PA, and the azimuthal angle increases in the clockwise direction.

We quantify the level of non-axisymmetry by evaluating the residual images. We define the "non-axisymmetry factor" as the standard deviation of the residual SNR image within a mask defined by R_{95} and reprojected onto the sky plane with the same geometrical parameters of the disk (see Table 6.2). This value is indicated in Table 6.3 and Fig. 6.13 presents the residual images with same SNR scale in order of increasing non-axisymmetry factor.

The disk geometrical parameters, derived from `galario` and subsequently employed in the `frank` fit, are obtained using a parametric model that assumes fixed values for

inclination, position angle, RA and Dec offsets for each disk. This implies that any misalignment within the disk will manifest in the residuals. As `galario` minimizes the difference between observed and model intensity at each sampled uv-point, the derived geometrical parameters primarily reflect the geometry of the disk region dominating the flux output, namely, the extended disk rather than the inner regions. This is evident in Fig. 6.13, where the most pronounced residuals tend to be concentrated in the inner regions for the majority of sources, leaving larger radii with residuals exhibiting $|\mathrm{SNR}| < 2$ (depicted in white). Notable exceptions include the four highly non-axisymmetric sources HD 143006, CQ Tau, MWC 758, and HD 135344B, which exhibit robust non-axisymmetries throughout their intensity distribution.

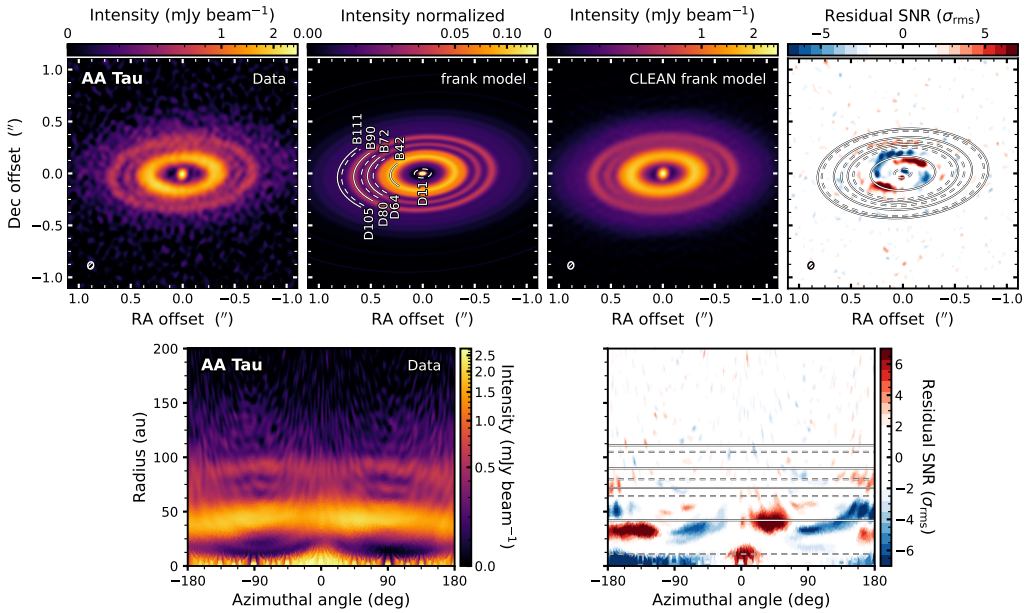

Figure 6.5: Comparison of data, `frank` model, CLEAN imaged `frank` model, residuals and polar plots of the data and the residuals for each disk (here showing AA Tau, continues in Figs. 6.6, 6.7, 6.8, 6.9, 6.10, 6.11, 6.12). (*From left to right, top to bottom*) *First panel*: Observed continuum data obtained with Briggs weighting and robust -0.5. The full width at half maximum (FWHM) of the synthesized beam is indicated by the ellipse in the bottom left corner. An asinh stretch is applied to the color scale to visually enhance the fainter emission. *Second panel*: Image of the frank fit swept over 2π and reprojected. The intensity is normalized and an asinh stretch is applied to the color scale. Each gap is indicated by a dashed arc and a label with the letter "D" (for *dark*) and the distance from the central star in au. Solid arcs and labels with letter "B" (for *bright*) indicate the rings. *Third panel*: `frank` model sampled at the same uv-points of the observation and imaged with CLEAN as the observed data. The color scale is the same as the data panel. *Fourth panel*: Residuals obtained subtracting the `frank model` from the data. The model visibilities were calculated at the same uv-points of the ALMA observations. The residual visibilities were imaged through CLEAN and with robust -0.5. The color scale shows the residuals in units of the observed noise ($\sigma_{\rm rms}$). Rings and gaps are marked with solid and dashed ellipses, respectively. *Fifth panel*: Polar plot of the data continuum image. *Sixth panel*: Polar plot of the non-axisymmetric residuals. The locations of rings and gaps is marked by solid and dashed horizontal lines, respectively.

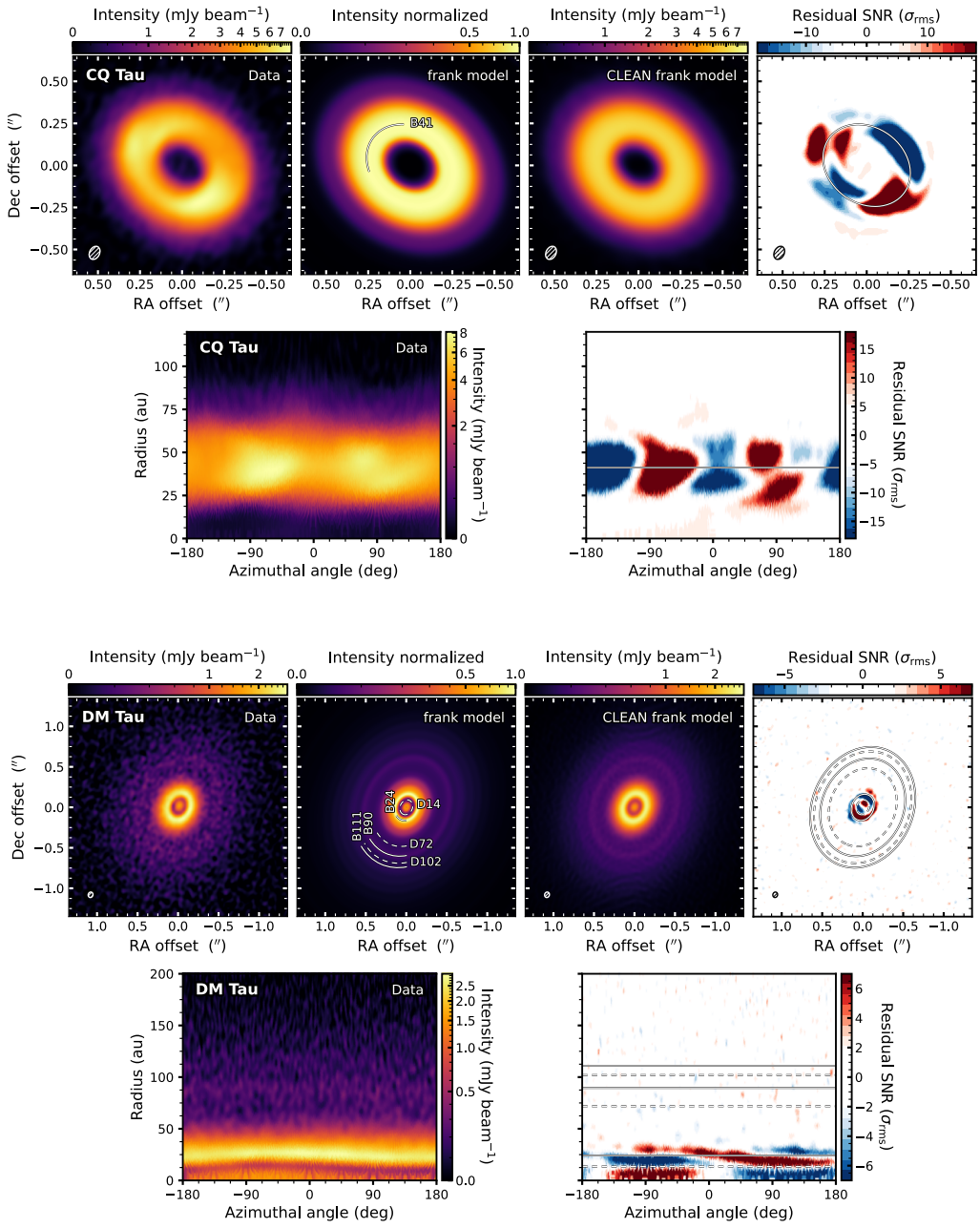

Figure 6.6: As Fig. 6.5 but for CQ Tau and DM Tau.

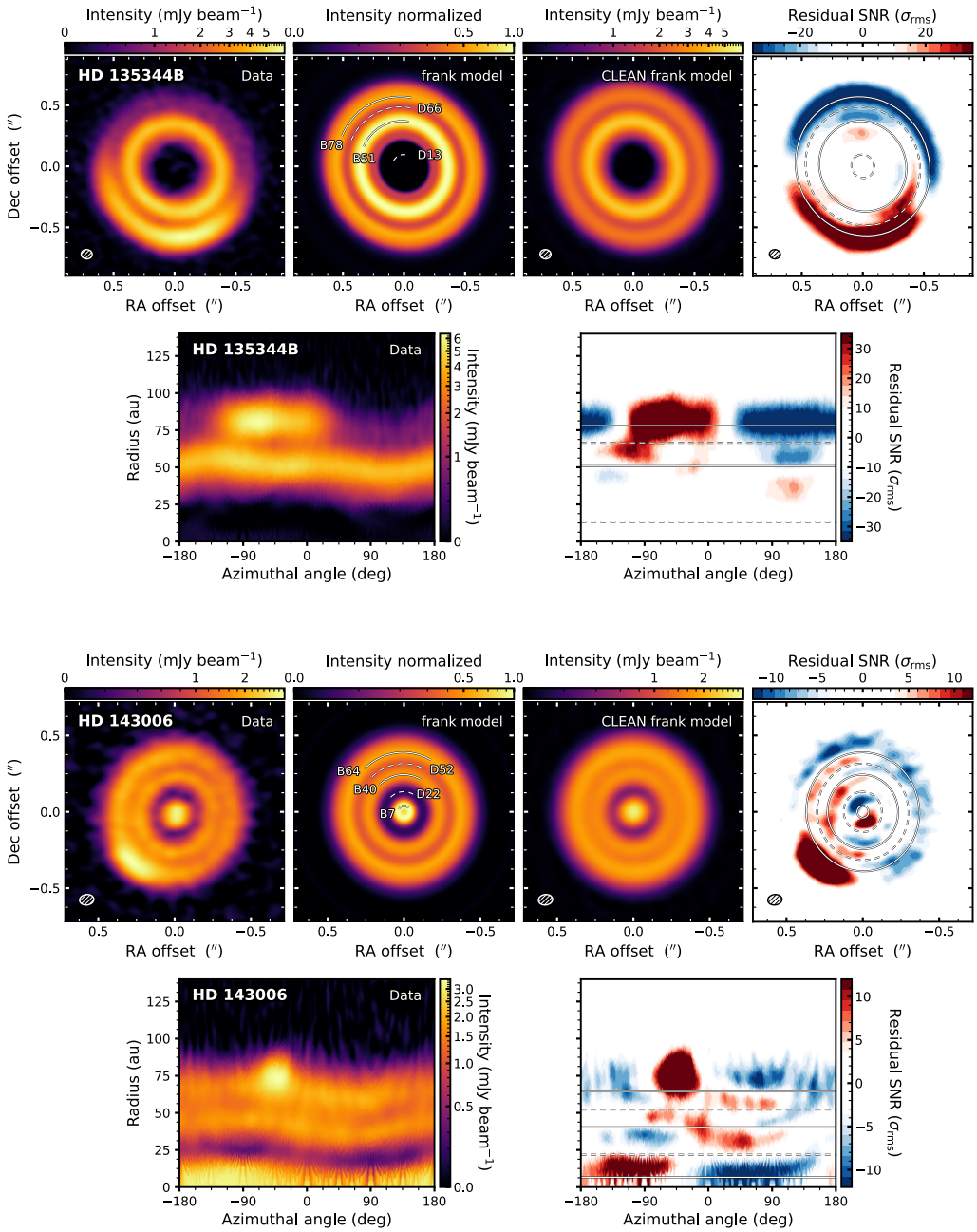

Figure 6.7: As Fig. 6.5 but for HD 135344B and HD 143006.

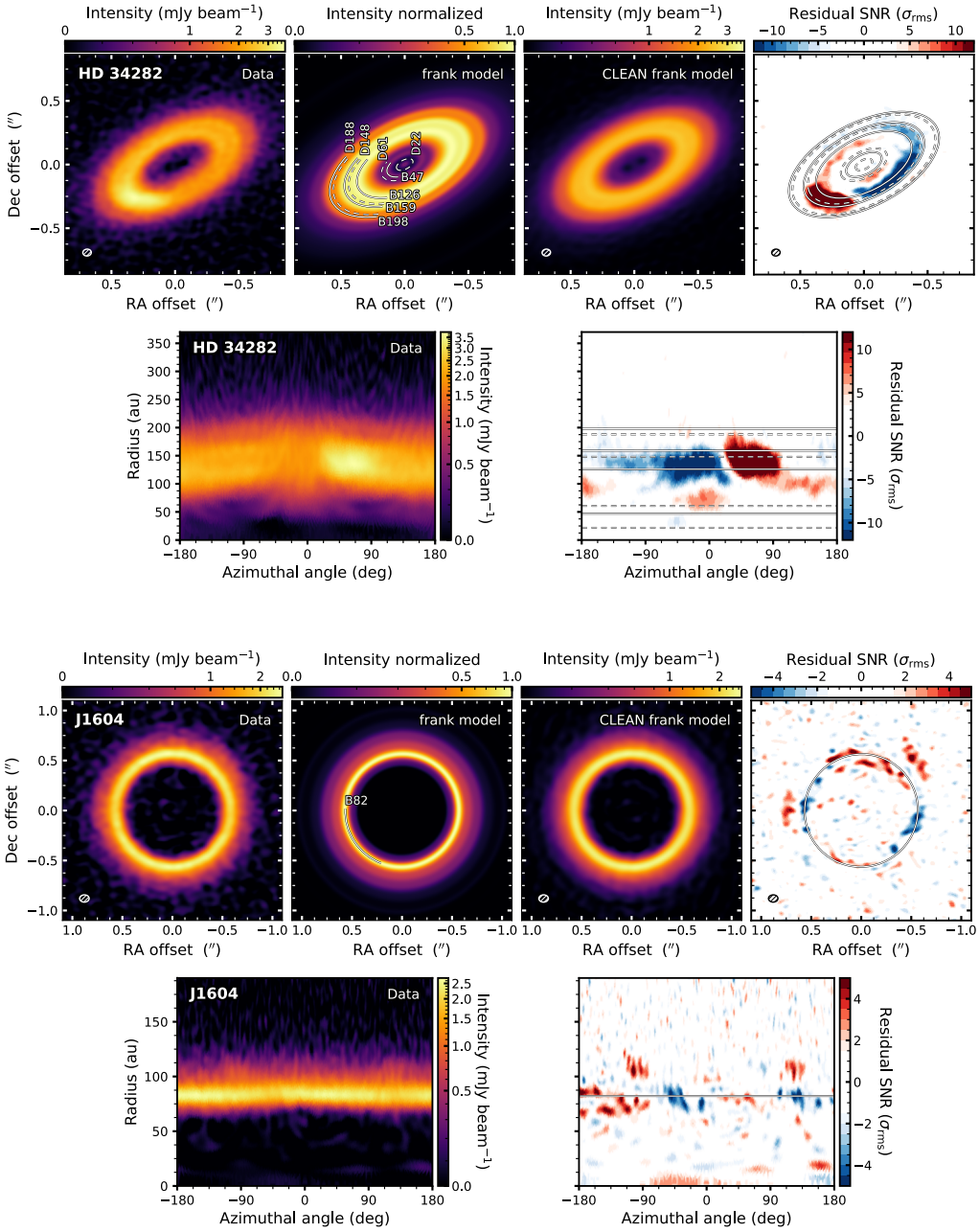

Figure 6.8: As Fig. 6.5 but for HD 34282 and J1604.

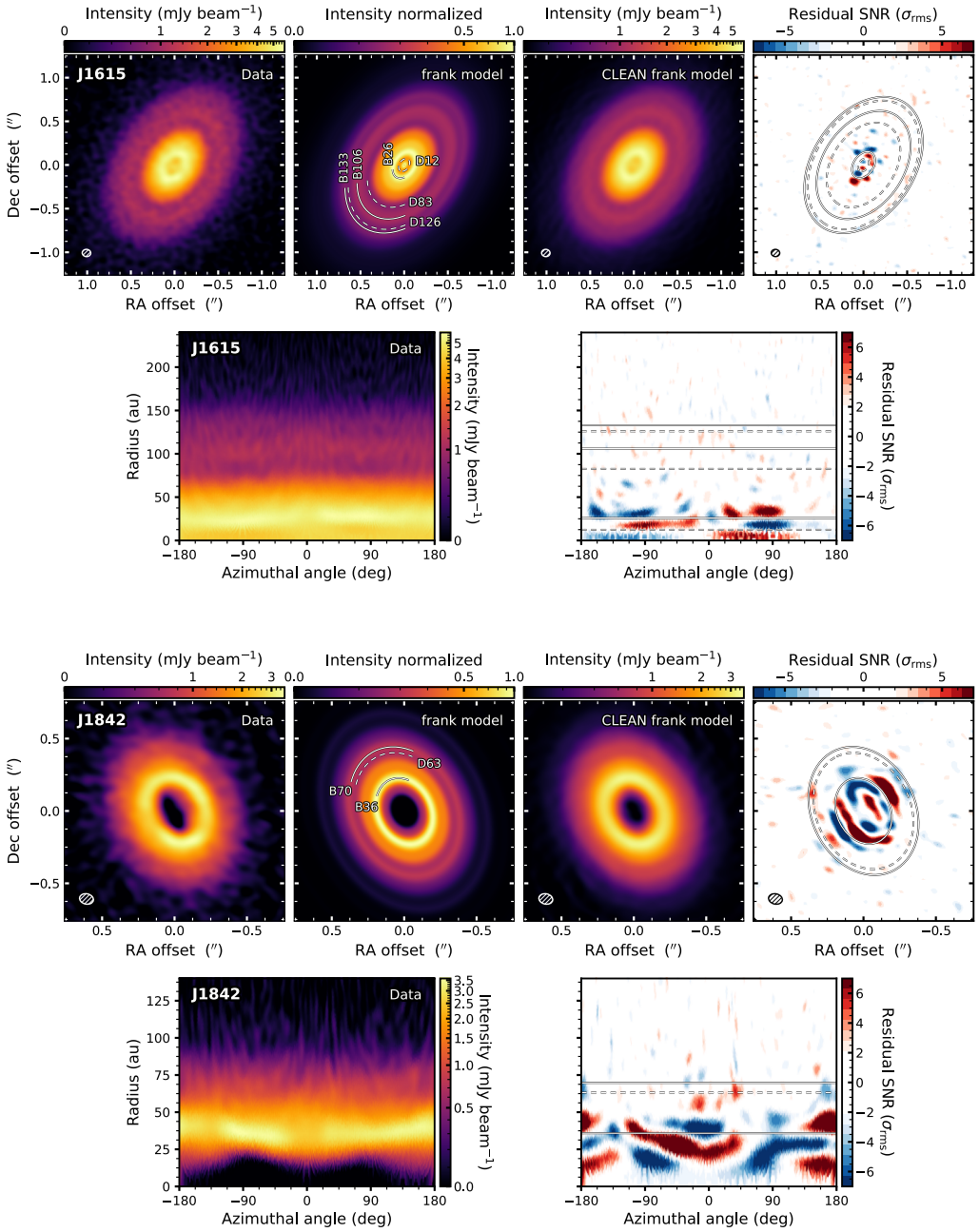

Figure 6.9: As Fig. 6.5 but for J1615 and J1842.

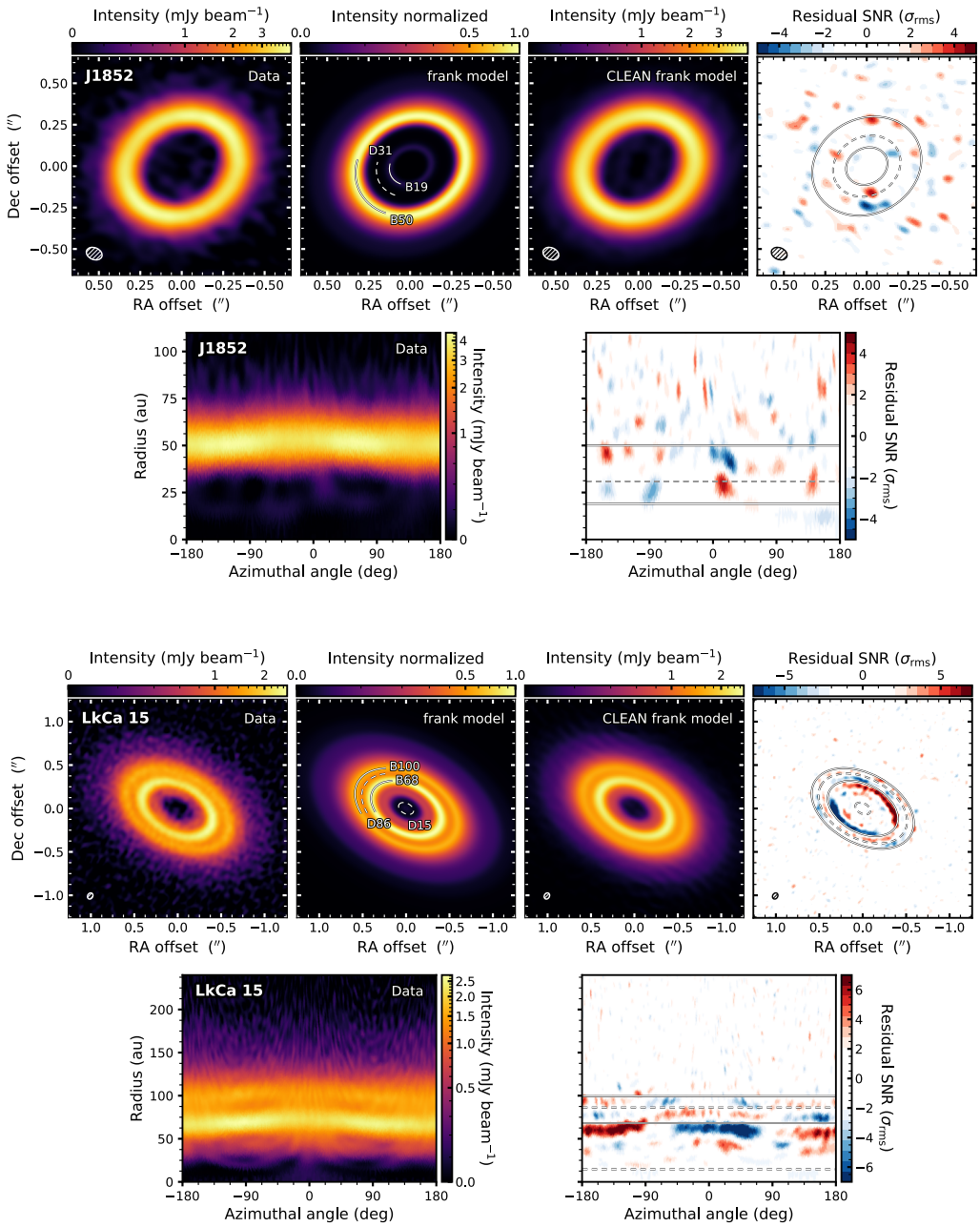

Figure 6.10: As Fig. 6.5 but for J1852 and LkCa 15.

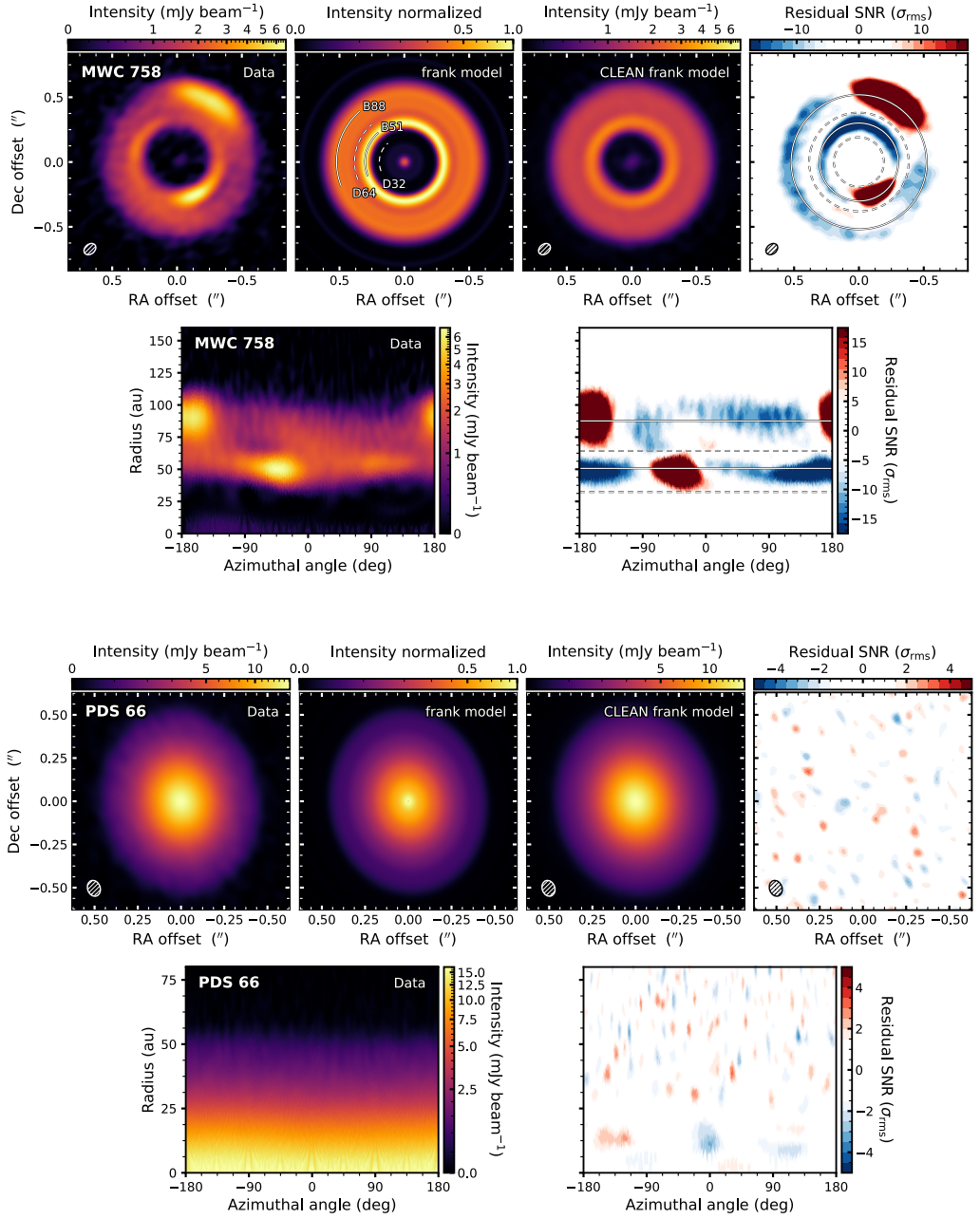

Figure 6.11: As Fig. 6.5 but for MWC 758 and PDS 66.

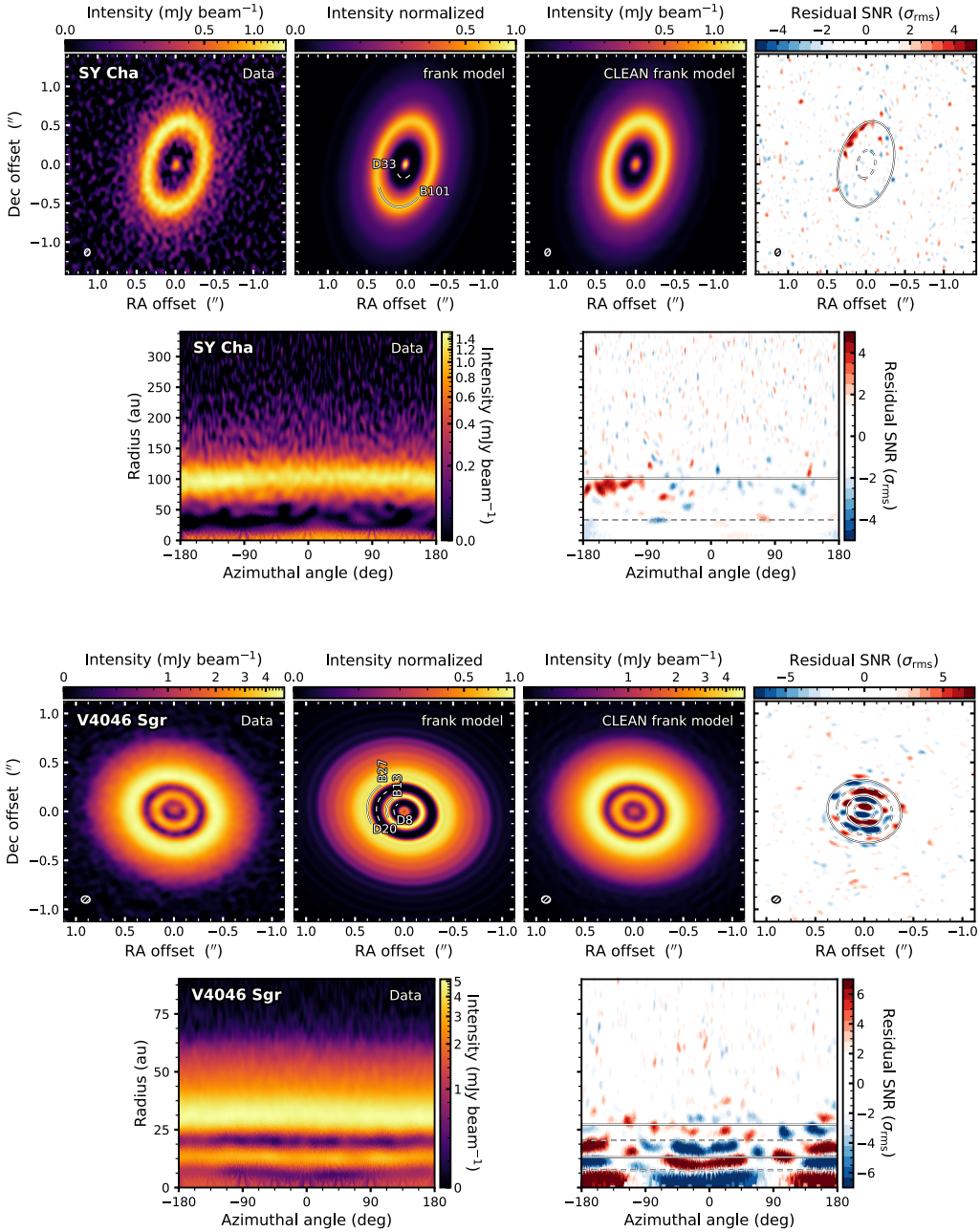

Figure 6.12: As Fig. 6.5 but for SY Cha and V4046 Sgr.

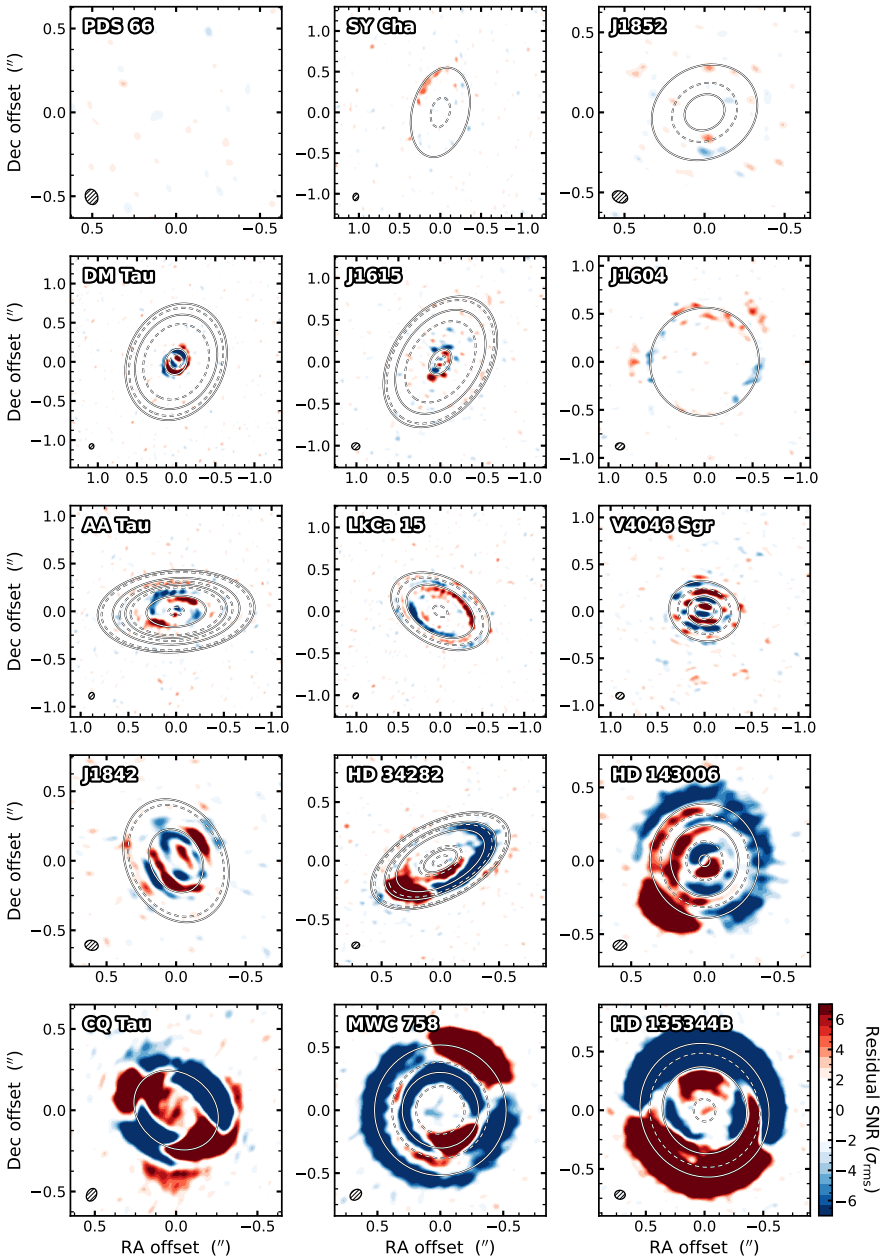

Figure 6.13: Gallery of residuals plot generated subtracting the `frank` model (sampled at the same uv-points of the observations) from the data and then imaged with CLEAN and robust -0.5. The source order is from the least to the most non-axisymmetric, according to the non-axisymmetry factor presented in Sect. 6.3.2 and reported in Table 6.3. The color scale represents the values of residual SNR in units of the observed noise ($\sigma_{\rm rms}$) for the respective observation and the same extremes are applied to each plot. Note that the spatial scales are different for every disk. Rings and gaps are marked with solid and dashed ellipses, respectively, while the synthesized beam is indicated by the ellipse in the lower left corner.

6.4 Discussion

6.4.1 Disk-specific analysis

AA Tau. We discern three distinct pairs of gaps and rings, along with one fainter outer pair (D105-B111). The non-axisymmetric features and shadows observed in the first ring (B42) align with the findings of Loomis et al. (2017), who presented $0.2''$ angular resolution observations. Notably, we detect residuals in the inner disk, possibly indicating a misalignment between the inner disk and the B42 ring. There is no sign of the dust inner streamers proposed by Loomis et al. (2017); however, higher resolution observations are necessary for confirmation. Based on our data and residuals, a plausible explanation involves a misaligned inner disk, casting shadows onto the B42 ring. This results in emission coming from shadowed and geometrically flatter regions, while the brighter areas, receiving more illumination from the central star, exhibit a greater vertical extension.

CQ Tau. Prominent non-axisymmetric features are evident. It should be noted that in these cases, the `frank` model, designed for axisymmetric emission, computes an intermediate intensity between the bright non-axisymmetric structures and the underlying fainter ring emission. This accounts for the pronounced red-blue patterns observed in the residuals. Our data also reveal a a faint inner disk with an integrated intensity of $\sim$200 μJy. This source was previously studied by Ubeira Gabellini et al. (2019) with lower resolution $0.15''$ ALMA 1.3 mm (Band 6) observations, along with hydrodynamical and radiative transfer simulations to explore the possibility of a planet within the cavity. More recently, Hammond et al. (2022) showed prominent spirals in SPHERE scattered light images, aligning with the non-axisymmetries in our images, and proposed the presence of an inner companion responsible for inducing such spirals.

DM Tau. It is characterized by a very extended faint emission, reaching $R_{95} = 245$ au. Strong residuals are only located in correspondence with the inner disk and the B24 ring. They are the result of the observed inner disk and B24 ring being slightly shifted toward the north-west compared to the center of the extended emission. This misalignment becomes particularly evident in the polar plots. The center of our axisymmetric model coincides with the center of the extended emission (as proven by the absence of significant residuals beyond the B24 ring), constituting the bulk of the total emission, hence dominating the `galario` fit. Possible interpretations of the observed residuals involve a misaligned inner disk or eccentricity effects, such as an eccentric companion carving the gap D14. Hashimoto et al. (2021) and Francis et al. (2022) studied DM Tau with $0.035''$ resolution 1.3 mm ALMA data. Interestingly, the outer gap-ring pairs (D72-B90 and D102-B111), recovered by `frank` in our dataset, become more evident their higher angular resolution continuum image.

HD 135344B. It exhibits the highest non-axisymmetry factor in our sample at 25.6 (see Table 6.3). This is caused by the bright arc in the southern region of the disk, contrasting with faint emission in the northern side. The `frank` fit models this structure as full ring (B78), generating strong positive residuals in the southern region and negative residuals in the northern part. The data polar plot indicates a B51 ring that is not precisely horizontal, suggesting the possibility of either a non-circular ring or an imperfectly retrieved inclination. HD 135344B has been extensively explored with ALMA multi-wavelength

observations by Cazzoletti et al. (2018) and high-resolution ($0.03''$) 1.3 mm observation by Casassus et al. (2021). The latter work revealed a tentative detection of a filament connecting the B51 and B78 rings. We identify strong residuals (SNR$>$35) at the same location, specifically, the red residual aligning with the D66 gap in the south-eastern region of the image and at an azimuthal angle of approximately $-110°$ in the residual polar plot.

HD 143006. The continuum emission from this source has been extensively studied as part of the DSHARP large program by Pérez et al. (2018), utilizing $0.046''$ resolution data at 1.3 mm. Even though unresolved in the image and in the intensity radial profile, our `frank` model manages to retrieve the first ring at 7 au, consistent with the radial location of 6 ± 1 au found by Huang et al. (2018). Pérez et al. (2018) derived an inclination of $24.1°$ for the inner disk and $17.0°$ for the outer disk, while our 2D `galario` model includes a single disk inclination retrieved at $18.7°$. Moreover, our residuals do not fully recover the spiral pattern indicated in the work of Andrews et al. (2021).

HD 34282. Our `frank` model identifies an inner faint disk and three gap-ring pairs, which were not resolved in the observations presented by van der Plas et al. (2017). The relevant non-axisymmetric feature on the south-east of the disk generates then the negative residuals, as a counterpart due to the axisymmetric nature of the `frank` fit.

J1604. We detect the presence of the shadows on the east and west side of the B82 ring that were previously identified by Stadler et al. (2023) with $0.02''$ angular resolution 1.3 mm ALMA observation. The high sensitivity of our data also allows to reveal, in both the data and the `frank` model intensity radial profiles, the presence of a new external pair of gap and ring, situated beyond R_{95} and therefore not included in our classification of annular substructures. The gap is located at 139.5 au ($0.965''$) and the ring at 148.1 au ($1.024''$). The external ring has a peak SNR of $\sim$14.

J1615. Similarly to DM Tau, this source presents the inner disk and the first B26 ring slightly shifted to the south-east from the center of the outer disk, producing the visible residuals. Lower resolution data of J1615 were presented in van der Marel et al. (2015), but with our observation we can resolve a total of three pairs of gaps and rings.

J1842. This disk exhibits two shadows within the emission of the B36 ring (particularly evident in the image with the linear stretch in Fig. 6.2) and shows clear signs of an elevated dust emission surface. In particular, the emission just inside the B36 ring on the west side of the cavity appears to originate from the inner edge of a vertically extended cavity wall. Moreover, the residual pattern, with alternating red and blue residuals along the minor axis, is consistent with the expected residuals obtained applying a flat model (as `frank` does) to an elevated emission surface, as illustrated in Appendix A of Andrews et al. (2021). In addition to the gap-ring pair D63-B70, the `frank` model retrieves another pair beyond R_{90}. The gap is estimated to be at 98.1 au ($0.650''$) and the ring at 105.6 au ($0.700''$). Differently from J1604, in this case, the substructures are visible only in the `frank` profile and not in the azimuthally averaged profile of the CLEAN image. Therefore, we exercise caution regarding the presence of this particular gap-ring pair.

J1852. The source is composed by the ring B50 and then both the azimuthally averaged CLEAN intensity radial profile and the `frank` model resolve the faint inner ring B19 inside the cavity. Notably, this inner ring was predicted by Villenave et al.

(2019), who performed a radiative transfer model to match SPHERE data, SED and low-resolution ALMA data for this disk. Their model produced a prediction for an ALMA image before convolution presenting a faint inner ring, suggesting also a possible composition of small dust grain with low millimeter opacity. In addition to the faint inner ring, an intriguing feature emerges both in the image data and in the residuals, located at the gap D31 on the southern side of the disk. The feature has a significance of $\sim 5\sigma$ and is situated adjacent to a negative residual with the same significance, tracing a small region where the observed B50 ring emission contracts compared to the `frank` model. Future higher-resolution observations are required to inspect the nature of this feature and determine whether it is genuine or an artifact.

LkCa 15. We recover with a significance of 3-4σ the residuals around the Lagrangian points previously studied by Long et al. (2022) using $\sim 0.05''$ resolution images at 0.9 and 1.3 mm. We also identify pronounced residuals along the minor axis, resembling the residuals presented in Facchini et al. (2020). This could be indicative of an elevated dust emission surface. Moreover, both the azimuthally averaged CLEAN intensity radial profile and the `frank` model present a shoulder in the extended emission at ~ 170 au.

MWC 58. It has the second-highest value of the non-axisymmetric factor, i.e., 17. The `frank` model identifies an inner disk and then two gap-ring pairs. This disk has been extensively studied, e.g., by Dong et al. (2018) with $0.04''$ resolution ALMA observations at 0.9 mm. Their work indicates that the spirals observed in near-infrared scattered light (Benisty et al. 2015) align with the continuum asymmetries.

PDS 66. This source stands out in the exoALMA sample as the only one that does not exhibit substructures in the continuum emission. All residuals show a significance of less than 4σ. `frank`, however, only identifies a subtle change in slope in the intensity radial profile at 45 au. Recently, PDS 66 has been analyzed by Ribas et al. (2023) with multiwavelength ALMA observations. Their 1.3 mm observations at $0.05''$ resolution also reveal a smooth disk. Our measured R_{68} and R_{90} align perfectly with the estimates made by Ribas et al. (2023) using data at 1.3 and 2.2mm, indicating a consistent dust continuum extent between 0.9 and 2.2 mm observing wavelengths. This provides additional evidence for optically thick emission at these wavelengths

SY Cha. Our data identify an inner disk in the middle of a cavity surrounded by the B101 ring and an extended fainter emission reaching a R_{95} of 228.1 au. The B101 ring shows a non-axisymmetric feature on its the northern side. This structure reflects what was observed by Orihara et al. (2023) using ALMA observation at 1.3 mm at $0.04''$ resolution.

V4046 Sgr. This disk exhibits both an inner disk and the first B13 ring shifted to the north relative to the center of the outer disk, akin to the cases of DM Tau and J1615. This causes the alternating red-blue residuals, evident also in the residual polar plot. This system hosts a tight binary system with a 2.4 day period (Rosenfeld et al. 2012). A possible explanation of the observed morphology might be a misalignment of the inner binary, causing the formation of two dust rings as proposed by Aly & Lodato (2020); Longarini et al. (2021). However, this is challenging given the system's tight binary configuration. Another hypothesis could involve a misaligned planet within the gap. Higher resolution observations at 1.3mm, as presented by Martinez-Brunner et al. (2022)

and Weber et al. (2022), reveal similar structures, although the misalignment of the inner disk is less pronounced.

6.4.2 Search for trends between non-axisymmetries and properties of disks and stars

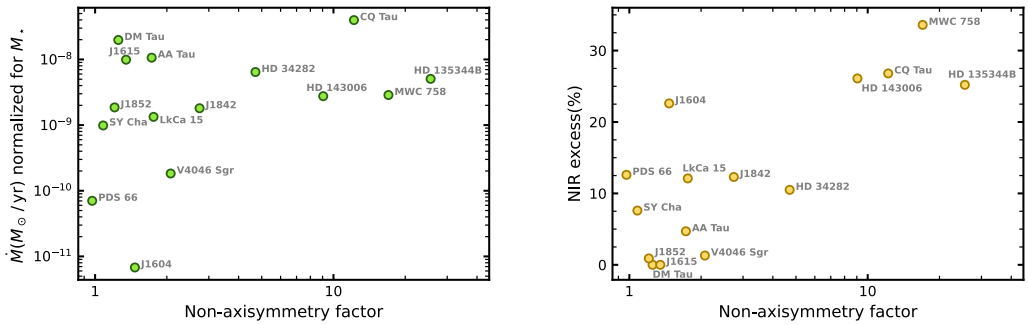

Figure 6.14: Search for correlations of the non-axisymmetry factor with the accretion rate and the near-infrared excess. *Left plot*: Log-log plot of the mass accretion rate (from Manara et al. 2022), normalized for the correlation with the stellar mass assuming $\dot{M} \propto M_\star^{1.8}$, (Manara et al. 2022), as a function of the non-axisymmetric factor, that is, the standard deviation of the residual SNR within R_{95} (see Sect. 6.3.2). *Right panel*: near-infrared excess (from Garufi et al. 2018) vs the non-axisymmetry factor in a linear-log scale.

The definition of the non-axisymmetry factor (see Sect. 6.3.2) is valuable for quantifying the morphological characteristics of each disk and investigating potential patterns with other disk and stellar properties The left plot of Fig 6.14 presents the mass accretion rate (from Manara et al. 2022) vs the non-axisymmetry factor. It is well known that the mass accretion rate $\dot{M}$ scales with the stellar mass $M_\star$ with a steeper-than-linear relation $\dot{M} \propto M_\star^\gamma$ with $\gamma \sim 1.6 - 2$ (Manara et al. 2022). To homogeneously compare the mass accretion rates across the 15 disks in our sample, we normalized the mass accretion rate for its dependence on the stellar mass by considering $\dot{M}/M_\star^{1.8}$, assuming $\gamma = 1.8$. This value is plotted on the y-axis of the left panel in Fig 6.14. On the other hand, the right plot shows the measured near-infrared (NIR) excess of each disk (taken from Garufi et al. 2018) against the corresponding non-axisymmetric factor. Even though a clear correlation is difficult to establish, both plots clearly show that the most asymmetric sources also exhibit the highest values of both the accretion rate and the NIR excess. Garufi et al. (2018) analyzed a substantial NIR dataset on protoplanetary disks, concluding that the presence of spirals and shadows is associated with a high NIR excess. Our results align with their findings, as NIR spirals often coincide with strong non-axisymmetric features in the millimeter dust continuum emission. A plausible explanation involves a perturber generating the NIR spirals, such as a stellar or planetary companion within the observed cavities in our most asymmetric sources, potentially triggering higher mass accretion onto the central star.

Part III

The influence of inner planets on compact protoplanetary disks

CHAPTER 7

Compact protoplanetary disks

7.1 The typical protoplanetary disk is compact

As previously discussed in Chapter 1 and demonstrated by the findings presented in Chapter 6, recent high-resolution ALMA observations have unveiled various protoplanetary disks exhibiting substructures in their dust continuum emission, such as gaps, rings, cavities, and non-axisymmetric features (e.g., ALMA Partnership et al. 2015; Andrews et al. 2018a; Long et al. 2018; Andrews 2020). However, these cases are not representative of the entire population of disks, because they contemplate only the brightest and most extended sources, whereas the average protoplanetary disk is compact and fainter. This pattern has been consistently highlighted by several complete surveys in different star-forming regions. For instance, Ansdell et al. (2016, 2018) conducted a survey involving 95 disks in the Lupus star-forming region, achieving a resolution of approximately $0.2''$ ($30\,\mathrm{au}$) and resolving the dust disks in 22 cases (see Fig. 7.1). Similarly, Long et al. (2019) observed a sample of 32 disks in Taurus, covering the full range of disk types for solar-mass stars, without any bias related to specific disk properties, achieving a high resolution of $\sim 0.12''$ ($\sim 16\,\mathrm{au}$). Among their findings, they identified 20 disks with a radius enclosing 95% of the flux ($R_{95\%}$) smaller than $50\,\mathrm{au}$. Additionally, Cieza et al. (2019b) observed 147 targets in ρ-Ophiuchi at $\sim 0.2''$ ($\sim 30\,\mathrm{au}$), successfully resolving 60 of them. Exploring more distant star-forming regions, Ansdell et al. (2017) directed their attention to σOrionis, examining 92 disks, while van Terwisga et al. (2020) conducted observations of 179 disks in the NGC 2024 cluster. Both studies utilized an angular resolution of $\sim 0.25''$ ($\sim 100\,\mathrm{au}$), resolving only few disks. From all these evidences, we can conclude that the majority of protoplanetary disks seem to have a dust radius of a few tens of au in radius, at least in the (sub)-millimeter dust, as also corroborated by the works of Tazzari et al. (2017) and Barenfeld et al. (2017).

7.2 Observational challenge

Despite constituting the majority of the population, compact disks have not enjoyed a central position in the observational spotlight, primarily due to the inherent challenges in their detection and characterization. One significant obstacle arises from the size-millimeter flux relation established by Andrews et al. (2018b) (Fig. 7.2. This relation

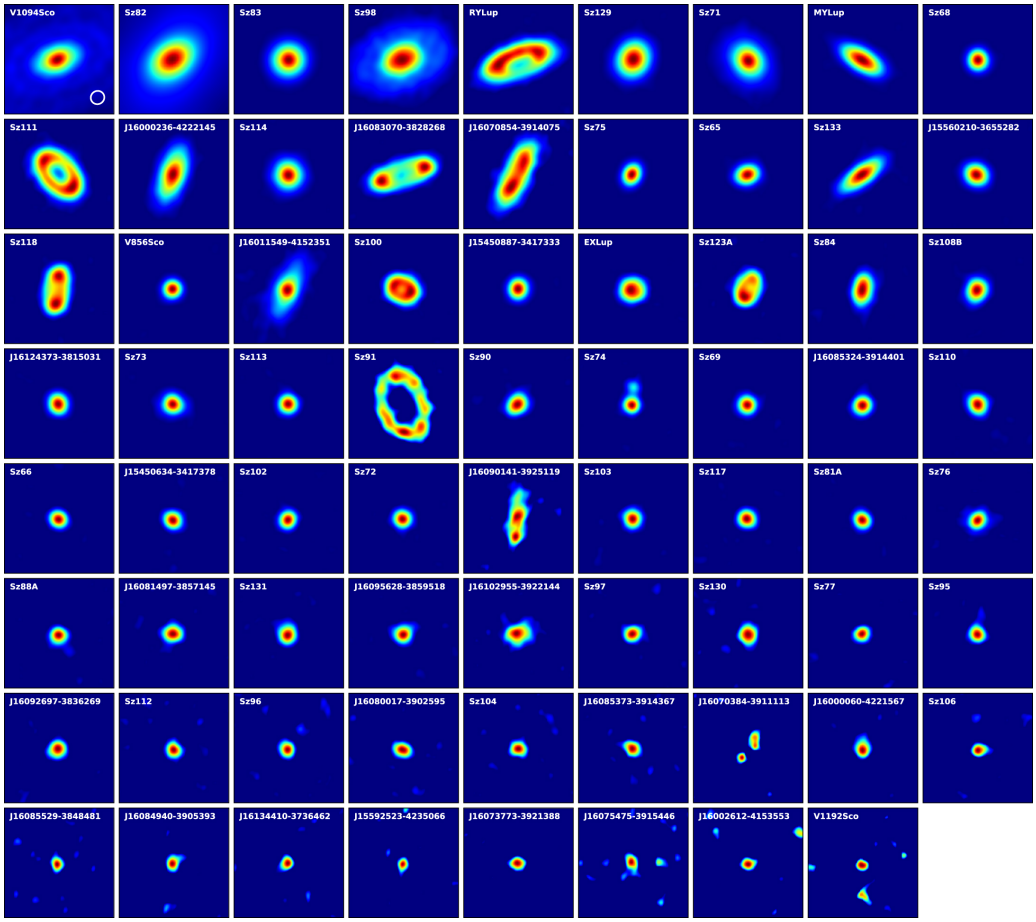

Figure 7.1: Continuum images of the 71 Lupus disks detected in the ALMA $1.3\,\mathrm{cm}$ survey by Ansdell et al. (2018), arranged in descending order of flux density. The images have sizes of $2'' \times 2''$, and the typical beam size is illustrated in the first panel. Each image is normalized, with the maximum set to the peak flux and the minimum clipped at twice the image rms.

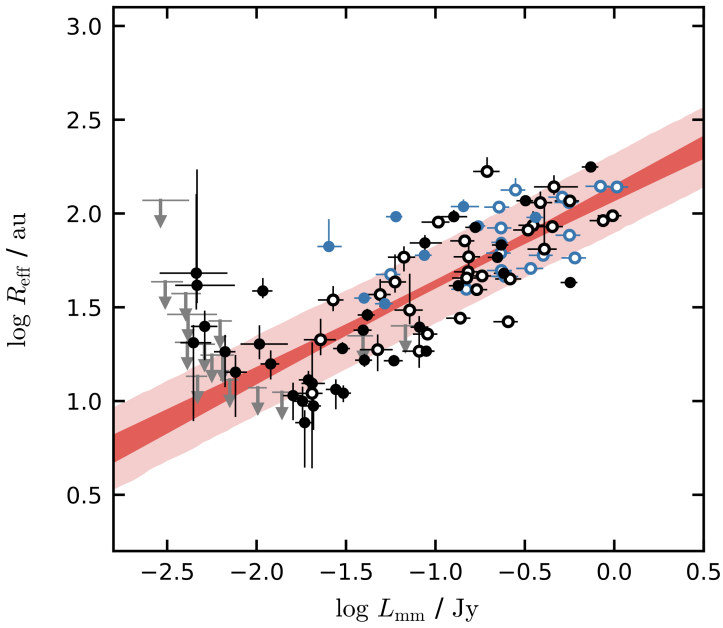

Figure 7.2: Relationship between millimeter continuum size and flux density from Andrews et al. (2018b). Black markers indicate two separate samples, while blue markers represent transition disks. Error bars indicate the 68% confidence intervals, while upper limits (at 95% confidence) are denoted by gray arrows. The dark shaded region represents the 68% confidence interval based on the scaling relation derived from their linear regression analysis on the combined sample. The lighter shaded region reflects the same trend, incorporating an additional scatter term.

underscores that compact disks, characterized by their smaller sizes, exhibit lower flux compared to their larger counterparts. Consequently, the diminished luminosity of these disks poses a substantial challenge for observational studies. The lower flux levels demand significantly increased integration times to achieve the resolution necessary for identifying potential substructures within these compact disks. Specifically, Andrews et al. (2018b) obtained the following relation between observed millimeter flux $F_{\rm mm}$ and dust radius $R_{\rm mm}$: $F_{\rm mm} \propto R_{\rm mm}^2$. Examining the correlation between observed noise ΔF_ν and observing time τ in interferometric observations, characterized by $\Delta F_\nu \propto 1/\sqrt{\tau}$, suggests that, when considered as an order of magnitude estimate, an integration time 16 times longer would be needed to reach an equivalent level of resolution for a protoplanetary disk with half the dust size.

7.3 The need for a dust trapping mechanism

As discussed in Section 2.2.3, radial drift is an exceptionally rapid process that, under normal circumstances, would result in all the dust within the disk falling onto the central star within a remarkably short time of only $10^3, \mathrm{yr}$. As previously mentioned, one effective mechanism to counteract this phenomenon is the presence of a dust trap, a

feature that has been well-documented in extended disks through ALMA observations, revealing numerous disks with gaps and rings. Nevertheless, some form of trapping must also be occurring in all compact disks; otherwise, their observation would not be feasible after a few Myr. This conclusion is supported by the findings of Toci et al. (2021). They consider the ratio between the dust and gas radii, denoted as $R_{\mathrm{CO}}/R_{\mathrm{dust}}$. Their approach involves modeling the temporal evolution of protoplanetary disks, considering the influence of factors such as viscous evolution, grain growth, and radial drift. Utilizing radiative transfer simulations, they calculate the dust and gas radii for their models, studying the evolution of $R_{\mathrm{CO}}/R_{\mathrm{dust}}$. The key result from their analysis is that, across a diverse range of disk mass, initial radius, and viscosity values, $R_{\mathrm{CO}}/R_{\mathrm{dust}}$ rapidly attains large values (> 5) within a short timeframe ($< 1\,\mathrm{Myr}$) due to radial drift. This contrasts with measurements in young star-forming regions like Lupus, with an average $R_{\mathrm{CO}}/R_{\mathrm{dust}} \approx 2.5$ (e.g., Sanchis et al. 2021). This suggests that dust radial drift is too efficient in their models. Therefore, Toci et al. (2021) propose that the most likely hypothesis is that undetected substructures must be present in most (if not all) the observed disks.

Jennings et al. (2022b) demonstrated the capability of the `frank` code (Jennings et al. 2020, see Sect. 6.2.2) to discern substructures in three compact disks with radii less than $50\,\mathrm{au}$. These disks were part of the survey conducted by Long et al. (2019), and interestingly, no substructures were evident in the CLEAN image or azimuthally averaged radial intensity profile. Additionally, their analysis extended across both compact and extended sources, revealing indications of unresolved substructures at small radii ($< 30\,\mathrm{au}$).

As we discussed, the most likely reason for the persistence of compact disks over a few Myr of evolution is the existence of pressure traps within the first tens of au. Moreover, these substructures must be long-lived rather than transient. What could give rise to these substructures? A plausible explanation involves the presence of an inner planet situated within the first tens of au, massive enough to create a pressure bump and halt radial drift. Intriguingly, this scenario aligns more closely with the structure of the Solar System, considering that Jupiter is approximately $5\,\mathrm{au}$ away from the Sun. In conclusion, despite the observational challenges, it is imperative to delve deeper into the study of compact disks to comprehensively understand the physical mechanisms governing typical protoplanetary disks. This endeavor may offer valuable insights into the formation processes of our own Solar System.

CHAPTER 8

Multiwavelength analysis of the compact disk CX Tau

*This chapter is based on the paper "Radio multiwavelength analysis of the compact disk CX Tau: Presence of strong free-free variability or anomalous microwave emission" by **Pietro Curone**, Leonardo Testi, Enrique Macías, Marco Tazzari, Stefano Facchini, Jonathan P. Williams, Cathie J. Clarke, Antonella Natta, Giovanni Rosotti, Claudia Toci, and Giuseppe Lodato, published on Astronomy and Astrophysics in September 2023, 677, A118.*

Protoplanetary disks are complex systems consisting of gas, dust, and ionized particles surrounding young stars, and they emit radiation over a wide range of wavelengths from radio to X-rays. A multiwavelength approach therefore becomes crucial to understanding the physical mechanisms occurring in disks and explain how they evolve and possibly go on to form planets.

In the last few decades, observations in the submillimeter to centimeter wavelength range revealed different emission mechanisms by analyzing their spectral flux density distributions (e.g., Rodmann et al. 2006; Ricci et al. 2010; Pascucci et al. 2014; Sheehan et al. 2016; Coutens et al. 2019). Within this particular context, a powerful diagnostic that is able to disentangle the various physical origins of the emission is the spectral index, $\alpha = \log_{10}[F_{\nu_1}/F_{\nu_2}] \ / \ \log_{10}[\nu_1/\nu_2]$, where F_{ν_1} and F_{ν_2} are the flux densities measured in the observing wavelengths, ν_1 and ν_2, respectively. We summarize the most common cases in Fig. 8.1, based on the dominant physical mechanism of emission. The first category (panel a) consists of disks in which the thermal emission from dust dominates at all wavelengths. Assuming optically thin emission and Rayleigh-Jeans approximation, dust emission follows a spectral index of $\alpha{\sim}2 + \beta$, where $0 \lesssim \beta \lesssim 2$ is the dust opacity spectral index and depends on the maximum grain size (see, e.g., Draine 2006; Ricci et al. 2010; Testi et al. 2014; Tazzari et al. 2021). The second category (panel b) includes disks in which dust emission dominates down to a wavelength of a few millimeters, followed by a change in the spectral index due to the contribution of free-free emission at longer wavelengths. Free-free emission originates through the interaction of free electrons with ions in the ionized gas present in the innermost regions of disks or in jets and its spectral index can range from -0.1 to 2.0 in the case of a totally optically thin or optically thick emission, respectively (Ubach et al. 2017). A typical value is $\alpha{\sim}0.6$, as predicted by the theoretical models of an expanding partially optically thick spherical wind (Panagia &

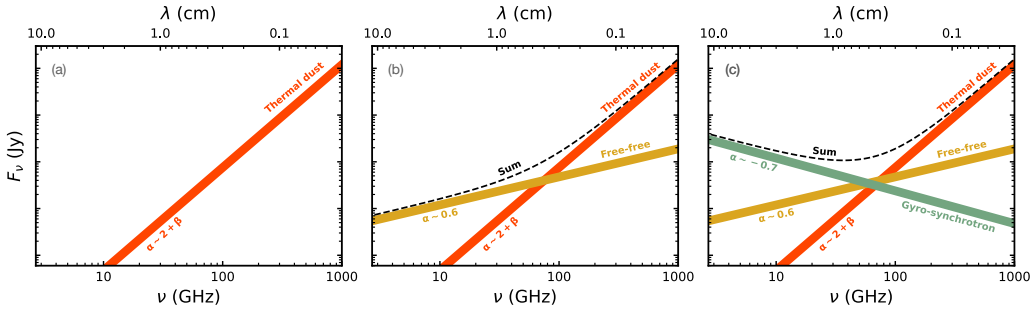

Figure 8.1: Illustrative plot for the main components in the continuum emission of a typical protoplanetary disk in the wavelength range between the submillimeter to the centimeter. The three panels are described in the main text.

Felli 1975) or a collimated conical jet (Reynolds 1986). Photoevaporative winds can also produce optically thin free-free emission with a spectral index of ~ -0.1 (Pascucci et al. 2012), and both jet and wind could coexist (e.g., Macías et al. 2016). Finally, the third category (panel c) includes disks in which a gyro-synchrotron outburst is occurring and dominates at centimeter wavelengths. This non-thermal emission arises from the interaction of electrons with the stellar magnetosphere. Its spectral index depends on the electron energy distribution and it is generally negative with a typical value of $\alpha \sim -0.7$ (Condon & Ransom 2016).

The advantages of detailed multiwavelength analysis to study single protoplanetary disks have been explored in a few recent papers (Carrasco-González et al. 2019 for HL Tau, Macías et al. 2021 for TW Hya, and Guidi et al. 2022 for HD 163296). In this work, we focus on CX Tau. It is a M2.5 star (Luhman 2018) located at a distance from the Sun of $126.5 \pm 0.3\,\mathrm{pc}$, as estimated by Bailer-Jones et al. (2021), using Gaia EDR3 (Gaia Collaboration et al. 2021). Simon et al. (2019) measured a dynamical mass of $0.38 \pm 0.02\,M_\odot$ and Andrews et al. (2013) obtained a stellar bolometric luminosity $L_\star = 0.38 \pm 0.05\,L_\odot$ and an effective temperature $T_{\rm eff} = 3475 \pm 130\,\mathrm{K}$. The estimated accretion rate is $7.1 \times 10^{-10}\,M_\odot\ \mathrm{yr}^{-1}$ (Hartmann et al. 1998b). From the infrared excess in the SED, Najita et al. (2007) classified the source as a transitional disk, but the presence of an inner cavity has not been detected with high angular resolution observations by Facchini et al. (2019). CX Tau hosts a compact dust disk and an extended gas disk, with a ratio between the gas and dust radii of 5.4 (Facchini et al. 2019), indicating that the disk evolution is dominated by dust radial drift (Weidenschilling 1977). This is in contrast to the majority of disks that show a ratio between the gas and dust radii of $\sim$2.5, interpreted by invoking planet formation that is halting dust radial drift (Sanchis et al. 2021, Toci et al. 2021).

CX Tau is an excellent candidate for a thorough multiwavelength analysis for two main reasons. First, it represents a typical protoplanetary disk, due to its small size along with a millimeter flux at the 50th percentile of the flux distribution of Class II disks in Taurus. Second, CX Tau has already been observed by the Atacama Large Millimeter/submillimeter Array (ALMA) in Band 6 ($1.3\,\mathrm{mm}$) at a high resolution of 0.04″

(corresponding to $\sim 5\,\mathrm{au}$), and the results are presented in Facchini et al. (2019). At this angular resolution, there is no sign of substructures and the data are consistent with a smooth disk model. The authors estimated a total flux density of $9.75\,\mathrm{mJy}$ and a radius enclosing 68% of the continuum flux density ($R_{68\%}$) equal to $14\,\mathrm{au}$. Moreover, they revealed that the brightness radial profile of CX Tau is consistent with the central regions of the profiles of DSHARP disks that are not in a binary system and do not present an inner cavity. Therefore, CX Tau is not a scaled-down version of more extended disks but differs from the latter only for the lack of rings at large radii.

In this work, we present observations from the Karl G. Jansky Very Large Array (VLA) of CX Tau in Ka ($9.0\,\mathrm{mm}$), K ($1.3\,\mathrm{cm}$), Ku ($2.0\,\mathrm{cm}$), and C ($6.0\,\mathrm{cm}$) bands. Combining these observations with archival data from ALMA in Band 7 ($0.9\,\mathrm{mm}$) and with values from the literature in the (sub)millimeter, we obtained a multiwavelength view of CX Tau. This work is organized as follows. Section 8.1 presents the observations and the procedures we used to reduce and calibrate them, Sect. 8.2 describes the analysis and the obtained results, and Sect. 8.3 discusses these findings in light of multiwavelength analyses in general.

8.1 Observations and data reduction

CX Tau was observed with VLA in the Ka band in B configuration (maximum baseline of $11.1\,\mathrm{km}$) on 12 October 2020 (VLA Project 20A-373, PI: M. Tazzari) with an on-source integration time of 1.6 hours. The spectral windows covered the range between 29 and 37 GHz (corresponding to wavelengths of $8.1 - 10.3\,\mathrm{mm}$). During the observation, 3C147 was used as bandpass and absolute flux calibrator, J0403+2600 as the pointing calibrator, and J0438+3004 as complex gain (amplitude and phase) calibrator.

Under the same VLA project, CX Tau was observed in the Ku band in C configuration (maximum baseline of $3.4\,\mathrm{km}$) on 2 and 4 March 2020 for a total on-source integration time of 24 minutes. The bandwidth extended from 12 to $18\,\mathrm{GHz}$ (wavelengths between 1.7 and $2.5\,\mathrm{cm}$). The flux and band calibrator was 3C147, the complex gain calibrator was J0431+2037, and both sources were used to calibrate the pointing.

For the C band, we have observations from two different VLA projects. Under project 20A-373, observations were performed in C configuration on 20 February 2020 with a total time on-source of 15 minutes. The wavelength coverage was from 4 to $8\,\mathrm{GHz}$ ($3.7 - 7.5\,\mathrm{cm}$). For the calibration, the same sources as for the Ku band data were used. Then, CX Tau was observed again in the C band but with an A configuration (maximum baseline of $36.4\,\mathrm{km}$) between 9 and 11 January 2021, for a total integration time of 3.8 hours (VLA Project 20B-299, PI: M. Tazzari). Here, 3C147 was used as bandpass and flux calibrator and J0403+2600 as complex gain calibrator.

Observations in the K band were performed more recently, on 9 April 2022 (VLA Project 22A-401, PI: M. Tazzari). The integration time was 15 minutes and the spectral windows ranged from 18.4 to $26.2\,\mathrm{GHz}$ (wavelengths from 1.1 to $1.6\,\mathrm{cm}$). 3C147 was employed for the calibration of pointing, bandpass, and flux, while J0403+2600 was the complex gain calibrator.

First, all these observations were calibrated by the VLA pipeline. Then, we per-

formed the self-calibration using the software CASA, version 6.2 (CASA Team et al. 2022). We executed a spectral average on each dataset taking into account the requirements to avoid bandwidth smearing[1], but did not employ time averaging during the self-calibration. For the imaging, we employed Briggs weighting with robust 1 as the best compromise between signal-to-noise ratio (SNR) and side lobes effects, and the mtmfs deconvolver to properly take into account the relevant bandwidth over observing frequency ratio in VLA data. We performed one round of phase-only self-calibration for the observations in the Ka and Ku bands obtaining improvements in the peak SNR by a factor of 2.3 and 2.9, respectively. For the C-band observation, we kept the observations from the two different configurations separate. In both cases, we executed one round of phase self-calibration always taking as a reference the flux density from the other sources in the field of view, given the lack of a detection for CX Tau emission at this wavelength. We obtained a modest $\sim$10% increase in the SNR. We placed a particular emphasis on the treatment of the K-band data, carefully checking the calibration executed with the VLA pipeline and performing four rounds of phase-only self-calibration which highly improved the peak SNR by a factor of 7.8 (see next Sect. 8.1.1 for details).

In addition to these VLA observations, we also reduced and calibrated the ALMA archival data in Band 7 (0.9 mm) from the project 2013.1.00426.S (PI: Yann Boehler) presented in Simon et al. (2017). We performed four rounds of phase-only self-calibration, for an improvement in the peak SNR of 20%.

8.1.1 Checks and treatment of the 1.3 cm VLA data

To address the unexpectedly high value of the 1.3 cm VLA data, we present evidence in this section to validate the data collection process and the self-calibration. We carefully examine the gain calibrator J0403+2600 to eliminate the possibility of an incorrect flux transfer that may have influenced the measurement of CX Tau's flux. The left panel of Fig. 8.2 presents the image of J0403+2600 from the observation weblog, where nothing seems to be worth of notice. The right panel of Fig. 8.2 shows the time variability of the flux of the calibrator, comparing the flux value measure in the CX Tau's execution block to the flux historical values from the source. During the CX Tau observation, the flux value of J0403+2600 is perfectly in line with the historical values. Therefore, the anomalously high value of the 1.3 cm data cannot be explained with an incorrect flux calibration.

We conducted a meticulous four-step phase-only self-calibration procedure. Prior to self-calibration, the RMS was measured at 9.5 muJy/beam, and the flux density from the CX Tau disk was 70 muJy, resulting in a peak S/N of 5.1. Throughout the self-calibration process, the RMS remained unchanged, while CX Tau's flux density steadily increased. The following are the details of each self-calibration step, along with the parameters used for the gaincal task in CASA:

1. We solved for shifts in polarization only with `gaintype = 'G'`, `combine = 'scan, spw'`, and `minsnr = 3`. As a result, the source flux density increased to 100 muJy.

[1] https://casadocs.readthedocs.io/en/v6.3.0/notebooks/synthesis_imaging.html

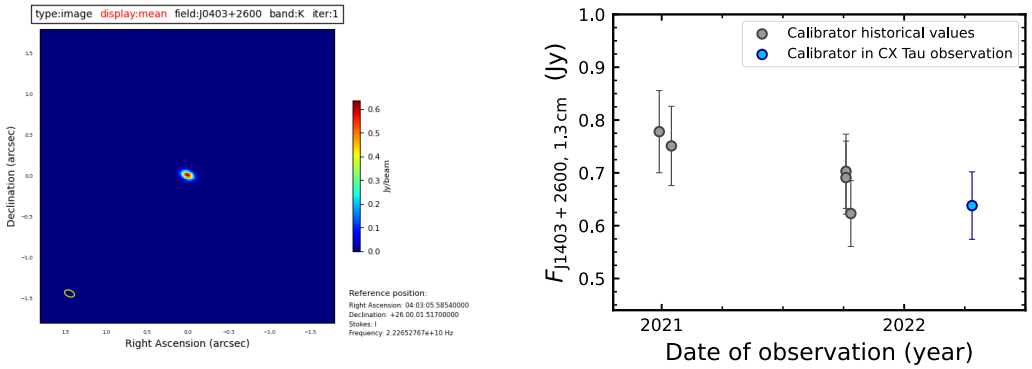

Figure 8.2: Checks on the gain calibrator J0403+2600 during the CX Tau observation at 1.3 cm. *Left panel*: Gain calibrator J0403+2600 image at 1.3 cm (K band) from the weblog of the CX Tau observation at the same wavelength. *Right panel*: Time variability of the 1.3 cm flux density from the gain calibrator J0403+2600.

2. We corrected shifts between spectral windows with `gaintype = 'T'`, `combine = 'scan'`, and `minsnr = 3`. CX Tau's flux density reached 160 muJy.

3. We obtained solutions for both polarization and spectral window shifts with parameters `gaintype = 'G'`, `combine = 'scan'`, `minsnr = 3`. This caused the flux density to rise to 260 muJy.

4. We repeated the same command in the fourth step but with a lower threshold for the S/N of the solutions (`gaintype='G'`, `combine='scan'`, `minsnr=2`).

At the conclusion of the process, the RMS remained consistent at 9.5 muJy/beam, while CX Tau's flux density increased to 420 muJy, resulting in a peak S/N of 40. It is important to notice that such RMS value is in excellent agreement with the theoretical noise predicted by the VLA exposure calculator[2] which is 9.0 muJy/beam. From the self-calibration procedure, we can infer that the increase in flux density, coupled with the unchanged RMS, is a result of phase decoherence that dispersed the flux from the central source throughout the field of view. As CX Tau's flux was not notably high, this effect had minimal impact on the RMS. Consequently, self-calibration successfully gathered and refocused the dispersed flux, leading to an increased integrated flux of the central source.

8.2 Analysis and results

8.2.1 Spectral flux density distribution

Figure 8.3 presents the spectral flux density distribution with all the observations in the submillimeter to centimeter range, including data from VLA, ALMA, the Submillimeter Array (SMA), and the Plateau de Bure Interferometer (PdBI) (Andrews & Williams 2005,

[2] https://obs.vla.nrao.edu/ect/

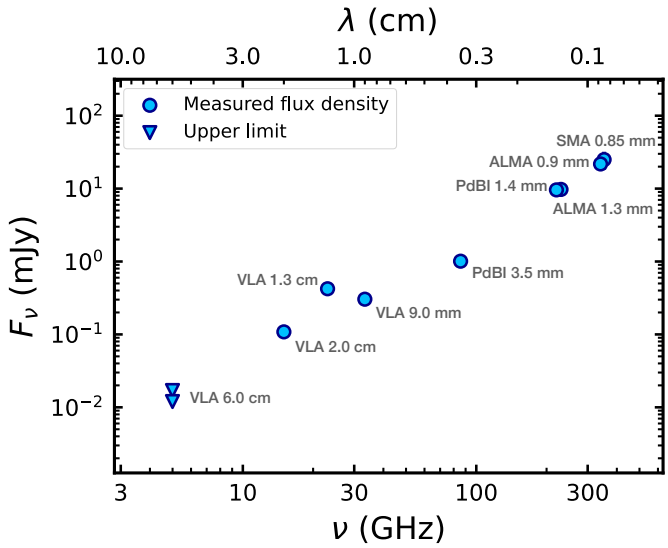

Figure 8.3: Spectral flux density distribution of CX Tau including data in the submillimeter to centimeter range. For each value of the flux density we report the total uncertainty including the statistical and systematic flux calibration errors. In most cases, the error bars fall within the plotted points. Non-detections are indicated by the upper limits, obtained as the flux from a visibility fit of a central point source plus $2 \times \mathrm{RMS}$.

Ricci et al. 2010, Piétu et al. 2014, Simon et al. 2017, Facchini et al. 2019). Figure 8.4 shows the images from the ALMA and VLA observations of CX Tau, along with a zoomed version of the highest angular resolution observation at $1.3\,\mathrm{mm}$ from Facchini et al. (2019). Table 8.1 provides a summary of the datasets used in this work and the derived properties.

To estimate the integrated flux density and, for the wavelengths where the source is resolved, the radial extent of the dust emission, we performed a characterization in the uv-plane using the code `galario` (Tazzari et al. 2018). It works by assuming a 1D or 2D model of the emission in the image plane and performing a Fourier transform to obtain the synthetic visibilities at the same uv-points of the observations. The best-fit model is found as the one that minimizes the χ^2 by sampling the parameter space with an Markov chain Monte Carlo (MCMC) approach using the `emcee` package (Foreman-Mackey et al. 2013). We computed the best-fit model assuming that the emission is axisymmetric. The observations with ALMA at $0.9\,\mathrm{mm}$ are spatially resolved, so we employed a Gaussian profile to model the intensity profile: $I(R) = f_0 \exp(-R/2\sigma^2)$, where f_0 is a normalization term, σ characterizes the Gaussian centered in the disk center, and R is the radial coordinate. The continuum emission in the VLA observations at $9.0\,\mathrm{mm}$ and $2.0\,\mathrm{cm}$ are unresolved, so we modeled the disk as a central point source $I(R) = f_0\,\delta(R)$, where $\delta(R)$ is the Dirac delta function. To perform this fit for the $2.0\,\mathrm{cm}$ data, we subtracted the CLEAN model visibilities of an external source in the field of view at an angular distance of $\sim 100''$ from CX Tau using the CASA task `uvsub`. In every run, we also fit for the right ascension and declination offsets ($\Delta\mathrm{RA}$, $\Delta\mathrm{Dec}$), but we kept fixed the disk

Table 8.1: Parameters of CX Tau observations at all the frequencies we considered.

Wavelength	Observatory	Observation date (d/m/y)	Beam (arcsec)	$F_{\rm tot}$ (mJy)	RMS (mJy beam^{-1})	ΔF_{stat} (mJy)	$\Delta F_{\rm tot}$ (mJy)	$R_{68\%}$ (au)
$^{(a)}0.85\,$mm	SMA	02/2004 - 01/2005	$\sim$15	25.0	6.0	6.0	6.5	-
$^{(\star)}0.9\,$mm	ALMA Band 7	07/2015 - 07/2016	0.28×0.19	21.8	0.12	0.38	2.2	16.9 ± 0.1
$^{(b)}1.3\,$mm	ALMA Band 6	11/2016 - 09/2017	0.06×0.03	9.75	0.020	0.12	0.98	14.0 ± 0.3
$^{(c)}1.3\,$mm	PdBI	12/2010 - 02/2013	0.6×0.4	9.6	0.2	0.2	0.98	-
$^{(d)}3.5\,$mm	PdBI	07-08/2007	$\sim 3-4$	1.01	0.13	0.13	0.16	-
$^{(\star)}9.0\,$mm	VLA Ka-band	12/10/2020	0.25×0.19	0.304	7×10^{-3}	4×10^{-3}	31×10^{-3}	-
$^{(\star)}1.3\,$cm	VLA K-band	09/04/2022	0.14×0.09	0.423	10×10^{-3}	6×10^{-3}	43×10^{-3}	$< 9.2 \pm 1.5$
$^{(\star)}2.0\,$cm	VLA Ku-band	02-04/03/2020	1.7×1.6	0.108	3×10^{-3}	2×10^{-3}	11×10^{-3}	-
$^{(\star)}6.0\,$cm	VLA C-band	C conf: 20/02/2020	4.2×3.6	$< 17 \times 10^{-3}$	8×10^{-3}	-	-	-
$^{(\star)}6.0\,$cm	VLA C-band	A conf: 09-11/01/2021	0.6×0.4	$< 12 \times 10^{-3}$	2×10^{-3}	-	-	-

Notes. $^{(\star)}$We have directly calibrated and analyzed these observations. For these data, the beam is taken from the images produced with Briggs weighting and robust 1. $^{(a)}$ $^{(b)}$ $^{(c)}$ $^{(d)}$ Values from Andrews & Williams (2005), Facchini et al. (2019), Piétu et al. (2014), and Ricci et al. (2010), respectively. Systematic calibration errors are assumed to be 10% of the total flux density, apart from VLA C-Band observations where we used a value of 5%. ALMA calibration errors are based on https://almascience.eso.org/documents-and-tools/cycle9/alma-technical-handbook, while VLA calibration errors follow the indications by NRAO at https://science.nrao.edu/facilities/vla/docs/manuals/oss/performance/fdscale. For the remaining observations, we refer to the respective papers.

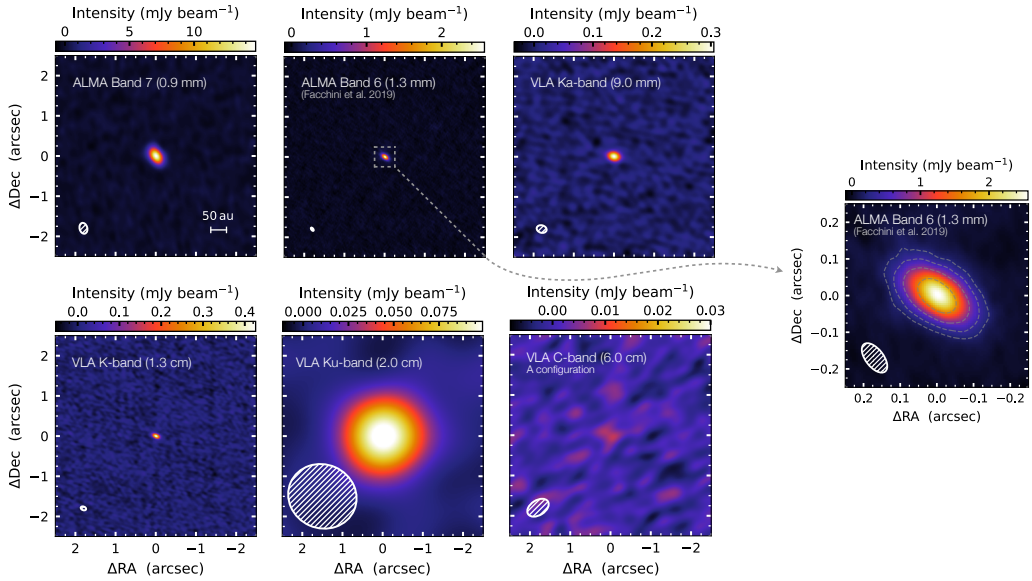

Figure 8.4: Continuum images of CX Tau from ALMA and VLA observations at different wavelengths, all obtained with Briggs weighting and robust 1. The full width at half maximum (FWHM) of the synthesized beam is indicated by the ellipse in the bottom left corner of each image. The rightmost panel shows a zoomed image of the ALMA 1.3 mm observation from Facchini et al. (2019) which has the highest angular resolution. Contours indicate the [5, 10, 20, 40]σ levels.

inclination and position angle from the estimates of Facchini et al. (2019) ($\mathrm{inc} = 55.1°$, $\mathrm{PA} = 66.2°$), as they were obtained with data that had a higher resolution and sensitivity than all the other observations. In the two 6.0 cm observations, a clear central source was not detected. To estimate a flux density upper limit, we adopted the same procedure as Barenfeld et al. (2016). We employed the `CASA` task `uvmodelfit` and fit a central point source to the visibilities of each dataset, after subtracting the other sources in the field of view with `uvsub`. To this value, we added $2 \times \mathrm{RMS}$, so that the upper limit contains the real source flux with a confidence level of 95%. At $1.3\,\mathrm{cm}$, despite the highest angular resolution available with the VLA at this wavelength ($\sim 0.1''$ corresponding to $\sim 13\,\mathrm{au}$), the source is dominated by an unresolved component but shows hints of a marginally resolved source. To extract the flux density, we fit these data with a point source, but an attempt to retrieve the radial extent is described in Sect. 8.2.3.

For all `galario` runs, we employed uniform priors and the intensity normalization factor f_0 was sampled logarithmically: $\log_{10}(f_0/(\mathrm{Jy/sr})) \in [0, 30]$, $\Delta\mathrm{RA} \in [-2, 2'']$, $\Delta\mathrm{Dec} \in [-2, 2'']$, and, for the fit of ALMA $0.9\,\mathrm{mm}$ observation, also $\sigma \in [0, 0.2'']$. In each run, we used 100 walkers that were well converged after ~ 1000 steps. Corner plots along with deprojected visibilities and best-fit model for data from ALMA Band 7 ($0.9\,\mathrm{mm}$) and VLA Ka ($9.0\,\mathrm{mm}$), K ($1.3\,\mathrm{cm}$), and Ku ($2.0\,\mathrm{mm}$) bands are shown in Figs. 8.5, 8.6, 8.7, and 8.8.

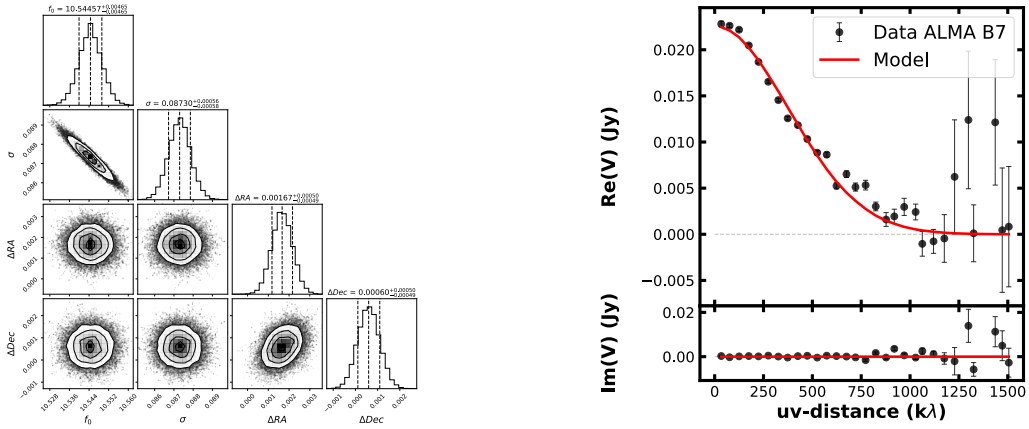

Figure 8.5: Results of the `galario` fit with a Gaussian model on ALMA Band 7 (0.9 mm) data. *Left panel*: Corner plot of the MCMC run. *Right panel*: Recentered and deprojected visibilities binned in 50kλ intervals and the best-fit model. Error bars are at 1σ.

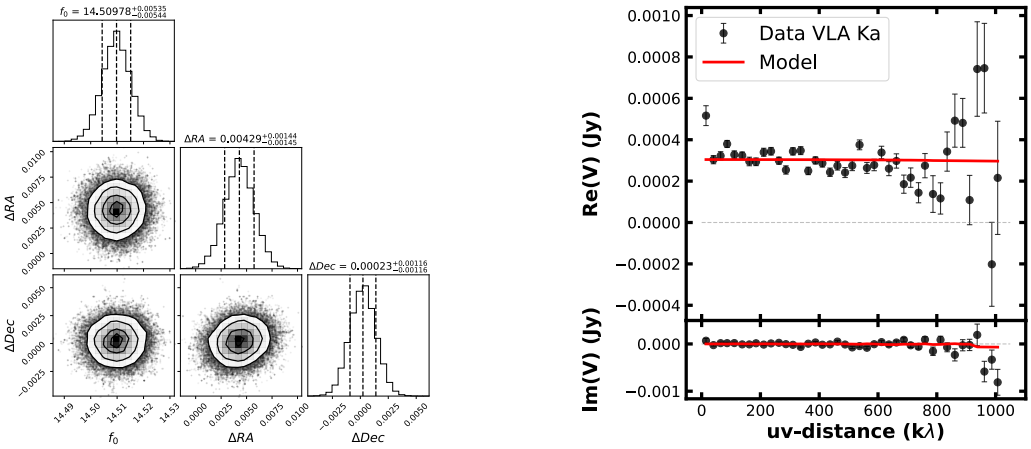

Figure 8.6: Results of the `galario` fit with a point source model on the VLA Ka-band (9.0 mm) data. *Left panel:* Corner plot of the MCMC run. *Right panel:* Recentered and deprojected visibilities binned in 25kλ intervals and the best-fit model. Error bars are at 1σ.

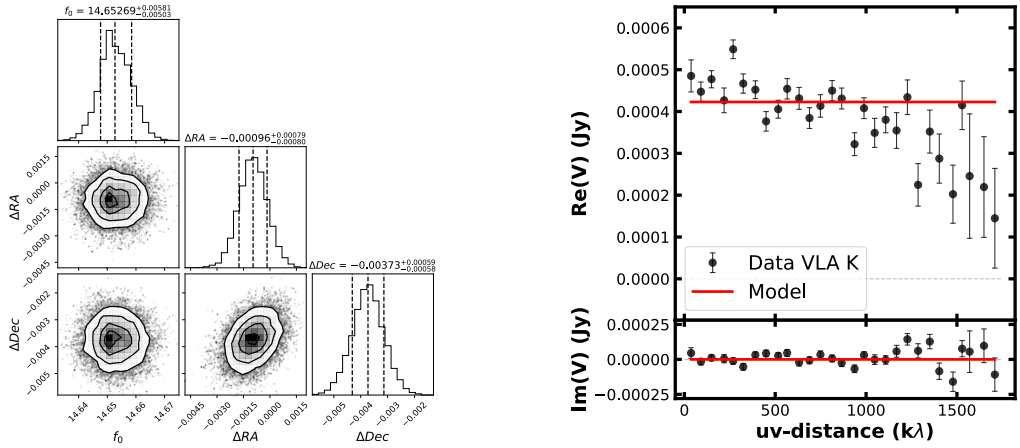

Figure 8.7: Results of the `galario` fit with a point source model on the VLA K-band (1.3 cm) data. *Left panel:* Corner plot of the MCMC run. *Right panel:* Recentered and deprojected visibilities binned in 60kλ intervals and the best-fit model. Error bars are at 1σ.

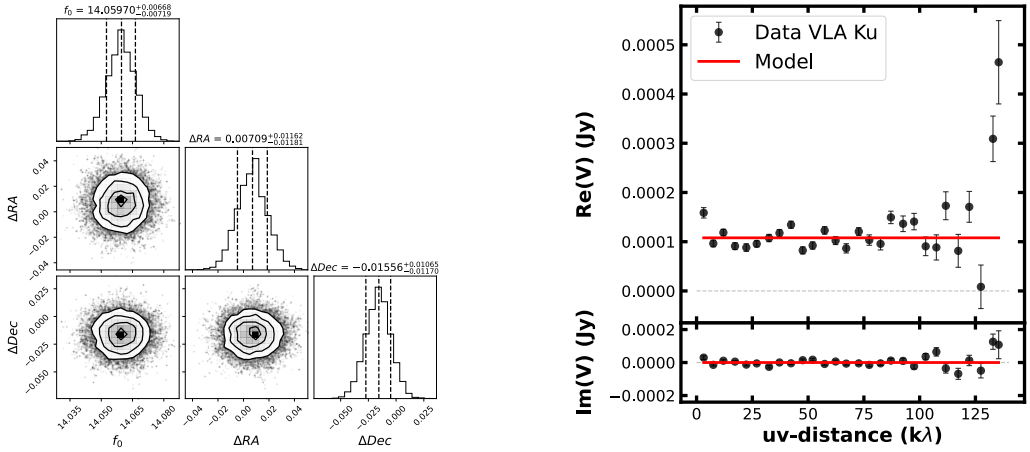

Figure 8.8: Results of the `galario` fit with a point source model on the VLA Ku-band (2.0 cm) data. *Left panel:* Corner plot of the MCMC run. *Right panel:* Recentered and deprojected visibilities binned in 5kλ intervals and the best-fit model. Error bars are at 1σ.

8.2.2 Evaluating time variability at centimeter wavelengths

Looking at the spectral density distribution in Fig 8.3, two characteristics appear particularly surprising. First, the two observations at $6.0\,\mathrm{cm}$ did not detect any emissions, despite the stringent upper limit of $12.0\,\mu\mathrm{Jy}$ provided by the data taken in A configuration. Second, the emission at $1.3\,\mathrm{cm}$ is significantly higher than the emissions in the adjacent bands at $9.0\,\mathrm{mm}$ and $2.0\,\mathrm{cm}$. In particular, the $1.3\,\mathrm{cm}$ observation has a flux density higher by a factor of $\sim$2 than a power-law fit between the emission at $9.0\,\mathrm{mm}$ and $2.0\,\mathrm{cm}$ would suggest. Checking the intraband spectral indices of these three VLA detections resulted for each observation in a value between $\sim$0.5 and 1.1. We show in Fig. 8.9 their intraband fluxes. We split each observation into two halves between high and low frequencies and extracted the flux densities. Then, we used a power law to fit the two intensities retrieved from each band and obtained the intraband spectral indices values $\alpha = 0.5, 0.7, 1.1$ for the data from the Ka, K, and Ku bands, respectively. Those values are compatible with the typical free-free spectral index $\alpha\sim0.6$ (Panagia & Felli 1975; Reynolds 1986), while excluding contributions from gyro-synchrotron emission that are typically characterized by a negative spectral index. Therefore, we interpret the VLA observations as dominated by free-free emission and explain the non-detections at $6.0\,\mathrm{cm}$ and the anomalously high emission at $1.3\,\mathrm{cm}$ as due to the time variability of free-free.

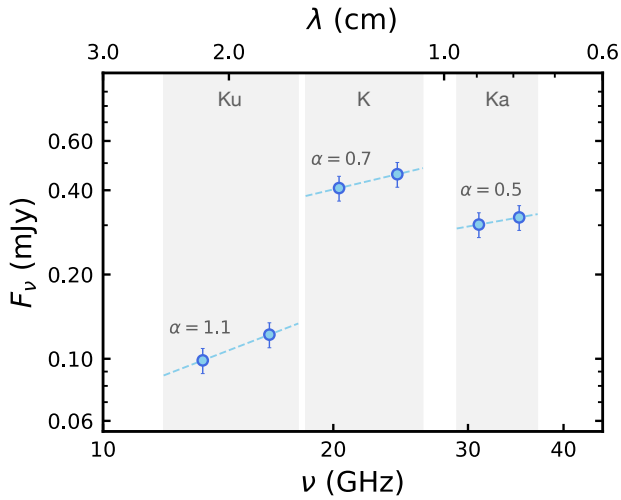

Figure 8.9: Spectral flux density distribution of CX Tau zoomed in on the VLA data in Ka ($9.0\,\mathrm{mm}$), K ($1.3\,\mathrm{cm}$), and Ku ($2.0\,\mathrm{mm}$) bands. Each observation is split into high and low frequencies and then fitted to obtain the intraband spectral indices reported in the plot.

The procedure we applied to evaluate the time variability is summarized in the left panel of Fig. 8.10. We first assumed that the flux density detected in the observations between $0.9\,\mathrm{mm}$ and $3.5\,\mathrm{mm}$ is dominated by dust emission only. Fitting a power-law to these data, we obtained a dust spectral index $\alpha_\mathrm{d} = 2.25 \pm 0.06$ (orange solid line), consistent with partially optically thick dust emission and/or grain growth in the assumption of optically thin emission and Rayleigh-Jeans approximation (Draine 2006).

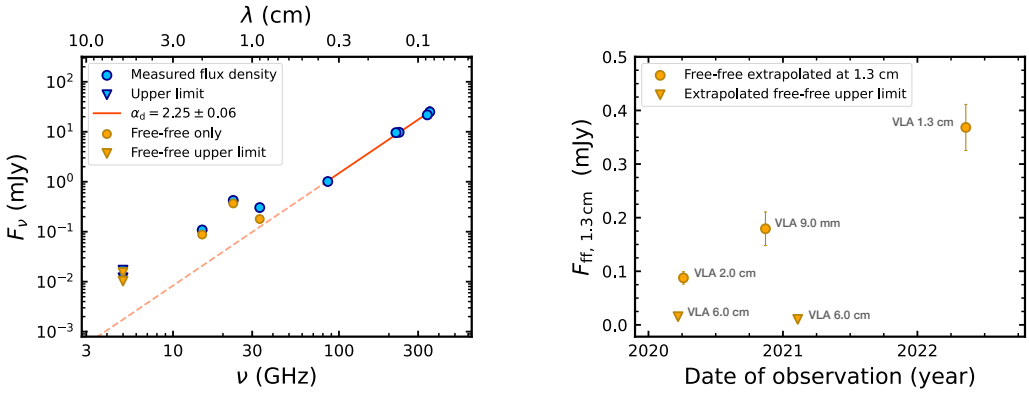

Figure 8.10: Extraction and time variability of the free-free component. *Left panel*: Flux density distribution of CX Tau, showing the dust emission fit (orange line) used to extract the free-free only estimates (yellow circles and arrows) from the measured flux densities and upper limits. *Right panel*: Time variability of extrapolated free-free estimates at 1.3 cm. The extrapolation was performed assuming a free-free spectral index of 0.7 ± 0.1. The values in the plot are labeled with the observation they came from originally.

Extrapolating the fit to centimeter wavelengths (orange dashed line) makes it apparent that the flux density from VLA detections diverges from millimeter data, in a way that resembles the behavior in panel b of Fig 8.1. Then, assuming that VLA detections only have contributions from free-free and dust emission, we obtained the estimates of free-free alone (yellow circles) by subtracting the extrapolation of the dust emission fit from the measured flux densities for the respective observing wavelength. With the intent of comparing the free-free emissions at the same wavelength, we chose $1.3\,\mathrm{cm}$ as the reference and extrapolated to this wavelength the free-free only estimates at the other VLA bands, assuming a spectral index $\alpha_{\rm ff} = 0.7 \pm 0.1$ consistent with the intraband spectral indices of the VLA detections. For the free-free extraction and extrapolation, the two upper limits at $6.0\,\mathrm{cm}$ are treated in the same way as the detections at $9.0\,\mathrm{mm}$, $1.3\,\mathrm{cm}$, and $2.0\,\mathrm{cm}$. We report in the right panel of Fig. 8.10 the extrapolated values of the free-free only emission at $1.3\,\mathrm{cm}$ as a function of the time of their respective observations. There is significant variability both in amplitude and also in time, particularly noticeable by the fact that the first non-detection at $6.0\,\mathrm{cm}$ and the $2.0\,\mathrm{cm}$ measurement are separated by $\sim$2 weeks. It should be noted that we used a constant spectral index for dust emission at all wavelengths to be conservative. Typically, the dust spectral index steepens at centimeter wavelengths due to grain properties and size distribution (Wilner et al. 2005). In spite of this, a steeper spectral index would not affect the evident variability in the extrapolated free-free emission.

8.2.3 Relation between dust radius and observing wavelength

Studying the dust radius dependence on observing wavelength provides a useful metric to assess disk evolution. Since different wavelengths are more sensitive to the emission of different dust grain sizes, we expect that the observed disk radius should change with

the observing frequency. Specifically, the theoretical prediction by Rosotti et al. (2019) (using dust evolution models that account for grain growth and drift by Birnstiel et al. 2012) suggests that at centimeter wavelengths, probing bigger grains subject to stronger radial drift (Weidenschilling 1977), the extent of a radial-drift-dominated disk should be smaller compared to the radii measured at shorter wavelengths.

For CX Tau, Facchini et al. (2019) at $1.3\,\mathrm{mm}$ measured a radius enclosing 68% of the flux density ($R_{68\%}$) of $14.0 \pm 0.3\,\mathrm{au}$. From the `galario` fit with a Gaussian profile of ALMA $0.9\,\mathrm{mm}$ data, we obtained $R_{68\%} = 16.9 \pm 0.1\,\mathrm{au}$. The VLA observation with the highest angular resolution is the one in the K band at $1.3\,\mathrm{cm}$ with a beam of $\sim 0.1''$. The right panel of Fig. 8.7 shows that the K-band ($1.3\,\mathrm{cm}$) observation is mostly non-resolved. However, a slight downward trend in the visibility profile is visible, possibly hinting at a resolved component in the data. To extract this component, we first excluded the visibilities at a uv-distance greater than 1300kλ as they are dominated by noise. Then, we considered only the visibilities in a range of uv-distances where they appear the flattest and we chose the interval between 850 and 1300kλ. We computed the average of the real parts of the visibilities and obtained a flux density of $0.37\,\mathrm{mJy}$, equivalent to the free-free only estimate obtained by subtracting the extrapolated dust emission from the total flux density value at $1.3\,\mathrm{cm}$ (indicated by the yellow circle at this wavelength in the left panel of Fig. 8.10). This procedure is visualized in Fig. 8.11. We subtracted the computed intensity value to the real parts of the visibilities having a uv-distance within 1300kλ getting as a result the visibility profile of the resolved dust emission component in the observation. To retrieve a dust size, we fit these visibilities with `galario` using a Gaussian model profile and the same parameters used in the fit of ALMA $0.9\,\mathrm{mm}$ data (see Sect. 8.2.1). The converged fit and the results are shown in Fig 8.12.

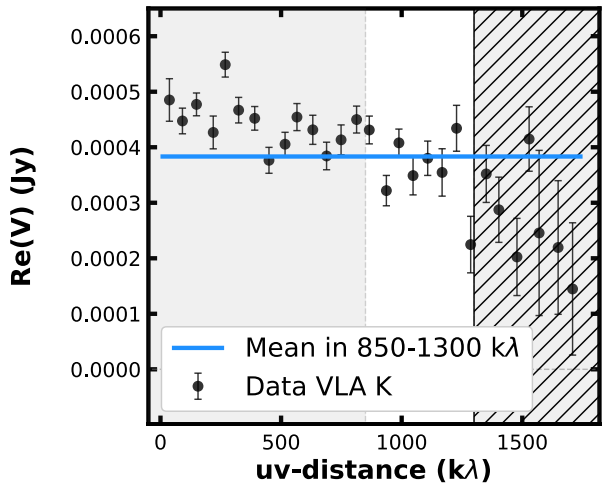

Figure 8.11: Real part of the visibilities from VLA K-band ($1.3\,\mathrm{cm}$) data binned in 60kλ intervals and overlaid blue line indicating their mean value between 850 and 1300kλ (range with white background). The hatched area contains the visibilities with a uv-distance greater than 1300kλ which have been excluded in the radius evaluation due to high noise.

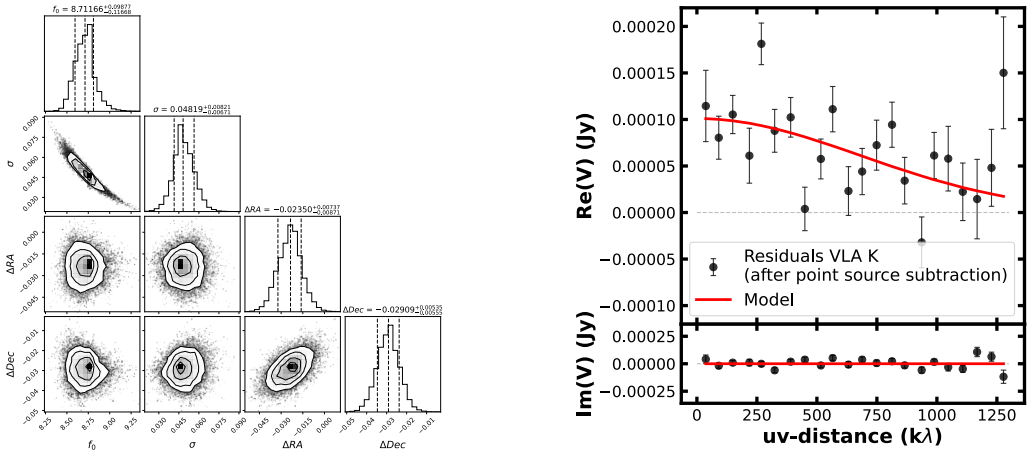

Figure 8.12: Results of the `galario` fit with a Gaussian model on VLA K-band (1.3 cm) residual data, after subtracting from the real part of the visibilities their mean values in the range of uv-distance [850, 1300]kλ and neglecting the visibilities over 1300kλ. *Left panel*: Corner plot of the MCMC run. *Right panel:* Recentered and deprojected visibilities binned in 60kλ intervals and best-fit model. Error bars are at 1σ.

With the explained procedure, we acquired a dust disk extent of $R_{68\%} = 9.2 \pm 1.5$ au. We interpret this value as an upper limit because the subtraction of a constant value to the real part of all visibilities implies that some unresolved dust emission has possibly been excluded, thereby skewing the inferred extent to a larger size. Figure 8.13 presents the relation between the measured $R_{68\%}$ (normalized to the value at 0.9 mm) and the observing wavelength for CX Tau compared to the radial drift prediction by Rosotti et al. (2019). The same relation is also shown for AS 209, FT Tau, DR Tau (data from Pérez et al. 2012; Tazzari et al. 2016), and the disks within the survey in Lupus of Tazzari et al. (2021). Unlike the other sources, CX Tau appears consistent with the theoretical prediction for a disk dominated by radial drift. This is in line with the fact that CX Tau is a rare example of a disk whose dust emission is smooth even with high-resolution ALMA observations (another example is PDS 66, Ribas et al. 2023). Moreover, the ratio between the gas and dust radii of 5.4 measured by Facchini et al. (2019) at 1.3 mm matches the results from the population synthesis study of Toci et al. (2021) for a Shakura & Sunyaev (1973) disk viscosity value of $\sim 10^{-3} - 10^{-4}$.

8.3 Discussion and conclusions

In this work, we present a multiwavelength view of the compact protoplanetary disk CX Tau in the submillimeter to centimeter range. After a careful subtraction of the contaminant emission, we detected dust thermal continuum at 1.3 cm, indicating the presence of large grains and the dominance of dust radial drift in the evolution of this disk. This is in line with the observed high ratio between the gas and dust radii consistent with radial drift (Facchini et al. 2019, Sanchis et al. 2021, Toci et al. 2021). Such a scenario im-

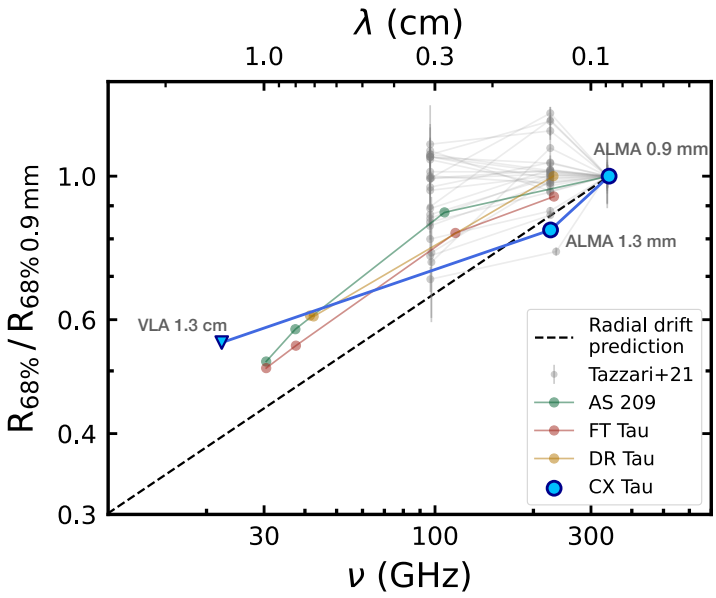

Figure 8.13: Relation between the measured $R_{68\%}$ (normalized to the value at 0.9 mm) and the observing wavelength for CX Tau, compared with the radial drift prediction by Rosotti et al. (2019) and with the same relation for AS 209, FT Tau, DR Tau (Pérez et al. 2012; Tazzari et al. 2016), and the disks of the Lupus survey by Tazzari et al. (2021).

plies that dust traps may not be forming within these disks – or, alternatively, the planet formation process is restricted to the inner regions. In either case, CX Tau presents an intriguing example suggesting the need for future observations with higher resolution.

We explain the peculiar scatter of the VLA data in the flux density distribution as the result of a strong time variability of unresolved free-free emission. Free-free emission is known to rarely vary in intensity by more than $\sim 30\%$ over a timescale of some weeks to a few months (e.g., Sheehan et al. 2016, Coutens et al. 2019). CX Tau, instead, shows a rapid variability of about two weeks associated with a change in intensity by a factor of ~ 20 (see the difference in the extrapolated free-free emission between the detection at 1.3 and the non-detections at $6.0\,\mathrm{cm}$ in the right panel of Fig. 8.10). Despite our results, some studies (e.g., Espaillat et al. 2019, 2022) have not reported evidence of variability in Class II sources, so it remains unclear what makes some systems variable (and not others).

Assuming that the free-free emission in CX Tau comes from a jet, we consider the evidence by Anglada et al. (2015) of an almost-linear relationship between the free-free emission of a radio jet and its momentum outflow rate. Thus, the observed variability of a factor of ~ 20 would imply approximately the same level of variability in $\dot{M}_{\rm acc}$ assuming that the jet velocity and the $\dot{M}_{\rm jet}/\dot{M}_{\rm acc}$ do not vary significantly (e.g., Cabrit 2007). Assuming, instead, that the free-free is emitted by a photoevaporative wind, the high state at 1.3 cm would correspond to an ionizing luminosity $\Phi_{\rm EUV} \sim 10^{40} - 10^{41}$ photons s^{-1} (Pascucci et al. 2012), which is considered typical in Class II sources (Coutens

et al. 2019). For variability of the order of a couple of weeks, the medium irradiated by this EUV source must be rather dense to ensure that the recombination timescale is short enough. In particular, the electron density of the ionized gas at sub-au scales would be $n > 10^6\,\mathrm{cm}^{-3}$ (Hollenbach & Gorti 2009) and this would correspond to a wind mass loss rate of $\sim 10^{-9}\,M_\odot\,\mathrm{yr}^{-1}$ (Hollenbach et al. 1994). Another possible description for the high-intensity observation at $1.3\,\mathrm{cm}$ could be also a radio flare, a known phenomenon due to the high level of activity in pre-main sequence stars (e.g., Bower et al. 2003, Forbrich et al. 2008, Rivilla et al. 2015 report radio flares from the Orion nebula cluster). However, it should be noticed that radio flares often exhibit a negative or flat spectral index, indicative of non-thermal gyro-synchrotron emission, which is contrary to what we have found. These radio flares are usually associated with X-ray flaring activity. Unfortunately, no X-ray observations of CX Tau are available for comparison. Additionally, the absence of spectra of CX Tau at other wavelengths prevents us from inspecting its accretion properties and supporting the interpretation of free-free variability. All these elements further highlight the peculiarity of the findings in CX Tau and warrant caution when interpreting millimeter and non-simultaneous centimeter wavelength observations when evaluating the strength of a non-dust emission component.

As another potential explanation for the observed behavior, we mention the contribution from anomalous microwave emission (AME), whose presence in protoplanetary disks has been claimed by Greaves et al. (2018). The origin of this emission is uncertain. It is thought to be the effect of electric dipole radiation from nanometric spinning dust grains (Draine & Lazarian 1998), but the carrier is still debated. Greaves et al. (2018) discarded an origin hypothesis from polycyclic aromatic hydrocarbons, in favor of one based on nanodiamonds. The presence of AME would generate a characteristic bump at a wavelength of $\sim$1 cm in the spectral flux density distribution (see Fig. 1 in Greaves & Mason 2022) that resembles the trend of CX Tau detections at $0.9\,\mathrm{mm}$, $1.3\,\mathrm{cm}$, and $2.0\,\mathrm{cm}$. Given the uncertainties around this emission mechanism and its properties in protoplanetary disks, simultaneous multiwavelength data are needed to corroborate this scenario.

Conclusions and future directions

In this Thesis, I explored various protoplanetary disks with distinct characteristics. These ranged from extended disks displaying notable substructures in dust emission to a disk surrounding a very low-mass star that may have undergone giant planet formation, as well as a compact, structureless disk exhibiting peculiar behavior whose origin remains uncertain. The methodologies employed in these studies were diverse, encompassing high-resolution ALMA observations, comprehensive numerical modeling involving hydrodynamical and radiative transfer simulations, and a multiwavelength analysis spanning from centimeter to sub-millimeter wavelengths, incorporating data from VLA, ALMA, and other interferometers. In all the examined systems, the presence of planets could potentially play a role, whether giant planets shaping observed dust substructures at tens or hundreds of astronomical units or inner planets generating unresolved substructures, preventing radial drift and leading to the formation of a compact disk. The key findings of this work can be summarized as follows:

- **Numerical modeling of the disk around the very low-mass star CIDA 1.**
  Exoplanet research has provided us with discoveries of planets around very low-mass (VLM) stars (e.g., TRAPPIST-1 and Proxima Centauri). However, current theoretical models strive to explain planet formation in these conditions and do not predict the development of giant planets. High-resolution ALMA observations of the disk around CIDA 1, a VLM star in Taurus, show substructures hinting at the presence of a massive planet. Chapter 5 presents the work aimed at reproducing the observed dust and gas emission of CIDA 1, assuming the structures are shaped by the interaction of the disk with a massive planet. I modeled the protoplanetary disk with a set of hydrodynamical and radiative transfer simulations, varying the mass and location of the embedded planet. The models indicate that a planet with a minimum mass of $1.4\,M_{\rm Jup}$ orbiting at a distance of $\sim$10 au can explain the morphology and location of the observed dust ring. Moreover, the model reproduces the observed low dust spectral index and the morphology of the ^{12}CO and ^{13}CO channel maps where the cloud absorption allowed a detection. These results suggest the presence of a massive planet orbiting CIDA 1, thus challenging our understanding of planet formation around VLM stars.

- **Characterization of the continuum substructures observed in the exoALMA disks.**
  The exoALMA Large Program is conducting the first planet hunting search in protoplanetary disks, aiming to detect local perturbations in the gas line emission attributable to the presence of planets. The program observed with high-sensitivity a sample of 15 disks displaying extended emission and dust substructures suggesting the presence of planets. In Chapter 6, I present the results of my work, focused on the morphological characterization of the dust substructures in this sample. Employing fitting procedures in the uv-space, I systematically characterized both axisymmetric and non-axisymmetric substructures for each source. Through a case-by-case analysis, I compared the exoALMA data with previous observations from ALMA or scattered light images, contributing to a deeper understanding of the origins of the observed substructures.

- **Multiwavelength analysis of the compact disk around CX Tau.**
  The prominent dust substructures observed for most protoplanetary disks, including those reported in Chapters 5 and 6, have all been observed at large distances from the central star. However, to comprehend the formation of terrestrial planets and our own Solar System, a thorough investigation of dust emission within the inner 10 au is crucial. In this region, the direct influence of the central star gives rise to additional emissions, necessitating a multiwavelength approach for a comprehensive understanding. In Chapter 8 I focus on CX Tau, arguably a disk representative of the bulk of the population, in terms of its size and mm-flux, rather than the usual bright and massive disks, which are outliers of the population. By combining observations from ALMA, VLA, and other interferometers, I have obtained the spectral flux density distribution of CX Tau across millimeter and centimeter wavelengths, showing peculiar features. To explain its behavior, I propose the possibility of high variability in the free-free emission even at short timescales. Alternatively, another fascinating interpretation is offered by the anomalous microwave emission, an elusive emission attributed to nanometric spinning dust.

Future perspectives

From the work presented in this Thesis, different possible future research directions emerge:

- **High-resolution characterization of compact disks**
  As emphasized in Chapter 7, bright and extended disks are outliers in the population, whereas compact disks, resembling our own Solar System, represent the prevailing norm. The recent observational endeavors have predominantly concentrated on large disks. However, in the upcoming years, there is a need to shift this focus toward compact systems. This includes conducting high-resolution and high-sensitivity campaigns to thoroughly examine their structures, evolutionary processes, and potential for planetary formation. A more detailed examination of compact disks is essential to enhance our comprehension of theories related to planet formation. This includes refining our understanding of core accretion,

which is still required explaining the formation of planets in the innermost regions. Additionally, it involves refining disk evolution theories, particularly in the context of typical disks, with a focus on the role of radial drift.

- **Search for planets embedded in disks**
  Currently, PDS 70 stands out as the sole Class II protoplanetary disk where unanimous agreement prevails regarding the presence of planets. Despite extensive observational efforts, detecting planets embedded within disks is becoming an increasingly challenging task. The work on continuum emission of the exoALMA disks aligns with this difficulty, possessing high sensitivity but failing to detect any clear circumplanetary disk. The reason behind the complexity of directly observing young planets in disks remains unclear. Future research should persist in addressing this issue, with confidence that the capabilities of James Webb Space Telescope and the Extremely Large Telescope have the potential to revolutionize this field.

- **Investigating gas kinematics within** $100\,\mathrm{au}$
  Most dust substructures in extended disks are typically observed within $100\,\mathrm{au}$. However, indications of localized gas perturbations, suggesting the presence of planets, are consistently detected at distances exceeding $100\,\mathrm{au}$. Achieving higher resolution in gas observations is essential for accurately linking gas perturbations to the observed dust substructures. This poses a challenging observational task, demanding longer integration times during data collection. Nonetheless, overcoming this challenge will significantly enhance our ability to constrain the presence of planets or unveil alternative mechanisms contributing to the formation of the observed structures.

- **Evaluating the occurrence rate of distant giant planets**
  Exoplanet search indicates that giant planets typically orbit at distances of $1 - 5\,\mathrm{au}$ from their host stars, akin to Jupiter in our Solar System. Nevertheless, the observation of dust substructures at distances of tens of au appears to be a common occurrence in extended protoplanetary disks. These planets may be attributed to gravitational instability during the early stages of the disk. However, the actual prevalence of such planets remains an unresolved query. Future analyses capable of the directly or indirectly assessing the presence of distance giant planets planets in a larger sample of disks will contribute to uncovering their true occurrence rate.

- **Accurate treatment of non-dust emissions in multiwavelength analyses**
  It is becoming evident that a comprehensive examination of dust emission necessitates a multiwavelength approach, incorporating longer centimeter wavelengths for observations with reduced optical depth. The introduction of ALMA Band 1 (with an observing wavelength of $\sim 7\,\mathrm{mm}$) and the forthcoming ngVLA (from 0.2 to $25\,\mathrm{cm}$) align with this approach. Nevertheless, the investigation of CX Tau underscores the critical importance of accurately addressing non-dust emissions, whether by considering free-free variability or accounting for anomalous microwave emission.

APPENDIX A

Physical constants

Table A.1: Values of relevant physical constants employed in this Thesis.

Quantity	Value cgs	Value SI
Solar mass $M_\odot$	1.99×10^{33} g	1.99×10^{30} kg
Solar luminosity $L_\odot$	3.83×10^{33} erg s^{-1}	3.83×10^{26} J s^{-1}
Solar radius $R_\odot$	6.96×10^{10} cm	6.96×10^{8} m
Jupiter mass $M_{\rm jup}$	1.90×10^{30} g	1.90×10^{27} kg
Earth mass $M_\oplus$	5.97×10^{27} g	5.97×10^{24} g
Astronomical unit au	1.5×10^{13} cm	1.5×10^{11} m
Parsec pc	3.09×10^{18} cm	3.09×10^{16} m
Light speed c	3.0×10^{10} cm s^{-1}	3.0×10^{8} m s^{-1}
Gravitational constant G	6.67×10^{-8} g^{-1}cm^{3}s^{-2}	6.67×10^{-11} kg^{-1}m^{3}s^{-2}
Boltzmann constant k_B	1.38×10^{-16} erg K^{-1}	1.38×10^{-23} J K^{-1}
Proton mass m_p	1.66×10^{24} g	1.66×10^{27} kg

APPENDIX B

Smoothed particle hydrodynamics

Smoothed particle hydrodynamics (SPH) has been originally formulated by Lucy (1977) and, independently, by Gingold & Monaghan (1977), as a numerical method for solving the equations of fluid dynamics. In this algorithm, the fluid is treated as an ensemble of diskrete particles, containing information such as position, mass and velocity, which allows to reconstruct the fluid properties. For a deeper description of SPH we refer to the reviews of Monaghan (2005) and Price (2012), while the SPH code PHANTOM is presented in Price et al. (2018b).

B.1 Basic concepts

We introduce SPH by describing how it computes density from an arbitrary distribution of point particles with fixed mass. Three possible approaches to this problem are illustrated in Figure B.1. In the left panel is represented the simplest method involving a regular mesh, where density is calculated by dividing the mass in each cell by its volume. The biggest limitation here is that dense/sparse regions will be over/undersampled, respectively. A second approach (central panel) is to remove the mesh and consider a sphere around the sampling point, whose radius scales with local number density of particles. In this way, the resolution problem of clustered/sparse regions is resolved, but this density estimate will be very noisy and sensitive to whether a particle near the edge of the volume is actually inside or outside the volume. This naturally leads to the idea of decreasing the influence of particles with their distance from the sampling point, obtaining a *smoothed* density estimate as it is actually done in SPH (right panel). In this third approach, density in the location $\mathbf{r}_a$ of the sampling particle is calculated through a weighted summation over neighboring particles, indicated by location $\mathbf{r}_b$ and with mass m_b, given by

$$\rho(\mathbf{r}_a) = \sum_{b=1}^{N_{\rm neigh}} m_b W(|\mathbf{r}_a - \mathbf{r}_b|, h), \tag{2.1}$$

where W is called *smoothing kernel* and is the weight function with dimensions of inverse volume and h is the *smoothing length*, which determines the rate of fall-off of W with distance. In order to respect total mass conservation, there is a normalization condition

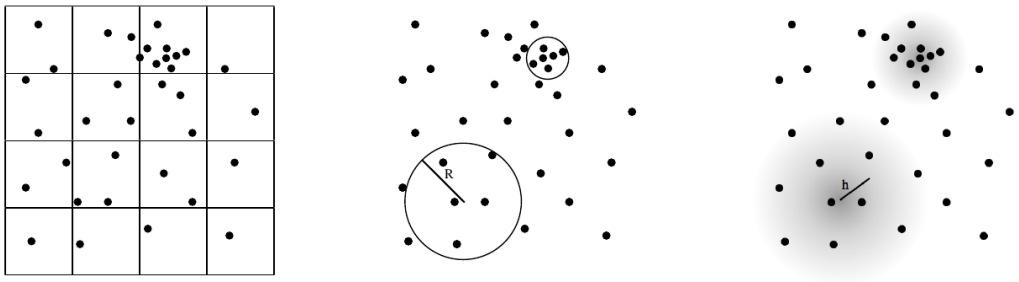

Figure B.1: Three possible ways to compute a continuous density field from a collection of point mass particles: with a regular mesh (left panel), with a sphere around the sampling point whose radius scales with the local number density of particles (central panel) or, as it is done in SPH, with a weighted sum over neighboring particles, where the weight decreases with distance from the sampling point (right panel).

on smoothing kernel

$$\int_V W(|\mathbf{r}' - \mathbf{r}_b|, h)\mathrm{d}V' = 1. \tag{2.2}$$

In practice, kernels used in SPH are Gaussian-like in shape but truncated at a finite radius, so that this compact support does not consider distant particles with negligible weight, saving much computational time. The most used kernel function in SPH are B-spline functions.

To set the smoothing length, we consider a collection of equal mass particles, with mass m, in three dimensions and impose that mass contained within the compact support of the kernel is a constant. In case of a cubic spline kernel, with radius $R_{\mathrm{kern}} = 2h$, we have

$$\rho(\mathbf{r}_a)\frac{4}{3}\pi\big(2h(\mathbf{r}_a)\big)^3 = N_{\mathrm{neigh}}m = const. \tag{2.3}$$

Therefore, we obtain

$$h(\mathbf{r}_a) = \eta\left(\frac{m}{\rho(\mathbf{r}_a)}\right)^{1/3}, \tag{2.4}$$

where η is a parameter specifying the smoothing length in units of the mean particle spacing $(m/\rho)^{1/3}$ and it contains information on N_{neigh}. Usually, $N_{\mathrm{neigh}} \sim 60$, corresponding to $\eta \sim 1.2$, and the number of neighboring particles must not be much higher than that, otherwise numerical instabilities arise. Since Eq. (2.1) and (2.4) are coupled, they have to be solved simultaneously, through an iterative method. This density estimate does not depend on time, but only on particle positions and masses.

Once we have a density estimate, the rest of SPH algorithm can be derived entirely from that. For instance, to obtain the equation of motion, we start from a diskrete Lagrangian for a system of point masses with velocity $\mathbf{v}$ and internal energy per unit mass u depending on density ρ and entropy s, given by

$$\mathcal{L} = \sum_b m_b\left[\frac{1}{2}v_b^2 - u_b(\rho_b, s_b)\right]. \tag{2.5}$$

Using the Euler-Lagrange equation

$$\frac{\mathrm{d}}{\mathrm{d}t}\left(\frac{\partial \mathcal{L}}{\partial \mathbf{v}_a}\right) - \frac{\partial \mathcal{L}}{\partial \mathbf{r}_a} = 0 \tag{2.6}$$

and the equation of state for an in ideal gas

$$P = (\gamma - 1)\rho u, \tag{2.7}$$

where γ is the adiabatic index, we eventually find the standard SPH expression for the equation of motion in the simplest case of a constant smoothing length

$$\frac{\mathrm{d}\mathbf{v}_a}{\mathrm{d}t} = -\sum_b m_b \left(\frac{P_a}{\rho_a^2} + \frac{P_b}{\rho_b^2}\right) \nabla_a W_{ab}, \tag{2.8}$$

where $W_{ab} \equiv W(|\mathbf{r}_a - \mathbf{r}_b|, h)$. It should be noted that the gradient of W does not need to be computed, since in SPH the smoothing kernel is a known function whose derivatives are already tabulated. The more general equation of motion in case of a variable smoothing length is

$$\frac{\mathrm{d}\mathbf{v}_a}{\mathrm{d}t} = -\sum_b m_b \left[\frac{P_a}{\Omega_\mathrm{a}\rho_a^2}\frac{\partial W_{ab}(h_a)}{\partial \mathbf{r}_a} + \frac{P_b}{\Omega_\mathrm{b}\rho_b^2}\frac{\partial W_{ab}(h_b)}{\partial \mathbf{r}_b}\right], \tag{2.9}$$

where Ω is a term accounting for the gradient of the smoothing length

$$\Omega_a \equiv \left[1 - \frac{\partial h_a}{\partial \rho_a}\sum_b m_b \frac{\partial W_{ab}(h_a)}{\partial h_a}\right]. \tag{2.10}$$

This formulation allows SPH to conserve exactly and simultaneously mass, momentum, angular momentum, energy and entropy. SPH also presents zero intrinsic dissipation.

B.2 PHANTOM code

PHANTOM (Price et al. 2018b) is a 3D Smoothed Particle Hydrodynamics and Magnetohydrodynamics code developed over the last decade for astrophysical applications. It has been widely used for modeling of protoplanetary disks, allowing to simulate dust-gas mixtures.

B.2.1 Artificial disk viscosity

As already stated, SPH has intrinsically zero dissipation. This means that in order to describe physical phenomena where dissipative terms are required, they must be explicitly added. A so-called *artificial viscosity* was originally implemented in SPH to treat shocks and discontinuities (Price 2008). Later, Lodato & Price (2010) proposed some changes to the formulation of artificial viscosity to better represent a Shakura & Sunyaev (1973) accretion disk viscosity. This formulation provides a kinematic shear artificial viscosity

$$\nu_\mathrm{AV} \approx \frac{1}{10}\alpha_\mathrm{AV} c_\mathrm{s} h, \tag{2.11}$$

where c_s is the sound speed, but also an unwanted coefficient of bulk viscosity

$$\zeta_{AV} \approx \frac{1}{6}\alpha_{AV} c_s h, \tag{2.12}$$

whose effect, however, is not so disadvantageous in a disk simulation. Substituting the α-prescription (2.66) $\nu_{SS} = \alpha_{SS} c_s H$ in (2.11), we obtain the relation between the Shakura & Sunyaev (1973) and the artificial α coefficients

$$\alpha_{SS} \approx \frac{1}{10}\alpha_{AV}\frac{\langle h \rangle}{H}, \tag{2.13}$$

where $\langle h \rangle$ is the azimuthally averaged smoothing length. In our PHANTOM simulations, we used this viscosity formulation. It is particularly useful because, once α_{SS} is set at the beginning of the simulation, it allows to check whether the scale height of the disk is resolved (i.e. if $\langle h \rangle / H < 1$) and to control that $\alpha_{AV} > 0.1$, otherwise viscosities smaller than this value produce disk spreading independent of the value of α_{AV}. However, α_{SS} is not fixed and can change its value throughout the simulation. Specifically, from (2.4) we know that $h \propto \rho^{-1/3}$, so it should be noted that in regions where density decreases, for instance in gaps or cavities of a disk, viscosity inevitably increases.

B.2.2 Dust-gas mixtures

There are two ways in PHANTOM to simulate the coupled evolution of dust and gas: two-fluid and one-fluid approach. The former discretizes the mixture in two distinct sets of dust and gas particles, treating the two components as separate fluids coupled by a drag term (Laibe & Price 2012a,b). However, this approach is not efficient in case of strong coupling between gas and dust, greatly increasing the computational time. This occurs since the code has to resolve the very short lengthscale separating the two fluids and the length of the simulation timestep is constrained by the small stopping time. For this reason, we used the one-fluid approach in our work.

In the one-fluid method, introduced by Laibe & Price (2014), the mixture is treated with just one set of particles, containing information of both dust and gas. In particular, this formulation prescribes the evolution equations for

1. the combined density of gas and dust $\rho_{tot} \equiv \rho_g + \rho_d$;
2. the dust fraction $\epsilon \equiv \rho_d / \rho_{tot}$ (so that $\rho_g = (1-\epsilon)\rho_{tot}$ and $\rho_d = \epsilon \rho_{tot}$);
3. the barycentric velocity $\mathbf{v}_{bar} \equiv (\rho_g \mathbf{v}_g + \rho_d \mathbf{v}_d)/\rho_{tot}$ of the dust and gas mixture;
4. the velocity difference between gas and dust $\Delta\mathbf{v} \equiv \mathbf{v}_d - \mathbf{v}_g$.

This approach cannot properly capture the velocity dispersion of large grains, but is particularly suited to treat small grains strongly coupled to the gas, with $\mathrm{St} \ll 1$, corresponding to a dust grain dimension $a_d \lesssim 1\,\mathrm{mm}$ for typical disk parameters.

Bibliography

ALMA Partnership, Brogan, C. L., Pérez, L. M., et al. 2015, *Astrophys. J. Lett.*, 808, L3

Aly, H. & Lodato, G. 2020, *Mon. Not. R. Astron. Soc.*, 492, 3306

André, P. 2002, in EAS Publications Series, Vol. 3, EAS Publications Series, ed. J. Bouvier & J.-P. Zahn, 1–38

Andre, P., Ward-Thompson, D., & Barsony, M. 2000, in Protostars and Planets IV, ed. V. Mannings, A. P. Boss, & S. S. Russell, 59

Andrews, S. M. 2020, *Ann. Rev. of Astron. Astrophys.*, 58, 483

Andrews, S. M., Elder, W., Zhang, S., et al. 2021, *Astrophys. J.*, 916, 51

Andrews, S. M., Huang, J., Pérez, L. M., et al. 2018a, *Astrophys. J. Lett.*, 869, L41

Andrews, S. M., Rosenfeld, K. A., Kraus, A. L., & Wilner, D. J. 2013, *Astrophys. J.*, 771, 129

Andrews, S. M., Terrell, M., Tripathi, A., et al. 2018b, *Astrophys. J.*, 865, 157

Andrews, S. M. & Williams, J. P. 2005, *Astrophys. J.*, 631, 1134

Andrews, S. M. & Williams, J. P. 2007a, *Astrophys. J.*, 671, 1800

Andrews, S. M. & Williams, J. P. 2007b, *Astrophys. J.*, 659, 705

Andrews, S. M., Wilner, D. J., Hughes, A. M., Qi, C., & Dullemond, C. P. 2009, Astrophysical Journal, 700, 1502

Anglada, G., Rodríguez, L. F., & Carrasco-Gonzalez, C. 2015, in Advancing Astrophysics with the Square Kilometre Array (AASKA14), 121

Anglada-Escudé, G., Amado, P. J., Barnes, J., et al. 2016, *Nature*, 536, 437

Ansdell, M., Williams, J. P., Manara, C. F., et al. 2017, *Astron. J.*, 153, 240

Ansdell, M., Williams, J. P., Trapman, L., et al. 2018, *Astrophys. J.*, 859, 21

Ansdell, M., Williams, J. P., van der Marel, N., et al. 2016, *Astrophys. J.*, 828, 46

Armitage, P. J. 2010, Astrophysics of Planet Formation (Cambridge University Press)

Armitage, P. J. 2020, Astrophysics of planet formation, 2nd edn. (Cambridge University Press)

Bailer-Jones, C. A. L., Rybizki, J., Fouesneau, M., Demleitner, M., & Andrae, R. 2021, *Astron. J.*, 161, 147

Balanis, , C. A. 2008, Modern Antenna Handbook

Ballabio, G., Dipierro, G., Veronesi, B., et al. 2018, *Mon. Not. R. Astron. Soc.*, 477, 2766

Barenfeld, S. A., Carpenter, J. M., Ricci, L., & Isella, A. 2016, *Astrophys. J.*, 827, 142
Barenfeld, S. A., Carpenter, J. M., Sargent, A. I., Isella, A., & Ricci, L. 2017, *Astrophys. J.*, 851, 85
Beckwith, S. V. W., Sargent, A. I., Chini, R. S., & Guesten, R. 1990, *Astron. J.*, 99, 924
Benisty, M., Bae, J., Facchini, S., et al. 2021, *Astrophys. J. Lett.*, 916, L2
Benisty, M., Juhasz, A., Boccaletti, A., et al. 2015, *Astron. Astrophys.*, 578, L6
Benítez-Llambay, P. & Masset, F. S. 2016, *Astrophys. J. Suppl.*, 223, 11
Bergin, E. A., Aikawa, Y., Blake, G. A., & van Dishoeck, E. F. 2007, in Protostars and Planets V, ed. B. Reipurth, D. Jewitt, & K. Keil, 751
Birnstiel, T., Klahr, H., & Ercolano, B. 2012, *Astron. Astrophys.*, 539, A148
Bitsch, B., Lambrechts, M., & Johansen, A. 2015, *Astron. Astrophys.*, 582, A112
Bohlin, R. C., Savage, B. D., & Drake, J. F. 1978, *Astrophys. J.*, 224, 132
Bollati, F., Lodato, G., Price, D. J., & Pinte, C. 2021, *Mon. Not. R. Astron. Soc.*, 504, 5444
Boss, A. P. 1997, Science, 276, 1836
Bower, G. C., Plambeck, R. L., Bolatto, A., et al. 2003, *Astrophys. J.*, 598, 1140
Briceno, C., Calvet, N., Gomez, M., et al. 1993, *Publ. Astron. Soc. Pac.*, 105, 686
Briggs, D. S. 1995, PhD thesis, New Mexico Institute of Mining and Technology
Bruderer, S. 2013, *Astron. Astrophys.*, 559, A46
Bruderer, S., van Dishoeck, E. F., Doty, S. D., & Herczeg, G. J. 2012, *Astron. Astrophys.*, 541, A91
Burke, B. F., Graham, & Wilkinson, P. N. 2019, An introduction to radio astronomy, 4th edition
Cabrit, S. 2007, in Star-Disk Interaction in Young Stars, ed. J. Bouvier & I. Appenzeller, Vol. 243, 203–214
Cadman, J., Rice, K., & Hall, C. 2021, *Mon. Not. R. Astron. Soc.*, 504, 2877
Cárcamo, M., Román, P. E., Casassus, S., Moral, V., & Rannou, F. R. 2018, Astronomy and Computing, 22, 16
Carrasco-González, C., Sierra, A., Flock, M., et al. 2019, *Astrophys. J.*, 883, 71
CASA Team, Bean, B., Bhatnagar, S., et al. 2022, *Publ. Astron. Soc. Pac.*, 134, 114501
Casassus, S., Cabrera, G. F., Förster, F., et al. 2006, *Astrophys. J.*, 639, 951
Casassus, S., Christiaens, V., Cárcamo, M., et al. 2021, *Mon. Not. R. Astron. Soc.*, 507, 3789
Cazzoletti, P., van Dishoeck, E. F., Pinilla, P., et al. 2018, *Astron. Astrophys.*, 619, A161
Chauvin, G., Lagrange, A. M., Dumas, C., et al. 2004, *Astron. Astrophys.*, 425, L29
Chauvin, G., Lagrange, A. M., Dumas, C., et al. 2005, *Astron. Astrophys.*, 438, L25
Cieza, L. A., Ruíz-Rodríguez, D., Hales, A., et al. 2019a, *Mon. Not. R. Astron. Soc.*, 482, 698
Cieza, L. A., Ruíz-Rodríguez, D., Hales, A., et al. 2019b, *Mon. Not. R. Astron. Soc.*, 482, 698
Clarke, C. J., Tazzari, M., Juhasz, A., et al. 2018, *Astrophys. J. Lett.*, 866, L6
Comeron, F., Rieke, G. H., Claes, P., Torra, J., & Laureijs, R. J. 1998, *Astron. Astrophys.*, 335, 522
Condon, J. J. & Ransom, S. M. 2016, Essential Radio Astronomy

Cornwell, T. J. 2008, IEEE Journal of Selected Topics in Signal Processing, 2, 793
Coutens, A., Liu, H. B., Jiménez-Serra, I., et al. 2019, *Astron. Astrophys.*, 631, A58
Crida, A., Morbidelli, A., & Masset, F. 2006, Icarus, 181, 587
Cuello, N., Dipierro, G., Mentiplay, D., et al. 2019, *Mon. Not. R. Astron. Soc.*, 483, 4114
Czekala, I., Jennings, J., Zawadzki, B., et al. 2023, MPoL-dev/MPoL: v0.2.0 Release
Czekala, I., Loomis, R. A., Teague, R., et al. 2021, *Astrophys. J. Suppl.*, 257, 2
Damasso, M., Del Sordo, F., Anglada-Escudé, G., et al. 2020, Science Advances, 6, eaax7467
Davis, C. J., Chrysostomou, A., Hatchell, J., et al. 2010, *Mon. Not. R. Astron. Soc.*, 405, 759
Dipierro, G. 2016, PhD thesis, University of Milan, Italy
Dipierro, G., Lodato, G., Testi, L., & de Gregorio Monsalvo, I. 2014, *Mon. Not. R. Astron. Soc.*, 444, 1919
Dipierro, G., Price, D., Laibe, G., et al. 2015a, *Mon. Not. R. Astron. Soc.*, 453, L73
Dipierro, G., Price, D., Laibe, G., et al. 2015b, *Mon. Not. R. Astron. Soc.*, 453, L73
Dodson-Robinson, S. E. & Salyk, C. 2011, *Astrophys. J.*, 738, 131
Dong, R., Liu, S.-y., Eisner, J., et al. 2018, *Astrophys. J.*, 860, 124
Draine, B. T. 2003, *Astrophys. J.*, 598, 1026
Draine, B. T. 2006, *Astrophys. J.*, 636, 1114
Draine, B. T. & Lazarian, A. 1998, *Astrophys. J.*, 508, 157
Dullemond, C. P., Juhasz, A., Pohl, A., et al. 2012, RADMC-3D: A multi-purpose radiative transfer tool, Astrophysics Source Code Library, record ascl:1202.015
Espaillat, C. C., Macías, E., Hernández, J., & Robinson, C. 2019, *Astrophys. J. Lett.*, 877, L34
Espaillat, C. C., Macías, E., Wendeborn, J., et al. 2022, *Astrophys. J.*, 924, 104
Facchini, S., Benisty, M., Bae, J., et al. 2020, *Astron. Astrophys.*, 639, A121
Facchini, S., Pinilla, P., van Dishoeck, E. F., & de Juan Ovelar, M. 2018, *Astron. Astrophys.*, 612, A104
Facchini, S., van Dishoeck, E. F., Manara, C. F., et al. 2019, *Astron. Astrophys.*, 626, L2
Faria, J. P., Suárez Mascareño, A., Figueira, P., et al. 2022, *Astron. Astrophys.*, 658, A115
Fedele, D., van den Ancker, M. E., Henning, T., Jayawardhana, R., & Oliveira, J. M. 2010, Astronomy and Astrophysics, 510, A72
Forbrich, J., Menten, K. M., & Reid, M. J. 2008, *Astron. Astrophys.*, 477, 267
Foreman-Mackey, D., Hogg, D. W., Lang, D., & Goodman, J. 2013, *Publ. Astron. Soc. Pac.*, 125, 306
Francis, L., Marel, N. v. d., Johnstone, D., et al. 2022, *Astron. J.*, 164, 105
Frank, J., King, A., & Raine, D. J. 2002, Accretion Power in Astrophysics: Third Edition (Cambridge University Press)
Fung, J. & Chiang, E. 2016, *Astrophys. J.*, 832, 105
Gaia Collaboration, Brown, A. G. A., Vallenari, A., et al. 2021, *Astron. Astrophys.*, 649, A1
Garufi, A., Benisty, M., Pinilla, P., et al. 2018, *Astron. Astrophys.*, 620, A94
Gillon, M., Triaud, A. H. M. J., Demory, B.-O., et al. 2017, *Nature*, 542, 456

Gingold, R. A. & Monaghan, J. J. 1977, Monthly Notices of the Royal Astronomical Society, 181, 375

Goldreich, P. & Tremaine, S. 1980, Astrophysical Journal, 241, 425

Goldreich, P. & Ward, W. R. 1973, *Astrophys. J.*, 183, 1051

Goodman, A. A., Benson, P. J., Fuller, G. A., & Myers, P. C. 1993, Astrophysical Journal, 406, 528

Greaves, J. S. & Mason, B. 2022, *Mon. Not. R. Astron. Soc.*, 513, 3180

Greaves, J. S., Scaife, A. M. M., Frayer, D. T., et al. 2018, Nature Astronomy, 2, 662

Guidi, G., Isella, A., Testi, L., et al. 2022, *Astron. Astrophys.*, 664, A137

Hammond, I., Christiaens, V., Price, D. J., et al. 2023, *Mon. Not. R. Astron. Soc.*, 522, L51

Hammond, I., Christiaens, V., Price, D. J., et al. 2022, *Mon. Not. R. Astron. Soc.*, 515, 6109

Hartmann, L., Calvet, N., Gullbring, E., & D'Alessio, P. 1998a, Astrophysical Journal, 495, 385

Hartmann, L., Calvet, N., Gullbring, E., & D'Alessio, P. 1998b, *Astrophys. J.*, 495, 385

Hashimoto, J., Muto, T., Dong, R., et al. 2021, *Astrophys. J.*, 911, 5

Haworth, T. J., Cadman, J., Meru, F., et al. 2020, *Mon. Not. R. Astron. Soc.*, 494, 4130

Hendler, N. P., Mulders, G. D., Pascucci, I., et al. 2017, *Astrophys. J.*, 841, 116

Hildebrand, R. H. 1983, *Quart. J. R. Astron. Soc.*, 24, 267

Högbom, J. A. 1974, *Astron. Astrophys. Supp. Ser.*, 15, 417

Hollenbach, D. & Gorti, U. 2009, *Astrophys. J.*, 703, 1203

Hollenbach, D., Johnstone, D., Lizano, S., & Shu, F. 1994, *Astrophys. J.*, 428, 654

Huang, J., Andrews, S. M., Dullemond, C. P., et al. 2018, *Astrophys. J. Lett.*, 869, L42

Hutchison, M., Price, D. J., & Laibe, G. 2018, *Mon. Not. R. Astron. Soc.*, 476, 2186

Ilee, J. D., Walsh, C., Jennings, J., et al. 2022, *Mon. Not. R. Astron. Soc.*, 515, L23

Izquierdo, A. F., Galván-Madrid, R., Maud, L. T., et al. 2018, *Mon. Not. R. Astron. Soc.*, 478, 2505

Izquierdo, A. F., Smith, R. J., Glover, S. C. O., et al. 2021a, *Mon. Not. R. Astron. Soc.*, 500, 5268

Izquierdo, A. F., Testi, L., Facchini, S., Rosotti, G. P., & van Dishoeck, E. F. 2021b, *Astron. Astrophys.*, 650, A179

Jennings, J., Booth, R. A., Tazzari, M., Clarke, C. J., & Rosotti, G. P. 2022a, *Mon. Not. R. Astron. Soc.*, 509, 2780

Jennings, J., Booth, R. A., Tazzari, M., Rosotti, G. P., & Clarke, C. J. 2020, *Mon. Not. R. Astron. Soc.*, 495, 3209

Jennings, J., Tazzari, M., Clarke, C. J., Booth, R. A., & Rosotti, G. P. 2022b, *Mon. Not. R. Astron. Soc.*, 514, 6053

Keppler, M., Benisty, M., Müller, A., et al. 2018, *Astron. Astrophys.*, 617, A44

Kratter, K. & Lodato, G. 2016, *Ann. Rev. of Astron. Astrophys.*, 54, 271

Kurtovic, N. T., Pinilla, P., Long, F., et al. 2021, *Astron. Astrophys.*, 645, A139

Lada, C. J. & Wilking, B. A. 1984, Astrophysical Journal, 287, 610

Laibe, G. & Price, D. J. 2012a, Monthly Notices of the Royal Astronomical Society, 420, 2345

Laibe, G. & Price, D. J. 2012b, Monthly Notices of the Royal Astronomical Society, 420, 2365

Laibe, G. & Price, D. J. 2014, *Mon. Not. R. Astron. Soc.*, 440, 2136

Lambrechts, M. & Johansen, A. 2012, *Astron. Astrophys.*, 544, A32

Larson, R. B. 1981, Monthly Notices of the Royal Astronomical Society, 194, 809

Lebreuilly, U., Hennebelle, P., Colman, T., et al. 2021, *Astrophys. J. Lett.*, 917, L10

Liebert, J. & Probst, R. G. 1987, *Ann. Rev. of Astron. Astrophys.*, 25, 473

Lin, D. N. C. & Papaloizou, J. 1979, Monthly Notices of the Royal Astronomical Society, 186, 799

Liu, B., Lambrechts, M., Johansen, A., Pascucci, I., & Henning, T. 2020, *Astron. Astrophys.*, 638, A88

Liu, Y., Dipierro, G., Ragusa, E., et al. 2019, *Astron. Astrophys.*, 622, A75

Lodato, G. 2008, New Astronomy Review, 52, 21

Lodato, G., Delgado-Donate, E., & Clarke, C. J. 2005, *Mon. Not. R. Astron. Soc.*, 364, L91

Lodato, G., Dipierro, G., Ragusa, E., et al. 2019, *Mon. Not. R. Astron. Soc.*, 486, 453

Lodato, G. & Price, D. J. 2010, *Mon. Not. R. Astron. Soc.*, 405, 1212

Lodato, G., Rampinelli, L., Viscardi, E., et al. 2023, *Mon. Not. R. Astron. Soc.*, 518, 4481

Long, F., Andrews, S. M., Zhang, S., et al. 2022, *Astrophys. J. Lett.*, 937, L1

Long, F., Herczeg, G. J., Harsono, D., et al. 2019, *Astrophys. J.*, 882, 49

Long, F., Pinilla, P., Herczeg, G. J., et al. 2018, *Astrophys. J.*, 869, 17

Longarini, C., Armitage, P. J., Lodato, G., Price, D. J., & Ceppi, S. 2023a, *Mon. Not. R. Astron. Soc.*, 522, 6217

Longarini, C., Lodato, G., Bertin, G., & Armitage, P. J. 2023b, *Mon. Not. R. Astron. Soc.*, 519, 2017

Longarini, C., Lodato, G., Toci, C., & Aly, H. 2021, *Mon. Not. R. Astron. Soc.*, 503, 4930

Loomis, R. A., Öberg, K. I., Andrews, S. M., & MacGregor, M. A. 2017, *Astrophys. J.*, 840, 23

Lucy, L. B. 1977, Astronomical Journal, 82, 1013

Luhman, K. L. 2018, *Astron. J.*, 156, 271

Lynden-Bell, D. & Pringle, J. E. 1974, Monthly Notices of the Royal Astronomical Society, 168, 603

Macías, E., Anglada, G., Osorio, M., et al. 2016, *Astrophys. J.*, 829, 1

Macías, E., Guerra-Alvarado, O., Carrasco-González, C., et al. 2021, *Astron. Astrophys.*, 648, A33

Manara, C. F., Ansdell, M., Rosotti, G. P., et al. 2022, arXiv e-prints, arXiv:2203.09930

Manara, C. F., Morbidelli, A., & Guillot, T. 2018, *Astron. Astrophys.*, 618, L3

Martinez-Brunner, R., Casassus, S., Pérez, S., et al. 2022, *Mon. Not. R. Astron. Soc.*, 510, 1248

Mathis, J. S., Rumpl, W., & Nordsieck, K. H. 1977, *Astrophys. J.*, 217, 425

Maury, A. J., André, P., Testi, L., et al. 2019, *Astron. Astrophys.*, 621, A76

Mayor, M. & Queloz, D. 1995, *Nature*, 378, 355

McCaughrean, M. J. & O'dell, C. R. 1996, Astronomical Journal, 111, 1977

McMullin, J. P., Waters, B., Schiebel, D., Young, W., & Golap, K. 2007, in Astronomical Society of the Pacific Conference Series, Vol. 376, Astronomical Data Analysis Software and Systems XVI, ed. R. A. Shaw, F. Hill, & D. J. Bell, 127

Mercer, A. & Stamatellos, D. 2020, *Astron. Astrophys.*, 633, A116

Miguel, Y., Cridland, A., Ormel, C. W., Fortney, J. J., & Ida, S. 2020, *Mon. Not. R. Astron. Soc.*, 491, 1998

Mohanty, S., Jayawardhana, R., & Basri, G. 2005, *Astrophys. J.*, 626, 498

Monaghan, J. J. 2005, Reports on Progress in Physics, 68, 1703

Morales, J. C., Mustill, A. J., Ribas, I., et al. 2019, Science, 365, 1441

Mulders, G. D., Pascucci, I., & Apai, D. 2015, *Astrophys. J.*, 814, 130

Mulders, G. D., Pascucci, I., Ciesla, F. J., & Fernandes, R. B. 2021, *Astrophys. J.*, 920, 66

Najita, J. R., Strom, S. E., & Muzerolle, J. 2007, *Mon. Not. R. Astron. Soc.*, 378, 369

Natta, A. & Testi, L. 2001, *Astron. Astrophys.*, 376, L22

Natta, A., Testi, L., Comerón, F., et al. 2002, *Astron. Astrophys.*, 393, 597

Okabe, A., Boots, B., Sugihara, K., & Chiu, S. N. 2000, Spatial Tessellations: Concepts and Applications of Voronoi Diagrams, 2nd edn., Series in Probability and Statistics (John Wiley and Sons, Inc.)

Orihara, R., Momose, M., Muto, T., et al. 2023, *Publ. Astron. Soc. Jpn.*, 75, 424

Panagia, N. & Felli, M. 1975, *Astron. Astrophys.*, 39, 1

Paneque-Carreño, T., Pérez, L. M., Benisty, M., et al. 2021, *Astrophys. J.*, 914, 88

Pascucci, I., Gorti, U., & Hollenbach, D. 2012, *Astrophys. J. Lett.*, 751, L42

Pascucci, I., Ricci, L., Gorti, U., et al. 2014, *Astrophys. J.*, 795, 1

Pascucci, I., Testi, L., Herczeg, G. J., et al. 2016, *Astrophys. J.*, 831, 125

Payne, M. J. & Lodato, G. 2007, *Mon. Not. R. Astron. Soc.*, 381, 1597

Pérez, L. M., Benisty, M., Andrews, S. M., et al. 2018, *Astrophys. J. Lett.*, 869, L50

Pérez, L. M., Carpenter, J. M., Chandler, C. J., et al. 2012, *Astrophys. J. Lett.*, 760, L17

Piétu, V., Guilloteau, S., Di Folco, E., Dutrey, A., & Boehler, Y. 2014, *Astron. Astrophys.*, 564, A95

Pinilla, P., Benisty, M., & Birnstiel, T. 2012a, *Astron. Astrophys.*, 545, A81

Pinilla, P., Birnstiel, T., Benisty, M., et al. 2013, *Astron. Astrophys.*, 554, A95

Pinilla, P., Birnstiel, T., Ricci, L., et al. 2012b, *Astron. Astrophys.*, 538, A114

Pinilla, P., Kurtovic, N. T., Benisty, M., et al. 2021, *Astron. Astrophys.*, 649, A122

Pinilla, P., Natta, A., Manara, C. F., et al. 2018, *Astron. Astrophys.*, 615, A95

Pinilla, P., Quiroga-Nuñez, L. H., Benisty, M., et al. 2017, *Astrophys. J.*, 846, 70

Pinte, C., Harries, T. J., Min, M., et al. 2009, *Astron. Astrophys.*, 498, 967

Pinte, C., Ménard, F., Duchêne, G., & Bastien, P. 2006, *Astron. Astrophys.*, 459, 797

Pinte, C., Price, D. J., Ménard, F., et al. 2020, *Astrophys. J. Lett.*, 890, L9

Pinte, C., Price, D. J., Ménard, F., et al. 2018, *Astrophys. J. Lett.*, 860, L13

Pinte, C., Teague, R., Flaherty, K., et al. 2023, in Astronomical Society of the Pacific Conference Series, Vol. 534, Protostars and Planets VII, ed. S. Inutsuka, Y. Aikawa, T. Muto, K. Tomida, & M. Tamura, 645

Pinte, C., van der Plas, G., Ménard, F., et al. 2019a, Nature Astronomy, 3, 1109
Pinte, C., van der Plas, G., Ménard, F., et al. 2019b, Nature Astronomy, 3, 1109
Pollack, J. B., Hubickyj, O., Bodenheimer, P., et al. 1996, Icarus, 124, 62
Price, D. J. 2007, *Pub. Astron. Soc. Aus.*, 24, 159
Price, D. J. 2008, Journal of Computational Physics, 227, 10040
Price, D. J. 2012, Journal of Computational Physics, 231, 759
Price, D. J., Cuello, N., Pinte, C., et al. 2018a, *Mon. Not. R. Astron. Soc.*, 477, 1270
Price, D. J., Wurster, J., Tricco, T. S., et al. 2018b, *Pub. Astron. Soc. Aus.*, 35, e031
Pringle, J. E. 1981, Annual Review of Astronomy and Astrophysics, 19, 137
Rabago, I. & Zhu, Z. 2021, *Mon. Not. R. Astron. Soc.*, 502, 5325
Ragusa, E., Dipierro, G., Lodato, G., Laibe, G., & Price, D. J. 2017, *Mon. Not. R. Astron. Soc.*, 464, 1449
Rau, U. & Cornwell, T. J. 2011, *Astron. Astrophys.*, 532, A71
Reissl, S., Wolf, S., & Brauer, R. 2016, *Astron. Astrophys.*, 593, A87
Reynolds, S. P. 1986, *Astrophys. J.*, 304, 713
Ribas, Á., Macías, E., Weber, P., et al. 2023, *Astron. Astrophys.*, 673, A77
Ricci, L., Testi, L., Natta, A., et al. 2010, *Astron. Astrophys.*, 512, A15
Ricci, L., Testi, L., Natta, A., et al. 2014, *Astrophys. J.*, 791, 20
Rilinger, A. M., Espaillat, C. C., & Macías, E. 2019, *Astrophys. J.*, 878, 103
Rivilla, V. M., Chandler, C. J., Sanz-Forcada, J., et al. 2015, *Astrophys. J.*, 808, 146
Rodmann, J., Henning, T., Chandler, C. J., Mundy, L. G., & Wilner, D. J. 2006, *Astron. Astrophys.*, 446, 211
Rosenfeld, K. A., Andrews, S. M., Wilner, D. J., & Stempels, H. C. 2012, *Astrophys. J.*, 759, 119
Rosotti, G. P., Juhasz, A., Booth, R. A., & Clarke, C. J. 2016, *Mon. Not. R. Astron. Soc.*, 459, 2790
Rosotti, G. P., Tazzari, M., Booth, R. A., et al. 2019, *Mon. Not. R. Astron. Soc.*, 486, 4829
Safronov, V. S. 1969, Evoliutsiia doplanetnogo oblaka.
Sanchis, E., Testi, L., Natta, A., et al. 2021, *Astron. Astrophys.*, 649, A19
Sanchis, E., Testi, L., Natta, A., et al. 2020, *Astron. Astrophys.*, 633, A114
Schaefer, G. H., Dutrey, A., Guilloteau, S., Simon, M., & White, R. J. 2009, *Astrophys. J.*, 701, 698
Shakura, N. I. & Sunyaev, R. A. 1973, *Astron. Astrophys.*, 24, 337
Sheehan, P. D., Eisner, J. A., Mann, R. K., & Williams, J. P. 2016, *Astrophys. J.*, 831, 155
Simon, M., Guilloteau, S., Beck, T. L., et al. 2019, *Astrophys. J.*, 884, 42
Simon, M., Guilloteau, S., Di Folco, E., et al. 2017, *Astrophys. J.*, 844, 158
Stadler, J., Benisty, M., Izquierdo, A., et al. 2023, *Astron. Astrophys.*, 670, L1
Tanaka, H., Takeuchi, T., & Ward, W. R. 2002, *Astrophys. J.*, 565, 1257
Tazzari, M., Beaujean, F., & Testi, L. 2018, *Mon. Not. R. Astron. Soc.*, 476, 4527
Tazzari, M., Clarke, C. J., Testi, L., et al. 2021, *Mon. Not. R. Astron. Soc.*, 506, 2804
Tazzari, M., Testi, L., Ercolano, B., et al. 2016, *Astron. Astrophys.*, 588, A53

Tazzari, M., Testi, L., Natta, A., et al. 2017, *Astron. Astrophys.*, 606, A88
Teague, R. 2019, The Journal of Open Source Software, 4, 1632
Testi, L., Birnstiel, T., Ricci, L., et al. 2014, in Protostars and Planets VI, ed. H. Beuther, R. S. Klessen, C. P. Dullemond, & T. Henning, 339–361
Testi, L., Natta, A., Scholz, A., et al. 2016, *Astron. Astrophys.*, 593, A111
Toci, C., Lodato, G., Christiaens, V., et al. 2020a, *Mon. Not. R. Astron. Soc.*, 499, 2015
Toci, C., Lodato, G., Fedele, D., Testi, L., & Pinte, C. 2020b, *Astrophys. J. Lett.*, 888, L4
Toci, C., Rosotti, G., Lodato, G., Testi, L., & Trapman, L. 2021, *Mon. Not. R. Astron. Soc.*, 507, 818
Tychoniec, Ł., Manara, C. F., Rosotti, G. P., et al. 2020, *Astron. Astrophys.*, 640, A19
Ubach, C., Maddison, S. T., Wright, C. M., et al. 2017, *Mon. Not. R. Astron. Soc.*, 466, 4083
Ubeira Gabellini, M. G., Miotello, A., Facchini, S., et al. 2019, *Mon. Not. R. Astron. Soc.*, 486, 4638
van der Marel, N., van Dishoeck, E. F., Bruderer, S., Pérez, L., & Isella, A. 2015, *Astron. Astrophys.*, 579, A106
van der Plas, G., Ménard, F., Canovas, H., et al. 2017, *Astron. Astrophys.*, 607, A55
van Terwisga, S. E., van Dishoeck, E. F., Mann, R. K., et al. 2020, *Astron. Astrophys.*, 640, A27
Veronesi, B., Paneque-Carreño, T., Lodato, G., et al. 2021, *Astrophys. J. Lett.*, 914, L27
Veronesi, B., Ragusa, E., Lodato, G., et al. 2020, *Mon. Not. R. Astron. Soc.*, 495, 1913
Villenave, M., Benisty, M., Dent, W. R. F., et al. 2019, *Astron. Astrophys.*, 624, A7
Villenave, M., Ménard, F., Dent, W. R. F., et al. 2021, *Astron. Astrophys.*, 653, A46
Visser, R., van Dishoeck, E. F., & Black, J. H. 2009, *Astron. Astrophys.*, 503, 323
Warren, S. G. & Brandt, R. E. 2008, Journal of Geophysical Research (Atmospheres), 113, D14220
Weber, P., Casassus, S., & Pérez, S. 2022, *Mon. Not. R. Astron. Soc.*, 510, 1612
Weidenschilling, S. J. 1977, *Mon. Not. R. Astron. Soc.*, 180, 57
Williams, J. P. & Best, W. M. J. 2014, *Astrophys. J.*, 788, 59
Williams, J. P., Cieza, L., Hales, A., et al. 2019, *Astrophys. J. Lett.*, 875, L9
Wilner, D. J., D'Alessio, P., Calvet, N., Claussen, M. J., & Hartmann, L. 2005, *Astrophys. J. Lett.*, 626, L109
Wilson, T. L., Rohlfs, K., & Huttemeister, S. 2012, Tools of Radio Astronomy, 5th edition
Wilson, T. L. & Rood, R. 1994, *Ann. Rev. of Astron. Astrophys.*, 32, 191
Wolszczan, A. & Frail, D. A. 1992, *Nature*, 355, 145
Zawadzki, B., Czekala, I., Loomis, R. A., et al. 2023, *Publ. Astron. Soc. Pac.*, 135, 064503
Zhu, Z., Andrews, S. M., & Isella, A. 2018, *Mon. Not. R. Astron. Soc.*, 479, 1850
Zubko, V. G., Mennella, V., Colangeli, L., & Bussoletti, E. 1996, *Mon. Not. R. Astron. Soc.*, 282, 1321

List of Publications

Refereed publications

Pietro Curone, Andrés F. Izquierdo, Leonardo Testi, Giuseppe Lodato, Stefano Facchini, Antonella Natta, Paola Pinilla, Nicolas T. Kurtovic, Claudia Toci, Myriam Benisty, Marco Tazzari, Francesco Borsa, Marco Lombardi, Carlo F. Manara, Enrique Sanchis, Luca Ricci, *A giant planet shaping the disk around the very low-mass star CIDA 1*, 2022, A&A, 665, A25.

Pietro Curone, Leonardo Testi, Enrique Macías, Marco Tazzari, Stefano Facchini, Jonathan P. Williams, Cathie J. Clarke, Antonella Natta, Giovanni Rosotti, Claudia Toci, Giuseppe Lodato, *Radio multiwavelength analysis of the compact disk CX Tau: Presence of strong free-free variability or anomalous microwave emission*, 2023, A&A, 677, A118.

Publications in preparation

Pietro Curone, Stefano Facchini, Leonardo Testi, and the exoALMA collaboration, *Analysis of the continuum emission in the exoALMA sample*.

Acknowledgments

Below, I report for completeness the formal acknowledgements sections of the individual projects presented in this Thesis:

- **Chapter 5: Modeling planet-disk interactions in the disk around the very low-mass star CIDA 1**
  We thank the anonymous referee for the constructive comments that helped improve this paper. This work was partly supported by the Italian Ministero dell Istruzione, Università e Ricerca through the grant Progetti Premiali 2012 – iALMA (CUP C52I13000140001), by the Deutsche Forschungs-gemeinschaft (DFG, German Research Foundation) - Ref no. 325594231 FOR 2634/1 TE 1024/1-1, and by the DFG cluster of excellence Origins (www.origins-cluster.de). This project has received funding from the European Union's Horizon 2020 research and innovation programme under the Marie Sklodowska-Curie grant agreement No. 823823 (RISE DUSTBUSTERS project) and from the European Research Council (ERC) via the ERC Synergy Grant *ECOGAL* (grant 855130). This paper makes use of the following ALMA data: ADS/JAO.ALMA#2018.1.00536.S, ADS/JAO.ALMA#2015.1.00934.S, and ADS/JAO.ALMA#2016.1.01511.S. ALMA is a partnership of ESO (representing its member states), NSF (USA) and NINS (Japan), together with NRC (Canada), MOST and ASIAA (Taiwan), and KASI (Republic of Korea), in cooperation with the Republic of Chile. The Joint ALMA Observatory is operated by ESO, AUI/NRAO and NAOJ. M.T. has been supported by the UK Science and Technology research Council (STFC) via the consolidated grant ST/S000623/1, and by the European Union's Horizon 2020 research and innovation programme under the Marie Sklodowska-Curie grant agreement No. 823823 (RISE DUSTBUSTERS project).

- **Chapter 8: Multiwavelength analysis of the compact disk CX Tau**
  We thank the anonymous referee for the highly valuable feedback that contributed to improving this paper. This work was partly supported by the Italian Ministero dell Istruzione, Università e Ricerca through the grant Progetti Premiali 2012 – iALMA (CUP C52I13000140001), by the Deutsche Forschungs-gemeinschaft (DFG, German Research Foundation) - Ref no. 325594231 FOR 2634/1 TE 1024/1-1, and

by the DFG cluster of excellence Origins (www.origins-cluster.de). This project has received funding from the European Union's Horizon 2020 research and innovation programme under the Marie Sklodowska-Curie grant agreement No. 823823 (RISE DUSTBUSTERS project) and from the European Research Council (ERC) via the ERC Synergy Grant *ECOGAL* (grant 855130). S.F. is funded by the European Union under the European Union's Horizon Europe Research & Innovation Programme 101076613 (UNVEIL). G.R. acknowledges support from the Netherlands Organisation for Scientific Research (NWO, program number 016.Veni.192.233). Funded by the European Union (ERC DiscEvol, project number 101039651). Views and opinions expressed are however those of the author(s) only and do not necessarily reflect those of the European Union or the European Research Council Executive Agency. Neither the European Union nor the granting authority can be held responsible for them. This paper makes use of the following ALMA data: ADS/JAO.ALMA#2013.1.00426.S,and ADS/JAO.ALMA#2016.1.00715.S. ALMA is a partnership of ESO (representing its member states), NSF (USA) and NINS (Japan), together with NRC (Canada), MOST and ASIAA (Taiwan), and KASI (Republic of Korea), in cooperation with the Republic of Chile. The Joint ALMA Observatory is operated by ESO, AUI/NRAO and NAOJ.

These three years of my PhD have been an incredible journey, and I am amazed by the growth I have experienced both as a scientist and as an individual. I genuinely hope to maintain this level of personal and professional development in the future. Now, I would like to extend my gratitude to all those who supported me during this period.

First and foremost, I express my deepest thanks to my supervisor, Leonardo Testi. Since my time as a Master's student, you believed in me, offering consistent and thoughtful guidance. Your direction in all the projects and proposals, along with your broad perspective, energy, and passion for science, will always be invaluable to me. I am honored to have been your PhD student, and I am sure that I will continue seeking your insights. My gratitude also extends to my co-supervisors, Marco Lombardi and Francesco Borsa, for providing diverse perspectives on the topics I encountered.

A special acknowledgment goes to Giuseppe Lodato for paving the way for me in this fascinating research field. Our discussions and your meticulous and logical reasoning have contributed significantly to my learning. I wish to express my profound gratitude to Stefano Facchini for the assistance provided since I was a Master's student. You have truly been a mentor to me. Thank you for giving me the chance to join the exoALMA collaboration. My thanks also go to Enrique Macías, from whom I gained valuable insights into interferometric observations during my year at ESO. I really appreciated your kindness and precision in all our discussions. A heartfelt thanks to Giovanni Rosotti for all the insightful suggestions you gave me. I am grateful to Antonella Natta for consistently providing precious comments. Anna Miotello and Carlo Manara, thank you for your help and support during my time in Munich.

I am deeply thankful to Jonathan Williams for exceptional support during my memorable months in Hawaii. Your enthusiasm and dedication were a source of inspiration and I sincerely appreciated your guidance on the exciting spectroastrometry project that broadened my expertise. I also want to express my thanks to Myriam Benisty and Gaël Chauvin for their unforgettable kindness when we met in Hawaii. Myriam, I am genuinely grateful for your warm hospitality in Nice, invaluable assistance across various projects and proposals and the help concerning my upcoming experience in Chile.

I would like to express my gratitude to Laura Pérez and Cornelis Dullemond for their constructive feedback on this Thesis, and to Cornelis and François Ménard for agreeing to be part of the committee for my defense.

A huge thank you to my PhD "bros" Cristiano and Simone. I feel very lucky to have embarked on this adventure alongside you both. Your friendship was a key part in making this PhD a fantastic journey. Special thanks to Marina, Giovanni, and Rossella (and, of course, Annamaria). Sharing the office with all of you has been a truly wonderful experience that I will always cherish. To the next generation of Milan PhD students—Alessandro, Luigi, Luna, and Viviana—I extend my best wishes. You are fortunate, as I was, to share this incredible experience with great colleagues and friends. Take the opportunity and make the most of it!

I would like to thank Andrés for his friendship and for always being a source of inspiration for me. Claudia, thank you for your invaluable help and welcoming attitude. I also extend my thanks to Francesco: talking with you has been illuminating since our days as bachelor's students in Pavia. Here is a probably non-exhaustive list

of people I've encountered over these three years whom I would like to thank: Martina, Benni, Nico, Enrico, Chiara, Giulio, Guglielmo, Alessia, Ugo and the ECOGAL collaboration, the Kinky Kids (Joe, Daniele, Andrés again, Brianna, Maria, Caitlyn, Tom) and the entire exoALMA collaboration. I am grateful also to the people I had the privilege to meet during my experience in Munich at ESO: Domi, Luca (see you in Santiago!), Marta, Justyn, Chi Yan, Aashish, Teresa, Victor, Adrien, Haochang, Rik, Łukasz, Aish, Josh, Stephen, Matti, Zsofi, Andrea, Ivanna, Keegan, Samuel, Simon, Alonso, Tuts, Claudia, Elena, Pierrick, and my great officemate Tadeja. Thanks also to Alexa and Adolfo whom I encountered while in Hawaii. A special and unique thank you goes to Alice.

Infine, il ringraziamento più grande va a mio fratello Giulio, mia mamma Marzia e mia papà Franco. Mi avete insegnato valori fondamentali quali l'educazione, la correttezza, l'etica del lavoro, l'autoironia e molto, molto altro. Mi avete dato pieno supporto in ogni occasione, sostenendomi sempre lungo la mia strada. Grazie di tutto!